2010

OPTICAL SPECTROSCOPY AND NEBULAR OXYGEN ABUNDANCES OF THE SPITZER/SINGS GALAXIES

J Moustakas

R Kennicutt

C Tremontt

D Dale5

J Smith

See next page for additional authors

Recommended Citation

Moustakas, J; Kennicutt, R; Tremontt, C; Dale5, D; Smith, J; and Calzetti, D, "OPTICAL SPECTROSCOPY AND NEBULAR OXYGEN ABUNDANCES OF THE SPITZER/SINGS GALAXIES" (2010). *Astronomy Department Faculty Publication Series*. 961.
10.1088/0067-0049/190/2/233

ApJS, in press
Preprint typeset using LaTeX style emulateapj v. 11/10/09

OPTICAL SPECTROSCOPY AND NEBULAR OXYGEN ABUNDANCES OF THE *SPITZER*/SINGS GALAXIES

John Moustakas[1], Robert C. Kennicutt, Jr.[2,3], Christy A. Tremonti[4], Daniel A. Dale[5], John-David T. Smith[6], Daniela Calzetti[7]

ApJS, in press

ABSTRACT

We present intermediate-resolution optical spectrophotometry of 65 galaxies obtained in support of the *Spitzer* Infrared Nearby Galaxies Survey (SINGS). For each galaxy we obtain a nuclear, circumnuclear, and semi-integrated optical spectrum designed to coincide spatially with mid- and far-infrared spectroscopy from the *Spitzer Space Telescope*. We make the reduced, spectrophotometrically calibrated one-dimensional spectra, as well as measurements of the fluxes and equivalent widths of the strong nebular emission lines, publically available. We use optical emission-line ratios measured on all three spatial scales to classify the sample into star-forming, active galactic nuclei (AGN), and galaxies with a mixture of star formation and nuclear activity. We find that the relative fraction of the sample classified as star-forming versus AGN is a strong function of the integrated light enclosed by the spectroscopic aperture. We supplement our observations with a large database of nebular emission-line measurements of individual H II regions in the SINGS galaxies culled from the literature. We use these ancillary data to conduct a detailed analysis of the radial abundance gradients and average H II-region abundances of a large fraction of the sample. We combine these results with our new integrated spectra to estimate the central and characteristic (globally-averaged) gas-phase oxygen abundances of all 75 SINGS galaxies. We conclude with an in-depth discussion of the absolute uncertainty in the nebular oxygen abundance scale.

Subject headings: atlases — galaxies: abundances — galaxies: fundamental parameters — galaxies: ISM — galaxies: stellar content — techniques: spectroscopic

1. INTRODUCTION

The *Spitzer* Infrared Nearby Galaxies Survey (SINGS) was designed to investigate the star formation and dust emission properties of 75 nearby galaxies using the full complement of instruments available on the *Spitzer Space Telescope* (Kennicutt et al. 2003a). With the survey now complete, SINGS has delivered to the astrophysics community among the most detailed mid- and far-infrared wide-field images and spectral maps of nearby galaxies ever obtained.[8]

Supplemented with ancillary multi-wavelength observations from the ultraviolet (UV) to the radio, these data have facilitated a wide range of studies of the global and small-scale interstellar medium (ISM) properties of galaxies and active galactic nuclei (AGN), including: analyses of the mid-infrared nebular, aromatic, and molecular hydrogen spectra of galactic nuclei and extranuclear H II regions (Smith et al. 2004, 2007; Roussel et al. 2007; Prescott et al. 2007; Dale et al. 2006, 2009); the construction of broadband $0.15 - 850$ μm galaxy spectral energy distributions (SEDs; Dale et al. 2005, 2007), and their interpretation using physical dust models (Draine et al. 2007; Muñoz-Mateos et al. 2009a,b); detailed studies of the mid- and far-infrared morphologies of both low-mass dwarfs (Cannon et al. 2006a,b; Walter et al. 2007) and massive early- and late-type galaxies (Regan et al. 2004; Murphy et al. 2006; Bendo et al. 2007); and the development of robust global and spatially resolved optical and infrared (IR) star formation rate (SFR) diagnostics (Calzetti et al. 2005, 2007, 2010; Kennicutt et al. 2007, 2009; Boquien et al. 2009, 2010), among others.

In addition to imaging and spectroscopy with *Spitzer*, SINGS has also assembled a large, homogeneous database of multi-wavelength observations designed to maximize the scientific impact and legacy value of the survey (Kennicutt et al. 2003a; Meurer et al. 2006; Dale et al. 2005; Daigle et al. 2006; Dale et al. 2007; Calzetti et al. 2007; Braun et al. 2007; Dicaire et al. 2008; Walter et al. 2008). As part of this larger effort, this paper presents intermediate-resolution, ($\sim$ 8 Å FWHM), high signal-to-noise ratio (S/N = $5 - 100$ pixel^{-1}) optical ($3600 - 6900$ Å) spectrophotometry of the SINGS galaxies on several spatial scales designed to match the coverage of the *Spitzer* spectroscopy, ranging from the inner nucleus, to spectra that enclose a significant fraction ($30\% - 100\%$) of the integrated optical light. In addition to making the reduced one-dimensional spectra publically available, we also provide measure-

[1] Center for Astrophysics and Space Sciences, University of California, San Diego, 9500 Gilman Drive, La Jolla, California, 92093
[2] Institute of Astronomy, University of Cambridge, Madingley Road, Cambridge CB3 0HA, UK
[3] Steward Observatory, University of Arizona, 933 N Cherry Ave., Tucson, AZ 85721
[4] Department of Astronomy, University of Wisconsin-Madison, 4524 Sterling Hall, 475 N. Charter Street, Madison, WI 53706
[5] Department of Physics and Astronomy, University of Wyoming, Laramie, WY, 82071
[6] Department of Physics and Astronomy, University of Toledo, Ritter Obs., MS #113, Toledo, OH 43606
[7] Department of Astronomy, University of Massachusetts, 710 N. Pleasant Street, Amherst, MA 01003
[8] Publically available at http://sings.stsci.edu and http://irsa.ipac.caltech.edu/data/SPITZER/SINGS.

ments of the strong nebular emission lines corrected for underlying stellar absorption using state-of-the-art stellar population synthesis models.

These optical spectra provide a valuable complement to the SINGS multi-wavelength dataset in several respects. First, the calibrated emission-line spectra provide measures of the instantaneous SFR and dust reddening that can be compared to independent measures of SFRs and extinctions derived from the UV and IR (e.g., Kennicutt et al. 2009; Calzetti et al. 2007, 2010; Rieke et al. 2009). The forbidden-line spectra provide gas-phase metal abundances and constrain the nature of the primary ionizing radiation sources (i.e., AGN vs. star formation), both of which are important for interpreting the infrared line spectra and SEDs, and for probing dependences of the dust properties and star formation on metallicity (e.g., Smith et al. 2007; Draine et al. 2007). Finally the optical stellar continuum provides valuable constraints on the stellar populations, and the properties of the stars that are responsible for heating the dust (e.g., Gordon et al. 2000; Cortese et al. 2008).

In this paper we combine our optical spectra with spectroscopy of individual H II regions culled from the literature to derive the nebular (gas-phase) metallicities[9] of the SINGS galaxies. Dust grains, which absorb and reradiate a significant fraction of the bolometric luminosity of a galaxy into the IR, are composed of heavy elements such as C, O, Mg, Si, and Fe (Draine 2003). Therefore, the infrared SED of a galaxy is fundamentally related to its chemical composition. For example, numerous studies have reported a link between the observed deficit of polycyclic aromatic hydrocarbon (PAH) emission in the mid-IR of galaxies more metal-poor than a threshold gas-phase oxygen abundance of $12 + \log(\mathrm{O/H}) \approx 8.1$ (e.g., Madden 2000; Engelbracht et al. 2005, 2008), which may be due, in part, to a paucity of metals from which to form these complex molecules (e.g., Draine et al. 2007). Integrated and monochromatic infrared SFR calibrations must also carefully consider metallicity effects, as galaxies at UV/optical wavelengths become increasingly transparent with decreasing metallicity and dust content (e.g., Draine et al. 2007; Calzetti et al. 2007, 2010; Zhu et al. 2008).

We organize the remainder of the paper as follows. In §2 we briefly describe the SINGS sample, present our optical spectrophotometry and measurements of the fluxes and equivalent widths of the strong optical emission lines, and describe our spectroscopic database of H II regions in the SINGS galaxies. We classify the sample into star-forming galaxies and AGN in §3, and present a detailed analysis of the nebular oxygen abundances of the sample based on an analysis of our optical spectra and the H II-region observations in §4. In §5 we provide a detailed discussion of the discrepancy among abundances derived using different strong-line methods. Finally, we summarize our results in §6.

2. OBSERVATIONS

[9] Unless otherwise indicated, in this paper we use the term *metallicity* to mean the gas-phase oxygen-to-hydrogen abundance ratio, $12 + \log(\mathrm{O/H})$. For reference, the currently favored solar oxygen abundance in these units is $12 + \log(\mathrm{O/H})_\odot = 8.69 \pm 0.05$ (Asplund et al. 2009).

2.1. *SINGS Sample and Properties*

The SINGS galaxies were selected using three principal criteria — morphology, optical luminosity, and infrared-to-optical luminosity ratio — such that the sample would span the broadest possible range of star formation and dust properties exhibited by nearby, normal galaxies (Kennicutt et al. 2003a). An approximate distance limit, $D \lesssim 30$ Mpc, was also imposed so that the interstellar medium could be studied with adequate spatial resolution with *Spitzer*. Galaxies hosting powerful AGN were intentionally excluded from the sample as a more complete sample of AGNs have been observed as part of complementary *Spitzer* Guaranteed Time Observer (GTO) programs (e.g., Weedman et al. 2005; Wu et al. 2009).

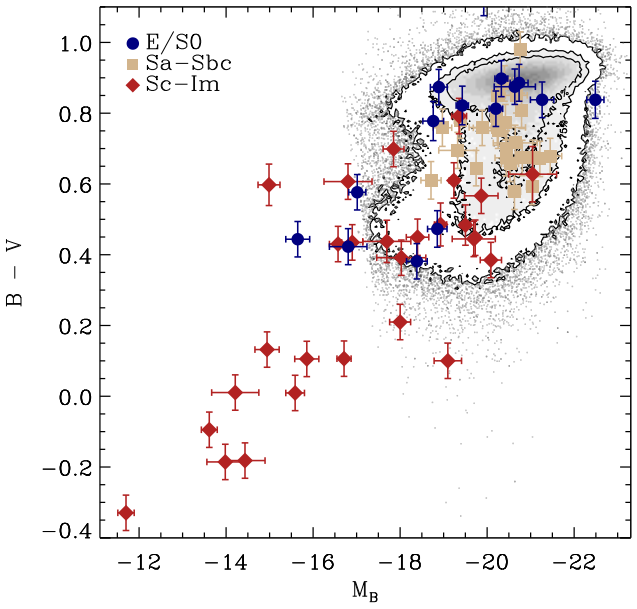

FIG. 1.— Optical color-magnitude diagram for the SINGS galaxies coded by morphological type: E/S0 (*dark blue points*), Sa-Sbc (*tan squares*), and Sc-Im (*dark red diamonds*). For comparison, the contoured greyscale image shows the color-magnitude diagram of a flux-limited sample of $\sim 5 \times 10^5$ SDSS galaxies. This figure demonstrates the broad range of optical luminosity and color spanned by the SINGS sample.

Table 1 presents some basic properties of the sample used in the current analysis. The table includes an updated set of distances based on a careful search of the literature. For galaxies without a direct distance estimate (e.g., from observations of Cepheid variables), we use their Hubble distance corrected for peculiar motions (Masters 2005) assuming $H_0 = 70$ km s^{-1} Mpc^{-1}. Optical B- and V-band photometry for the SINGS sample has been taken either from Muñoz-Mateos et al. (2009a) or Dale et al. (2007), listed in order of preference. The photometry in Muñoz-Mateos et al. (2009a) for 54/75 galaxies is based on a careful curve-of-growth analysis and recalibration of imaging available in the literature (Prugniel & Heraudeau 1998; Dale et al. 2007). They provide asymptotic (integrated) B- and V-band magnitudes for 22 of these objects, and integrated *ugriz* magnitudes from the SDSS (York et al. 2000) for the other 32 galaxies. The SDSS magnitudes were transformed

to B- and V-band magnitudes using the statistical linear transformations derived by Blanton & Roweis (2007) based on a large sample of SDSS galaxies. The absolute B-band magnitudes, M_B, and $B-V$ colors in Table 1 have been corrected for foreground Galactic reddening (Schlegel et al. 1998) and converted to the Vega system using the AB-to-Vega conversions in Blanton & Roweis (2007). We adopt a minimum photometric error of 10% and 5% in M_B and $B-V$, respectively.

One of the strengths of the SINGS sample is that it was designed to span a broad range of galaxy properties. We illustrate this point in Figure 1 where we plot $B-V$ versus M_B of the full sample, divided into three bins of morphological type. For comparison, we show the corresponding color-magnitude diagram for a flux-limited ($r_{\rm AB} < 17.6$) sample of $\sim 5\times10^5$ SDSS galaxies at $0.01 < z < 0.25$ selected from the NYU Value-Added Galaxy Catalog[10] (NYU-VAGC; Blanton et al. 2005) and the SDSS Data Release 7 (DR7; Abazajian et al. 2009). The rest-frame luminosities of the SDSS galaxies were estimated using K-CORRECT (v. 4.1.4; Blanton & Roweis 2007).[11] Among bright ($M_B < -18$) galaxies, the two samples span a comparable range of luminosity and color, whereas the SINGS sample includes a significant number of faint blue galaxies.

2.2. *Nuclear, Circumnuclear, and Radial-Strip Spectroscopy*

2.2.1. *Observations & Reductions*

The overall strategy guiding our optical observing program was to complement the mid- and far-infrared spectra of the SINGS sample obtained as part of the principal *Spitzer* observations (Kennicutt et al. 2003a; Smith et al. 2007; Dale et al. 2009). Briefly, the infrared observations produce low-resolution ($\mathcal{R}\approx100$) $5-15$ μm spectral cubes of the central $34''\times55''$ of each galaxy, and $10-37$ μm spectral cubes of the inner $18''\times24''$ at higher resolution, $\mathcal{R}\approx600$, using the IRS spectrograph (Houck et al. 2004).[12] In addition, there are $15-38$ μm radial strip IRS spectra at $\mathcal{R}\approx100$ enclosing a $56''$ wide rectangular aperture that extend over $30\%-100\%$ of the optical diameter of each galaxy, and complementary low-resolution ($\mathcal{R}\approx15$) $55-95$ μm radial strip spectra of approximately the same region using the MIPS instrument in SED mode (Rieke et al. 2004).

The optical spectra were obtained between 2001 November and 2006 May at the Bok 2.3-meter telescope on Kitt Peak for galaxies in the northern hemisphere, and at the CTIO 1.5-meter telescope for galaxies in the southern hemisphere. At the Bok telescope we used the B&C spectrograph and a 400 mm^{-1} grating, blazed at $\sim$ 5200 Å, to obtain spectral coverage from $3600-6900$ Å at $\sim$ 8 Å FWHM ($\mathcal{R}\approx700$) resolution through a $200''\times2\farcs5$ slit. The CTIO observations were obtained using the R-C spectrograph and a 300 mm^{-1} grating (#9), blazed at $\sim$ 4000 Å, which provided spectral coverage from $3450-6900$ Å at $\sim$ 8.5 Å FWHM ($\mathcal{R}\approx600$) resolution through a $460''\times3''$ slit.

We used the long-slit drift-scanning technique pioneered by Kennicutt (1992a) to obtain integrated optical spectra over the same physical area targeted by the IRS and MIPS observations. Drift-scanning consists of driving a long-slit back-and-forth perpendicular to the slit during a single exposure in order to build a luminosity-weighted integrated spectrum of a large spatially extended area at the spectral resolution of a narrow slit (Kennicutt 1992a; Jansen et al. 2000; Gavazzi et al. 2004; Moustakas & Kennicutt 2006a). For each object we obtained a circumnuclear spectrum targeting the central regions of each galaxy, and a large rectangular radial-strip spectrum spatially coincident with the IRS and MIPS observations (see below). We also obtained a pointed (spatially fixed) spectrum centered on the nucleus of each object. The total exposure time for the radial strip, circumnuclear, and nuclear spectra ranged from $20-60$, $10-30$, and $5-10$ minutes, respectively, usually split into two or more exposures to allow cosmic rays to be identified.

The data reduction steps consisted of overscan- and bias-subtraction, flat-fielding, a correction for the varying illumination pattern, and sky subtraction (see Moustakas & Kennicutt 2006a for details). We combined multiple exposures using inverse variance weighting while iteratively rejecting cosmic rays. The galaxies in SINGS with the largest projected angular diameters usually required multiple pointings to achieve full spatial coverage of the corresponding infrared spectra, or to ensure that the sky was adequately sampled. For these objects we obtained $2-6$ overlapping spectra, which we subsequently stitched together by examining the spatial profiles in the overlap region. Flux-calibration was facilitated by observations of standard stars selected from the *HST*/CALSPEC[13] (Bohlin et al. 2001) and Massey et al. (1988) star lists. We estimate that our *relative* spectrophotometric accuracy is $\lesssim\pm5\%$ across the full spectral range (see also Moustakas & Kennicutt 2006a).

We extracted one-dimensional spectra using a $2\farcs5\times2\farcs5$ (or $2\farcs5\times3\farcs0$ for the CTIO spectra) and $20''\times20''$ aperture for each nuclear and circumnuclear spectrum, respectively. The radial strip spectra were extracted over a $(0.55\times D_{25})\times\Delta_{\rm scan}$ arcsec^2 rectangular region, where D_{25} is the major-axis diameter of each galaxy (see Table 1) and $\Delta_{\rm scan}=56''$ (in some cases $55''$) is the drift-scan length perpendicular to the slit. The position angle and drift-scan length of each radial-strip spectrum was chosen to maximize the spatial overlap with the corresponding IRS spectra having at least double coverage in both spectral orders (see Appendix A and Smith et al. 2004 for more details). Finally, all the spectra were corrected for foreground Galactic reddening (O'Donnell 1994; Schlegel et al. 1998) assuming $R_V\equiv A_V/E(B-V)=3.1$ (see Table 1).

Table 2 summarizes our observations; we present the data themselves in Appendix A. We obtained at least one optical spectrum for 65 galaxies, or 87% of the SINGS sample. Three of the ten objects without any spectra—NGC 5408, IC 4710, and NGC 7552— are in the southern hemisphere and were not accessible during the 2001 December CTIO observing run. The remaining seven

[10] http://sdss.physics.nyu.edu/vagc

[11] http://howdy.physics.nyu.edu/index.php/Kcorrect

[12] The center of NGC 3034=M 82 was a reserved target; therefore, it was not mapped by SINGS with the IRS instrument, although we did obtain optical spectra of its center (see Appendix A).

[13] http://www.stsci.edu/hst/observatory/cdbs/calspec.html

galaxies lacking an optical spectrum— Ho II, M 81 Dw A, Ho I, Ho IX, DDO 154, DDO 165, and NGC 6822— are faint, low surface-brightness dwarfs for which we were unable to obtain usable data. In total, we obtained nuclear, circumnuclear, and radial-strip spectra for 57, 65, and 62 of the SINGS galaxies, respectively.

In Figure 2 we characterize the range of spatial scales spanned by our observations by plotting the distribution of B-band light fraction and the physical area (in kpc^2) subtended by our nuclear, circumnuclear, and radial-strip spectra. The light fractions were measured from the B-band images of the SINGS galaxies by projecting the rectangular apertures listed in Table 2 and computing the fraction of light within each aperture relative to the integrated flux (Dale et al. 2007). Our circumnuclear spectra enclose $0.54\% - 80\%$ of the integrated optical light, with a typical (median) value of 12%, while our radial-strip spectra enclose $16\% - 96\%$ of the integrated light, with a median value of 49%. Therefore, our circumnuclear and radial-strip spectra should be representative of the central and integrated (globally averaged) optical properties, respectively, of most of the galaxies in the sample (Kewley et al. 2005).

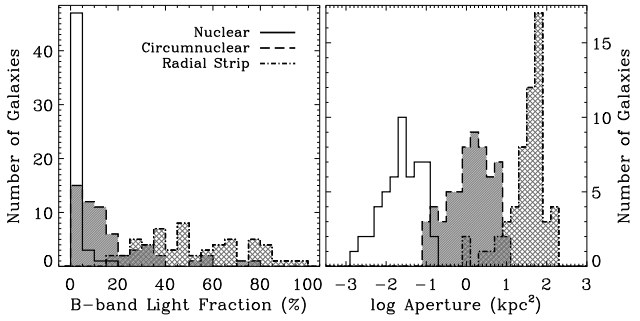

FIG. 2.— Distribution of (*left*) B-band light fraction and (*right*) physical area (in kpc^2) subtended by our nuclear (*solid*), circumnuclear (*dashed*), and radial-strip (*dot-dashed*) spectra. The median light fraction enclosed by our nuclear, circumnuclear, and radial-strip spectra is 0.84%, 12%, and 49%, respectively, corresponding to a physical area of 0.17×0.17 kpc^2, 1.2×1.2 kpc^2, and 6.6×6.6 kpc^2. Thus, our radial-strip spectra should be representative of the integrated (globally-averaged) properties of the sample for most objects, while our circumnuclear spectra should be representative of the central regions of most galaxies.

2.2.2. *Optical Emission-Line Measurements*

With the latest generation of high-resolution stellar population synthesis models it has become possible to separate accurately the stellar continuum spectrum of a galaxy from its integrated emission-line spectrum, so that the emission-line strengths can be studied free from the systematic effects of Balmer and metal-line absorption (e.g., Brinchmann et al. 2004; Cid Fernandes et al. 2005; Moustakas & Kennicutt 2006a; Asari et al. 2007).

We fit each spectrum using the Bruzual & Charlot (2003, hereafter BC03) stellar population synthesis models assuming the Chabrier (2003) initial mass function between 0.1 and 100 $\mathcal{M}_\odot$. We model the data as a non-negative linear combination of ten BC03 models with ages ranging between 5 Myr and 13 Gyr and three different metallicities: $Z = 0.004$, 0.02, 0.05. We derive the best-fitting model, separately for each stellar metallicity, using a modified version of the pPXF[14] continuum-fitting code (Cappellari & Emsellem 2004). First, we isolate the $3700 - 4850$ Å spectral range to derive the absorption-line redshift of the galaxy, $z_{\rm abs}$, and an estimate of the velocity dispersion, $\sigma_{\rm disp}$, deconvolved for the instrumental resolution of our spectra and the BC03 models. Next, we model the full spectral range, fixing $z_{\rm abs}$ and $\sigma_{\rm disp}$ at the derived values and aggressively mask pixels that may be affected by emission lines, sky-subtraction residuals, or telluric absorption. We treat reddening as a free parameter assuming the Calzetti et al. (2000) dust attenuation law. Finally, we choose the stellar metallicity that results in the best fit (i.e., lowest reduced χ^2).

We emphasize that our principal objective in modeling the underlying stellar continuum is to obtain a pure emission-line spectrum that has been corrected self-consistently for stellar absorption, *not* to constrain star-formation history and stellar metallicity within each spectroscopic aperture. Star-formation history, age, metallicity, and dust reddening are notoriously degenerate, which means that the multidimensional parameter space is a very complex manifold that likely contains numerous local minima. Our simple χ^2 minimization algorithm is ill-suited for solving this kind of problem, although more general methods for inferring these quantities from integrated optical spectra have been developed (e.g., Panter et al. 2003; Gallazzi et al. 2005; Ocvirk et al. 2006; Cid Fernandes et al. 2007; Tojeiro et al. 2007; Blanton & Roweis 2007). For our purposes, we have verified that varying our model assumptions does not significantly impact the measured emission-line strengths. Specifically, we checked that fixing the stellar metallicity of the models to solar, adopting a different extinction law (e.g., O'Donnell 1994; Charlot & Fall 2000; Gordon et al. 2003), assuming a different initial mass function (Salpeter 1955), or changing the number of model ages yields emission-line strengths that are within the statistical uncertainties for most objects.

Given the best-fitting stellar continuum, we subtract it from the data to obtain a pure emission-line spectrum corrected for stellar absorption. Next, we remove any remaining residuals (typically of order a few percent) due to imperfect sky-subtraction or template mismatch using a 51-pixel sliding median. Finally, we model the strong optical emission lines — [O II] λ3727, Hγ λ4340, Hβ λ4861, [O III] $\lambda\lambda$4959, 5007, [N II] $\lambda\lambda$6548, 6584, Hα λ6563, and [S II] $\lambda\lambda$6716, 6731 — as individual Gaussian line-profiles using a modified version of the GANDALF[15] emission-line fitting code (Sarzi et al. 2006; Schawinski et al. 2007), constraining the [O III] λ5007/[O III] λ4959 and [N II] λ6584/[N II] λ6548 doublet ratios to be 3:1 (Osterbrock & Ferland 2006). We perform the emission-line fitting in two iterations. First, we tie the redshifts and intrinsic velocity widths (deconvolved for the instrumental resolution) of the forbidden and Balmer lines together to aid in the detection and deblending of weak lines (Tremonti et al. 2004). On the second iteration

[14] http://www-astro.physics.ox.ac.uk/∼mxc/idl
[15] http://www.strw.leidenuniv.nl/sauron

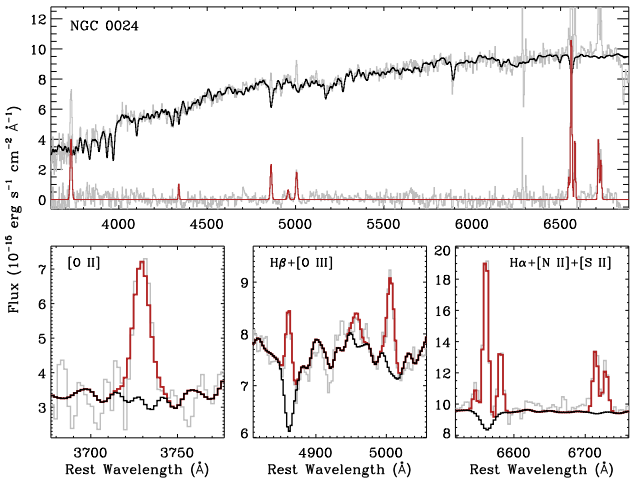

FIG. 3.— Demonstration of our stellar continuum and emission-line fitting technique applied to the circumnuclear spectrum of NGC 0024. In the top panel we plot the observed spectrum (*grey*) and the best-fitting continuum model (*black*), where the limits of the plot have been chosen to emphasize the stellar continuum over the emission lines. For reference, the best-fitting continuum spectrum at this spatial scale of NGC 0024 has $Z = 0.02$, a luminosity-weighted age of ~ 10 Gyr, and $E(B-V) = 0.048$ mag of dust reddening, although as we emphasize in §2.2.2 these physical quantities should not be overinterpreted. In the lower portion of the top panel we plot the residual (continuum-subtracted) spectrum (*grey, centered around zero flux*) and the best-fitting emission-line spectrum (*dark red*). The bottom three panels show zoomed-in portions of the data and best-fitting model centered around [O II] λ3727, Hβ and [O III] $\lambda\lambda$4959, 5007, and Hα, [N II] $\lambda\lambda$6548, 6584, and [S II] $\lambda\lambda$6716, 6731, from left to right. The amount of stellar absorption underlying the Hβ emission line highlights the importance of proper continuum subtraction when studying the integrated emission-line properties of galaxies.

we relax most of the constraints on the line-profiles and use the best-fitting parameters from the first iteration as initial guesses. This second step is necessary for two reasons: first, our knowledge of the wavelength-dependent instrumental resolution is imperfect, which the code can compensate for by allowing the velocity widths of the emission lines to vary with wavelength; and second [O II] λ3727 is, in fact, a doublet which is better represented at the spectral resolution of our data as a single, slightly broader Gaussian line than two closely-spaced Gaussian line-profiles. Note that even on the second iteration, however, we (separately) constrain the redshifts and velocity widths of the [O III], [N II], and [S II] doublets to have the same values.

For a handful of AGN in our sample we had to include a second, broad component for the Hα, Hβ, and Hγ Balmer lines in order to obtain a satisfactory fit to the observed line-profiles. Specifically, our nuclear spectra of the following objects required both broad and narrow Balmer lines: NGC 1566, NGC 3031, NGC 4579, NGC 4594, and NGC 5033. The emission-line contribution from the broad-line region obviously depends on the enclosed light-fraction of the spectrum. Therefore, for our circumnuclear spectrum of NGC 4594 we did *not* need to include broad Balmer lines. Finally, among our radial-strip spectra the only galaxy that required broad Balmer emission lines was NGC 1566.

Figure 3 shows an example of our stellar continuum and emission-line fitting technique applied to the circumnuclear spectrum of NGC 0024, which is typical in terms of S/N. Our best-fitting absorption- and emission-model for the central region of NGC 0024 is clearly a good representation of the data, and this result is typical (see Appendix A). In the lower-middle panel of Figure 3 we focus on the wavelengths around Hβ and the [O III] doublet to highlight the amount of stellar absorption affecting the Hβ emission line. In this example the amount of Hβ absorption is ~ 2.9 Å, a considerable fraction of the absorption-corrected emission-line equivalent width, ~ 3.5 Å, which emphasizes the importance of subtracting the underlying stellar continuum when studying the integrated emission lines of galaxies. For reference, the mean Hβ stellar absorption for the full sample is 2.5 ± 1 Å, slightly larger than the amount of absorption found by previous studies (McCall et al. 1985; Kobulnicky & Phillips 2003), presumably because of the lower instrumental resolution of our spectra.

Tables 3 and 4 list the fluxes and rest-frame equivalent widths (EWs) of the emission lines with significant detections measured from our nuclear, circumnuclear, and radial-strip spectra. We construct the EW of each line by dividing the integrated flux in each line by the mean surrounding continuum (Moustakas & Kennicutt 2006a). For the broad-line AGN identified above these tables only give the flux and EW of the narrow-line component of the Balmer lines. For the detection of a line to be considered significant we require the amplitude of the best-fitting Gaussian model to be $> 3\sigma_c$ above the residual (continuum-subtracted) spectrum, where σ_c is the standard deviation of the residual spectrum near the line. We further recommend that for most applications a minimum signal-to-noise (S/N) ratio cut S/N > 2 be applied to the fluxes and EWs given in Tables 3 and 4.

2.3. *Ancillary H II-Region Spectroscopy*

We supplement our integrated and nuclear optical spectra with previously published optical line-ratios of 561 H II regions in 38 of the SINGS galaxies (see Appendix B). These data are complementary in several respects. First, as discussed in §2.2.1, we were unable to obtain an integrated optical spectrum of most of the faint, low-surface brightness dwarfs in SINGS, which are among the most metal-poor galaxies in the sample (Kennicutt et al. 2003a; Walter et al. 2007). Fortunately, previously published optical spectroscopy of least one H II region in most of these objects exists, enabling us to estimate their gas-phase oxygen abundances self-consistently with respect to the rest of the sample (see §4.3). Second, unlike an integrated optical spectrum of a galaxy, the spectrum of an individual H II region typically exhibits a much simpler underlying stellar continuum, mitigating continuum-subtraction errors and enabling faint lines to be detected and measured. In addition, each integrated spectrum is a surface-brightness weighted average of all the H II-regions contained within the spectroscopic aperture, and likely includes contributions from diffuse- and shock-ionized gas emission (Kennicutt 1992b; Lehnert & Heckman 1994; Dopita et al. 2006b), although we do not expect these effects to be a significant source of bias in our abundance estimates (Kobulnicky et al. 1999; Pilyugin et al. 2004a; Moustakas & Kennicutt 2006b). Finally, the emission-

line spectrum of an H II-region is impervious to AGN contamination, which can be a significant source of systematic error when deriving oxygen abundances from the strong nebular lines (see §3). On the other hand, our database of H II-region line-ratios constitutes an heterogeneous compilation of data from the literature. Although we have made every effort to select only high-fidelity observations, the data are not of uniform quality for all galaxies, a point that should be kept in mind in the subsequent analysis. Appendix B contains details regarding how the emission-line database was built and tabulates the properties of each H II region used in the subsequent analysis.

3. OPTICAL SPECTRAL CLASSIFICATIONS

Neglecting the AGN contribution to the optical emission-line spectrum of a galaxy can lead to catastrophic errors in the derived oxygen abundances, particularly those that rely on the [O III]/Hβ ratio (Kewley & Ellison 2008). Therefore, we classify the SINGS galaxies into three broad categories: AGN, star-forming (SF) galaxies, and composite systems, or SF/AGN, as defined below; further separating the AGN into Seyferts (Seyfert 1943) and LINERs (Heckman 1980; Kewley et al. 2006; Ho 2008) is beyond the scope of this paper. A detailed investigation of the nuclear properties of the SINGS galaxies using both optical and infrared diagnostic diagrams has also been performed by Dale et al. (2006).

Clearly, the degree to which the observed emission-line spectrum is 'contaminated' by an AGN depends both on the level of AGN activity, and on the area (e.g., in kpc^2) subtended by the spectroscopic aperture. For example, a galaxy with an AGN-like nuclear spectrum may have a circumnuclear or radial strip spectrum that is dominated by the integrated emission from star-forming regions in the disk. In these objects, we can use the circumnuclear and radial-strip spectra to obtain a reliable estimate of the oxygen abundance, but not the nuclear spectrum. Consequently, we classify each object in SINGS using all three of our nuclear, circumnuclear, and radial strip spectra, where available.

In Figure 4 we plot the [N II] λ6584/Hα versus [O III] λ5007/Hβ emission-line diagnostic diagram (Baldwin et al. 1981; Veilleux & Osterbrock 1987), which has been shown to be a sensitive diagnostic of AGN activity (Kewley et al. 2000, 2001b; Kauffmann et al. 2003; Stasińska et al. 2006). We plot line-ratios measured from our nuclear, circumnuclear, and radial strip spectra as green triangles, orange points, and blue squares, respectively. In order to be included in this diagram all four emission lines must have S/N $>$ 2 (see §2.2.2). The contoured greyscale shows for comparison the distribution of SDSS emission-line galaxies in this diagram.[16] We use the Kewley et al. (2001a) and Kauffmann et al. (2003) classification curves to separate the SINGS galaxies into SF, AGN, and SF/AGN: we classify galaxies above and to the right of the Kewley et al. curve as AGN; galaxies below and to the left of the Kauffmann et al. curve as SF; and objects between the two curves as SF/AGN.

[16] The emission-line measurements for the SDSS sample described in §2.1 were taken from the publically available MPA/JHU database (http://www.mpa-garching.mpg.de/SDSS/DR7).

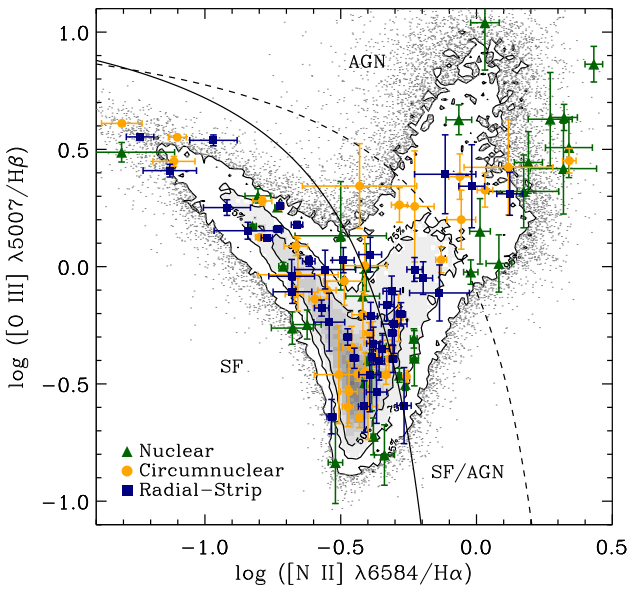

FIG. 4.— Emission-line diagnostic diagram used to separate star-forming (SF) galaxies from active galactic nuclei (AGN). We plot line-ratios based on our nuclear, circumnuclear, and radial-strip spectra using green triangles, orange points, and blue squares, respectively. The contoured greyscale shows for comparison the distribution of SDSS emission-line galaxies in this diagram. The solid and dashed lines are the empirical and theoretical boundaries between SF galaxies and AGN defined by Kauffmann et al. (2003) and Kewley et al. (2001a), respectively. We identify objects positioned above and to the right of the Kewley et al. curve as AGN, objects located below and to the left of the Kauffmann et al. curve as SF, and objects lying between the two curves as composite systems, or SF/AGN.

For some objects either Hβ or [O III] were not detected; however, we can still use the [N II]/Hα ratio to discriminate between star-forming galaxies and AGN because the star-forming galaxy sequence asymptotes to a roughly constant [N II]/Hα ratio as the [O III]/Hβ ratio diminishes (see Fig. 4; Kauffmann et al. 2003). Examining Figure 4, for these objects we adopt $\log$ ([N II]/Hα) $= -0.25$ as the boundary between AGN and star-forming galaxies.

Table 5 summarizes the results of classifying the SINGS galaxies using our optical spectra. A question mark in any of these columns indicates that we failed to detect one or more of the requisite emission lines. As a consistency check we also classified our sample using the nuclear emission-line fluxes published by Ho et al. (1997), which are available for nearly half (35/75) the SINGS sample. We find that our nuclear classifications generally agree very well with the classifications derived using the Ho et al. (1997) line-ratios.

For many applications it is useful to have a single spectral class for each galaxy, which we provide in the last column of Table 5. This final classification was generally adopted from our nuclear spectrum; therefore, the final classification tends to favor AGN. However, we emphasize that for many objects the AGN contributes negligibly to the central or integrated spectrum of the galaxy, as traced by our circumnuclear and radial-strip spectra, respectively.

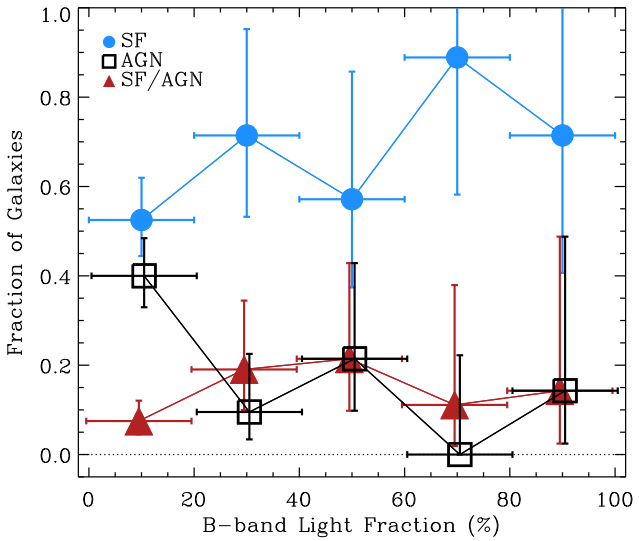

FIG. 5.— Fraction of galaxies classified as SF (*filled blue points*), AGN (*open black squares*), and SF/AGN (*filled red triangles*) as a function of the *B*-band light-fraction. At fixed light fraction the symbols have been offset slightly from one another for clarity. The asymmetric 1σ error bars are based on the number of galaxies in each bin based on the formulae in Gehrels (1986). We find a positive (negative) correlation between the fraction of objects classified as SF (AGN) with increasing light fraction, while the proportion of objects classified as SF/AGN stays roughly constant. We caution against over-interpreting these results, however, because they are sensitive to sample selection effects and incompleteness in the spectral classifications (e.g., missing classifications due to undetected emission lines.).

We illustrate this last point explicitly in Figure 5, where we plot the proportion of galaxies classified as SF, AGN, and SF/AGN as a function of the *B*-band light fraction (see §2.2.1). We find the anticipated trend that the fraction of galaxies classified as SF increases with enclosed light fraction at the expense of the proportion of objects classified as AGN, while the fraction of galaxies classified as SF/AGN remains roughly constant at $\sim 15\%$. However, we note that these results are sensitive to incompleteness in our spectral classifications (e.g., due to undetected emission lines), and to sample selection effects (e.g., SINGS intentionally excluded powerful AGN; Kennicutt et al. 2003a). These various effects should be considered carefully depending on the specific application of the derived optical classifications.

4. OXYGEN ABUNDANCE ANALYSIS

Our objective in this section is to derive the gas-phase metallicities of all 75 SINGS galaxies. There are two broad issues to consider. First, given an optical spectrum, the observed emission-line ratios must be converted into an estimate of the gas-phase metallicity, a procedure that is subject to both random and systematic uncertainties. Second, for each galaxy we often have multiple oxygen abundance estimates sampling a wide range of spatial scales; these various measurements must be combined in a sensible way to ensure a consistent set of metallicities for the full sample.

We address the first question in §4.1, where we discuss the general methodology of deriving the gas-phase metallicity of a star-forming galaxy or H II region from its observed emission-line spectrum. As numerous studies have pointed out (Kewley & Ellison 2008, and references therein), there exist large $(0.1 - 0.7$ dex) systematic discrepancies among existing empirical and theoretical methods of estimating oxygen abundances. Consequently, the *absolute* uncertainty in the nebular abundance scale is a factor of ~ 5. To explore this issue, we therefore compute oxygen abundances using two different methods. In §4.2 and §4.3 we apply these two methods to derive oxygen abundances from our nuclear, circumnuclear, and radial-strip spectra, and from our ancillary H II- region spectroscopy, respectively. We combine all the available abundance measurements for each galaxy in §4.4 based on the estimated fraction of the integrated optical light enclosed by each spectroscopic aperture, resulting in an estimate of the *central* and *characteristic*, or globally-averaged metallicity of each galaxy.

4.1. *Strong-Line Abundance Calibration*

The most direct, physically motivated method of deriving the oxygen abundance of an H II region or star-forming galaxy is to measure the electron temperature (T_e) of the ionized gas using the intensity (relative to a hydrogen recombination line) of one or more temperature-sensitive auroral line such as [O III] λ4363, [N II] λ5755, [S III] λ6312, and [O II] λ7325 (Dinerstein 1990; Skillman 1998; Garnett 2002a; Stasińska 2007). This technique is frequently referred to as the *direct*, or T_e, method of deriving abundances. Unfortunately, the requisite lines are intrinsically faint, particularly in metal-rich galaxies and star-forming regions, and in general are not detected in our spectra. Therefore, we must rely on a so-called *strong-line* abundance calibration to estimate the metallicity of the ionized gas. Strong-line abundance calibrations essentially relate the oxygen abundance to one or more line-ratios involving the strongest recombination and collisionally excited (forbidden) lines (e.g., [O II] λ3727, Hα, Hβ, [O III] $\lambda\lambda$4959, 5007, [N II] $\lambda\lambda$6548, 6584, and [S II] $\lambda\lambda$6716, 6731). Although strong-line methods are *indirect* and often model-dependent, they are important because they can be used to infer the physical conditions in star-forming galaxies across a significant fraction of cosmic time (Kennicutt 1998; Pettini 2006; De Lucia 2009); moreover, the direct method is not without its own limitations, as we discuss in §5.

Over the last three decades numerous strong-line calibrations have been developed, but in general they fall into one of three categories: semi-empirical, empirical, and theoretical. The older, *semi-empirical* calibrations were generally tied to electron temperature abundance measurements at low metallicity and photoionization models at high metallicity (e.g., Alloin et al. 1979; Pagel et al. 1979; Edmunds & Pagel 1984; McCall et al. 1985; Dopita & Evans 1986; Skillman 1989). These hybrid calibrations were born from the observational difficulty of measuring the electron temperature of metal-rich H II regions, which remains challenging even with 6 – 10-meter class telescopes (e.g., Castellanos et al. 2002; Kennicutt et al. 2003b; Garnett et al. 2004b; Bresolin et al. 2004, 2005, but see Kinkel & Rosa 1994 for a heroic early effort). By contrast, the more recent *empirical* methods are calibrated against high-quality observations of individual H II regions with measured direct (i.e., T_e-based) oxygen abundances (Pilyugin

2000, 2001; Denicoló et al. 2002; Pettini & Pagel 2004; Pilyugin & Thuan 2005; Pérez-Montero & Díaz 2005; Nagao et al. 2006; Stasińska 2006; Yin et al. 2007; Peimbert et al. 2007).[17] One of the limitations of the empirical calibrations, especially in the metal-rich regime, is that they are based on observations of relatively small samples of high-excitation H II regions, whereas most integrated spectra of galaxies exhibit softer ionizing radiation fields (see §5). Finally, the class of *theoretical* abundance calibrations are based on *ab initio* photoionization model calculations, in which various nebular emission-line ratios are tracked as a function of the input metallicity and ionization parameter (McGaugh 1991; Dopita et al. 2000, 2006a; Charlot & Longhetti 2001; Kewley & Dopita 2002).[18]

Among published strong-line calibrations there exist large, poorly understood systematic discrepancies, in the sense that empirical calibrations generally yield oxygen abundances that are factors of $1.5-5$ *lower* than abundances derived using theoretical calibrations (Kennicutt et al. 2003b; Garnett et al. 2004b; Bresolin et al. 2004, 2005; Shi et al. 2006; Nagao et al. 2006; Liang et al. 2006; Yin et al. 2007; Kewley & Ellison 2008). Unfortunately, the physical origin of this systematic discrepancy remains unresolved. Therefore, we have chosen to compute the oxygen abundances of the SINGS galaxies using two different strong-line calibrations: the theoretical calibration published by Kobulnicky & Kewley (2004, hereafter KK04), and the empirical Pilyugin & Thuan (2005, hereafter PT05) calibration. Our goal is not to conduct a detailed intercomparison of all the available calibrations (see, e.g., Kewley & Ellison 2008), but instead to bracket the range of oxygen abundances one would derive using existing strong-line calibrations. We discuss the various strengths and limitations of the abundances derived using these two calibrations in §5.

The KK04 and PT05 calibrations we have chosen both rely on the metallicity-sensitive R_{23} parameter (Pagel et al. 1979):

$$R_{23} \equiv \frac{[\mathrm{O\ II}]\ \lambda 3727 + [\mathrm{O\ III}]\ \lambda\lambda 4959, 5007}{\mathrm{H}\beta\ \lambda 4861}. \quad (1)$$

The principal advantage of R_{23} as an oxygen abundance diagnostic is that it is directly proportional to both principal ionization states of oxygen, unlike other diagnostics that have a second-order dependence on the abundance of other elements like nitrogen and sulfur. Moreover, because R_{23} depends on blue rest-wavelength lines, it can be used to study the chemical history of star-forming galaxies over a significant fraction of cosmic time (Pettini et al. 2001; Kobulnicky et al. 2003; Kobulnicky & Kewley 2004; Savaglio et al. 2005; Maiolino et al. 2008; J. Moustakas et al., in prep.). The disadvantages of R_{23} are that it is sensitive to AGN contamination, and it must be corrected for stellar absorption and dust attenuation (but see Kobulnicky & Phillips 2003; J. Moustakas et al., in prep.). An additional complication is that the relation between R_{23} and metallicity is famously double-valued (see, e.g., Fig. 6). Metal-rich objects lie on the *upper* R_{23} branch, while metal-poor galaxies and H II regions lie on the *lower* branch; the transition between the upper and lower R_{23} branches is called the *turn-around* region. The non-monotonic relation between R_{23} and O/H arises because in metal-rich star-forming regions R_{23} decreases with increasing O/H as the far-IR fine-structure lines (predominantly [O III] $\lambda 52$ μm and [O III] $\lambda 88$ μm) increasingly dominate the nebular cooling. At low metallicity, on the other hand, the optical transitions dominate the nebular cooling, and so R_{23} decreases in tandem with decreasing metallicity because its strength is directly proportional to the abundance of oxygen atoms.

For the KK04 calibration, we have

$$12+\log(\mathrm{O/H})_{\mathrm{lower}} = 9.40 + 4.65x - 3.17x^2 - \log(q)\,(0.272 + 0.547x - 0.513x^2), \quad (2)$$

and

$$12+\log(\mathrm{O/H})_{\mathrm{upper}} = 9.72 - 0.777x - 0.951x^2 - 0.072x^3 - 0.811x^4 - \log(q)\,(0.0737 - 0.0713x - 0.141x^2 + 0.0373x^3 - 0.058x^4), \quad (3)$$

for galaxies on the lower and upper branch, respectively, where $x \equiv \log(R_{23})$. The ionization parameter q in cm s^{-1} is given by

$$\log(q) = 32.81 - 1.153y^2 + z(-3.396 - 0.025y + 0.1444y^2) \times [4.603 - 0.3119y - 0.163y^2 + z(-0.48 + 0.0271y + 0.02037y^2)]^{-1}, \quad (4)$$

where $z \equiv 12+\log(\mathrm{O/H})$, $y \equiv \log(O_{32})$, and

$$O_{32} \equiv \frac{[\mathrm{O\ III}]\ \lambda\lambda 4959, 5007}{[\mathrm{O\ II}]\ \lambda 3727} \quad (5)$$

characterizes the hardness of the ionizing radiation field (Kewley & Dopita 2002). Hereafter we will use the dimensionless ionization parameter $U \equiv q/c$ where $c = 2.99\times10^{10}$ cm s^{-1} is the speed-of-light (Kewley & Dopita 2002).[19] Note that equations (2)-(4) must be solved iteratively for both the ionization parameter and the oxygen abundance; convergence is typically achieved in a handful of iterations.

For the PT05 calibration, we have

$$12+\log(\mathrm{O/H})_{\mathrm{lower}} = \frac{R_{23} + 106.4 + 106.8P - 3.40P^2}{17.72 + 6.60P + 6.95P^2 - 0.302R_{23}}, \quad (6)$$

[17] Strictly speaking, the 'empirical' calibrations presented by Pettini & Pagel (2004) and Denicoló et al. (2002) do include a handful of metal-rich H II regions whose abundances were derived using photoionization models.

[18] Confusingly, some of these theoretical calibrations are occasionally refered to as 'semi-empirical' calibrations (e.g., Kennicutt & Garnett 1996; Croxall et al. 2009).

[19] The ionization parameter also can be written as $U \propto (n_{\mathrm{e}} f^2 Q)^{1/3}$, where n_{e} is the electron density, f is the volume filling factor, and Q is the rate of photoionizing photons injected into the gas by massive stars (Shields 1990).

and

$$12+\log(\mathrm{O/H})_{\rm upper} = \frac{R_{23}+726.1+842.2P+337.5P^2}{85.96+82.76P+43.98P^2+1.793R_{23}}, \quad (7)$$

for the lower and upper branch, respectively, where

$$P \equiv \frac{[\mathrm{O\ III}]\ \lambda\lambda 4959,5007}{[\mathrm{O\ II}]\ \lambda 3727+[\mathrm{O\ III}]\ \lambda\lambda 4959,5007} \quad (8)$$

is an excitation parameter (Pilyugin 2001) that is analogous to equation (4) for the KK04 calibration.

The KK04 calibration is an updated parameterization of the Kewley & Dopita (2002) R_{23} calibration, which is based on the state-of-the-art photoionization model calculations carried out by Dopita et al. (2000) and Kewley et al. (2001a).[20] The PT05 calibration, by comparison, is based on an extensive compilation of H II-regions from the literature with well-determined electron temperatures, and is a significant improvement over the original calibrations presented in Pilyugin (2000, 2001). Note, however, that due to a paucity of electron temperature measurements for low-excitation regions, the PT05 calibration is only strictly applicable to star-forming regions with $P \gtrsim 0.4$ (see §5).

We selected these two particular calibrations for several reasons. First, as indicated above, they bracket the range of oxygen abundances one would derive using other strong-line calibrations, thereby serving as useful limiting cases. Second, they are relatively recent, and therefore they utilize the best available observations, atomic data, and theoretical stellar atmospheres. Third, they are both two-parameter calibrations which account for variations in excitation at fixed metallicity (McGaugh 1991; Pilyugin 2000, 2001). Finally, they provide separate calibrations for objects on the lower and upper R_{23} branches, and therefore can be applied to a sample such as SINGS which spans a wide range of luminosity and gas-phase metallicity. We refer the interested reader to Pérez-Montero & Díaz (2005), Liang et al. (2006), and Kewley & Ellison (2008) for a detailed intercomparison of these and other popular strong-line calibrations.

4.2. *Nuclear, Circumnuclear, and Radial-Strip Abundances*

In this section we derive oxygen abundances for the SINGS galaxies from our nuclear, circumnuclear, and radial-strip spectra. In order for a spectrum to be included for chemical abundance analysis we require Hα, Hβ, [O II] λ3727, and [O III] λ5007 to be measured with a minimum S/N > 2 (see §2.2.2). We also remove spectra dominated by the central AGN, but retain those classified as SF/AGN (see §3 and Table 5). A total of 42/65 galaxies (65%) satisfy these criteria, of which 33/44 (79%) have at least two optical spectra.

[20] Note that we do not use the calibration explicitly recommended by Kobulnicky & Kewley (2004), which they obtain by averaging equations (2) and (3) with the corresponding equations from McGaugh (1991). Although the differences between these two particular calibrations are not large (< 0.1 dex), we generally advocate using one calibration derived from the same set of observations or theoretical models.

Following standard practice we correct the emission-line fluxes for dust reddening using the observed Balmer decrement, $(\mathrm{H}\alpha/\mathrm{H}\beta)_{\rm obs}$ assuming an intrinsic case B recombination value of $(\mathrm{H}\alpha/\mathrm{H}\beta)_{\rm int} = 2.86^{+0.18}_{-0.11}$, where the uncertainty reflects the variation in $(\mathrm{H}\alpha/\mathrm{H}\beta)_{\rm int}$ with electron temperature (Storey & Hummer 1995; Osterbrock & Ferland 2006). Assuming a foreground dust screen and the O'Donnell (1994) Milky Way extinction curve, the reddening is given by $E(B-V) = 2.184 \times \log_{10}[(\mathrm{H}\alpha/\mathrm{H}\beta)_{\rm obs}/(\mathrm{H}\alpha/\mathrm{H}\beta)_{\rm int}]$ (Calzetti 2001; Moustakas et al. 2006). Table 6 lists the observed Hα/Hβ ratios and corresponding $E(B-V)$ values inferred from our nuclear, circumnuclear, and radial-strip spectra. In some cases the measured Hα/Hβ ratio was less than, but statistically consistent with, the adopted intrinsic ratio (within 1σ). For these spectra we set $E(B-V)$ equal to zero and propagate the statistical uncertainty in Hα/Hβ into the reddening error.

Next, we use the reddening-corrected line-fluxes and equations (1), (5), and (8) to derive R_{23}, O_{32}, and P, respectively. Before computing oxygen abundances, however, every galaxy must be assigned to either the lower or upper branch of the KK04 and PT05 calibration (see §4.1). Following Contini et al. (2002), we assign galaxies to the lower branch if $\log([\mathrm{N\ II}]/\mathrm{H}\alpha) < -1$ and $\log([\mathrm{N\ II}]/[\mathrm{O\ II}]) < -1.05$, while we identify upper-branch objects as having $\log([\mathrm{N\ II}]/\mathrm{H}\alpha) > -1$ and $\log([\mathrm{N\ II}]/[\mathrm{O\ II}]) > -0.8$ (see also Kewley & Ellison 2008). In some cases these criteria are either inconclusive or cannot be applied because of a poorly measured [N II] line, in which case we use the optical luminosity to choose the most likely branch (see §4.4).

Because the R_{23}-O/H relation is double-valued, special care is required when computing the oxygen abundances of objects near the *turn-around* region, where the upper and lower branches intercept. In particular, objects that are statistically consistent with being on *either* the upper branch *or* the lower branch must have correspondingly large abundance errors. In addition, measurement uncertainties or residual AGN contamination occasionally result in an R_{23} parameter that is larger than ~ 10, the approximate theoretical limit for photoionization by massive stars (Kewley & Dopita 2002). Although these objects formally lie "off" the R_{23} calibration, rather than rejecting them outright, which is typically what has been done in the literature, it is better to assess whether they are statistically consistent with being *on* the R_{23} calibration under consideration. In Figure 6 we illustrate the quantitative procedure we have developed to compute R_{23}-based oxygen abundances that addresses all these issues. Here, we focus on the KK04 calibration, but the same procedure applies to the PT05 calibration and, indeed, to any R_{23}-based abundance calibration.

In the left panels of Figure 6 we plot R_{23} versus $12+\log(\mathrm{O/H})$ for three hypothetical galaxies. The curves show the KK04 calibration for three representative values of the ionization parameter, $\log(U) = -3.77$ (*solid*), -2.87 dex (*dotted*), and -2.30 dex (*dashed*). In each panel the filled red point corresponds to the oxygen abundance on the upper branch, while the filled blue triangle corresponds to the lower-branch solution (for the same object). In the top-left panel the upper- and lower-branch solutions are distinct and well-separated: once

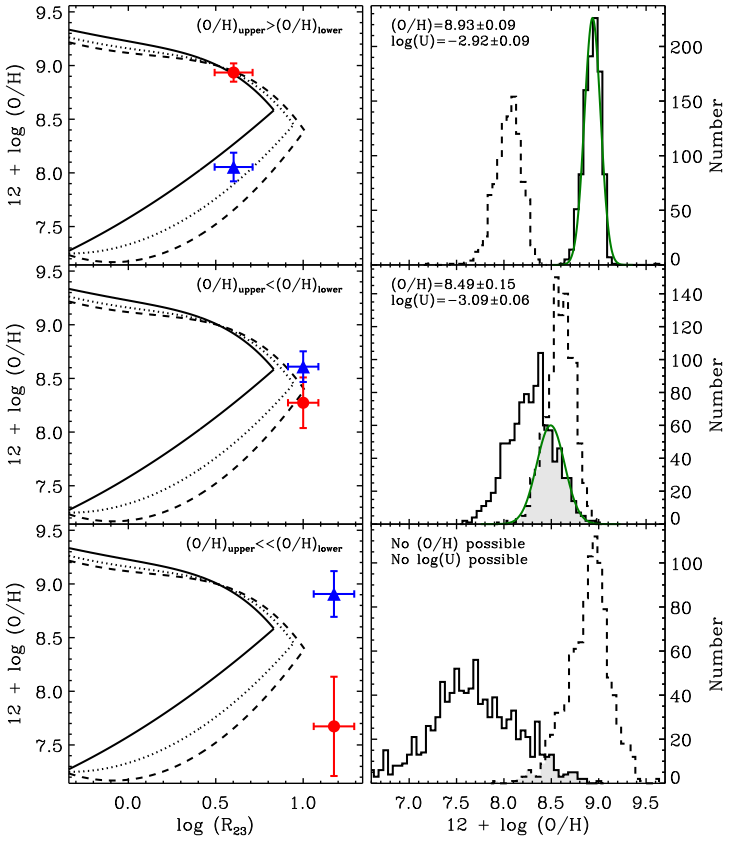

FIG. 6.— Illustration of the methodology we use to derive oxygen abundances and ionization parameters. The algorithm uses the measured errors on R_{23} and O_{32} to derive a realistic abundance uncertainty for objects that are near the *turn-around* region of the R_{23}-O/H relation, and to ascertain quantitatively whether an object is formally "off" the R_{23}-O/H calibration. These particular examples use the KK04 calibration, but the method can be applied to any R_{23}-based abundance calibration. Each row corresponds to a different hypothetical galaxy or H II region. In the left-hand panels we plot R_{23} vs. oxygen abundance for three representative ionization parameters, $\log(U) = -3.77$ (*solid*), -2.87 (*dotted*), and -2.30 (*dashed*). The red point and blue triangle in each panel shows the resulting metallicity assuming the object lies on the upper and lower R_{23} branch, respectively. [Note that this method does *not* decide whether an object is on the upper or lower branch; that choice is an *input* into this algorithm (see §4.1).] The right-hand panels show, for each object, the Monte Carlo distribution of oxygen abundances corresponding to the solution on the upper (*solid histogram*) and lower branch (*dashed histogram*), based on the errors on the line-fluxes after 500 trials. (*Top*) For this galaxy the upper and lower-branch solutions are distinct and well-separated. Assuming the object belongs on the upper branch, the final metallicity and error are given by the mean and standard deviation of the solid histogram, represented by the green Gaussian profile in the top-right panel. (*Middle*) Here, the metallicity on the lower R_{23} branch is formally larger than the upper-branch metallicity, which is not physical. However, given the uncertainties on R_{23} and O_{32}, a *subset* of the possible abundance solutions have $(\mathrm{O/H})_{\mathrm{upper}} > (\mathrm{O/H})_{\mathrm{lower}}$, shown as the shaded histogram in the middle-right panel. Consequently, we adopt the mean and standard deviation of the distribution of abundances in the shaded overlap region as the final metallicity and uncertainty in this situation, illustrated with the green Gaussian profile. (*Bottom*) The R_{23} parameter measured for this galaxy places it well outside the region of parameter space defined by the KK04 calibration: $(\mathrm{O/H})_{\mathrm{upper}} \ll (\mathrm{O/H})_{\mathrm{lower}}$; therefore, no estimate of the oxygen abundance or ionization parameter is possible for this object.

the appropriate branch has been chosen (e.g., using the criteria described above), the corresponding metallicity follows. The top-right panel shows the resulting Monte Carlo distribution of $12+\log(\mathrm{O/H})$ values corresponding to the solution on the upper (*solid histogram*) and lower branch (*dashed histogram*), assuming Gaussian errors on the [O II], [O III], and Hβ line-fluxes after 500 trials. Assuming that this object belongs on the upper branch, the 1σ uncertainty on $12+\log(\mathrm{O/H})$ is given by the width of the solid histogram; a Gaussian profile (*green curve*) of the appropriate width has been overplotted to guide the eye. The identical procedure leads to the uncertainty on the ionization parameter, $\log(U)$.

The middle panels in Figure 6 illustrate a more ambiguous, albeit frequently encountered situation. In this case the formal solution on the lower branch is *larger* than the solution on the upper branch (note that the blue triangle is now above the red circle). In the middle-right panel the overlapping, shaded region corresponds to values of R_{23} and O_{32} that lie *on* the KK04 calibration, that is, where $(\mathrm{O/H})_{\mathrm{upper}} > (\mathrm{O/H})_{\mathrm{lower}}$. If the central values of the two distributions are within 1σ of one another, as measured by the width of the shaded histogram (*green Gaussian profile*), we adopt the *average* of the two solutions as the oxygen abundance, and the width of the shaded histogram as the 1σ uncertainty. We further characterize the R_{23} branch as *ambiguous*. In practice, these types of objects all have KK04 abundances equal to the abundance around the turn-around region, ≈ 8.5 dex; however, they also have large abundance errors, which reflects the R_{23} branch ambiguity.

Finally, the bottom panels in Figure 6 illustrate a situation in which no oxygen abundance measurement is possible using the KK04 calibration. Here, the upper- and lower-branch solutions are statistically inconsistent with one another, given the measurement uncertainties; therefore no solution exists, and these objects must be rejected.

Applying the above procedure to the star-forming galaxies in our sample we derive R_{23} branches, ionization and excitation parameters, and gas-phase oxygen abundances, as well as robust uncertainties, using both the KK04 and PT05 calibrations. For reference, we are able to estimate oxygen abundances using the KK04 calibration for all the star-forming SINGS galaxies, and for all but one object (the circumnuclear spectrum of NGC 5474) using the PT05 calibration. We list the results in Table 7 and discuss them in §4.4.

4.3. *H II-Region Abundances*

In the previous section we derived oxygen abundances using our new nuclear and integrated optical spectra. Here, we analyze the abundances of the SINGS galaxies using our H II-region database (see §2.3). In §4.3.1 we use these data to constrain the form of the radial abundance gradient in 21 of the SINGS galaxies, and in §4.3.2 we compute the average oxygen abundances of all 38 galaxies with observations of at least one H II region.

4.3.1. *Radial Gradients*

Building on L. H. Aller's pioneering study of H II regions in M 33 (Aller 1942), Searle (1971) was the first to suggest that disk galaxies might possess radial abundance gradients. Subsequent work confirmed his interpretation that the gas-phase metallicity of disk galaxies, including the Milky Way, decreases from the center outward (e.g., Webster & Smith 1983; Shaver et al.

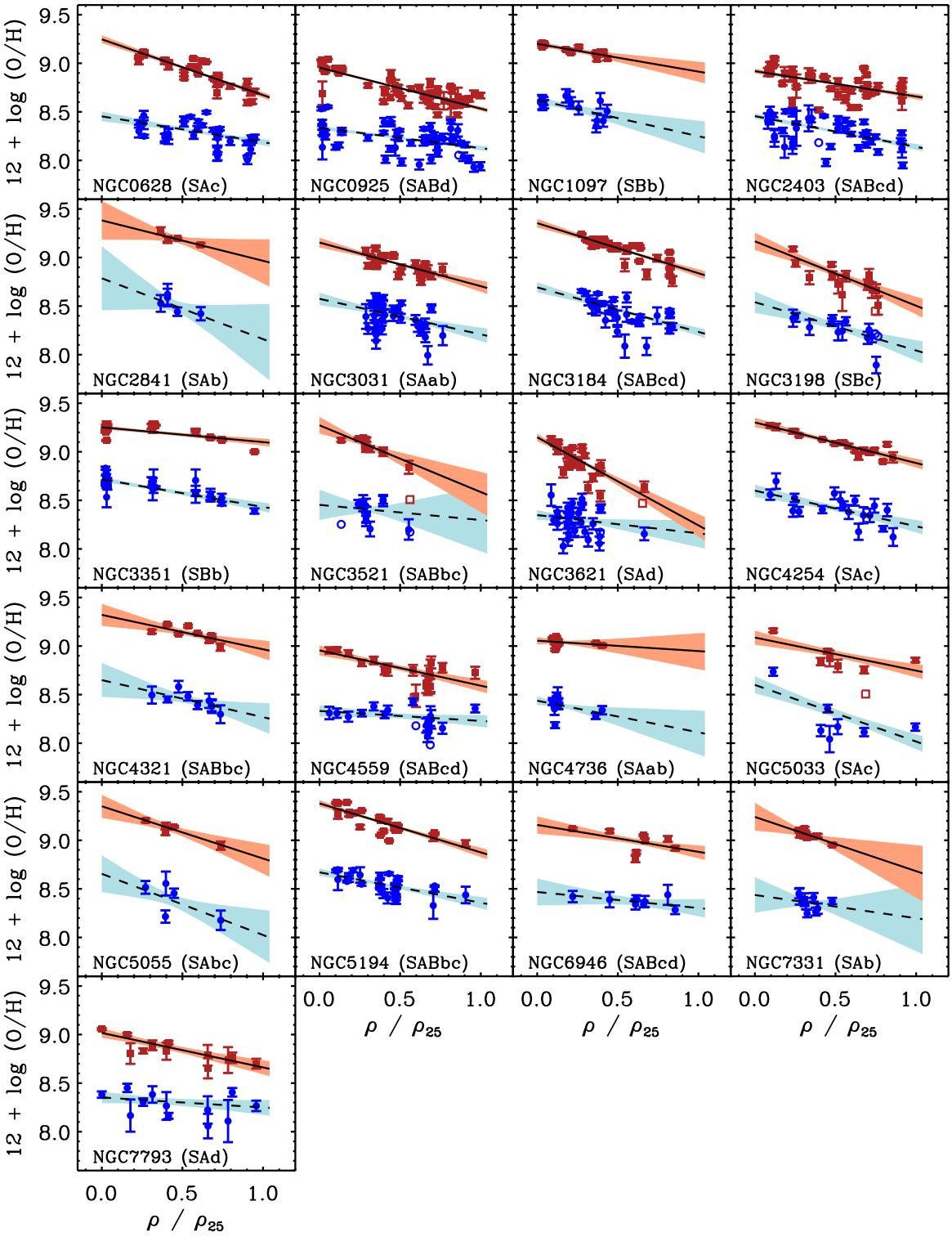

FIG. 7.— Oxygen abundance vs. deprojected galactocentric radius for individual H II regions in 21 of the SINGS galaxies. The dark red squares and blue points correspond to oxygen abundances computed using the KK04 and PT05 calibration, respectively; open symbols without error bars represent H II regions with an ambiguous R_{23} branch (see §4.2 and Fig. 6). The solid and dashed lines show the best-fitting linear abundance gradients based on each calibration, and the light-red and light-blue shaded regions reflect the 1σ range of gradients that are consistent with the observations. We provide the galaxy name and visual morphology of each object for reference in the lower-left corner of each panel. We find that the KK04 calibration yields abundances that are a factor of ~ 4 higher than those based on the PT05 calibration, and that the abundance gradients derived using the KK04 calibration are systematically steeper.

1983; Garnett & Shields 1987; Vila-Costas & Edmunds 1992; Zaritsky et al. 1994; Kennicutt & Garnett 1996; Garnett et al. 1997; van Zee et al. 1998; Dutil & Roy 1999; Pilyugin et al. 2004b; Rosolowsky & Simon 2008; Rosales-Ortega 2009). Abundance gradient measurements are important because they provide crucial constraints on the (time-dependent) inside-out gas accretion and star-formation histories of galactic disks (e.g., Molla et al. 1996; Boissier & Prantzos 1999; Prantzos & Boissier 2000; Carigi et al. 2005; Colavitti et al. 2009; Marcon-Uchida et al. 2010).

An accurate measurement of the abundance gradient of a galaxy requires observations of a minimum number of H II regions spanning a large enough fraction of the disk to constrain the slope (Zaritsky et al. 1994; Dutil & Roy 2001; Bresolin et al. 2009). Among the 75 SINGS galaxies, there are 21 disk galaxies with published spectroscopy for five or more H II regions spanning at least 10% of the disk radius, ρ_{25} (see Table 1). In Figure 7 we plot oxygen abundance versus normalized deprojected galactocentric radius, ρ/ρ_{25}, for all the star-forming regions in these objects. We derive oxygen abundances using both the KK04 (*filled dark red squares*) and PT05 (*filled dark blue points*) abundance calibrations assuming the R_{23} branches listed in Table 8. We plot H II regions with an ambiguous R_{23} branch, according to the criteria defined in §4.2, using open symbols without error bars; these regions are not used when fitting the abundance gradient. Finally, we add 0.05 dex in quadrature to the statistical abundance uncertainty of each H II region to ensure that the fit is not dominated by a small number of objects with the smallest statistical errors. We model the radial gradient in each galaxy, separately for the KK04 and PT05 abundance calibration, using a weighted linear least-squares fit, and plot the results using solid and dashed lines in Figure 7, respectively. The light-red and light-blue shaded regions reflect the 1σ range of linear gradients that are consistent with the observations, accounting for the covariance matrix of the best-fitting parameters. We tabulate the derived abundance gradients and uncertainties in Table 8, and discuss the results below and in §4.4.

Figure 7 illustrates the well-known observation that disk galaxies exhibit a wide range of abundance gradient slopes. Using the KK04 calibration, the radial gradients in these objects range from -0.91 dex ρ_{25}^{-1} in the late-type disk galaxy NGC 3621, to -0.11 dex ρ_{25}^{-1} in the SAab galaxy NGC 4736, with a mean slope of -0.42 ± 0.19 dex ρ_{25}^{-1}. Using the PT05 calibration the abundance gradients are generally shallower, as we discuss below; the average slope is -0.33 ± 0.16 dex ρ_{25}^{-1}, ranging from -0.63 dex ρ_{25}^{-1} in NGC 5055, to -0.10 dex ρ_{25}^{-1} in the barred galaxy NGC 4559. These gradients imply a factor of $\sim 1.7-4$ decrease in the oxygen abundances of galaxies from the center to the optical edge of the disk using the KK04 calibration, or a factor of $\sim 1.5-3$ using the PT05 calibration. Using the KK04-based abundances we find a weak correlation between abundance gradient slope and Hubble type in the sense that early-type disk galaxies tend to exhibit shallower abundance gradients, confirming previous studies that also relied on theoretical strong-line calibrations (e.g., Oey & Kennicutt 1993; Zaritsky et al. 1994; Garnett et al. 1997). By contrast, the PT05-based abundance gradients are independent of Hubble type (see also Pilyugin et al. 2004b). There is also no statistically significant correlation between B-luminosity and slope using either calibration, although a noisy, but significant correlation appears if the slope is expressed in physical units, i.e., dex kpc^{-1}, owing to the tendency for luminous disk galaxies to be larger (Garnett et al. 1997; Blanton & Moustakas 2009). Finally, previous studies have suggested that barred galaxies exhibit shallower abundance gradients (e.g., Vila-Costas & Edmunds 1992; Dutil & Roy 1999), presumably due to enhanced mixing via bar-driven radial inflows of gas (Kormendy & Kennicutt 2004, and references therein); unfortunately, there are too few galaxies in our sample to test this hypothesis.

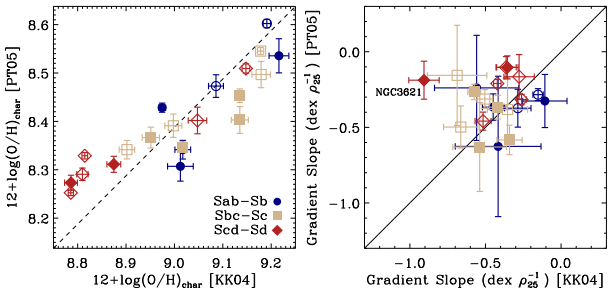

FIG. 8.— Comparison of the (*left*) characteristic abundances and (*right*) abundance gradient slopes derived using the KK04 and PT05 calibrations. Open (filled) symbols indicate barred (unbarred) galaxies, and the different symbols and colors correspond to the following range of morphological types: Sab-Sb (*dark blue points*); Sbc-Sc (*tan squares*); and Scd-Sd (*dark red diamonds*). We find that the characteristic abundances derived using the KK04 calibration are, on average, ~ 0.6 dex higher than those based on the PT05 calibration (*dashed line*), although the difference varies from $0.55-0.65$ dex from low to high metallicity. To first order, the abundance gradient slopes derived using either calibration are correlated; however, to second order the KK04 calibration results in moderately steeper abundance gradients. NGC 3621, the galaxy with the most discrepant abundance gradient, has been labeled in the right panel and is discussed in §4.3.1.

Perhaps the most striking result in Figure 7 is the considerable systematic offset between the two abundance scales: the oxygen abundances derived using the theoretical KK04 calibration are, on average, a factor of ~ 4 higher than those based on the empirical PT05 calibration. We quantify this result in Figure 8 (*left*), where we compare the *characteristic* abundances of these galaxies derived using each calibration. The characteristic abundance is defined as the oxygen abundance at $\rho = 0.4\rho_{25}$ (Zaritsky et al. 1994; Garnett 2002b), which has been shown by Moustakas & Kennicutt (2006b) to be statistically consistent with the luminosity-weighted mean metallicity of the whole galaxy based on integrated spectroscopy (see also Kobulnicky et al. 1999; Pilyugin et al. 2004a; Rosales-Ortega 2009). Open and filled symbols in this figure differentiate between barred and unbarred galaxies, respectively, and the symbols types correspond to different morphological classes: Sab-Sb (*blue points*); Sbc-Sc (*pink squares*); and Scd-Sd (*tan diamonds*). The characteristic abundances of these galaxies based on the KK04 calibration are 0.61 ± 0.06 dex higher than the corresponding metallicities derived using the PT05 cali-

bration (*dashed line*). The residuals are also a weak function of metallicity: below $12+\log(\mathrm{O/H})_{\mathrm{KK04}} \lesssim 8.95$, the PT05 characteristic abundances are offset by ~ 0.55 dex from the KK04 abundances, while at higher metallicity the offset is slightly larger, ~ 0.65 dex.

Returning to Figure 7, we find that despite the significant zeropoint offset in the two abundance scales, to first order the *slope* of the abundance gradients in these galaxies are correlated (see also Moustakas & Kennicutt 2006b and Rosales-Ortega 2009). We quantify this result in Figure 8 (*right*), where we find a well-defined, albeit noisy correlation between the abundance gradient slopes derived using the PT05 and KK04 calibrations. The most significant outlier from the one-to-one relation (*solid line*) is NGC 3621: according to the KK04 calibration the abundance gradient slope is -0.91 ± 0.10 dex ρ_{25}^{-1}, considerably steeper than the slope derived using the PT05 calibration, -0.19 ± 0.13 dex ρ_{25}^{-1}. We emphasize that the steep slope derived for NGC 3621 using the KK04 calibration is not being driven by either of the H II regions at $\rho/\rho_{25} \approx 0.65$ (S3A1 and S3A2; see Appendix B); we obtain a slope that is within the statistical error whether or not these regions are included in the fit.

To second order, however, the abundance gradients derived using the KK04 calibration are systematically steeper. Excluding the three galaxies with the least well-determined abundance gradients (NGC 2841, NGC 3521, and NGC 7331; see Table 8 and Fig. 7), the weighted mean difference in slope is 0.10 ± 0.02 dex ρ_{25}^{-1}. Bresolin et al. (2009) report a similar result for NGC 0300; they find that various theoretical strong-line abundance diagnostics yield steeper abundance gradients than the gradient inferred from electron-temperature abundance estimates. Indeed, for NGC 5194 the abundance gradient slope we derive using the empirical PT05 calibration, -0.31 ± 0.06 dex ρ_{25}^{-1}, is statistically consistent with the slope derived by Bresolin et al. (2004), -0.28 ± 0.14 dex ρ_{25}^{-1}, using a sample of 10 H II regions with high-quality electron temperature measurements; by comparison, the theoretical KK04 calibration yields a slope that is $\sim 50\%$ steeper, -0.50 ± 0.05 dex ρ_{25}^{-1}. In the context of galactic chemical evolution models (e.g., Prantzos & Boissier 2000; Marcon-Uchida et al. 2010), the slope of the abundance gradient in a disk galaxy places tight constraints on its radially and time-dependent gas-accretion and star-formation history, making it important to determine whether the steeper or shallower gradients predicted by the KK04 or PT05 calibration, respectively, are more correct. On the other hand, the abundance differences at ρ_{25} due to the slightly different gradients are typically < 0.1 dex, negligible compared to the zeroth-order systematic difference in the two abundance scales, ~ 0.6 dex. Nevertheless, these results emphasize the need for a resolution to the nebular abundance scale discrepancy (see §5).

The final point we raise regarding Figure 7 is the amount and possible physical origin of the dispersion in metallicity at fixed galactocentric radius. Relative to the KK04-based abundance gradients, the dispersion ranges from $0.03-0.11$ dex, with a mean value of ± 0.06 dex. The scatter around the best-fitting PT05-based abundance gradients is $0.05-0.18$ dex, or ± 0.10 dex, on average. It is interesting to determine why the dispersion in metallicity when using the PT05 calibration is $\sim 50\%$ larger than when adopting the KK04 calibration. Correlating the abundance residuals against various properties of the H II regions, we find that the larger dispersion is being driven primarly by low-excitation ($P \lesssim 0.2$) H II regions. As emphasized in §4.1, the paucity of low-excitation H II regions with electron temperature abundance measurements means that the PT05 calibration is not well-constrained in this regime (see also the discussion in §5); therefore, PT05-based abundances of low-excitation H II regions may be susceptible to additional systematic errors (i.e., due to extrapolation). Consequently, in the subsequent discussion we focus exclusively on the dispersion around the KK04-based abundance gradients.

The dispersion we measure is comparable to or smaller than the scatter reported by previous studies, $\pm 0.1 - 0.2$ dex (e.g., McCall et al. 1985; Zaritsky et al. 1994; van Zee et al. 1998). One reason we measure a smaller dispersion in metallicity at fixed galactocentric radius compared to these older studies, even though we are using data compiled from the very same surveys, is because the KK04 calibration accounts for variations in metallicity *and* ionization for a given emission-line spectrum. Neglecting the tendency for metal-poor (i.e., outer) H II regions to have harder ionizing radiation fields would introduce additional scatter due to the variation in physical conditions among different H II regions. Kennicutt & Garnett (1996) speculate that in M101 the dispersion is metallicity may be due to large-scale deviations from azimuthal symmetry in the gas disk, perhaps due to tidal interactions with its nearby companions. One way to test this hypothesis is to build two-dimensional abundance maps of statistically significant samples of nearby galaxies, which has become possible recently with the latest generation of integral-field-unit spectrographs (e.g., Rosales-Ortega et al. 2010; Blanc et al. 2010).

4.3.2. *Average H II-Region Oxygen Abundances*

In this section we consider all 38 SINGS galaxies with observations of one or more H II regions (see Appendix B), including the 21 objects studied in §4.3.1, and compute the average H II-region metallicity of each galaxy assuming the R_{23} branches listed in Table 8. Specifically, we compute the average metallicity as the unweighted mean of all the individual H II-region abundances in each object. To ensure a reliable estimate we exclude H II regions with an ambiguous R_{23} branch assignment (see §4.2), as well as regions beyond the optical diameter of the galaxy (i.e., those with $\rho/\rho_{25} > 1$). Estimating the uncertainty in the average metallicity is not straightforward because galaxies exhibit genuine abundance inhomogeneities, although the amplitude of these variations are expected to be relatively small in dwarf galaxies (e.g., van Zee et al. 2006). Consequently, we compute the error in the average metallicity as the unweighted standard deviation of the distribution of oxygen abundances, but require the resulting uncertainty to be greater than or equal to the mean statistical uncertainty of the individual measurements. This method ensures that we do not underestimate the metallicity error in galaxies with only a handful of H II regions. We list the final average abundances and uncertainties for all 38

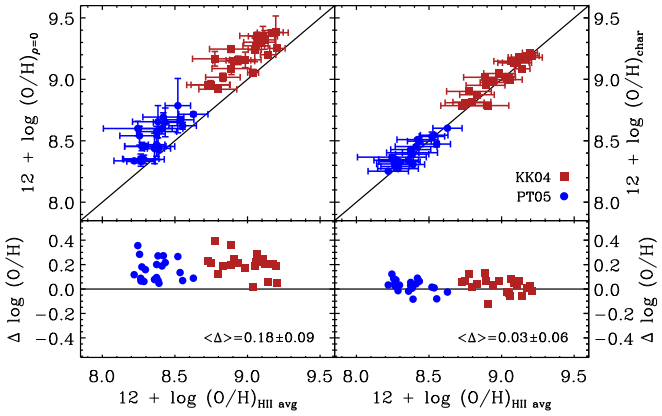

FIG. 9.— Comparison of the average H II-region oxygen abundance vs. (*left*) the metallicity at $\rho = 0$, and (*right*) the characteristic oxygen abundance (defined at $\rho/\rho_{25} = 0.4$) for the 21 SINGS galaxies with measured radial gradients (see Fig. 7). We plot abundances computed using the KK04 and PT05 calibration as dark red squares and blue points, respectively, and the solid line in each panel represents the line-of-equality. The lower panels show the abundance residuals without error bars for clarity, and give the mean and standard deviation of the residuals for both abundance calibrations. This comparison shows that the extrapolated central metallicity is, on average, a factor of ~ 1.5 higher than the average H II-region metallicity in this sample, while the average and characteristic abundances are statistically consistent with one another with a 1σ scatter of $\lesssim \pm 15\%$ and no significant systematic offset. We conclude that the average H II-region abundance is a reliable proxy for the characteristic metallicity when the radial gradient cannot be constrained.

galaxies in Table 8.

In Figure 9 we compare the average abundances we derive against the (*left*) central ($\rho = 0$) and (*right*) characteristic ($\rho/\rho_{25} = 0.4$) oxygen abundances for the 21 SINGS galaxies with measured radial gradients (§4.3.1). The dark red squares and blue points correspond to the KK04 and PT05 abundance calibration, respectively, and the solid line is the line-of-equality. The upper panels compare the abundances directly and include error bars, while the lower panels plot the residuals without error bars, for clarity. The mean and standard deviation of the residuals are given in the lower panels. We find that the central oxygen abundances in these galaxies are 0.18 ± 0.09 dex, or a factor of $1.2 - 1.9$ higher than the average metallicity, while the characteristic and average oxygen abundances agree to within $\lesssim \pm 15\%$) with no statistically significant systematic offset, independent of the adopted abundance calibration. This result indicates that, to first order, the average H II-region metallicity is a reliable surrogate for the characteristic abundance in galaxies where we are unable to constrain the form of the radial abundance gradient.

4.4. *Synthesis: Central and Characteristic Oxygen Abundances of the SINGS Galaxies*

In the previous two sections we derived several different estimates of the gas-phase oxygen abundances for each SINGS galaxy spanning a wide range of spatial scales (see Tables 7 and 8). For most applications, however, a single, characteristic oxygen abundance that is representative of the whole galaxy may be desired; in other applications, a nuclear or central metallicity may be needed. The goal of this section, therefore, is to combine all the various abundance measurements to derive a uniform set of characteristic (i.e., globally averaged) and central oxygen abundances for the full sample.

We begin our analysis with Figure 10 by plotting *all* the oxygen abundances listed in Tables 7 and 8 versus ρ/ρ_{25}. We plot abundances determined from our nuclear, circumnuclear, and radial-strip spectra using dark blue crosses, magenta triangles, and orange diamonds, respectively. We derive an approximate ρ/ρ_{25} value for each spectrum by computing the mean radius of the spectroscopic aperture, $\rho \approx \sqrt{\Delta_{\parallel}\Delta_{\perp}}/2$, where $\Delta_{\parallel}$ and $\Delta_{\perp}$ is the diameter of the extraction aperture along and perpendicular to the slit, respectively (see Table 2). Our results are not sensitive to the details of this calculation, as our goal is simply to distinguish between, for example, a nuclear spectrum that encloses a small fraction of the light of the galaxy (e.g., $\rho/\rho_{25} \approx 0.02$ for NGC 1482) and a radial-strip spectrum that extends over a much larger area relative to the size of the galaxy (e.g., $\rho/\rho_{25} \approx 0.52$ for NGC 1705). We plot the characteristic ($\rho/\rho_{25} = 0.4$) and central ($\rho = 0$) abundances determined from our radial metallicity gradients (see §4.3.1) as green squares and light blue stars, respectively. Finally, we plot the average H II-region abundances derived in §4.3.2 as dark red points at $\rho/\rho_{25} = 0.5$. Note that we only plot the average H II-region abundances of objects without measured radial gradients so that the same H II regions are not counted twice.

Next, we divide Figure 10 into central and characteristic metallicity regimes at $\rho/\rho_{25} = 0.1$ (*vertical dashed line*). For each galaxy, we define the central abundance as the weighted average of all the available abundances at $\rho/\rho_{25} < 0.1$; similarly, we define the characteristic metallicity of each galaxy as the weighted average of all the abundances at $\rho/\rho_{25} > 0.1$. Although this division is somewhat arbitrary, once again our goal is to ensure that we are not averaging metallicities originating from widely disparate parts of the galaxy. Note that by using the weighted average we tend to favor metallicities derived from the H II regions, which typically have smaller uncertainties than the metallicities derived from our nuclear and integrated spectra. Occasionally the average central metallicity is formally *lower* than the characteristic metallicity, although the difference is never statistically significant (i.e., never $> 1\sigma$). In other cases, either the central or characteristic metallicity carries a considerably larger uncertainty because it is based on a single abundance estimate. For these objects we adopt the weighted average of all the available metallicities at $0 < \rho/\rho_{25} < 1$ as indicative of both the central and characteristic abundance. We list the final set of oxygen abundances, using both the KK04 and PT05 abundance calibrations, in Table 9.

Summarizing, Table 9 contains central and characteristic abundances for 55 galaxies, or $\sim 73\%$ of the SINGS sample. The characteristic abundances range from $12 + \log(\mathrm{O/H})_{\mathrm{KK04}} = 8.00 - 9.21$ based on the KK04 calibration, or $12 + \log(\mathrm{O/H})_{\mathrm{PT05}} = 7.54 - 8.60$ using the PT05 calibration. Among the 20 objects with no metallicity estimate, 16 (80%) are early-type, bulge-dominated galaxies lacking prominent emission lines in their integrated spectrum (e.g., NGC 0584, NGC 5866), or their optical emission-line spectrum is dominated by

the central AGN (e.g., NGC 1266, NGC 4579). Unfortunately, H II regions either are not present in these galaxies, or have not been observed. The remaining four objects are late-type galaxies (e.g., NGC 3938), including three dwarfs (M 81 Dw A, NGC 4236, and IC 4710), for which we were unable to obtain a useful optical spectrum (see §2.2.1), and for which no H II regions have been observed in these objects based on our search of the literature (see Appendix B).

In an effort to make our compilation of oxygen abundances for the SINGS galaxies as comprehensive as possible, we derive an *approximate* metallicity for the remaining 20 galaxies using the B-band luminosity-metallicity ($L-Z$) relation. The statistical correlation between optical luminosity (or stellar mass) and gas-phase metallicity has been known for several decades (e.g., Lee et al. 2006a, and references therein), and provides a useful tool for deriving a rough estimate of the metallicities of the SINGS galaxies without spectroscopic abundances. We emphasize that the metallicities we derive using the $L-Z$ relation may be susceptible to additional systematic biases. In particular, the bulk of the objects without spectroscopic abundances are early-type galaxies which may not obey the same underlying $L-Z$ relation defined by late-type galaxies. In fact, early-type disk galaxies exhibit shallower radial abundance gradients and higher overall metallicities than late-type galaxies (§4.3.1; Garnett & Shields 1987; Oey & Kennicutt 1993; Zaritsky et al. 1994; Dutil & Roy 1999), although the latter correlation is likely driven by the fact that early-type galaxies tend to be more luminous, and therefore more metal rich. On the other hand, we derive the B-band $L-Z$ relation using all the galaxies in SINGS with spectroscopic abundances, including a number of early-type disk galaxies, which should mitigate some of these systematic effects.

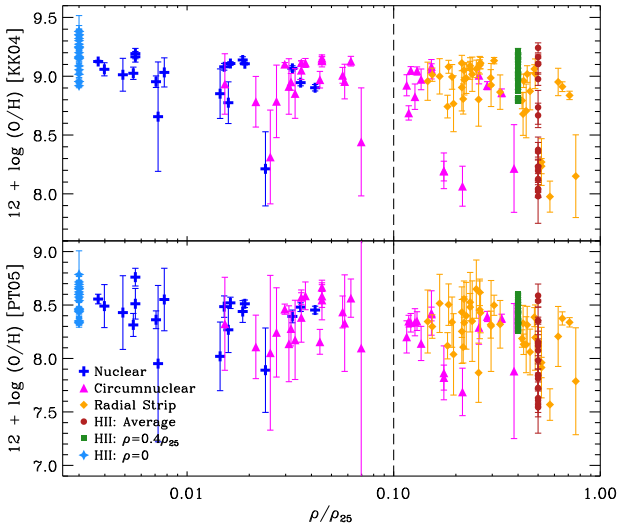

FIG. 10.— Oxygen abundance vs. normalized galactocentric radius based on all the available data and the (*top*) KK04 and (*bottom*) PT05 abundance calibration. We plot abundances inferred from our nuclear, circumnuclear, and radial-strip spectra using dark blue crosses, magenta triangles, and orange diamonds, respectively, and the average, characteristic, and central H II-region abundances as dark red points, green squares, and light blue stars, respectively. Note that we only plot the average H II-region abundances of galaxies without measured radial gradients (§4.3.1) so that the same H II regions are not counted twice. We estimate ρ/ρ_{25} for our nuclear, circumnuclear, and radial-strip spectra using the effective radius of the spectroscopic aperture relative to ρ_{25}, as described in §4.4. By definition the characteristic abundances correspond to $\rho/\rho_{25}=0.4$, and for simplicity we assign the average H II-region abundances a relative radius of $\rho/\rho_{25}=0.5$ (see Fig. 9, *right*). Finally, we plot the central ($\rho=0$) H II-region abundances based on the measured abundance gradients at $\rho/\rho_{25}=0.003$ so that they appear on this logarithmic plot. We derive the central abundance of each galaxy by averaging all the available abundances with $\rho/\rho_{25}<0.1$, and the characteristic abundance of each galaxy as the weighted average of the individual metallicities with $\rho/\rho_{25}>0.1$, as indicated by the vertical dashed line.

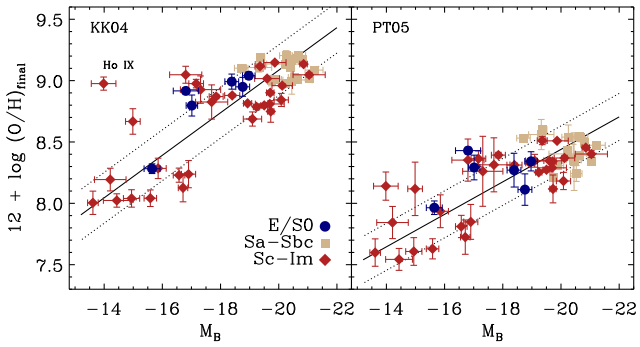

FIG. 11.— B-band luminosity-metallicity relation using the *final* characteristic (*left*) KK04 and (*right*) PT05 oxygen abundances of the SINGS galaxies (see Table 9). The symbols correspond to broad bins of morphological type: E-Sa (*dark blue points*), Sab-Sbc (*tan squares*), and Sc-Im (*dark red diamonds*). The solid lines indicate the linear ordinary least-squares bisector fits to each luminosity-metallicity relation, and the dotted lines correspond to the 1σ scatter around the best fit, ±0.2 dex. In the left panel we label Ho IX, a tidal-dwarf galaxy in the M 81 group that is considerably more metal-rich than comparably luminous galaxies.

With these caveats in mind, in Figure 11 we plot the B-band $L-Z$ relation for the SINGS galaxies using the (*left*) KK04 and (*right*) PT05 abundance calibrations and the characteristic oxygen abundances listed in Table 9. The symbols correspond to three broad bins of morphological type: E-Sa (*dark blue points*), Sab-Sbc (*tan squares*), and Sc-Im (*dark red diamonds*). Ho IX, a metal-rich tidal-dwarf galaxy (Makarova et al. 2002; Croxall et al. 2009), deviates significantly from the KK04-based luminosity-metallicity relation, and has been labeled in this figure. The solid lines show the linear ordinary least-squares bisector fits to each set of abundances (Isobe et al. 1990), while the dotted lines in each panel indicate the 1σ residual scatter in either $L-Z$ relation, ±0.2 dex. Using these $L-Z$ relations we estimate the oxygen abundances of all the SINGS galaxies and list the results in Table 9.

The $L-Z$ relations we obtain are:

$$12+\log(\mathrm{O/H})_{\mathrm{KK04}} = (5.62\pm0.24)+(-0.173\pm0.012)M_B \quad (9)$$

and

$$12+\log(\mathrm{O/H})_{\mathrm{PT05}} = (5.79\pm0.21)+(-0.132\pm0.011)M_B \quad (10)$$

using the KK04 and PT05 abundance calibration, respectively. Comparing these results with previously determined B-band $L-Z$ relations is difficult because the slope and intercept are sensitive to sample selec-

tion effects (e.g., the distribution of absolute magnitudes) and, obviously, the adopted abundance calibration. For example, Tremonti et al. (2004) obtained a steeper $L - Z$ relation, $12 + \log(\mathrm{O/H}) = 5.24 - 0.185 M_B$ based on a large sample of SDSS galaxies with $-18 \gtrsim M_B \gtrsim -23$ and a theoretical abundance calibration. By comparison, Lee et al. (2006a) studied a sample of 25 nearby galaxies with $-11 \gtrsim M_B \gtrsim -18$ and oxygen abundances derived using the direct method and obtained $12 + \log(\mathrm{O/H}) = 5.94 - 0.128 M_B$. Other studies have obtained $L - Z$ relation slopes ranging from -0.149 dex mag^{-1} to -0.280 dex mag^{-1} (Skillman et al. 1989; Hidalgo-Gamez & Olofsson 1998; Lee et al. 2004; Lamareille et al. 2004; Salzer et al. 2005; van Zee & Haynes 2006; J. Moustakas et al., in prep.). Given the impact of the assumed abundance calibration and sample selection effects we conclude that equations (9) and (10) are both reasonable descriptions of the B-band $L - Z$ relation for the SINGS galaxies.

5. DISCUSSION OF THE NEBULAR ABUNDANCE SCALE

The factor of ~ 5 absolute uncertainty in the nebular abundance scale poses one of the most important outstanding problems in observational astrophysics. In this paper we have sidestepped this issue by computing the gas-phase metallicities of the SINGS galaxies using two independent strong-line calibrations: PT05, which was empirically calibrated against electron-temperature abundance measurements of individual H II regions; and KK04, a purely theoretical calibration based on a large grid of state-of-the-art photoionization model calculations (see §4.1). We have seen that the KK04 calibration yields abundances that are ~ 0.6 dex higher than metallicities derived using the PT05 calibration, *based on the same input emission-line ratios.* The question we explore in this section is: "Which set of oxygen abundances should one use?"

As discussed in §4.1, the absolute uncertainty in the nebular abundance scale is largely due to the systematic difference between abundances computed using empirical versus theoretical calibrations (see, e.g., Fig. 2 in Kewley & Ellison 2008). Therefore, we begin our discussion by exploring the various strengths and limitations of the empirical and theoretical strong-line methods (see Stasińska 2010 for a complementary discussion). Our principal conclusion is that the empirical calibrations likely underestimate the 'true' metallicity by $\sim 0.2 - 0.3$ dex, while the theoretical calibrations yield abundances that may be too high by the same amount; a compromise procedure, therefore, would be to *average* the two abundance estimates presented in §4.4 and Table 9. We conclude with a brief discussion of other strong-line abundance calibrations.

One indirect argument in favor of empirical abundance calibrations is that they generally yield abundances for L^* (i.e., typical) galaxies that are more consistent with the oxygen abundance of the Sun, $12 + \log(\mathrm{O/H})_\odot = 8.69 \pm 0.05$ (Asplund et al. 2009). For example, luminous, metal-rich galaxies on the empirical abundance scale have $12 + \log(\mathrm{O/H}) \approx 8.5 - 8.9$, or $(0.7 - 1.6) \times Z_\odot$, while the metallicities of the same galaxies using the theoretical strong-line calibrations are $8.8 - 9.2$ dex, or $(1.3 - 3.2) \times Z_\odot$ (Fig. 11; Tremonti et al. 2004; Salzer et al. 2005; Pilyugin et al. 2007; Kewley & Ellison 2008). Consequently, on the empirical abundance scale L^* galaxies like the Milky Way have roughly solar metallicity, whereas theoretical abundance methods suggest that the overwhelming majority of star-forming galaxies in the local universe are more metal-rich than the Sun (see, e.g., Fig. 4 in Tremonti et al. 2004).[21] Application of the Copernican principal suggests that the theoretical abundance scale is likely too high given the currently accepted solar oxygen abundance (but see Serenelli et al. 2009).

Another powerful way to test the absolute zeropoint in the nebular abundance scale is to compare the gas-phase oxygen abundances of H II regions in the Milky way and other nearby galaxies against the *stellar* abundances of young O-, B-, and A-type stars in the same galaxies. Bresolin et al. (2009) performed this experiment by obtaining high-quality electron temperature measurements of 28 H II regions in the nearby late-type galaxy NGC 0300. They compared the inferred gas-phase abundance gradient with the stellar gradient derived from observations of blue supergiants in the same galaxy (Urbaneja et al. 2005; Kudritzki et al. 2008) and found excellent statistical agreement. Pilyugin et al. (2006) reported a similar result for the Milky Way; they applied an empirical strong-line method (Pilyugin 2005) to observations of Galactic H II regions and found excellent agreement with the stellar oxygen abundance gradient from Daflon & Cunha (2004) over a similar range of Galactocentric radii. By comparison, three widely-used theoretical strong-line calibrations (McGaugh 1991; Kewley & Dopita 2002; Tremonti et al. 2004) applied to the H II regions in NGC 0300 yielded abundance gradients that were offset from the stellar gradient toward higher metallicity by $0.3 - 0.5$ dex (Bresolin et al. 2009).

Despite these successes, direct and empirical abundance methods may systematically *underestimate* the oxygen abundances of star-forming regions, especially in the metal-rich regime. For example, using the direct method Esteban et al. (2004) measured the oxygen abundance of the Orion nebula to be $12 + \log(\mathrm{O/H}) = 8.51 \pm 0.03$. However, this metallicity is $\sim 0.2 - 0.3$ dex lower than the oxygen abundances of B-type stars in the solar neighborhood and in the Orion nebula (i.e., young stars within ~ 1 kpc; Cunha et al. 2006; Przybilla et al. 2008; Simón-Díaz 2010). One way to (partially) resolve this discrepancy would be if oxygen atoms are depleted by $0.1 - 0.2$ dex onto dust grains (Jenkins 2004; Cartledge et al. 2006), although presumably this correction would affect the abundances derived from the theoretical methods in the same way. Alternatively, if H II regions exhibit significant spatial temperature fluctuations then the abundances derived from collisionally excited lines such [O III] λ4363 could be biased low.

Peimbert (1967) was the first to point out that temperature inhomogeneities in H II regions could cause the electron temperature inferred from the collisionally excited forbidden lines to be overestimated, and therefore the abundance to be underestimated (Stasińska 2005; Bresolin 2006). He defined a quantity, t^2, equal to the root-mean-square deviation of the temperature from the mean value. Temperature inhomogenieties are expected

[21] Note, however, that the metallicities derived from the SDSS 3″ diameter fiber spectra may be too high by ~ 0.1 dex due to aperture bias (Tremonti et al. 2004; Kewley et al. 2005).

to be more severe in metal-rich H II regions because the higher efficiency of metal-line cooling leads to strong temperature gradients as a function of distance from the ionizing star or star cluster (Garnett 1992; Stasińska 2002, 2005). Typically, direct abundances, and the empirical methods that are calibrated against them, assume $t^2 = 0$. Unfortunately, deriving t^2 is very challenging observationally; it has been measured in a relatively small number of metal-rich [$12 + \log(\mathrm{O/H})_{T_e} \gtrsim 8.1$] Galactic and extragalactic H II regions (García-Rojas & Esteban 2007; Esteban et al. 2009, and references therein). Using the intensity of the faint, temperature-insensitive metal recombination lines, the He I recombination line spectrum, and the electron temperature implied by the Balmer discontinuity, these studies suggest $t^2 = 0.03 - 0.07$ for metal-rich H II regions, corresponding to an upward revision of the abundances derived from empirical methods of $0.2-0.3$ dex (the so-called abundance discrepancy factor; García-Rojas & Esteban 2007; Esteban et al. 2009). Indeed, applying a correction for $t^2 \neq 0$ to the oxygen abundance of Orion implied by the direct method, Esteban et al. (2004) obtain $12 + \log(\mathrm{O/H}) = 8.67 \pm 0.04$, in much better agreement with the mean abundance of B-type stars in the same star-forming region, $12 + \log(\mathrm{O/H}) = 8.74 \pm 0.04$ (Simón-Díaz 2010), assuming that ~ 0.1 dex of oxygen atoms are locked in dust grains.

These observations suggest that it might be possible to develop an empirical strong-line calibration using abundances measured from metal recombination lines, which are not susceptible to temperature fluctuations (Peimbert & Peimbert 2005; Peimbert et al. 2007; Bresolin 2007). Peimbert et al. (2007) derive such a calibration for R_{23} using a small number (~ 20) of metal-rich, high-excitation emission-line galaxies and H II regions. For a given value of R_{23}, this calibration yields oxygen abundances that are ~ 0.25 dex, or a factor of ~ 1.8 higher than the abundances implied by the direct and empirical methods assuming $t^2 = 0$. However, this calibration should be used with caution because it has been tested on a relatively small, biased (metal-rich, high-excitation) sample of Galactic and extragalactic H II regions. In addition, recent theoretical work suggests that abundances derived from recombination lines may not be as unbiased as once believed (Stasińska et al. 2007; Ercolano et al. 2007; Ercolano 2009). Additional observations of the Balmer discontinuities and O II recombination-line intensities of H II regions spanning a wider range of metallicity and physical conditions would be of considerable value.

As alluded to above, one of the principal limitations of the empirical strong-line abundance methods is that they are only strictly applicable to H II regions and star-forming galaxies spanning the same range of excitation and metallicity as the H II regions that were used to build the calibration. To illustrate this point, in Figure 12 we plot the (reddening-corrected) R_{23} parameter versus excitation, P, for star-forming galaxies in the SDSS and a *representative* sample of metal-rich H II regions with well-measured electron temperatures (*red squares*; Garnett et al. 1997; van Zee et al. 1998; Kennicutt et al. 2003b; Kniazev et al. 2004; Bresolin et al. 2004, 2005; Izotov & Thuan 2004; Izotov et al. 2006; Rosolowsky & Simon 2008). The symbol size for each H II region is proportional to its oxygen abundance in the range $12+\log(\mathrm{O/H})_{T_e} \approx 8.2-8.95$ assuming $t^2 = 0$. Because all these objects are on the upper R_{23} branch, P increases in tandem with nebular excitation, while a decrease in R_{23} corresponds to an increase in metallicity, as indicated by the arrows in Figure 12. This figure demonstrates that star-forming galaxies in the SDSS are lower-excitation and more metal-rich than the bulk of the H II regions with direct abundance estimates.[22] Note that a similar conclusion would be reached if EW(Hβ) had been used as a measure of excitation (see, e.g., Fig. 5 in Bresolin 2007): the median EW(Hβ) value of the SDSS galaxies is ~ 6 Å, nearly a factor of 15 smaller than the median EW(Hβ) of the H II regions, ~ 85 Å. The practical implication of this result is that empirical abundance calibrations such as PT05 should *not* in general be applied to large emission-line galaxy surveys such as the SDSS because

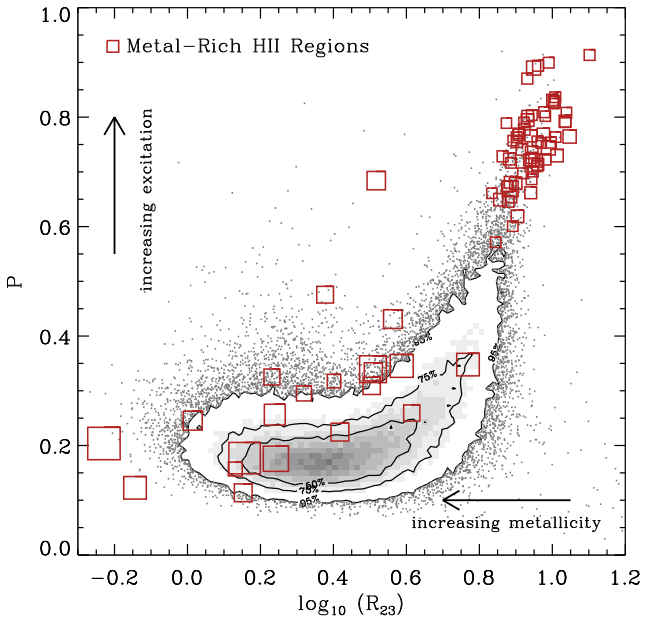

FIG. 12.— Metallicity-sensitive R_{23} parameter vs. excitation, P, for star-forming galaxies in the SDSS (*contoured greyscale*) and a representative sample of metal-rich H II regions with well-measured electron temperatures collected from the literature (*red squares*; Garnett et al. 1997; van Zee et al. 1998; Kennicutt et al. 2003b; Kniazev et al. 2004; Bresolin et al. 2004, 2005; Izotov & Thuan 2004; Izotov et al. 2006; Rosolowsky & Simon 2008). The symbol size for each H II region is proportional to its metallicity, ranging from $12 + \log(\mathrm{O/H})_{T_e} = 8.21$ (H143 in M101; Kennicutt et al. 2003b) to 8.94 dex (H11 in M83; Bresolin et al. 2005). This scatterplot demonstrates that the bulk of the galaxies in the SDSS are low-excitation, whereas most metal-rich H II regions with well-measured electron temperatures are high-excitation, which is a well-known observational bias (see also Fig. 12 in Pilyugin & Thuan 2005). The practical implication is that empirical abundance calibrations such as PT05 in general should *not* be applied to large emission-line galaxy surveys such as the SDSS because the calibrations would be extrapolated to a part of physical parameter space that is not well-constrained by current observations.

[22] As indicated in the previous footnote, at least some of the tendency for the SDSS galaxies to appear metal-rich and low-excitation may be due to aperture bias.

the calibrations would be extrapolated to a part of physical parameter space that is not well-constrained by current observations.

Meanwhile, theoretical strong-line abundance calibrations have the advantage that they are based on models that, by construction, span a wide range of ionization parameter ($-3.5 < \log(U) < -1.9$), metallicity ($0.0001 < Z < 0.05$), and stellar effective temperature (McGaugh 1991; Dopita et al. 2000; Charlot & Longhetti 2001; Kewley et al. 2001a; Moy et al. 2001; Dopita et al. 2006a; Martín-Manjón et al. 2010; Levesque et al. 2010). In these methods the UV (i.e., photoionizing) spectral energy distribution of a young star cluster is coupled to a photoionization code such as CLOUDY (Ferland et al. 1998) or MAPPINGS (Sutherland & Dopita 1993) and the output emission-line spectrum is studied as a function of input parameters. In recent years there have been significant improvements in the evolutionary tracks for young stars, including the effects of mass loss and rotation (Vázquez & Leitherer 2005), the calculation of non-LTE, line-blanketed stellar atmospheres (Simón-Díaz & Stasińska 2008), and the inclusion of dust grains in the photoionization models (Shields & Kennicutt 1995; Groves et al. 2004). Despite these improvements, however, some problems persist. For example Levesque et al. (2010) find that the latest generation of photoionizing spectra are too soft to reproduce the observed [S II]/Hα ratios of nearby star-forming galaxies. Photoionization codes also have difficulty reproducing the observed line-strengths of the auroral lines (Stasińska & Schaerer 1999; Jamet et al. 2005), and predict insignificant temperature fluctuations within H II regions (Baldwin et al. 1991), in contradiction with the (albeit limited) observations. The theoretical methods also rely on a number of simplifying assumptions regarding the electron density, volume filling factor, and nebular geometry (e.g., spherically symmetric, plane-parallel); the metal-abundance pattern, including the proportion of each metal depleted onto dust grains; the initial mass function, star-formation history (e.g., instantaneous, continuous, stochastic), and age of the central cluster; and chemical evolution effects (e.g., the relationship between primary and secondary nitrogen), among others. In addition to the discrepancies alluded to above, a breakdown in one or more of these assumptions may be responsible for the seemingly "high" oxygen abundances predicted by theoretical strong-line calibrations.

So what are the ways forward? From the observational standpoint, high-quality optical spectrophotometry of larger samples of H II regions in nearby galaxies is clearly warranted. These observations should span a wide wavelength range in order to include a large number of independent electron temperature and density diagnostics, and should target H II regions spanning a wide range of metallicity and excitation (e.g., Kennicutt et al. 2003b; Bresolin et al. 2005; Bresolin 2007; Rosolowsky & Simon 2008; Esteban et al. 2009). In particular, a concerted effort to measure the Balmer discontinuities and metal recombination lines in metal-rich H II regions will elucidate the prevalence and relative importance of temperature-fluctuations, and will help constrain empirical strong-line calibrations in the metal-rich regime. Although these observations are extraordinarily challenging, they are possible with the latest generation of multi-object spectrographs on 8− and 10−meter class telescopes (e.g., Keck/DEIMOS, LBT/MODS, VLT/XSHOOTER, etc.). These observations also will help establish the radial and azimuthal dependence of abundances in nearby galaxies; many existing observations are more than twenty-five years old, and for many systems data are available for only a handful of H II regions (Fig. 7; Pilyugin et al. 2004b). Finally, observations of the mid- and far-infrared metal cooling lines (e.g., [S III] λ19 μm, [O III] λ52 μm, [N III] λ57 μm, [O III] λ88 μm, [N II] λ122 μm), which are insensitive to variations in electron temperature, will be crucial in establishing the abundances of metal-rich H II regions (Martín-Hernández et al. 2002; Garnett et al. 2004a; Rudolph et al. 2006; Rubin et al. 2008). Spectroscopy from $60 - 210$ μm with the PACS instrument on-board the *Herschel Space Telescope* (e.g., from the KINGFISH project; Poglitsch et al. 2008) will expand significantly the number of star-forming regions observed in the critical far-infrared wavelength regime.

Improvements in the grid-based theoretical strong-line abundance calibrations are also warranted. In particular, a systematic exploration of the input parameters and simplifying assumptions in the models (e.g., Moy et al. 2001; Mathis & Wood 2005; Ercolano et al. 2007, 2010; Levesque et al. 2010) may elucidate the origin of the discrepancy between theoretical and empirical abundances. For example, Yin et al. (2007) show that the difference in the oxygen abundances derived using the direct method and the Charlot & Longhetti (2001) photoionization models (Brinchmann et al. 2004; Tremonti et al. 2004) correlates strongly with the N/O abundance ratio. Because nitrogen is both a primary and secondary nucleosynthetic product, the N/O ratio varies systematically with oxygen abundance, as well as the time since the most recent episode of star formation (Edmunds & Pagel 1978; Contini et al. 2002; Mouhcine & Contini 2002; Pilyugin et al. 2003; Izotov et al. 2006), a complexity that is not reflected in the grid-based theoretical calibrations. Finally, we note that *tailored* photoionization models of individual H II regions frequently *can* be tuned to reproduce most or all the observed emission-line ratios (e.g., Castellanos et al. 2002; Garnett et al. 2004a, but see Jamet et al. 2005). This result again suggests the possibility of an as-yet unidentified shortcoming in the *grid-based* theoretical calibrations.

Summarizing the preceding discussion, we find that empirical abundance calibrations may underestimate the oxygen abundances of H II regions and star-forming galaxies because of systematic biases (e.g., temperature fluctuations) in the T_e-based abundances that are used to calibrate the empirical methods. Empirical methods also suffer from a shortage of metal-rich H II regions with measured electron temperatures, which means that the calibrations are being extrapolated to an unconstrained region of parameter space when applied to large galaxy samples such as the SDSS. On the other hand, indirect evidence suggests that theoretical calibrations yield abundances that are too high, possibly due to one or more simplifying assumptions in the photoionization model grids. Therefore, until these issues are resolved, we recommend that any study utilizing the oxygen abundances provided in Table 9 be carried out either using the *relative* (KK04 or PT05) abundances of the sample, or using *both* the KK04 and PT05 abundances separately, to

ensure that the conclusions are not affected by the error in the absolute zeropoint of the nebular abundance scale. Alternatively, if a single set of oxygen abundances for the SINGS galaxies is required, a compromise procedure would be to *average* the KK04 and PT05 metallicities and conservatively adopt the *difference* in the two metallicity estimates as the metallicity error for each galaxy.

Although we have focused exclusively on the R_{23} parameter to compute oxygen abundances, over the past three decades many other strong-line calibrations have been developed for estimating the abundances of H II regions and star-forming galaxies. Among the most popular diagnostics are those based on the [N II] λ6584 emission line (e.g., [N II]/Hα, [N II]/[O II], and [O III]/[N II]; Alloin et al. 1979; Storchi-Bergmann et al. 1994; van Zee et al. 1998; Kewley & Dopita 2002; Pettini & Pagel 2004; Liang et al. 2006), although calibrations based on an assortment of other forbidden lines have been proposed (Dopita & Evans 1986; Vilchez & Esteban 1996; Díaz & Pérez-Montero 2000; Pérez-Montero & Díaz 2005; Nagao et al. 2006; Stasińska 2006; Wu et al. 2008; Okada et al. 2008), as well as techniques designed to model all the emission lines simultaneously (Charlot & Longhetti 2001; Brinchmann et al. 2004; Maier et al. 2006). Most [N II]-based calibrations have the advantage that, unlike R_{23}, they vary monotonically with metallicity. On the other hand, for most galaxies [N II] is usually weaker than [O II], [O III], and Hβ, and it is more sensitive to contributions from shock-ionized gas and a non-thermal (i.e., AGN) photoionizing continuum.[23] As discussed above, oxygen abundances inferred from [N II] also depend implicitly on the recent star formation history of the galaxy, which may introduce non-negligible systematic errors (e.g., Yin et al. 2007). Nevertheless, because [N II] is observable from the ground to $z \sim 2$, strong-line calibrations that rely on this line provide an important window into the gas-phase abundances of high-redshift galaxies (Shapley et al. 2004, 2005; Maier et al. 2005; Erb et al. 2006, 2010; Hainline et al. 2009).

One final cautionary note is that both empirical and theoretical strong-line methods have been calibrated against observations of H II regions and star-forming galaxies in the nearby universe, and may not be applicable at higher redshift where the physical conditions in galaxies may differ dramatically from physical conditions in local galaxies (Shapley et al. 2005; Liu et al. 2008; Brinchmann et al. 2008; Hainline et al. 2009; Lehnert et al. 2009). Testing the validity of locally calibrated abundance diagnostics in higher-redshift galaxies, therefore, will be an important objective of the first generation of highly multiplexed near-infrared spectrographs and, eventually, with the NIRSpec instrument onboard the *James Webb Space Telescope*, through observations of the full complement of rest-frame optical emission-line diagnostics at high redshift.

6. SUMMARY

[23] A notable exception is the abundance-sensitive [N II]/[O II] ratio, which is insensitive to variations in excitation because [N II] and [O II] have similar ionization potentials (Bresolin 2007; Kewley & Ellison 2008); on the other hand, [N II]/[O II] is sensitive to dust reddening.

We have obtained intermediate-resolution ($\sim$ 8 Å FWHM), high signal-to-noise ratio (S/N = 5 – 100 pixel^{-1}) optical ($\sim$ 3600 – 6900 Å) spectrophotometry of the SINGS galaxies on three spatial scales to complement and enhance the legacy value of existing mid- and far-infrared observations obtained as part of the *Spitzer*/SINGS legacy program. Our integrated circumnuclear and radial-strip spectra characterize the central and globally-averaged optical properties of each galaxy, respectively, and are spatially coincident with mid- ($\sim 5 - 38$ μm) and far-infrared ($\sim 55 - 95$ μm) spectral cubes from the IRS spectrograph and the MIPS instrument in SED-mode, respectively. A third optical spectrum targeting the nucleus of each galaxy provides a reliable means of identifying galaxies hosting an AGN, among other applications. We make the fully reduced, spectrophotometrically calibrated one-dimensional spectra available to the community. In addition, we use state-of-the art stellar population synthesis models to separate the underlying stellar continuum from the optical emission-line spectrum, and generate tables of the fluxes and equivalent widths of the strongest optical emission lines. Together with existing ancillary multi-wavelength observations of the sample, these data should facilitate a broad range of studies on the physical properties of nearby galaxies.

As a first effort demonstrating the utility of these data, we classify the sample into star-forming (SF), AGN, and SF/AGN on three spatial scales, and carry out a detailed analysis of the gas-phase oxygen abundances of the SINGS sample using our optical spectra and observations of more than 550 H II regions. Our principal results are:

1. We find that the proportion of galaxies classified as SF and AGN is a strong function of the fraction of the integrated B-band light enclosed by the spectroscopic aperture. The fraction of the sample classified as AGN decreases from $\approx 40\%$ to $\lesssim 15\%$ as the B-band light fraction increases from $\sim 10\%$ to $\gtrsim 60\%$, with a corresponding increase in the fraction of galaxies classified as SF. The $\sim 15\%$ incidence rate of objects classified as SF/AGN, on the other hand, is roughly independent of enclosed light fraction.

2. Because of significant systematic differences among oxygen abundances computed using different methods, we compute oxygen abundances using both a theoretical (KK04) and an empirical (PT05) strong-line abundance calibration, both based on the popular R_{23} parameter. We measure a systematic offset of ~ 0.6 dex between the two nebular abundances, in the sense that the theoretical KK04 calibration yields significantly higher metallicities. These two calibrations were chosen because they bracket the full range of metallicities one would obtain using other popular strong-line abundance calibrations, and because they could be applied to such a diverse sample such as SINGS.

3. We carry out a detailed analysis of the radial abundance gradients in 21 of the SINGS galaxies using both calibrations. We find that the slope of

the abundance gradients inferred from these two calibrations are generally correlated; however, to second order the theoretical KK04 calibration results in systematically steeper abundance gradients, which has significant implications for constraining disk-galaxy formation models. In addition, the dispersion in metallicity at fixed galactocentric radius is $\sim 50\%$ larger when using the empirical PT05 calibration, presumably because the PT05 calibration is not well-constrained for low-excitation H II regions.

4. We combine all the available abundance measurements, including abundances inferred from our nuclear, circumnuclear, and radial-strip spectra, H II regions, and the B-band luminosity-metallicity relation, to compute the mean characteristic and central oxygen abundances of whole SINGS sample using both the KK04 and PT05 strong-line calibrations. These abundances should facilitate a wide range of studies between the metal content and infrared emission properties of nearby galaxies.

5. Finally, we discuss some of the possible origins of the systematic differences in nebular abundance computed using direct or empirical versus theoretical strong-line abundance calibrations. We conclude that additional observations of H II regions spanning a wide range of physical conditions, as well as improvements in the theoretical models, are imperative for resolving this important outstanding problem.

Preliminary values of the oxygen abundances presented in this paper already have been used in several publications by the SINGS team. Smith et al. (2007) and Draine et al. (2007) found a remarkable decrease in the PAH emission-line strengths and the proportion of dust mass locked up in PAH grains below a characteristic oxygen abundance $12 + \log(\mathrm{O/H})_{\mathrm{PT05}} \approx 8.1$. Calzetti et al. (2007, 2010) investigated the metallicity dependence of the 8, 24, 70, and 160 μm monochromatic luminosities as quantitative SFR diagnostics; they found a strong metallicity dependence for $L(8\ \mu\mathrm{m})$, hampering its suitability for high-redshift studies. Bendo et al. (2008) compared the radial variations in the 8 μm/24 μm and 8 μm/160 μm ratios against the radial abundance gradients in a subset of the face-on disk galaxies in SINGS and concluded that metallicity was *not* the dominant parameter driving the observed trends. And finally Muñoz-Mateos et al. (2009a) found that both the total-infrared to far-UV luminosity ratio (i.e., $L_{\mathrm{TIR}}/L_{\mathrm{FUV}}$) and the UV spectral slope (i.e., β) depend significantly on gas-phase oxygen abundance, owing to the tendency for metal-rich, star-forming galaxies to be dustier.

These applications illustrate the broad utility of the measured optical emission-line strengths, spectral classifications, and derived oxygen abundances of the SINGS galaxies, and should facilitate a diversity of future studies into the dust emission and star formation properties of nearby galaxies.

We gratefully acknowledge Moire Prescott for assistance with some of the observations, Stuart Ryder and Henry Lee for providing their published H II-region data in electronic format, Juan-Carlos Muñoz-Mateos for assistance assembling the optical photometry of the sample, the Bok 2.3-meter telescope operators, Dennis Means and Vic Hansen, for their expertise during the course of this survey, and illuminating conversations with James Aird, Michael Blanton, Alison Coil, David Hogg, Janice Lee, Leonidas Moustakas, and Amelia Stutz. The authors would also like to thank Bruce Draine for insightful comments on an early draft of the manuscript, and the referee, Fabio Bresolin, for suggestions that improved the clarity of the manuscript. This work has relied extensively on the invaluable IDLUTILS software library developed by M. R. Blanton, S. Burles, D. P. Finkbeiner, D. W. Hogg, and D. J. Schlegel, and on the Goddard IDL library maintained by W. Landsman. We also thank M. Cappellari and M. Sarzi for generously making their continuum- and emission-line fitting software, PPXF and GANDALF, respectively, publically available.

This research has made extensive use of NASA's Astrophysics Data System Bibliographic Services, the VizieR catalog access tool, and the NASA/IPAC Extragalactic Database, which is operated by the Jet Propulsion Laboratory, California Institute of Technology, under contract with the National Aeronautics and Space Administration. The Digitized Sky Surveys were produced at the Space Telescope Science Institute under U.S. Government grant NAG W-2166. The images of these surveys are based on photographic data obtained using the Oschin Schmidt Telescope on Palomar Mountain and the UK Schmidt Telescope. The plates were processed into the present compressed digital form with the permission of these institutions.

Funding for the Sloan Digital Sky Survey (SDSS) and SDSS-II has been provided by the Alfred P. Sloan Foundation, the Participating Institutions, the National Science Foundation, the U.S. Department of Energy, the National Aeronautics and Space Administration, the Japanese Monbukagakusho, and the Max Planck Society, and the Higher Education Funding Council for England. The SDSS Web site is http://www.sdss.org/.

The SDSS is managed by the Astrophysical Research Consortium (ARC) for the Participating Institutions. The Participating Institutions are the American Museum of Natural History, Astrophysical Institute Potsdam, University of Basel, University of Cambridge, Case Western Reserve University, The University of Chicago, Drexel University, Fermilab, the Institute for Advanced Study, the Japan Participation Group, The Johns Hopkins University, the Joint Institute for Nuclear Astrophysics, the Kavli Institute for Particle Astrophysics and Cosmology, the Korean Scientist Group, the Chinese Academy of Sciences (LAMOST), Los Alamos National Laboratory, the Max-Planck-Institute for Astronomy (MPIA), the Max-Planck-Institute for Astrophysics (MPA), New Mexico State University, Ohio State University, University of Pittsburgh, University of Portsmouth, Princeton University, the United States Naval Observatory, and the University of Washington.

Facilities: Bok (Boller & Chivens spectrograph); CTIO:1.5m (R-C spectrograph)

APPENDIX

PRESENTATION OF THE SPECTRA

The SINGS galaxies were selected to span a broad range of morphological types, optical luminosities, and infrared properties, and this diversity is clearly reflected in their optical spectra. Figures A1-A2 present the reduced one-dimensional spectra[24] in erg s^{-1} cm^{-2} Å^{-1} versus rest-frame wavelength in Å. We plot the data in grey and overplot the best-fitting stellar continuum model (see §2.2.2) in black. For each galaxy, we also show an optical Digitized Sky Survey image to illustrate how our spectroscopic apertures compare to the optical extent of the galaxy (*dashed purple ellipse*; see Table 1). The size of the spectroscopic apertures corresponding to our radial-strip and circumnuclear spectra are shown as a red rectangle and blue square, respectively. The dotted yellow rectangle shows the spatial coverage of the corresponding *Spitzer*/IRS long-low spectrum obtained as part of SINGS where there was at least double coverage in both spectral orders (Smith et al. 2004, 2007). In some cases there is a mismatch between the orientation angle of the IRS and optical radial-strip spectra. This difference occurs because many of the optical spectra were obtained before the IRS spectra had been observed, or even scheduled. For these objects when we were planning the optical observations we made the best effort to select a position angle for the optical spectrum based on the predicted/constrained position angle of the IRS observations.

H II-REGION DATABASE

We performed a search of the literature to find published observations of H II regions in the SINGS sample, resulting in data on 561 star-forming regions in $\sim 50\%$ of the sample (38/75 galaxies) drawn from 36 distinct papers published between 1984 and 2009. In order to be included in our catalog, the [O II] λ3727, Hβ, and [O III] λ5007 line-strengths must have been measured to enable an estimate of the gas-phase abundance (see §4.3). While this catalog is not exhaustive, it does include all the major spectroscopic surveys of H II regions in nearby galaxies conducted to date (e.g., McCall et al. 1985; Zaritsky et al. 1994; van Zee et al. 1998). In general, we gave preference to the most recent observations over older data obtained using non-linear detectors, which may be biased (Torres-Peimbert et al. 1989). We also only tabulated data based on traditional spectrophotometry, not narrowband imaging (e.g., Belley & Roy 1992; Dutil & Roy 1999), which may suffer from a variety of systematic errors (Dutil & Roy 2001). Finally, observations of the same H II region by different authors were retained as independent observations.

For each H II region we tabulated the fluxes and uncertainties of the strong nebular emission lines, as well as the coordinates of each star-forming region relative to the galactic nucleus. In most cases the published emission-line strengths had been corrected for both underlying stellar absorption and dust reddening. Where necessary, however, we applied a statistical EW(Hβ) = 1.9 Å correction (McCall et al. 1985) to the Balmer lines and dereddened the line-strengths using the observed Hα/Hβ Balmer decrement as described in §4.2. In all cases we assumed that [O III] λ4959 was 0.34 times the intensity of [O III] λ5007 (Osterbrock & Ferland 2006). Finally, the coordinates were used to derive the deprojected galactocentric radius of each H II-region using the position and inclination angles listed in Table 1.

Table 10 provides the derived properties of the H II regions used, including the H II region name and reference to the literature, the deprojected galactocentric radius, the R_{23}, O_{32}, and P parameters (see §4.1), and the oxygen abundances derived using the KK04 and PT05 strong-line calibrations, assuming the R_{23} branches listed in Table 7. H II regions whose oxygen abundance could not be derived based on the quantitative criteria described in §4.2, or which had ambiguous R_{23} branches using either abundance calibration, are identified in the table using footnotes. More detailed information on each H II region (e.g., relative coordinates, emission-line ratios, etc.) are available from the first author as a binary FITS table upon request.

REFERENCES

Abazajian, K. N., Adelman-McCarthy, J. K., Agüeros, M. A., Allam, S. S., Allende Prieto, C., An, D., Anderson, K. S. J., Anderson, S. F., et al. 2009, ApJS, 182, 543

Aller, L. H. 1942, ApJ, 95, 52

Alloin, D., Collin-Souffrin, S., Joly, M., & Vigroux, L. 1979, A&A, 78, 200

Asari, N. V., Cid Fernandes, R., Stasińska, G., Torres-Papaqui, J. P., Mateus, A., Sodré, L., Schoenell, W., & Gomes, J. M. 2007, MNRAS, 381, 263

Asplund, M., Grevesse, N., Sauval, A. J., & Scott, P. 2009, ARA&A, 47, 481

Baldwin, J. A., Ferland, G. J., Martin, P. G., Corbin, M. R., Cota, S. A., Peterson, B. M., & Slettebak, A. 1991, ApJ, 374, 580

Baldwin, J. A., Phillips, M. M., & Terlevich, R. 1981, PASP, 93, 5

Belley, J., & Roy, J.-R. 1992, ApJS, 78, 61

Bendo, G. J., Calzetti, D., Engelbracht, C. W., Kennicutt, R. C., Meyer, M. J., Thornley, M. D., Walter, F., Dale, D. A., Li, A., & Murphy, E. J. 2007, MNRAS, 380, 1313

Bendo, G. J., Draine, B. T., Engelbracht, C. W., Helou, G., Thornley, M. D., Bot, C., Buckalew, B. A., Calzetti, D., Dale, D. A., Hollenbach, D. J., Li, A., & Moustakas, J. 2008, MNRAS, 389, 629

Blanc, G. A., Gebhardt, K., Heiderman, A., Evans, II, N. J., Jogee, S., van den Bosch, R., Marinova, I., Weinzirl, T., et al. 2010, astro-ph/1001.5035

Blanton, M. R., & Moustakas, J. 2009, ARA&A, 47, 159

Blanton, M. R., & Roweis, S. 2007, AJ, 133, 734

Blanton, M. R., Schlegel, D. J., Strauss, M. A., Brinkmann, J., Finkbeiner, D., Fukugita, M., Gunn, J. E., Hogg, D. W., et al. 2005, AJ, 129, 2562

Bohlin, R. C., Dickinson, M. E., & Calzetti, D. 2001, AJ, 122, 2118

Boissier, S., & Prantzos, N. 1999, MNRAS, 307, 857

Boquien, M., Bendo, G., Calzetti, D., Dale, D., Engelbracht, C., Kennicutt, R., Lee, J. C., van Zee, L., & Moustakas, J. 2010, ApJ, 713, 626

Boquien, M., Calzetti, D., Kennicutt, R., Dale, D., Engelbracht, C., Gordon, K. D., Hong, S., Lee, J. C., & Portouw, J. 2009, ApJ, 706, 553

[24] Available electronically at http://sings.stsci.edu and http://ssc.spitzer.caltech.edu/legacy.

Brandenburg, H. J., & Skillman, E. D. 1998, in Bulletin of the American Astronomical Society, Vol. 30, Bulletin of the American Astronomical Society, 1354–+
Braun, R., Oosterloo, T. A., Morganti, R., Klein, U., & Beck, R. 2007, A&A, 461, 455
Bresolin, F. 2006, astro-ph/0608410
—. 2007, ApJ, 656, 186
Bresolin, F., Garnett, D. R., & Kennicutt, R. C. 2004, ApJ, 615, 228
Bresolin, F., Gieren, W., Kudritzki, R., Pietrzyński, G., Urbaneja, M. A., & Carraro, G. 2009, ApJ, 700, 309
Bresolin, F., Kennicutt, R. C., & Garnett, D. R. 1999, ApJ, 510, 104
Bresolin, F., & Kennicutt, Jr., R. C. 2002, ApJ, 572, 838
Bresolin, F., Schaerer, D., González Delgado, R. M., & Stasińska, G. 2005, A&A, 441, 981
Brinchmann, J., Charlot, S., White, S. D. M., Tremonti, C., Kauffmann, G., Heckman, T., & Brinkmann, J. 2004, MNRAS, 351, 1151
Brinchmann, J., Pettini, M., & Charlot, S. 2008, MNRAS, 385, 769
Bruzual, G., & Charlot, S. 2003, MNRAS, 344, 1000
Calzetti, D. 2001, PASP, 113, 1449
Calzetti, D., Armus, L., Bohlin, R. C., Kinney, A. L., Koornneef, J., & Storchi-Bergmann, T. 2000, ApJ, 533, 682
Calzetti, D., Kennicutt, R. C., Engelbracht, C. W., Leitherer, C., Draine, B. T., Kewley, L., Moustakas, J., Sosey, M., et al. 2007, ApJ, 666, 870
Calzetti, D., Kennicutt, Jr., R. C., Bianchi, L., Thilker, D. A., Dale, D. A., Engelbracht, C. W., Leitherer, C., Meyer, M. J., et al. 2005, ApJ, 633, 871
Calzetti, D., Wu, S., Hong, S., Kennicutt, R. C., Lee, J. C., Dale, D. A., Engelbracht, C. W., van Zee, L., et al. 2010, ApJ, 714, 1256
Cannon, J. M., Smith, J.-D. T., Walter, F., Bendo, G. J., Calzetti, D., Dale, D. A., Draine, B. T., Engelbracht, C. W., et al. 2006a, ApJ, 647, 293
Cannon, J. M., Walter, F., Armus, L., Bendo, G. J., Calzetti, D., Draine, B. T., Engelbracht, C. W., Helou, G., et al. 2006b, ApJ, 652, 1170
Cappellari, M., & Emsellem, E. 2004, PASP, 116, 138
Carigi, L., Peimbert, M., Esteban, C., & García-Rojas, J. 2005, ApJ, 623, 213
Cartledge, S. I. B., Lauroesch, J. T., Meyer, D. M., & Sofia, U. J. 2006, ApJ, 641, 327
Castellanos, M., Díaz, A. I., & Terlevich, E. 2002, MNRAS, 329, 315
Chabrier, G. 2003, PASP, 115, 763
Charlot, S. ., & Fall, S. M. 2000, ApJ, 539, 718
Charlot, S. ., & Longhetti, M. 2001, MNRAS, 323, 887
Ciardullo, R., Feldmeier, J. J., Jacoby, G. H., Kuzio de Naray, R., Laychak, M. B., & Durrell, P. R. 2002, ApJ, 577, 31
Cid Fernandes, R., Asari, N. V., Sodré, L., Stasińska, G., Mateus, A., Torres-Papaqui, J. P., & Schoenell, W. 2007, MNRAS, 375, L16
Cid Fernandes, R., Mateus, A., Laerte, S. J., Stasinska, G., & Gomes, J. M. 2005, MNRAS, 358, 363
Colavitti, E., Cescutti, G., Matteucci, F., & Murante, G. 2009, A&A, 496, 429
Contini, T., Treyer, M. A., Sullivan, M., & Ellis, R. S. 2002, MNRAS, 330, 75
Cortese, L., Boselli, A., Franzetti, P., Decarli, R., Gavazzi, G., Boissier, S., & Buat, V. 2008, MNRAS, 386, 1157
Croxall, K. V., van Zee, L., Lee, H., Skillman, E. D., Lee, J. C., Côté, S., Kennicutt, R. C., & Miller, B. W. 2009, ApJ, 705, 723
Cunha, K., Hubeny, I., & Lanz, T. 2006, ApJ, 647, L143
Daflon, S., & Cunha, K. 2004, ApJ, 617, 1115
Daigle, O., Carignan, C., Amram, P., Hernandez, O., Chemin, L., Balkowski, C., & Kennicutt, R. 2006, MNRAS, 367, 469
Dale, D. A., Bendo, G. J., Engelbracht, C. W., Gordon, K. D., Regan, M. W., Armus, L., Cannon, J. M., Calzetti, D., et al. 2005, ApJ, 633, 857
Dale, D. A., Gil de Paz, A., Gordon, K. D., Hanson, H. M., Armus, L., Bendo, G. J., Bianchi, L., Block, M., et al. 2007, ApJ, 655, 863
Dale, D. A., Smith, J. D. T., Armus, L., Buckalew, B. A., Helou, G., Kennicutt, Jr., R. C., Moustakas, J., et al. 2006, ApJ, 646, 161
Dale, D. A., Smith, J. D. T., Schlawin, E. A., Armus, L., Buckalew, B. A., Cohen, S. A., Helou, G., Jarrett, T. H., et al. 2009, ApJ, 693, 1821
De Lucia, G. 2009, astro-ph/0912.1862
de Vaucouleurs, G., de Vaucouleurs, A., Corwin, H. G., Buta, R. J., Paturel, G., & Fouque, P. 1991, Third Reference Catalogue of Bright Galaxies (Volume 1-3, XII, 2069 pp. 7 figs.. Springer-Verlag Berlin Heidelberg New York)
Denicoló, G., Terlevich, R., & Terlevich, E. 2002, MNRAS, 330, 69
Díaz, A. I., & Pérez-Montero, E. 2000, MNRAS, 312, 130
Díaz, Á. I., Terlevich, E., Castellanos, M., & Hägele, G. F. 2007, MNRAS, 382, 251
Diaz, A. I., Terlevich, E., Vilchez, J. M., Pagel, B. E. J., & Edmunds, M. G. 1991, MNRAS, 253, 245
Dicaire, I., Carignan, C., Amram, P., Hernandez, O., Chemin, L., Daigle, O., de Denus-Baillargeon, M.-M., Balkowski, C., Boselli, A., Fathi, K., & Kennicutt, R. C. 2008, MNRAS, 385, 553
Dinerstein, H. L. 1990, in Astrophysics and Space Science Library, Vol. 161, The Interstellar Medium in Galaxies, ed. H. A. Thronson Jr. & J. M. Shull, 257–285
Dopita, M. A., & Evans, I. N. 1986, ApJ, 307, 431
Dopita, M. A., Fischera, J., Sutherland, R. S., Kewley, L. J., Leitherer, C., Tuffs, R. J., Popescu, C. C., van Breugel, W., & Groves, B. A. 2006a, ApJS, 167, 177
Dopita, M. A., Fischera, J., Sutherland, R. S., Kewley, L. J., Tuffs, R. J., Popescu, C. C., van Breugel, W., Groves, B. A., & Leitherer, C. 2006b, ApJ, 647, 244
Dopita, M. A., Kewley, L. J., Heisler, C. A., & Sutherland, R. S. 2000, ApJ, 542, 224
Draine, B. T. 2003, ARA&A, 41, 241
Draine, B. T., Dale, D. A., Bendo, G., Gordon, K. D., Smith, J. D. T., Armus, L., Engelbracht, C. W., et al. 2007, ApJ, 663, 866
Drozdovsky, I. O., & Karachentsev, I. D. 2000, A&AS, 142, 425
Durret, F., & Bergeron, J. 1988, A&AS, 75, 273
Dutil, Y., & Roy, J. 1999, ApJ, 516, 62
Dutil, Y., & Roy, J.-R. 2001, AJ, 122, 1644
Edmunds, M. G., & Pagel, B. E. J. 1978, MNRAS, 185, 77P
—. 1984, MNRAS, 211, 507
Engelbracht, C. W., Gordon, K. D., Rieke, G. H., Werner, M. W., Dale, D. A., & Latter, W. B. 2005, ApJ, 628, L29
Engelbracht, C. W., Rieke, G. H., Gordon, K. D., Smith, J.-D. T., Werner, M. W., Moustakas, J., Willmer, C. N. A., & Vanzi, L. 2008, ApJ, 678, 804
Erb, D. K., Pettini, M., Shapley, A. E., Steidel, C. C., Law, D. R., & Reddy, N. A. 2010, astro-ph/1006.5456
Erb, D. K., Shapley, A. E., Pettini, M., Steidel, C. C., Reddy, N. A., & Adelberger, K. L. 2006, ApJ, 644, 813
Ercolano, B. 2009, MNRAS, 397, L69
Ercolano, B., Bastian, N., & Stasińska, G. 2007, MNRAS, 379, 945
Ercolano, B., Wesson, R., & Bastian, N. 2010, MNRAS, 401, 1375
Esteban, C., Bresolin, F., Peimbert, M., García-Rojas, J., Peimbert, A., & Mesa-Delgado, A. 2009, ApJ, 700, 654
Esteban, C., Peimbert, M., García-Rojas, J., Ruiz, M. T., Peimbert, A., & Rodríguez, M. 2004, MNRAS, 355, 229
Ferguson, A. M. N., Gallagher, J. S., & Wyse, R. F. G. 1998, AJ, 116, 673
Ferland, G. J., Korista, K. T., Verner, D. A., Ferguson, J. W., Kingdon, J. B., & Verner, E. M. 1998, PASP, 110, 761
Ferrarese, L., Ford, H. C., Huchra, J., Kennicutt, Jr., R. C., Mould, J. R., Sakai, S., Freedman, W. L., Stetson, P. B., et al. 2000a, ApJS, 128, 431
Ferrarese, L., Mould, J. R., Kennicutt, Jr., R. C., Huchra, J., Ford, H. C., Freedman, W. L., Stetson, P. B., Madore, B. F., et al. 2000b, ApJ, 529, 745
Freedman, W. L., Madore, B. F., Gibson, B. K., Ferrarese, L., Kelson, D. D., Sakai, S., Mould, J. R., Kennicutt, R. C., et al. 2001, ApJ, 553, 47
Gallazzi, A., Charlot, S., Brinchmann, J., White, S. D. M., & Tremonti, C. A. 2005, MNRAS, 362, 41
García-Rojas, J., & Esteban, C. 2007, ApJ, 670, 457

Garnett, D. R. 1992, AJ, 103, 1330
—. 2002a, astro-ph/0211148
—. 2002b, ApJ, 581, 1019
Garnett, D. R., Edmunds, M. G., Henry, R. B. C., Pagel, B. E. J., & Skillman, E. D. 2004a, AJ, 128, 2772
Garnett, D. R., Kennicutt, R. C., & Bresolin, F. 2004b, ApJ, 607, L21
Garnett, D. R., & Shields, G. A. 1987, ApJ, 317, 82
Garnett, D. R., Shields, G. A., Peimbert, M., Torres-Peimbert, S., Skillman, E. D., Dufour, R. J., Terlevich, E., & Terlevich, R. J. 1999, ApJ, 513, 168
Garnett, D. R., Shields, G. A., Skillman, E. D., Sagan, S. P., & Dufour, R. J. 1997, ApJ, 489, 63
Gavazzi, G., Zaccardo, A., Sanvito, G., Boselli, A., & Bonfanti, C. 2004, A&A, 417, 499
Gehrels, N. 1986, ApJ, 303, 336
Gordon, K. D., Clayton, G. C., Misselt, K. A., Landolt, A. U., & Wolff, M. J. 2003, ApJ, 594, 279
Gordon, K. D., Clayton, G. C., Witt, A. N., & Misselt, K. A. 2000, ApJ, 533, 236
Groves, B. A., Dopita, M. A., & Sutherland, R. S. 2004, ApJS, 153, 9
Guseva, N. G., Izotov, Y. I., & Thuan, T. X. 2000, ApJ, 531, 776
Hainline, K. N., Shapley, A. E., Kornei, K. A., Pettini, M., Buckley-Geer, E., Allam, S. S., & Tucker, D. L. 2009, ApJ, 701, 52
Heckman, T. M. 1980, A&A, 87, 152
Henry, R. B. C., Pagel, B. E. J., & Chincarini, G. L. 1994, MNRAS, 266, 421
Hidalgo-Gamez, A. M., & Olofsson, K. 1998, A&A, 334, 45
Ho, L. C. 2008, ARA&A, 46, 475
Ho, L. C., Filippenko, A. V., & Sargent, W. L. W. 1997, ApJS, 112, 315
Houck, J. R., Roellig, T. L., van Cleve, J., Forrest, W. J., Herter, T., Lawrence, C. R., Matthews, K., Reitsema, H. J., et al. 2004, ApJS, 154, 18
Isobe, T., Feigelson, E. D., Akritas, M. G., & Babu, G. J. 1990, ApJ, 364, 104
Izotov, Y. I., Stasińska, G., Meynet, G., Guseva, N. G., & Thuan, T. X. 2006, A&A, 448, 955
Izotov, Y. I., & Thuan, T. X. 2004, ApJ, 602, 200
Jamet, L., Stasińska, G., Pérez, E., González Delgado, R. M., & Vílchez, J. M. 2005, A&A, 444, 723
Jansen, R. A., Fabricant, D., Franx, M., & Caldwell, N. 2000, ApJS, 126, 331
Jarrett, T. H., Chester, T., Cutri, R., Schneider, S. E., & Huchra, J. P. 2003, AJ, 125, 525
Jenkins, E. B. 2004, in Origin and Evolution of the Elements, ed. A. McWilliam & M. Rauch, 336–+
Jha, S., Riess, A. G., & Kirshner, R. P. 2007, ApJ, 659, 122
Karachentsev, I. D., Karachentseva, V. E., Huchtmeier, W. K., & Makarov, D. I. 2004, AJ, 127, 2031
Karachentsev, I. D., Makarov, D. I., Sharina, M. E., Dolphin, A. E., Grebel, E. K., Geisler, D., Guhathakurta, P., Hodge, P. W., et al. 2003, A&A, 398, 479
Karachentsev, I. D., Sharina, M. E., & Huchtmeier, W. K. 2000, A&A, 362, 544
Kauffmann, G., Heckman, T. M., Tremonti, C., Brinchmann, J., Charlot, S., White, S. D. M., Ridgway, S. E., Brinkmann, J., et al. 2003, MNRAS, 346, 1055
Kennicutt, R. 1998, in Liege International Astrophysical Colloquia, ed. B. Kaldeich, 81–+
Kennicutt, R. C. 1992a, ApJS, 79, 255
—. 1992b, ApJ, 388, 310
Kennicutt, R. C., Armus, L., Bendo, G., Calzetti, D., Dale, D. A., Draine, B. T., Engelbracht, C. W., Gordon, K. D., et al. 2003a, PASP, 115, 928
Kennicutt, R. C., Bresolin, F., & Garnett, D. R. 2003b, ApJ, 591, 801
Kennicutt, R. C., & Garnett, D. R. 1996, ApJ, 456, 504
Kennicutt, R. C., Hao, C., Calzetti, D., Moustakas, J., Dale, D. A., Bendo, G., Engelbracht, C. W., Johnson, B. D., & Lee, J. C. 2009, ApJ, 703, 1672
Kennicutt, R. C., & Skillman, E. D. 2001, AJ, 121, 1461
Kennicutt, Jr., R. C., Calzetti, D., Walter, F., Helou, G., Hollenbach, D. J., Armus, L., Bendo, G., Dale, D. A., et al. 2007, ApJ, 671, 333
Kewley, L. J., & Dopita, M. A. 2002, ApJS, 142, 35
Kewley, L. J., Dopita, M. A., Sutherland, R. S., Heisler, C. A., & Trevena, J. 2001a, ApJ, 556, 121
Kewley, L. J., & Ellison, S. L. 2008, ApJ, 681, 1183
Kewley, L. J., Groves, B., Kauffmann, G., & Heckman, T. 2006, MNRAS, 372, 961
Kewley, L. J., Heisler, C. A., Dopita, M. A., & Lumsden, S. 2001b, ApJS, 132, 37
Kewley, L. J., Heisler, C. A., Dopita, M. A., Sutherland, R., Norris, R. P., Reynolds, J., & Lumsden, S. 2000, ApJ, 530, 704
Kewley, L. J., Jansen, R. A., & Geller, M. J. 2005, PASP, 117, 227
Kinkel, U., & Rosa, M. R. 1994, A&A, 282, L37
Kniazev, A. Y., Pustilnik, S. A., Grebel, E. K., Lee, H., & Pramskij, A. G. 2004, ApJS, 153, 429
Kobulnicky, H. A., Kennicutt, R. C., & Pizagno, J. L. 1999, ApJ, 514, 544
Kobulnicky, H. A., & Kewley, L. J. 2004, ApJ, 617, 240
Kobulnicky, H. A., & Phillips, A. C. 2003, ApJ, 599, 1031
Kobulnicky, H. A., Willmer, C. N. A., Phillips, A. C., Koo, D. C., Faber, S. M., Weiner, B. J., Sarajedini, V. L., Simard, L., et al. 2003, ApJ, 599, 1006
Kong, X., & Cheng, F. Z. 2002, A&A, 389, 845
Kormendy, J., & Kennicutt, Jr., R. C. 2004, ARA&A, 42, 603
Kudritzki, R., Urbaneja, M. A., Bresolin, F., Przybilla, N., Gieren, W., & Pietrzyński, G. 2008, ApJ, 681, 269
Lamareille, F., Mouhcine, M., Contini, T., Lewis, I., & Maddox, S. 2004, MNRAS, 350, 396
Lee, H., Grebel, E. K., & Hodge, P. W. 2003a, A&A, 401, 141
Lee, H., McCall, M. L., Kingsburgh, R. L., Ross, R., & Stevenson, C. C. 2003b, AJ, 125, 146
Lee, H., & Skillman, E. D. 2004, ApJ, 614, 698
Lee, H., Skillman, E. D., Cannon, J. M., Jackson, D. C., Gehrz, R. D., Polomski, E. F., & Woodward, C. E. 2006a, ApJ, 647, 970
Lee, H., Skillman, E. D., & Venn, K. A. 2006b, ApJ, 642, 813
Lee, J. C., Salzer, J. J., & Melbourne, J. 2004, ApJ, 616, 752
Lehnert, M. D., & Heckman, T. M. 1994, ApJ, 426, L27
Lehnert, M. D., Nesvadba, N. P. H., Tiran, L. L., Matteo, P. D., van Driel, W., Douglas, L. S., Chemin, L., & Bournaud, F. 2009, ApJ, 699, 1660
Leonard, D. C., Filippenko, A. V., Li, W., Matheson, T., Kirshner, R. P., Chornock, R., Van Dyk, S. D., Berlind, P., Calkins, M. L., Challis, P. M., Garnavich, P. M., Jha, S., & Mahdavi, A. 2002, AJ, 124, 2490
Levesque, E. M., Kewley, L. J., & Larson, K. L. 2010, AJ, 139, 712
Liang, Y. C., Yin, S. Y., Hammer, F., Deng, L. C., Flores, H., & Zhang, B. 2006, ApJ, 652, 257
Liu, X., Shapley, A. E., Coil, A. L., Brinchmann, J., & Ma, C.-P. 2008, ApJ, 678, 758
Macri, L. M., Stetson, P. B., Bothun, G. D., Freedman, W. L., Garnavich, P. M., Jha, S., Madore, B. F., & Richmond, M. W. 2001, ApJ, 559, 243
Madden, S. C. 2000, New Astronomy Review, 44, 249
Maier, C., Lilly, S. J., Carollo, C. M., Meisenheimer, K., Hippelein, H., & Stockton, A. 2006, ApJ, 639, 858
Maier, C., Lilly, S. J., Carollo, C. M., Stockton, A., & Brodwin, M. 2005, ApJ, 634, 849
Maiolino, R., Nagao, T., Grazian, A., Cocchia, F., Marconi, A., Mannucci, F., Cimatti, A., Pipino, A., et al. 2008, A&A, 488, 463
Makarova, L., Karachentsev, I., Takalo, L. O., Heinaemaeki, P., & Valtonen, M. 1998, A&AS, 128, 459
Makarova, L. N., Grebel, E. K., Karachentsev, I. D., Dolphin, A. E., Karachentseva, V. E., Sharina, M. E., Geisler, D., Guhathakurta, P., et al. 2002, A&A, 396, 473
Marcon-Uchida, M. M., Matteucci, F., & Costa, R. D. D. 2010, astro-ph/1004.4139
Martín-Hernández, N. L., Peeters, E., Morisset, C., Tielens, A. G. G. M., Cox, P., Roelfsema, P. R., Baluteau, J., Schaerer, D., et al. 2002, A&A, 381, 606
Martín-Manjón, M. L., García-Vargas, M. L., Mollá, M., & Díaz, A. I. 2010, MNRAS, 200
Masegosa, J., Moles, M., & del Olmo, A. 1991, A&A, 249, 505
Massey, P., Strobel, K., Barnes, J. V., & Anderson, E. 1988, ApJ, 328, 315

Masters, K. L. 2005, PhD thesis, Cornell University, United States – New York
Mathis, J. S., & Wood, K. 2005, MNRAS, 360, 227
Matsumoto, H., Tsuru, T. G., Koyama, K., Awaki, H., Canizares, C. R., Kawai, N., Matsushita, S., & Kawabe, R. 2001, ApJ, 547, L25
McCall, M. L., Rybski, P. M., & Shields, G. A. 1985, ApJS, 57, 1
McGaugh, S. S. 1991, ApJ, 380, 140
Mei, S., Blakeslee, J. P., Côté, P., Tonry, J. L., West, M. J., Ferrarese, L., Jordán, A., Peng, E. W., Anthony, A., & Merritt, D. 2007, ApJ, 655, 144
Meurer, G. R., Hanish, D. J., Ferguson, H. C., Knezek, P. M., Kilborn, V. A., Putman, M. E., Smith, R. C., Koribalski, B., et al. 2006, ApJS, 165, 307
Miller, B. W., & Hodge, P. 1996, ApJ, 458, 467
Molla, M., Ferrini, F., & Diaz, A. I. 1996, ApJ, 466, 668
Mouhcine, M., & Contini, T. 2002, A&A, 389, 106
Moustakas, J., & Kennicutt, R. C. 2006a, ApJS, 164, 81
Moustakas, J., Kennicutt, R. C., & Tremonti, C. A. 2006, ApJ, 642, 775
Moustakas, J., & Kennicutt, Jr., R. C. 2006b, ApJ, 651, 155
Moy, E., Rocca-Volmerange, B., & Fioc, M. 2001, A&A, 365, 347
Muñoz-Mateos, J. C., Gil de Paz, A., Boissier, S., Zamorano, J., Dale, D. A., Pérez-González, P. G., Gallego, J., Madore, B. F., et al. 2009a, ApJ, 701, 1965
Muñoz-Mateos, J. C., Gil de Paz, A., Zamorano, J., Boissier, S., Dale, D. A., Pérez-González, P. G., Gallego, J., Madore, B. F., et al. 2009b, ApJ, 703, 1569
Murphy, E. J., Braun, R., Helou, G., Armus, L., Kenney, J. D. P., Gordon, K. D., Bendo, G. J., Dale, D. A., et al. 2006, ApJ, 638, 157
Nagao, T., Maiolino, R., & Marconi, A. 2006, A&A, 459, 85
Ocvirk, P., Pichon, C., Lançon, A., & Thiébaut, E. 2006, MNRAS, 365, 46
O'Donnell, J. E. 1994, ApJ, 422, 158
Oey, M. S., & Kennicutt, R. C. 1993, ApJ, 411, 137
Okada, Y., Onaka, T., Miyata, T., Okamoto, Y. K., Sakon, I., Shibai, H., & Takahashi, H. 2008, ApJ, 682, 416
Osterbrock, D. E., & Ferland, G. J. 2006, Astrophysics of gaseous nebulae and active galactic nuclei (Astrophysics of gaseous nebulae and active galactic nuclei, 2nd. ed. by D.E. Osterbrock and G.J. Ferland. Sausalito, CA: University Science Books, 2006)
Pagel, B. E. J., Edmunds, M. G., Blackwell, D. E., Chun, M. S., & Smith, G. 1979, MNRAS, 189, 95
Panter, B., Heavens, A. F., & Jimenez, R. 2003, MNRAS, 343, 1145
Peimbert, A., & Peimbert, M. 2005, in Revista Mexicana de Astronomia y Astrofisica Conference Series, Vol. 23, Revista Mexicana de Astronomia y Astrofisica Conference Series, ed. S. Torres-Peimbert & G. MacAlpine, 9–14
Peimbert, A., Peimbert, M., & Ruiz, M. T. 2005, ApJ, 634, 1056
Peimbert, M. 1967, ApJ, 150, 825
Peimbert, M., Peimbert, A., Esteban, C., García-Rojas, J., Bresolin, F., Carigi, L., Ruiz, M. T., & López-Sánchez, Á. R. 2007, in Revista Mexicana de Astronomia y Astrofisica, vol. 27, Vol. 29, Revista Mexicana de Astronomia y Astrofisica Conference Series, 72–79
Pérez-Montero, E., & Díaz, A. I. 2005, MNRAS, 361, 1063
Pettini, M. 2006, astro-ph/0603066
Pettini, M., & Pagel, B. E. J. 2004, MNRAS, 348, L59
Pettini, M., Shapley, A. E., Steidel, C. C., Cuby, J., Dickinson, M., Moorwood, A. F. M., Adelberger, K. L., & Giavalisco, M. 2001, ApJ, 554, 981
Pietrzyński, G., Gieren, W., Udalski, A., Bresolin, F., Kudritzki, R.-P., Soszyński, I., Szymański, M., & Kubiak, M. 2004, AJ, 128, 2815
Pilyugin, L. S. 2000, A&A, 362, 325
—. 2001, A&A, 369, 594
—. 2005, A&A, 436, L1
Pilyugin, L. S., Contini, T., & Vílchez, J. M. 2004a, A&A, 423, 427
Pilyugin, L. S., & Thuan, T. X. 2005, ApJ, 631, 231
Pilyugin, L. S., Thuan, T. X., & Vílchez, J. M. 2003, A&A, 397, 487
—. 2006, MNRAS, 210
—. 2007, MNRAS, 376, 353
Pilyugin, L. S., Vílchez, J. M., & Contini, T. 2004b, A&A, 425, 849
Poglitsch, A., Waelkens, C., Bauer, O. H., Cepa, J., Feuchtgruber, H., Henning, T., van Hoof, C., Kerschbaum, F., Krause, O., Renotte, E., Rodriguez, L., Saraceno, P., & Vandenbussche, B. 2008, in Society of Photo-Optical Instrumentation Engineers (SPIE) Conference Series, Vol. 7010, Society of Photo-Optical Instrumentation Engineers (SPIE) Conference Series
Prantzos, N., & Boissier, S. 2000, MNRAS, 313, 338
Prescott, M. K. M., Kennicutt, Jr., R. C., Bendo, G. J., Buckalew, B. A., Calzetti, D., Engelbracht, C. W., Gordon, K. D., Hollenbach, D. J., et al. 2007, ApJ, 668, 182
Prugniel, P., & Heraudeau, P. 1998, A&AS, 128, 299
Przybilla, N., Nieva, M., & Butler, K. 2008, ApJ, 688, L103
Regan, M. W., Thornley, M. D., Bendo, G. J., Draine, B. T., Li, A., Dale, D. A., Engelbracht, C. W., Kennicutt, Jr., R. C., et al. 2004, ApJS, 154, 204
Rieke, G. H., Alonso-Herrero, A., Weiner, B. J., Pérez-González, P. G., Blaylock, M., Donley, J. L., & Marcillac, D. 2009, ApJ, 692, 556
Rieke, G. H., Young, E. T., Engelbracht, C. W., Kelly, D. M., Low, F. J., Haller, E. E., Beeman, J. W., Gordon, K. D., et al. 2004, ApJS, 154, 25
Rosales-Ortega, F. F. 2009, PhD thesis, PhD Thesis, University of Cambridge, 2010.
Rosales-Ortega, F. F., Kennicutt, R. C., Sánchez, S. F., Díaz, A. I., Pasquali, A., Johnson, B. D., & Hao, C. N. 2010, MNRAS, 405, 735
Rosolowsky, E., & Simon, J. D. 2008, ApJ, 675, 1213
Roussel, H., Helou, G., Hollenbach, D. J., Draine, B. T., Smith, J. D., Armus, L., Schinnerer, E., Walter, F., et al. 2007, ApJ, 669, 959
Roussel, H., Helou, G., Smith, J. D., Draine, B. T., Hollenbach, D. J., Moustakas, J., Spoon, H. W., Kennicutt, R. C., et al. 2006, ApJ, 646, 841
Rubin, R. H., Simpson, J. P., Colgan, S. W. J., Dufour, R. J., Brunner, G., McNabb, I. A., Pauldrach, A. W. A., Erickson, E. F., Haas, M. R., & Citron, R. I. 2008, MNRAS, 387, 45
Rudolph, A. L., Fich, M., Bell, G. R., Norsen, T., Simpson, J. P., Haas, M. R., & Erickson, E. F. 2006, ApJS, 162, 346
Ryder, S. D. 1995, ApJ, 444, 610
Salpeter, E. E. 1955, ApJ, 121, 161
Salzer, J. J., Lee, J. C., Melbourne, J., Hinz, J. L., Alonso-Herrero, A., & Jangren, A. 2005, ApJ, 624, 661
Sarzi, M., Falcón-Barroso, J., Davies, R. L., Bacon, R., Bureau, M., Cappellari, M., de Zeeuw, P. T., Emsellem, E., et al. 2006, MNRAS, 366, 1151
Savaglio, S., Glazebrook, K., Le Borgne, D., Juneau, S., Abraham, R. G., Chen, H., Crampton, D., McCarthy, P. J., et al. 2005, ApJ, 635, 260
Schawinski, K., Thomas, D., Sarzi, M., Maraston, C., Kaviraj, S., Joo, S., Yi, S. K., & Silk, J. 2007, MNRAS, 382, 1415
Schlegel, D. J., Finkbeiner, D. P., & Davis, M. 1998, ApJ, 500, 525
Searle, L. 1971, ApJ, 168, 327
Serenelli, A. M., Basu, S., Ferguson, J. W., & Asplund, M. 2009, ApJ, 705, L123
Seth, A. C., Dalcanton, J. J., & de Jong, R. S. 2005, AJ, 129, 1331
Seyfert, C. K. 1943, ApJ, 97, 28
Shapley, A. E., Coil, A. L., Ma, C., & Bundy, K. 2005, ApJ, 635, 1006
Shapley, A. E., Erb, D. K., Pettini, M., Steidel, C. C., & Adelberger, K. L. 2004, ApJ, 612, 108
Sharina, M. E., Karachentsev, I. D., & Tikhonov, N. A. 1996, A&AS, 119, 499
Shaver, P. A., McGee, R. X., Newton, L. M., Danks, A. C., & Pottasch, S. R. 1983, MNRAS, 204, 53
Shi, F., Kong, X., & Cheng, F. Z. 2006, A&A, 453, 487
Shields, G. A. 1990, ARA&A, 28, 525
—. 1991, PASP, 103, 916
Shields, J. C., & Kennicutt, Jr., R. C. 1995, ApJ, 454, 807
Simón-Díaz, S. 2010, A&A, 510, A260000+
Simón-Díaz, S., & Stasińska, G. 2008, MNRAS, 389, 1009
Skillman, E. D. 1989, ApJ, 347, 883
Skillman, E. D. 1998, in Stellar astrophysics for the local group: VIII Canary Islands Winter School of Astrophysics, ed. A. Aparicio, A. Herrero, & F. Sánchez, 457–+

Skillman, E. D., Kennicutt, R. C., & Hodge, P. W. 1989, ApJ, 347, 875
Smith, J. D. T., Dale, D. A., Armus, L., Draine, B. T., Hollenbach, D. J., Roussel, H., Helou, G., Kennicutt, Jr., R. C., et al. 2004, ApJS, 154, 199
Smith, J. D. T., Draine, B. T., Dale, D. A., Moustakas, J., Kennicutt, Jr., R. C., Helou, G., Armus, L., Roussel, H., et al. 2007, ApJ, 656, 770
Stasińska, G. 2002, in Revista Mexicana de Astronomia y Astrofisica Conference Series, Vol. 12, Revista Mexicana de Astronomia y Astrofisica Conference Series, ed. W. J. Henney, J. Franco, & M. Martos, 62–69
Stasińska, G. 2005, A&A, 434, 507
—. 2006, A&A, 454, L127
—. 2007, astro-ph/0704.0348
Stasińska, G. 2010, in IAU Symposium, Vol. 262, IAU Symposium, ed. G. Bruzual & S. Charlot, 93–96
Stasińska, G., Cid Fernandes, R., Mateus, A., Sodré, L., & Asari, N. V. 2006, MNRAS, 371, 972
Stasińska, G., Comte, G., & Vigroux, L. 1986, A&A, 154, 352
Stasińska, G., & Schaerer, D. 1999, A&A, 351, 72
Stasińska, G., Tenorio-Tagle, G., Rodríguez, M., & Henney, W. J. 2007, A&A, 471, 193
Stauffer, J. R., & Bothun, G. D. 1984, AJ, 89, 1702
Storchi-Bergmann, T., Calzetti, D., & Kinney, A. L. 1994, ApJ, 429, 572
Storchi-Bergmann, T., Kinney, A. L., & Challis, P. 1995, ApJS, 98, 103
Storchi-Bergmann, T., Wilson, A. S., & Baldwin, J. A. 1996, ApJ, 460, 252
Storey, P. J., & Hummer, D. G. 1995, MNRAS, 272, 41
Sutherland, R. S., & Dopita, M. A. 1993, ApJS, 88, 253
Tajer, M., Trinchieri, G., Wolter, A., Campana, S., Moretti, A., & Tagliaferri, G. 2005, A&A, 435, 799
Tojeiro, R., Heavens, A. F., Jimenez, R., & Panter, B. 2007, MNRAS, 381, 1252
Tonry, J. L., Dressler, A., Blakeslee, J. P., Ajhar, E. A., Fletcher, A. B., Luppino, G. A., Metzger, M. R., & Moore, C. B. 2001, ApJ, 546, 681
Torres-Peimbert, S., Peimbert, M., & Fierro, J. 1989, ApJ, 345, 186
Tosi, M., Sabbi, E., Bellazzini, M., Aloisi, A., Greggio, L., Leitherer, C., & Montegriffo, P. 2001, AJ, 122, 1271
Tremonti, C. A., Heckman, T. M., Kauffmann, G., Brinchmann, J., Charlot, S., White, S. D. M., Seibert, M., Peng, E. W., et al. 2004, ApJ, 613, 898
Tully, R. B. 1974, ApJS, 27, 437
Tully, R. B., Pierce, M. J., Huang, J., Saunders, W., Verheijen, M. A. W., & Witchalls, P. L. 1998, AJ, 115, 2264
Urbaneja, M. A., Herrero, A., Bresolin, F., Kudritzki, R., Gieren, W., Puls, J., Przybilla, N., Najarro, F., & Pietrzyński, G. 2005, ApJ, 622, 862
van Zee, L., & Haynes, M. P. 2006, ApJ, 636, 214
van Zee, L., Haynes, M. P., & Salzer, J. J. 1997, AJ, 114, 2479
van Zee, L., Salzer, J. J., Haynes, M. P., O'Donoghue, A. A., & Balonek, T. J. 1998, AJ, 116, 2805
van Zee, L., Skillman, E. D., & Haynes, M. P. 2006, ApJ, 637, 269
Vázquez, G. A., & Leitherer, C. 2005, ApJ, 621, 695
Veilleux, S., & Osterbrock, D. E. 1987, ApJS, 63, 295
Vila-Costas, M. B., & Edmunds, M. G. 1992, MNRAS, 259, 121
Vilchez, J. M., & Esteban, C. 1996, MNRAS, 280, 720
Walter, F., Brinks, E., de Blok, W. J. G., Bigiel, F., Kennicutt, R. C., Thornley, M. D., & Leroy, A. 2008, AJ, 136, 2563
Walter, F., Cannon, J. M., Roussel, H., Bendo, G. J., Calzetti, D., Dale, D. A., Draine, B. T., Helou, G., et al. 2007, ApJ, 661, 102
Webster, B. L., & Smith, M. G. 1983, MNRAS, 204, 743
Weedman, D. W., Hao, L., Higdon, S. J. U., Devost, D., Wu, Y., Charmandaris, V., Brandl, B., Bass, E., & Houck, J. R. 2005, ApJ, 633, 706
Witt, A. N., & Gordon, K. D. 2000, ApJ, 528, 799
Wu, Y., Bernard-Salas, J., Charmandaris, V., Lebouteiller, V., Hao, L., Brandl, B. R., & Houck, J. R. 2008, ApJ, 673, 193
Wu, Y., Charmandaris, V., Huang, J., Spinoglio, L., & Tommasin, S. 2009, ApJ, 701, 658
Yin, S. Y., Liang, Y. C., Hammer, F., Brinchmann, J., Zhang, B., Deng, L. C., & Flores, H. 2007, A&A, 462, 535
York, D. G., et al. 2000, AJ, 120, 1579
Zaritsky, D., Kennicutt, R. C., & Huchra, J. P. 1994, ApJ, 420, 87
Zhu, Y., Wu, H., Cao, C., & Li, H. 2008, ApJ, 686, 155

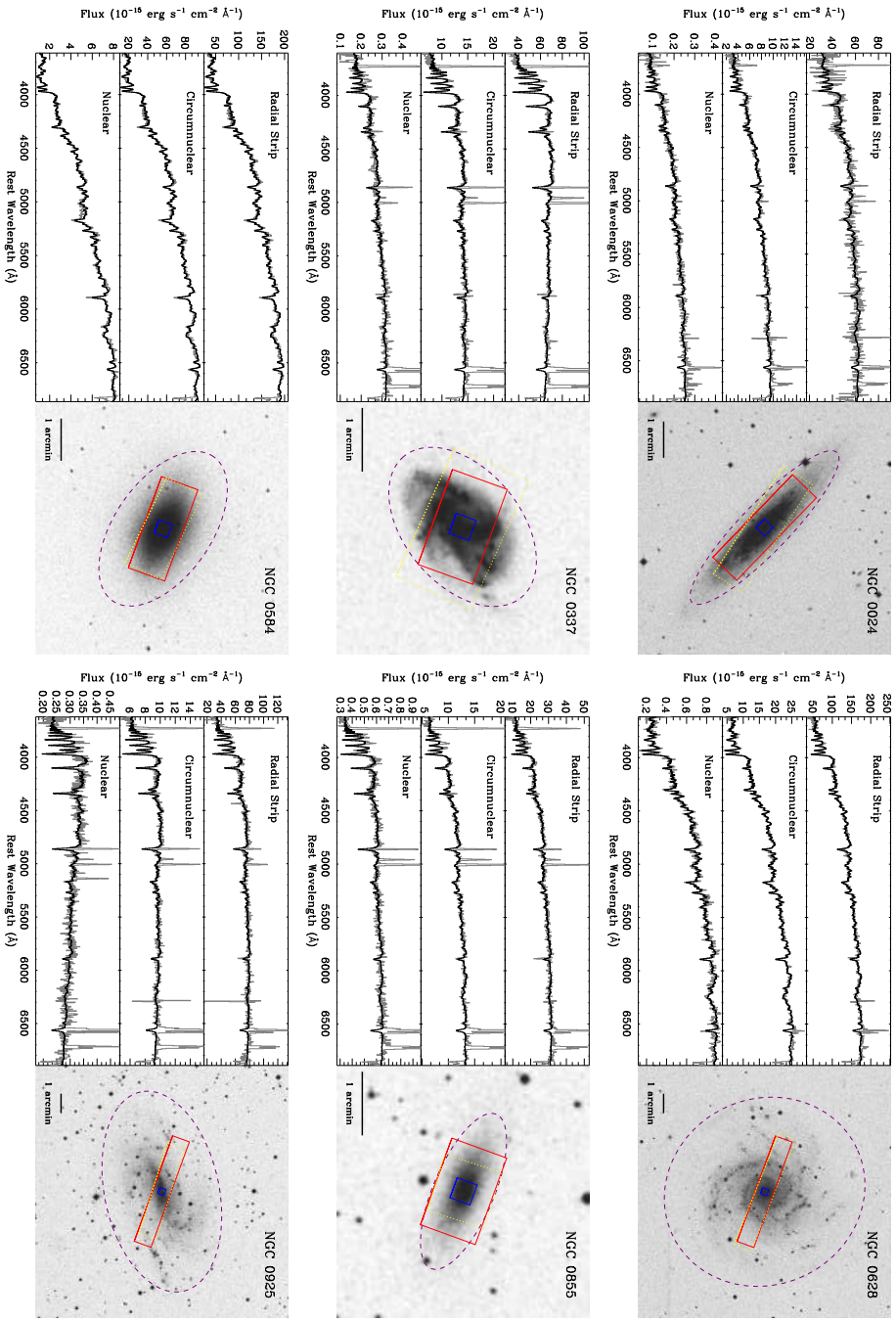

FIG. A1.— The left panels plot the nuclear, circumnuclear, and radial-strip spectra optical spectra of the first six SINGS galaxies; the observed spectra are shown in grey and the best-fitting stellar continuum fit is overplotted in black (see §2.2.2). The right panels show the size of the circumnuclear (*blue square*) and radial-strip (*red rectangle*) spectroscopic apertures, overlaid on an optical DSS image of each galaxy. The dashed purple ellipse indicates the optical extent of the galaxy (see Table 1), and the dotted yellow rectangle shows the spatial coverage of the *Spitzer*/IRS radial-strip long-low spectrum obtained as part of SINGS (Smith et al. 2004, 2007).

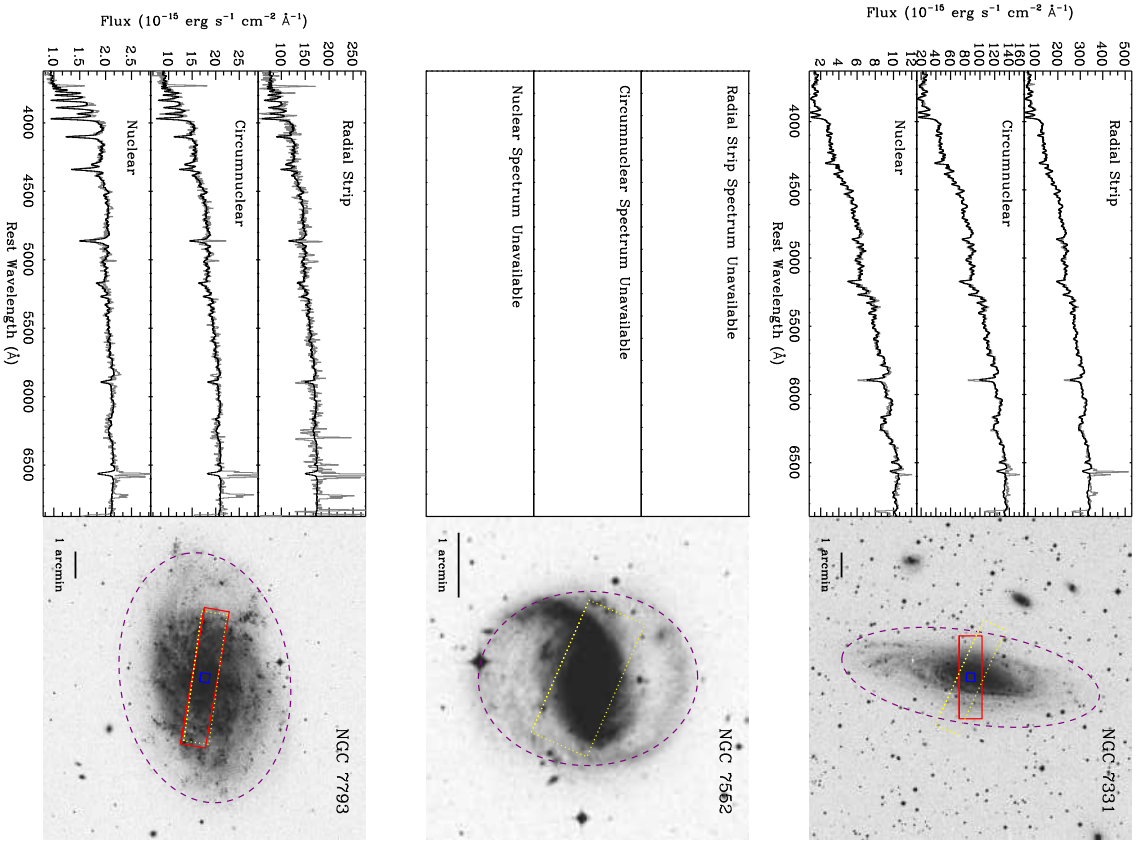

FIG. A2.— Same of Fig. A1, but for the final three SINGS galaxies. Note that the visualizations for the intervening galaxies can be found in the online edition of the published ApJS paper.

TABLE 1
Properties of the SINGS Galaxies

Galaxy (1)	Type (2)	$E(B-V)$ (mag) (3)	ρ_{25} (arcmin) (4)	i (deg) (5)	θ (deg) (6)	M_B (mag) (7)	$B-V$ (mag) (8)	D (Mpc) (9)	Distance Method (10)	Distance Ref. (11)
NGC 0024	SAc	0.020	2.88	82	46	-17.31 ± 0.69	0.68 ± 0.05	7.3 ± 2.3	Flow	1
NGC 0337	SBd	0.112	1.44	52	130	-20.09 ± 0.24	0.38 ± 0.05	22.4 ± 2.3	Flow	1
NGC 0584	E4	0.042	2.08	58	55	-19.92 ± 0.22	1.13 ± 0.05	20.1 ± 1.9	SBF	2
NGC 0628	SAc	0.070	5.24	24	25	-19.60 ± 0.43	0.50 ± 0.05	7.3 ± 1.4	BS	3
NGC 0855	E	0.071	1.32	71	67	-17.01 ± 0.20	0.58 ± 0.05	9.73 ± 0.76	SBF	2
NGC 0925	SABd	0.076	5.24	57	102	-19.24 ± 0.11	0.61 ± 0.05	9.12 ± 0.17[a]	Ceph	4
NGC 1097	SBb	0.027	4.67	48	130	-21.21 ± 0.31	0.67 ± 0.05	17.1 ± 2.3	Flow	1
NGC 1266	SB0 pec	0.098	0.77	53	108	-18.89 ± 0.19	0.87 ± 0.05	30.0 ± 2.3	Flow	1
NGC 1291	SB0/a	0.013	4.89	34	156	-20.64 ± 0.47	0.87 ± 0.05	10.8 ± 2.3	Flow	1
NGC 1316	SAB0	0.021	6.01	46	50	-22.49 ± 0.20	0.84 ± 0.05	21.5 ± 1.7	SBF	2
NGC 1377	S0	0.028	0.89	62	92	-18.85 ± 0.22	0.47 ± 0.05	25.0 ± 2.3	Flow	1
NGC 1404	E1	0.011	1.66	27	163	-20.73 ± 0.21	0.89 ± 0.05	20.8 ± 1.7	Mult	5
NGC 1482	SA0 pec	0.040	1.23	57	103	-18.76 ± 0.24	0.78 ± 0.06	23.2 ± 2.3	Flow	1
NGC 1512	SBab	0.011	4.46	52	90	-19.32 ± 0.43	0.69 ± 0.05	11.8 ± 2.3	Flow	1
NGC 1566	SABbc	0.009	4.16	38	60	-21.45 ± 0.26	0.68 ± 0.05	20.4 ± 2.3	Flow	1
NGC 1705	SA0 pec	0.008	0.95	43	50	-15.65 ± 0.27	0.44 ± 0.05	5.10 ± 0.60	TRGB	6
NGC 2403	SABcd	0.040	10.94	57	128	-18.93 ± 0.14	0.49 ± 0.06	3.13 ± 0.14	Ceph	4
Ho II	Im	0.032	3.97	38	16	-16.71 ± 0.16	0.11 ± 0.05	3.39 ± 0.20	TRGB	7
M 81 Dw A	I?	0.020	0.65	59	···	-11.70 ± 0.19	-0.33 ± 0.05	3.55 ± 0.26	TRGB	7
DDO 053	Im	0.038	0.77	30	121	-13.61 ± 0.18	-0.09 ± 0.05	3.56 ± 0.25	TRGB	7
NGC 2798	SBa pec	0.020	1.28	70	160	-18.97 ± 0.22	0.76 ± 0.05	26.2 ± 2.3	Flow	1
NGC 2841	SAb	0.015	4.06	66	147	-20.67 ± 0.25	0.85 ± 0.05	14.1 ± 1.5	Ceph	8
NGC 2915	I0	0.275	0.95	61	130	-15.85 ± 0.28	0.11 ± 0.05	3.78 ± 0.45	TRGB	7
Ho I	IABm	0.050	1.82	36	···	-14.94 ± 0.28	0.13 ± 0.05	3.84 ± 0.46	TRGB	7
NGC 2976	SAc pec	0.071	2.94	65	143	-17.16 ± 0.25	0.62 ± 0.05	3.56 ± 0.38	TRGB	7
NGC 3049	SBab	0.038	1.09	49	25	-18.71 ± 0.23	0.61 ± 0.05	23.9 ± 2.3	Flow	1
NGC 3031	SAab	0.080	13.46	60	157	-20.22 ± 0.13	0.79 ± 0.05	3.55 ± 0.13[a]	Ceph	4
NGC 3034	I0	0.156	5.61	70	65	-19.36 ± 0.17	0.79 ± 0.05	3.89 ± 0.25	TRGB	9
Ho IX	Im	0.079	1.26	36	···	-13.98 ± 0.42	-0.19 ± 0.05	3.70 ± 0.70	Mem	7
M 81 Dw B	Im	0.081	0.44	49	140	-14.21 ± 0.54	0.01 ± 0.05	5.3 ± 1.3	BS	7
NGC 3190	SAa pec	0.025	2.18	72	125	-20.40 ± 0.15	0.88 ± 0.05	26.4 ± 1.3	SN	10
NGC 3184	SABcd	0.017	3.71	21	135	-19.87 ± 0.38	0.57 ± 0.05	11.1 ± 1.9	SN	11
NGC 3198	SBc	0.012	4.26	70	35	-19.71 ± 0.13	0.49 ± 0.05	13.68 ± 0.50[a]	Ceph	4
IC 2574	SABm	0.036	6.59	68	50	-16.90 ± 0.24	0.43 ± 0.05	4.02 ± 0.41	TRGB	7
NGC 3265	E	0.024	0.64	40	73	-18.39 ± 0.24	0.38 ± 0.05	23.2 ± 2.3	Flow	1
Mrk 33	Im pec	0.012	0.50	21	150	-17.85 ± 0.24	0.70 ± 0.05	22.9 ± 2.3	Flow	1
NGC 3351	SBb	0.028	3.71	48	13	-19.38 ± 0.14	0.78 ± 0.05	9.33 ± 0.39[a]	Ceph	4
NGC 3521	SABbc	0.057	5.48	64	163	-20.65 ± 0.50	0.72 ± 0.05	10.1 ± 2.3	Flow	1
NGC 3621	SAd	0.081	6.15	56	159	-19.50 ± 0.12	0.48 ± 0.06	6.55 ± 0.18[a]	Ceph	4
NGC 3627	SABb	0.033	4.56	65	173	-20.45 ± 0.13	0.70 ± 0.05	9.38 ± 0.35[a]	Ceph	4
NGC 3773	SA0	0.027	0.59	32	165	-16.81 ± 0.43	0.42 ± 0.05	11.9 ± 2.3	Flow	1
NGC 3938	SAc	0.021	2.69	24	29	-19.84 ± 0.39	0.48 ± 0.05	13.4 ± 2.3	Flow	1
NGC 4125	E6 pec	0.019	2.88	58	95	-21.26 ± 0.27	0.84 ± 0.05	23.9 ± 2.8	SBF	2
NGC 4236	SBdm	0.015	10.94	74	162	-18.00 ± 0.24	0.21 ± 0.05	4.45 ± 0.45	TRGB	7
NGC 4254	SAc	0.039	2.69	30	24	-20.85 ± 0.13	0.56 ± 0.05	16.50 ± 0.60[b]	Mem	12
NGC 4321	SABbc	0.026	3.71	32	30	-20.81 ± 0.12	0.67 ± 0.05	14.32 ± 0.46[a]	Ceph	4
NGC 4450	SAab	0.028	2.62	43	175	-20.24 ± 0.13	0.85 ± 0.05	16.50 ± 0.60[b]	Mem	12
NGC 4536	SABbc	0.018	3.79	67	130	-19.75 ± 0.11	0.64 ± 0.05	14.45 ± 0.27[a]	Ceph	4
NGC 4552	E	0.041	2.56	24	150	-20.33 ± 0.15	0.90 ± 0.05	15.92 ± 0.81	Mult	5
NGC 4559	SABcd	0.018	5.36	68	150	-19.69 ± 0.50	0.44 ± 0.05	10.3 ± 2.3	Flow	1
NGC 4569	SABab	0.047	4.78	65	23	-21.03 ± 0.13	0.59 ± 0.05	16.50 ± 0.60[b]	Mem	12
NGC 4579	SABb	0.041	2.94	38	95	-20.79 ± 0.13	0.81 ± 0.05	16.50 ± 0.60[b]	Mem	12
NGC 4594	SAa	0.051	4.36	68	90	-20.76 ± 0.13	0.98 ± 0.05	9.33 ± 0.34	Mult	5
NGC 4625	SABm pec	0.018	1.09	30	28	-16.80 ± 0.55	0.61 ± 0.05	9.2 ± 2.3	Flow	1
NGC 4631	SBd	0.017	7.74	89	86	-19.73 ± 0.11	0.45 ± 0.05	7.62 ± 0.14	TRGB	13
NGC 4725	SABab pec	0.012	5.36	46	35	-20.42 ± 0.12	0.77 ± 0.05	11.91 ± 0.33[a]	Ceph	4
NGC 4736	SAab	0.018	5.61	36	105	-19.89 ± 0.21	0.76 ± 0.05	5.20 ± 0.43	SBF	2
DDO 154	IBm	0.009	1.51	44	35	-14.43 ± 0.46	-0.18 ± 0.05	4.30 ± 0.89	BS	14
NGC 4826	SAab	0.041	5.00	59	115	-20.25 ± 0.22	0.75 ± 0.05	7.48 ± 0.69	SBF	2
DDO 165	Im	0.024	1.73	58	90	-15.59 ± 0.21	0.01 ± 0.05	4.57 ± 0.40	TRGB	7
NGC 5033	SAc	0.012	5.36	64	170	-20.12 ± 0.35	0.69 ± 0.05	14.8 ± 2.3	Flow	1
NGC 5055	SAbc	0.018	6.30	56	105	-20.23 ± 0.65	0.76 ± 0.05	7.8 ± 2.3	Flow	1
NGC 5194	SABbc pec	0.035	5.61	20[c]	163	-20.63 ± 0.14	0.58 ± 0.05	7.62 ± 0.35[d]	PNLF	15
NGC 5195	SB0 pec	0.035	2.88	38	79	-19.43 ± 0.14	0.82 ± 0.05	7.62 ± 0.35[d]	PNLF	15
Tol 89	SBdm	0.066	1.41	54	172	-19.10 ± 0.32	0.10 ± 0.05	16.7 ± 2.3	Flow	1
NGC 5408	IBm	0.068	0.81	62	62	-16.57 ± 0.20	0.43 ± 0.05	4.81 ± 0.38	TRGB	7
NGC 5474	SAcd pec	0.011	2.39	27	98	-17.69 ± 0.55	0.44 ± 0.06	6.8 ± 1.7	BS	16
NGC 5713	SABbc pec	0.039	1.38	27	10	-20.53 ± 0.20	0.66 ± 0.05	29.4 ± 2.3	Flow	1
NGC 5866	S0	0.013	2.34	68	128	-20.20 ± 0.16	0.81 ± 0.05	15.42 ± 0.85	SBF	2
IC 4710	SBm	0.089	1.82	40	4	-18.03 ± 0.56	0.39 ± 0.05	9.0 ± 2.3	Flow	1
NGC 6822	IBm	0.231	7.74	50[e]	122[e]	-14.99 ± 0.25[e]	0.60 ± 0.06[e]	0.470 ± 0.050	Ceph	17
NGC 6946	SABcd	0.342	5.74	32	53	-21.04 ± 0.55	0.63 ± 0.08	6.8 ± 1.7	BS	18
NGC 7331	SAb	0.091	5.24	72	171	-21.05 ± 0.13	0.67 ± 0.05	14.52 ± 0.60[a]	Ceph	4

TABLE 1 — *Continued*

Galaxy (1)	Type (2)	$E(B-V)$ (mag) (3)	ρ_{25} (arcmin) (4)	i (deg) (5)	θ (deg) (6)	M_B (mag) (7)	$B-V$ (mag) (8)	D (Mpc) (9)	Distance Method (10)	Distance Ref. (11)
NGC 7552	SBab	0.014	1.69	38	1	-20.44 ± 0.26	0.67 ± 0.05	21.0 ± 2.3	Flow	1
NGC 7793	SAd	0.019	4.67	48	98	-18.40 ± 0.26	0.45 ± 0.05	3.91 ± 0.43	TRGB	7

REFERENCES. — (1) Masters (2005); (2) Tonry et al. (2001); (3) Sharina et al. (1996); (4) Freedman et al. (2001); (5) Ferrarese et al. (2000b); (6) Tosi et al. (2001); (7) Karachentsev et al. (2003); (8) Macri et al. (2001); (9) Ferrarese et al. (2000a); (10) Jha et al. (2007); (11) Leonard et al. (2002); (12) Mei et al. (2007); (13) Seth et al. (2005); (14) Makarova et al. (1998); (15) Ciardullo et al. (2002); (16) Drozdovsky & Karachentsev (2000); (17) Pietrzyński et al. (2004); (18) Karachentsev et al. (2000).

NOTE. — (1) SINGS galaxy name; (2) Morphological type from Kennicutt et al. (2003a); (3) Color excess used to correct the optical spectroscopy and photometry for foreground Galactic reddening (Schlegel et al. 1998); (4) Radius of the major axis at the $\mu_B = 25$ mag arcsec^{-2} isophote (de Vaucouleurs et al. 1991); (5-6) Galaxy inclination and position angles (de Vaucouleurs et al. 1991; Jarrett et al. 2003). We compute the inclination angle, i, following Tully et al. (1998): $\sin(i) = 1.02 \times \sqrt{1-(b/a)^2}$, where (b/a) is the minor-to-major axis ratio at $\mu_B = 25$ mag arcsec^{-2} (de Vaucouleurs et al. 1991), or the isophotal axis ratio at $\mu_{K_s} = 20$ mag arcsec^{-2} (Jarrett et al. 2003); (7-8) Absolute B-band magnitude and $B-V$ color, both relative to Vega (Dale et al. 2007; Muñoz-Mateos et al. 2009a) (see §2.1 for more details); (9-11) Distance, distance method, and corresponding reference to the literature. The distance methods have the following meaning: Flow = Hubble distance assuming $H_0 = 70$ km s^{-1} Mpc^{-1} corrected for peculiar motions; SBF = surface-brightness fluctuations; BS = bright stars (supergiants); Ceph = Cepheid variables; Mult = an average of multiple, cross-calibrated techniques; TRGB = tip of the red-giant branch; Mem = group/cluster membership; SN = supernova; PNLF = planetary nebula luminosity function.

[a] For these objects we adopt the *HST* Key Project Cepheid distance uncorrected for metallicity variations (see Freedman et al. 2001).

[b] NGC 4254, NGC 4450, NGC 4569, and NGC 4579 have been placed at the distance of the Virgo cluster (16.5 ± 0.6 Mpc; Mei et al. 2007).

[c] For NGC 5194 we adopt the kinematic inclination angle determined by Tully (1974).

[d] The interacting pair NGC 5194 (M 51 a) and NGC 5195 have been placed at a common distance.

[e] For NGC 6822 we adopt the kinematic inclination and position angle derived by Brandenburg & Skillman (1998). We have also adjusted the apparent B- and V-band magnitudes for this object from Dale et al. (2007) by -0.37 mag to better match the B-band magnitude from Karachentsev et al. (2004).

TABLE 2
Journal of Observations

Galaxy	Nuclear					Circumnuclear					Radial Strip			
	Aperture[a]	θ_{slit}[b]	t_{exp}[c]	Phot[d]	Notes[e]	Aperture[a]	θ_{slit}[b]	t_{exp}[c]	Phot[d]	Notes[e]	Aperture[a]	θ_{slit}[b]	t_{exp}[c]	Phot[d]
NGC 0024	$2\farcs5 \times 2\farcs5$	177	300	Y	···	$20'' \times 20''$	46	75	Y	···	$190'' \times 55''$	46	109	Y
NGC 0337	$2\farcs5 \times 2\farcs5$	25	600	Y	1	$20'' \times 20''$	70	75	Y	···	$95'' \times 55''$	70	109	Y
NGC 0584	$2\farcs5 \times 2\farcs5$	25	300	Y	···	$20'' \times 20''$	70	75	Y	···	$138'' \times 55''$	70	109	Y
NGC 0628	$2\farcs5 \times 2\farcs5$	70	300	Y	···	$20'' \times 20''$	70	150	Y	···	$346'' \times 55''$	70	109	Y
NGC 0855	$2\farcs5 \times 2\farcs5$	70	300	Y	···	$20'' \times 20''$	70	75	Y	···	$86'' \times 55''$	70	109	N
NGC 0925	$2\farcs5 \times 2\farcs5$	70	300	Y	···	$20'' \times 20''$	70	112	Y	···	$346'' \times 55''$	70	109	Y
NGC 1097	$2\farcs5 \times 3\farcs0$	110	600	Y	···	$20'' \times 20''$	110	192	Y	···	$308'' \times 56''$	70	192	Y
NGC 1266	$2\farcs5 \times 2\farcs5$	70	600	Y	···	$20'' \times 20''$	70	75	Y	···	$51'' \times 55''$	70	109	Y
NGC 1291	$2\farcs5 \times 3\farcs0$	5	1200	N	···	$20'' \times 20''$	5	192	N	···	$293'' \times 56''$	5	192	N
NGC 1316	$2\farcs5 \times 3\farcs0$	60	1200	Y	···	$20'' \times 20''$	60	192	Y	···	$288'' \times 56''$	60	192	Y
NGC 1377	$2\farcs5 \times 2\farcs5$	0	300	Y	···	$20'' \times 20''$	90	75	Y	···	$58'' \times 55''$	90	109	N
NGC 1404	$2\farcs5 \times 3\farcs0$	75	1200	Y	···	$20'' \times 20''$	75	192	Y	···	$109'' \times 56''$	75	192	Y
NGC 1482	$2\farcs5 \times 3\farcs0$	110	600	N	···	$20'' \times 20''$	90	75	Y	···	$81'' \times 56''$	110	96	N
NGC 1512	$2\farcs5 \times 3\farcs0$	50	900	Y	···	$20'' \times 20''$	50	192	Y	···	$294'' \times 56''$	50	192	Y
NGC 1566	$2\farcs5 \times 3\farcs0$	60	1200	Y	···	$20'' \times 20''$	60	192	Y	···	$275'' \times 56''$	60	192	Y
NGC 1705	$2\farcs5 \times 3\farcs0$	50	1200	Y	···	$20'' \times 20''$	50	192	Y	···	$62'' \times 56''$	50	192	Y
NGC 2798	$2\farcs5 \times 2\farcs5$	103	300	Y	1	$20'' \times 20''$	103	75	Y	1	$84'' \times 55''$	103	109	Y
NGC 2841	$2\farcs5 \times 2\farcs5$	90	300	Y	···	$20'' \times 20''$	90	75	Y	···	$268'' \times 56''$	135	120	N
NGC 2915	$2\farcs5 \times 3\farcs0$	150	1200	Y	···	$20'' \times 20''$	150	192	Y	···	$62'' \times 56''$	150	192	Y
NGC 2976	$2\farcs5 \times 2\farcs5$	153	600	Y	···	$20'' \times 20''$	90	150	Y	4	$194'' \times 56''$	129	80	Y
NGC 3049	$2\farcs5 \times 2\farcs5$	111	300	Y	···	$20'' \times 20''$	111	75	Y	···	$72'' \times 55''$	115	105	N
NGC 3031	$2\farcs5 \times 2\farcs5$	75	300	Y	···	$20'' \times 20''$	90	75	Y	···	$800'' \times 56''$	157	80	Y
NGC 3190	$2\farcs5 \times 2\farcs5$	115	300	Y	···	$20'' \times 20''$	115	75	Y	···	$144'' \times 55''$	115	109	Y
NGC 3184	$2\farcs5 \times 2\farcs5$	0	300	Y	···	$20'' \times 20''$	124	75	Y	···	$245'' \times 55''$	124	109	Y
NGC 3198	$2\farcs5 \times 2\farcs5$	90	600	Y	4	$20'' \times 20''$	120	75	Y	1	$180'' \times 55''$	120	109	Y
NGC 3265	$2\farcs5 \times 2\farcs5$	120	300	Y	···	$20'' \times 20''$	120	75	Y	···	$42'' \times 55''$	120	109	Y
Mrk 33	$2\farcs5 \times 2\farcs5$	59	300	Y	···	$20'' \times 20''$	110	75	Y	···	$33'' \times 55''$	110	109	Y
NGC 3351	$2\farcs5 \times 2\farcs5$	134	300	Y	···	$20'' \times 20''$	110	192	N	···	$245'' \times 55''$	115	109	Y
NGC 3521	$2\farcs5 \times 3\farcs0$	110	1200	Y	···	$20'' \times 20''$	110	96	Y	···	$263'' \times 56''$	110	192	Y
NGC 3621	$2\farcs5 \times 3\farcs0$	150	1200	Y	···	$20'' \times 20''$	150	192	Y	···	$230'' \times 56''$	140	192	Y
NGC 3627	$2\farcs5 \times 2\farcs5$	115	300	Y	···	$20'' \times 20''$	115	75	Y	···	$200'' \times 55''$	115	109	Y
NGC 3773	$2\farcs5 \times 2\farcs5$	115	300	Y	···	$20'' \times 20''$	115	75	Y	···	$38'' \times 55''$	115	109	Y
NGC 3938	$2\farcs5 \times 2\farcs5$	81	300	Y	···	$20'' \times 20''$	90	75	Y	···	$177'' \times 56''$	133	80	N
NGC 4125	$2\farcs5 \times 2\farcs5$	13	300	Y	···	$20'' \times 20''$	90	75	Y	···	$190'' \times 56''$	90	80	N
NGC 4254	$2\farcs5 \times 2\farcs5$	120	300	Y	···	$20'' \times 20''$	120	75	Y	···	$177'' \times 55''$	120	109	Y
NGC 4321	$2\farcs5 \times 2\farcs5$	60	300	Y	···	$20'' \times 20''$	120	75	Y	···	$245'' \times 56''$	121	80	Y
NGC 4450	$2\farcs5 \times 2\farcs5$	120	300	Y	···	$20'' \times 20''$	120	75	Y	···	$173'' \times 55''$	120	109	Y
NGC 4536	$2\farcs5 \times 2\farcs5$	168	600	Y	···	$20'' \times 20''$	115	75	Y	···	$250'' \times 55''$	115	109	Y
NGC 4552	$2\farcs5 \times 2\farcs5$	120	300	Y	···	$20'' \times 20''$	120	75	Y	···	$169'' \times 55''$	120	109	Y
NGC 4559	$2\farcs5 \times 2\farcs5$	90	300	Y	···	$20'' \times 20''$	90	75	Y	···	$354'' \times 55''$	135	109	Y
NGC 4569	$2\farcs5 \times 2\farcs5$	120	300	Y	···	$20'' \times 20''$	120	75	Y	···	$172'' \times 55''$	120	109	Y
NGC 4579	$2\farcs5 \times 2\farcs5$	90	300	Y	···	$20'' \times 20''$	90	75	Y	···	$194'' \times 55''$	120	109	Y
NGC 4594	$2\farcs5 \times 2\farcs5$	20	300	Y	···	$20'' \times 20''$	113	75	Y	···	$287'' \times 55''$	113	163	N
NGC 4625	$2\farcs5 \times 2\farcs5$	90	300	Y	···	$20'' \times 20''$	90	75	Y	···	$72'' \times 56''$	143	80	Y
NGC 4725	$2\farcs5 \times 2\farcs5$	70	600	N	···	$20'' \times 20''$	120	75	N	···	$292'' \times 55''$	120	109	N
NGC 4736	$2\farcs5 \times 2\farcs5$	82	300	Y	···	$20'' \times 20''$	90	75	Y	···	$370'' \times 56''$	118	80	N
NGC 4826	$2\farcs5 \times 2\farcs5$	60	300	Y	···	$20'' \times 20''$	120	75	Y	···	$330'' \times 55''$	120	109	Y
NGC 5033	$2\farcs5 \times 2\farcs5$	77	600	Y	···	$20'' \times 20''$	90	75	Y	···	$354'' \times 56''$	150	80	Y
NGC 5055	$2\farcs5 \times 2\farcs5$	90	300	Y	···	$20'' \times 20''$	90	75	Y	···	$416'' \times 56''$	120	80	N
NGC 5194	$2\farcs5 \times 2\farcs5$	90	300	Y	···	$20'' \times 20''$	90	75	Y	···	$370'' \times 56''$	158	80	Y
NGC 5195	$2\farcs5 \times 2\farcs5$	90	300	Y	···	$20'' \times 20''$	90	75	Y	···	$190'' \times 56''$	118	80	N
NGC 5713	$2\farcs5 \times 2\farcs5$	150	300	Y	···	$20'' \times 20''$	115	225	Y	···	$90'' \times 55''$	113	109	Y
NGC 5866	$2\farcs5 \times 2\farcs5$	120	600	Y	···	$20'' \times 20''$	120	75	Y	···	$154'' \times 55''$	120	109	Y
NGC 6946	$2\farcs5 \times 2\farcs5$	140	300	Y	···	$20'' \times 20''$	90	75	Y	···	$379'' \times 56''$	37	80	Y
NGC 7331	$2\farcs5 \times 2\farcs5$	90	300	Y	···	$20'' \times 20''$	90	75	Y	···	$200'' \times 55''$	90	109	Y
NGC 7793	$2\farcs5 \times 3\farcs0$	80	1200	Y	···	$20'' \times 20''$	80	192	Y	···	$308'' \times 56''$	80	192	Y

Note. — Summary of our nuclear, circumnuclear, and radial-strip observations of the SINGS galaxies.

[a] Spectrophotometric extraction aperture along and perpendicular to the slit.

[b] Long-slit position angle, measured positive from North to East, in degrees.

[c] Effective exposure time, as defined in Moustakas & Kennicutt (2006a), in seconds.

[d] Flag indicating whether the spectra were obtained during photometric (Y) or non-photometric conditions (N).

[e] Extraction notes: (1) Extended spatial profile; (2) One or more foreground stars subtracted; (3) Multiple pointings stitched together; (4) Extraction centered on bright H II region; (5) Residual foreground stellar contamination.

TABLE 3
Optical Emission-Line Fluxes

Galaxy	[O II] λ3727	Hγ λ4340	Hβ λ4861	[O III] λ5007	Hα λ6563	[N II] λ6584	[S II] λ6716	[S II] λ6731
				Nuclear				
NGC 0024	1.02 ± 0.36	···	0.42 ± 0.19	0.57 ± 0.17	2.73 ± 0.46	0.86 ± 0.30	0.68 ± 0.26	0.46 ± 0.18
NGC 0337	6.02 ± 0.39	0.68 ± 0.17	2.20 ± 0.17	1.24 ± 0.15	9.69 ± 0.34	2.31 ± 0.26	2.78 ± 0.22	2.15 ± 0.24
NGC 0584	4.0 ± 1.4	···	···	4.7 ± 2.2	···	···	···	···
NGC 0628	···	···	···	···	···	···	···	···
NGC 0855	8.51 ± 0.56	1.16 ± 0.29	4.49 ± 0.27	8.99 ± 0.31	23.53 ± 0.70	3.69 ± 0.39	5.29 ± 0.61	3.67 ± 0.39
NGC 0925	3.75 ± 0.40	0.62 ± 0.20	2.57 ± 0.21	1.41 ± 0.19	8.76 ± 0.36	1.84 ± 0.32	2.25 ± 0.42	1.22 ± 0.19
NGC 1097	6.69 ± 0.89	···	2.88 ± 0.82	8.00 ± 0.77	19.7 ± 2.1	30.6 ± 1.5	9.0 ± 1.7	6.1 ± 1.2
NGC 1266	1.34 ± 0.31	···	···	1.36 ± 0.21	6.0 ± 1.0	21.28 ± 0.61	5.93 ± 0.64	3.99 ± 0.39
NGC 1291	5.29 ± 0.91	···	1.32 ± 0.83	5.62 ± 0.77	8.7 ± 2.2	14.5 ± 1.6	6.6 ± 1.4	6.6 ± 1.7
NGC 1316	21.7 ± 2.4	···	···	12.6 ± 2.4	16.1 ± 8.0	59.5 ± 6.1	21.9 ± 5.2	22.4 ± 5.7
NGC 1377	···	···	···	···	···	1.72 ± 0.39	···	···
NGC 1404	···	4.1 ± 2.3	···	···	···	···	7.5 ± 4.0	···
NGC 1482	4.84 ± 0.84	3.54 ± 0.49	13.71 ± 0.54	2.59 ± 0.46	165.2 ± 1.7	68.9 ± 1.2	23.1 ± 1.1	19.29 ± 0.87
NGC 1512	···	···	···	1.62 ± 0.42	3.0 ± 1.3	4.76 ± 0.92	···	···
NGC 1566	21.3 ± 1.4	2.6 ± 1.5	16.3 ± 2.4	68.9 ± 1.2	89.6 ± 7.0	77.1 ± 5.9	17.2 ± 1.8	17.7 ± 1.7
NGC 1705	···	···	7.49 ± 0.67	13.02 ± 0.62	24.9 ± 1.6	1.86 ± 0.96	···	···
NGC 2798	19.4 ± 1.1	7.82 ± 0.50	32.01 ± 0.85	11.02 ± 0.70	218.0 ± 2.4	113.4 ± 1.5	27.7 ± 1.3	25.9 ± 1.4
NGC 2841	10.0 ± 1.4	1.4 ± 1.1	4.7 ± 1.6	9.9 ± 1.3	15.9 ± 4.4	23.8 ± 2.7	10.2 ± 3.3	10.3 ± 3.0
NGC 2915	11.1 ± 1.4	···	6.28 ± 0.57	19.30 ± 0.62	26.6 ± 1.0	1.31 ± 0.59	2.00 ± 0.94	1.19 ± 0.55
NGC 2976	15.27 ± 0.70	4.02 ± 0.31	10.91 ± 0.31	10.95 ± 0.27	61.66 ± 0.76	11.98 ± 0.42	7.10 ± 0.45	5.74 ± 0.32
NGC 3049	30.89 ± 0.81	11.71 ± 0.45	28.09 ± 0.40	9.00 ± 0.41	100.5 ± 1.0	38.93 ± 0.71	11.71 ± 0.50	10.68 ± 0.47
NGC 3031	48.2 ± 3.3	29.6 ± 6.0	37 ± 19	116.8 ± 4.7	162 ± 43	252 ± 33	49.9 ± 7.0	59.0 ± 9.4
NGC 3034	11.21 ± 0.96	9.35 ± 0.71	39.18 ± 0.81	12.32 ± 0.66	514.3 ± 3.3	281.4 ± 2.4	65.2 ± 1.5	69.3 ± 1.9
NGC 3190	6.7 ± 1.1	···	···	···	5.8 ± 3.2	21.8 ± 2.7	4.6 ± 1.3	5.7 ± 1.8
NGC 3184	1.36 ± 0.37	0.75 ± 0.19	3.45 ± 0.23	0.50 ± 0.20	25.60 ± 0.62	7.74 ± 0.44	2.77 ± 0.34	2.52 ± 0.35
NGC 3198	0.52 ± 0.27	0.26 ± 0.12	1.17 ± 0.13	0.41 ± 0.15	15.86 ± 0.46	6.52 ± 0.31	2.60 ± 0.38	1.82 ± 0.20
NGC 3265	16.92 ± 0.76	5.39 ± 0.44	18.47 ± 0.40	7.44 ± 0.42	120.4 ± 1.3	48.13 ± 0.85	17.56 ± 0.72	14.36 ± 0.66
Mrk 33	96.6 ± 1.6	23.41 ± 0.75	65.33 ± 0.85	117.25 ± 0.94	291.8 ± 2.5	54.0 ± 1.1	30.0 ± 1.1	24.16 ± 0.83
NGC 3351	3.73 ± 0.69	3.64 ± 0.39	10.09 ± 0.45	1.59 ± 0.47	29.7 ± 1.1	13.6 ± 1.0	4.06 ± 0.77	3.53 ± 0.75
NGC 3521	···	···	···	···	···	···	···	···
NGC 3621	5.60 ± 0.63	···	0.85 ± 0.39	9.29 ± 0.44	7.58 ± 0.69	8.14 ± 0.64	2.83 ± 0.60	2.32 ± 0.59
NGC 3627	6.07 ± 0.78	···	···	8.50 ± 0.86	22.1 ± 2.0	27.7 ± 2.0	12.7 ± 1.5	11.7 ± 1.6
NGC 3773	39.0 ± 1.1	10.42 ± 0.45	29.48 ± 0.44	43.88 ± 0.48	139.5 ± 1.2	20.85 ± 0.69	13.79 ± 0.63	10.19 ± 0.48
NGC 3938	···	···	···	···	0.87 ± 0.49	0.87 ± 0.40	···	···
NGC 4125	6.26 ± 0.89	···	···	4.27 ± 0.95	10.0 ± 2.3	13.7 ± 1.7	8.1 ± 2.1	···
NGC 4254	0.94 ± 0.38	···	1.88 ± 0.31	1.87 ± 0.31	20.65 ± 0.94	8.10 ± 0.68	1.32 ± 0.58	1.37 ± 0.66
NGC 4321	3.95 ± 0.68	···	1.85 ± 0.47	2.62 ± 0.53	20.7 ± 1.4	21.4 ± 1.1	5.19 ± 0.84	4.90 ± 0.95
NGC 4450	15.62 ± 0.79	···	3.08 ± 0.88	9.91 ± 0.66	18.2 ± 3.5	39.8 ± 2.2	13.1 ± 1.2	13.2 ± 1.5
NGC 4536	8.65 ± 0.50	2.03 ± 0.29	9.54 ± 0.35	4.71 ± 0.41	80.4 ± 1.5	47.3 ± 1.0	19.3 ± 1.1	14.89 ± 0.76
NGC 4552	···	3.4 ± 1.2	5.2 ± 1.2	4.7 ± 1.8	13.6 ± 8.7	7.8 ± 4.4	···	···
NGC 4559	1.48 ± 0.40	0.67 ± 0.19	0.90 ± 0.12	···	5.31 ± 0.28	1.92 ± 0.22	1.43 ± 0.35	1.03 ± 0.26
NGC 4569	27.1 ± 2.9	5.8 ± 1.4	21.6 ± 1.8	20.5 ± 1.8	116.5 ± 5.4	110.9 ± 4.3	30.6 ± 3.9	24.4 ± 3.0
NGC 4579	41.4 ± 1.7	2.12 ± 0.89	9.1 ± 1.1	39.5 ± 1.3	55.6 ± 5.9	116.8 ± 4.3	46.5 ± 2.8	42.4 ± 2.7
NGC 4594	30.6 ± 2.4	3.3 ± 1.9	8.6 ± 3.7	22.6 ± 3.0	45 ± 11	94 ± 12	26.6 ± 4.2	31.0 ± 5.9
NGC 4625	0.69 ± 0.30	···	0.39 ± 0.17	···	2.47 ± 0.39	1.16 ± 0.31	1.11 ± 0.39	1.03 ± 0.38
NGC 4725	1.33 ± 0.29	···	0.27 ± 0.21	2.55 ± 0.26	1.06 ± 0.49	1.48 ± 0.55	···	···
NGC 4736	28.7 ± 5.0	···	···	9.9 ± 2.1	19 ± 14	31 ± 11	13.9 ± 5.1	13.8 ± 4.2
NGC 4826	16.7 ± 1.4	···	6.8 ± 1.3	7.0 ± 1.4	42.0 ± 3.9	50.8 ± 2.9	20.1 ± 3.0	16.1 ± 2.3
NGC 5033	4.70 ± 0.59	0.55 ± 0.46	1.68 ± 0.76	7.14 ± 0.42	14.2 ± 2.4	26.5 ± 2.0	6.6 ± 1.3	5.7 ± 1.0
NGC 5055	3.78 ± 0.91	···	···	3.00 ± 0.61	5.4 ± 1.7	8.6 ± 2.0	6.1 ± 2.5	···
NGC 5194	16.1 ± 1.3	···	5.46 ± 0.94	39.8 ± 1.0	48.0 ± 3.4	129.7 ± 2.7	21.4 ± 1.8	22.0 ± 2.0
NGC 5195	3.8 ± 1.0	···	···	4.2 ± 1.2	6.4 ± 2.8	32.2 ± 2.0	23.9 ± 6.5	···
NGC 5713	6.14 ± 0.56	1.96 ± 0.27	8.83 ± 0.38	4.05 ± 0.39	64.3 ± 1.0	29.01 ± 0.79	10.60 ± 0.60	8.98 ± 0.60
NGC 5866	1.08 ± 0.33	···	0.26 ± 0.19	0.82 ± 0.24	1.59 ± 0.53	2.83 ± 0.45	···	···
NGC 6946	···	···	7.36 ± 0.87	3.00 ± 0.73	128.9 ± 2.8	76.1 ± 2.0	19.9 ± 1.7	21.3 ± 2.0
NGC 7331	6.9 ± 1.6	···	···	12.4 ± 1.9	11.9 ± 3.8	11.7 ± 3.3	···	···
NGC 7793	5.96 ± 0.81	···	4.01 ± 0.54	3.00 ± 0.54	17.1 ± 1.0	6.50 ± 0.85	3.51 ± 0.80	2.77 ± 0.68
				Circumnuclear				
NGC 0024	51.0 ± 8.0	7.0 ± 3.5	26.3 ± 4.1	22.8 ± 4.1	107.6 ± 6.9	35.1 ± 5.8	36.4 ± 6.1	24.8 ± 4.2
NGC 0337	222.5 ± 9.2	36.1 ± 4.9	123.1 ± 5.0	89.6 ± 4.9	668 ± 11	169.7 ± 7.6	154.9 ± 7.9	104.4 ± 5.1
NGC 0584	···	···	···	···	···	···	···	···
NGC 0628	···	···	22.9 ± 6.2	21.1 ± 4.9	81.4 ± 8.6	17.9 ± 5.8	···	···
NGC 0855	199.7 ± 7.3	27.4 ± 3.6	104.0 ± 4.0	198.2 ± 4.0	461.3 ± 8.3	75.0 ± 5.9	109.7 ± 6.2	81.6 ± 4.7
NGC 0925	129.7 ± 6.5	21.3 ± 3.8	72.2 ± 3.4	55.0 ± 3.8	345.2 ± 8.3	73.7 ± 5.4	81.5 ± 6.2	57.5 ± 4.5
NGC 1097	257 ± 26	131 ± 15	470 ± 14	163 ± 14	3067 ± 56	1424 ± 37	366 ± 30	322 ± 26
NGC 1266	82.2 ± 7.9	···	6.7 ± 4.1	45.1 ± 4.7	137 ± 26	348 ± 18	83.2 ± 9.8	72.9 ± 8.4
NGC 1291	35 ± 12	17.9 ± 8.0	20 ± 13	40.7 ± 8.1	52 ± 21	51 ± 14	···	···
NGC 1316	322 ± 40	···	···	149 ± 27	208 ± 69	505 ± 57	244 ± 67	215 ± 62
NGC 1377	19.6 ± 6.1	···	···	13.7 ± 3.6	16.6 ± 6.4	14.9 ± 5.6	7.6 ± 5.4	7.3 ± 6.1
NGC 1404	···	···	···	···	···	···	···	···
NGC 1482	73.0 ± 10.0	16.0 ± 2.9	78.8 ± 3.4	31.8 ± 3.6	874 ± 14	416.1 ± 9.4	167.0 ± 9.1	139.2 ± 7.5
NGC 1512	65 ± 13	23.0 ± 5.6	96.7 ± 6.6	34.3 ± 6.0	484 ± 15	188 ± 13	69 ± 11	58.1 ± 9.1
NGC 1566	184 ± 13	···	···	329 ± 11	587 ± 60	542 ± 32	131 ± 14	111 ± 15
NGC 1705	342 ± 10	86.6 ± 5.4	256.9 ± 5.7	1048.4 ± 7.4	975 ± 12	48.2 ± 8.3	81.4 ± 8.9	55.4 ± 5.6
NGC 2403	32.6 ± 6.4	···	20.0 ± 3.7	20.2 ± 4.5	103.6 ± 9.9	40.2 ± 6.6	32.2 ± 7.1	20.3 ± 4.7

TABLE 3 — *Continued*

Galaxy	[O II] λ3727	Hγ λ4340	Hβ λ4861	[O III] λ5007	Hα λ6563	[N II] λ6584	[S II] λ6716	[S II] λ6731
DDO 053	58.8 ± 5.4	17.0 ± 1.9	36.3 ± 1.9	80.4 ± 2.0	137.6 ± 5.2	···	9.5 ± 3.3	10.4 ± 3.4
NGC 2798	141.0 ± 6.5	35.7 ± 3.6	160.3 ± 4.8	72.7 ± 4.6	1258 ± 16	614 ± 11	207.4 ± 9.2	184.0 ± 8.0
NGC 2841	86 ± 13	49 ± 11	···	105 ± 15	···	123 ± 26	100 ± 42	···
NGC 2915	481 ± 28	69 ± 11	238 ± 11	668 ± 12	876 ± 19	67 ± 12	107 ± 13	67.7 ± 8.2
NGC 2976	104.3 ± 6.4	20.0 ± 3.4	68.9 ± 3.7	54.7 ± 3.7	287.8 ± 8.5	81.0 ± 5.8	64.1 ± 6.0	48.6 ± 4.5
NGC 3049	155.4 ± 7.1	48.7 ± 3.3	153.0 ± 4.1	53.2 ± 3.3	800.4 ± 9.8	292.4 ± 6.4	111.1 ± 5.7	96.2 ± 5.5
NGC 3031	441 ± 39	190 ± 110	···	746 ± 45	800 ± 170	1120 ± 100	···	1100 ± 120
NGC 3034	347 ± 23	176 ± 13	796 ± 16	271 ± 14	9127 ± 54	5040 ± 35	1449 ± 27	1357 ± 25
M 81 Dw B	40.9 ± 5.8	6.9 ± 2.8	20.5 ± 2.4	51.5 ± 2.5	89.5 ± 5.0	···	12.2 ± 5.5	8.7 ± 3.5
NGC 3190	62.3 ± 5.5	···	···	36.7 ± 7.2	47 ± 33	101 ± 22	···	···
NGC 3184	24.7 ± 7.2	10.3 ± 3.0	37.7 ± 3.4	9.5 ± 3.0	190.2 ± 7.3	75.8 ± 5.5	29.5 ± 5.4	27.3 ± 5.5
NGC 3198	7.1 ± 4.1	···	5.8 ± 2.5	10.5 ± 3.4	72.6 ± 6.6	43.0 ± 5.9	20.8 ± 5.6	15.7 ± 4.2
IC 2574	45.5 ± 6.9	12.6 ± 4.0	22.7 ± 2.8	79.0 ± 2.9	103.5 ± 6.6	···	13.3 ± 5.2	···
NGC 3265	78.6 ± 5.8	13.4 ± 3.1	64.1 ± 3.2	33.3 ± 3.1	414.2 ± 7.9	166.7 ± 5.8	75.8 ± 6.2	64.1 ± 4.8
Mrk 33	696 ± 11	132.6 ± 4.4	409.3 ± 5.0	739.8 ± 5.4	1917 ± 16	363.4 ± 8.2	213.1 ± 7.7	177.1 ± 7.0
NGC 3351	141 ± 14	89.4 ± 7.4	378.9 ± 8.0	85.9 ± 8.1	2121 ± 21	786 ± 16	239 ± 13	190 ± 11
NGC 3521	···	···	···	56 ± 18	166 ± 34	126 ± 28	52 ± 26	67 ± 39
NGC 3621	83 ± 13	···	52.8 ± 7.6	96.9 ± 8.6	358 ± 13	186 ± 11	84 ± 12	56.7 ± 8.7
NGC 3627	111 ± 15	···	···	87 ± 11	116 ± 26	222 ± 24	···	150 ± 140
NGC 3773	395.3 ± 8.1	76.5 ± 3.3	225.4 ± 3.6	301.0 ± 3.5	967.3 ± 9.8	154.0 ± 5.4	141.6 ± 6.8	99.0 ± 4.5
NGC 3938	···	···	23.2 ± 4.1	8.0 ± 3.6	123.7 ± 8.2	38.5 ± 7.6	···	···
NGC 4125	86 ± 12	···	22 ± 10	47.8 ± 9.7	93 ± 49	162 ± 25	67 ± 25	34 ± 15
NGC 4236	···	···	···	···	···	···	···	···
NGC 4254	21.9 ± 6.7	···	56.9 ± 4.8	16.7 ± 5.0	510 ± 14	173 ± 11	51 ± 11	36.1 ± 7.1
NGC 4321	63 ± 13	24.0 ± 6.6	159.3 ± 8.7	40.3 ± 7.5	1209 ± 21	406 ± 17	92 ± 14	82 ± 12
NGC 4450	88.1 ± 7.8	···	19.1 ± 8.5	50.5 ± 7.2	99 ± 33	129 ± 22	72 ± 15	62 ± 12
NGC 4536	124.2 ± 6.8	29.7 ± 3.7	122.8 ± 4.4	54.2 ± 4.8	1227 ± 17	555 ± 11	268 ± 10	210.2 ± 8.2
NGC 4552	···	···	···	82 ± 23	···	···	···	···
NGC 4559	58.3 ± 6.3	6.2 ± 3.5	34.0 ± 3.4	21.2 ± 4.3	211.5 ± 9.3	80.7 ± 6.7	48.1 ± 6.0	46.1 ± 5.7
NGC 4569	168 ± 14	···	61.2 ± 8.9	130 ± 10	483 ± 27	519 ± 19	189 ± 19	152 ± 16
NGC 4579	318 ± 13	···	···	193 ± 11	280 ± 200	704 ± 37	299 ± 29	196 ± 18
NGC 4594	214 ± 47	···	···	173 ± 55	460 ± 370	310 ± 260	258 ± 97	···
NGC 4625	41.2 ± 5.1	13.6 ± 3.1	36.7 ± 3.1	17.4 ± 3.3	186.7 ± 6.4	77.5 ± 5.1	40.5 ± 5.8	27.1 ± 3.6
NGC 4631	102.9 ± 6.5	9.9 ± 2.8	49.0 ± 3.6	60.0 ± 3.5	290.9 ± 8.2	62.9 ± 6.0	59.7 ± 5.9	37.6 ± 3.9
NGC 4725	23.3 ± 8.5	···	···	20.0 ± 4.3	···	···	14.8 ± 7.0	···
NGC 4736	454 ± 69	···	···	247 ± 58	···	510 ± 110	···	···
NGC 4826	208 ± 14	22 ± 10	136 ± 13	146 ± 12	1007 ± 34	746 ± 24	281 ± 26	228 ± 23
NGC 5033	44.4 ± 9.7	···	45.1 ± 9.5	109.2 ± 8.2	398 ± 26	346 ± 23	76 ± 13	60 ± 13
NGC 5055	49.0 ± 9.4	···	29.4 ± 7.1	46.7 ± 7.5	193 ± 18	169 ± 14	91 ± 18	68 ± 14
NGC 5194	325 ± 15	19.2 ± 9.7	91 ± 10	258 ± 11	581 ± 31	1276 ± 25	266 ± 30	185 ± 20
NGC 5195	42 ± 11	···	···	69 ± 11	57 ± 26	231 ± 19	107 ± 28	···
Tol 89	474 ± 16	109.3 ± 4.9	293.9 ± 5.0	1046.3 ± 6.5	1266 ± 11	100.2 ± 7.5	109.5 ± 6.8	73.5 ± 4.4
NGC 5474	25.1 ± 5.3	···	5.5 ± 2.0	12.1 ± 2.3	28.0 ± 5.2	10.4 ± 4.7	···	···
NGC 5713	111.4 ± 6.7	26.8 ± 3.0	111.8 ± 3.2	45.2 ± 3.3	765.8 ± 8.4	329.5 ± 6.5	142.6 ± 7.0	107.4 ± 4.9
NGC 5866	39 ± 14	···	···	45.1 ± 8.9	42 ± 15	86 ± 14	26 ± 13	30 ± 14
NGC 6946	···	···	77.2 ± 9.6	46.6 ± 9.0	1068 ± 24	552 ± 17	174 ± 17	151 ± 16
NGC 7331	122 ± 12	···	···	120 ± 16	277 ± 48	156 ± 26	···	···
NGC 7793	96 ± 11	17.9 ± 6.9	77.8 ± 6.6	35.2 ± 6.7	390 ± 12	135.5 ± 9.3	75 ± 11	51.2 ± 7.1
				Radial Strip				
NGC 0024	584 ± 94	···	275 ± 39	268 ± 34	1101 ± 96	305 ± 74	250 ± 58	238 ± 50
NGC 0337	1469 ± 38	169 ± 14	649 ± 14	937 ± 17	3184 ± 34	593 ± 23	695 ± 28	512 ± 19
NGC 0584	···	···	···	102 ± 36	···	···	···	···
NGC 0628	···	58 ± 29	228 ± 35	···	878 ± 75	358 ± 52	189 ± 51	121 ± 36
NGC 0855	402 ± 22	62.1 ± 9.2	153 ± 10	272.4 ± 9.5	708 ± 19	85 ± 17	189 ± 17	146 ± 15
NGC 0925	841 ± 61	178 ± 33	422 ± 31	330 ± 29	1618 ± 71	340 ± 54	458 ± 49	385 ± 47
NGC 1097	595 ± 65	244 ± 42	797 ± 44	322 ± 39	5190 ± 96	2558 ± 68	724 ± 72	617 ± 52
NGC 1266	132 ± 17	···	···	53.4 ± 7.7	144 ± 36	345 ± 31	140 ± 29	···
NGC 1291	···	···	···	···	440 ± 300	···	···	···
NGC 1316	800 ± 180	···	···	410 ± 140	···	850 ± 530	590 ± 280	650 ± 300
NGC 1377	···	···	···	···	···	···	···	···
NGC 1404	···	···	194 ± 73	···	···	···	···	···
NGC 1482	309 ± 34	55 ± 12	198 ± 11	124 ± 12	1553 ± 42	819 ± 24	395 ± 26	261 ± 15
NGC 1512	293 ± 70	61 ± 23	211 ± 31	120 ± 30	1079 ± 72	537 ± 46	187 ± 47	175 ± 42
NGC 1566	952 ± 83	···	···	544 ± 52	3700 ± 110	1873 ± 76	770 ± 89	584 ± 64
NGC 1705	1216 ± 29	249 ± 11	680 ± 12	2431 ± 16	2600 ± 26	150 ± 17	308 ± 16	210 ± 13
NGC 2403	4590 ± 600	1000 ± 350	2790 ± 290	2540 ± 330	13420 ± 600	2800 ± 530	3089 ± 490	2280 ± 330
DDO 053	180 ± 11	39.1 ± 5.0	119.5 ± 4.6	197.6 ± 5.2	450 ± 13	···	34.6 ± 9.4	25.2 ± 5.8
NGC 2798	171 ± 15	44.1 ± 8.0	170 ± 10	88.4 ± 9.0	1289 ± 26	632 ± 17	228 ± 19	188 ± 14
NGC 2841	460 ± 110	106 ± 64	435 ± 84	336 ± 66	1430 ± 270	1050 ± 180	410 ± 130	337 ± 92
NGC 2915	1175 ± 73	154 ± 28	480 ± 28	1233 ± 24	1892 ± 43	140 ± 32	299 ± 27	209 ± 20
NGC 2976	1514 ± 83	221 ± 44	948 ± 41	631 ± 42	4634 ± 83	1246 ± 72	1086 ± 65	727 ± 52
NGC 3049	206 ± 13	47.5 ± 6.9	178.6 ± 5.9	72.7 ± 6.8	925 ± 15	328 ± 10	151.1 ± 9.6	109.4 ± 8.5
NGC 3031	3759 ± 610	···	1550 ± 510	2360 ± 330	5100 ± 2800	4200 ± 1900	···	···
M 81 Dw B	85 ± 10	15.5 ± 4.1	42.4 ± 4.1	95.2 ± 3.6	163 ± 13	···	18.8 ± 6.4	16.0 ± 5.5
NGC 3190	95 ± 38	···	···	65 ± 20	···	132 ± 34	···	86 ± 57
NGC 3184	144 ± 35	18 ± 16	172 ± 20	60 ± 21	1005 ± 39	407 ± 34	174 ± 41	135 ± 28
NGC 3198	298 ± 28	37 ± 13	138 ± 11	147 ± 14	864 ± 24	279 ± 25	204 ± 27	121 ± 16

TABLE 3 — *Continued*

Galaxy	[O II] λ3727	Hγ λ4340	Hβ λ4861	[O III] λ5007	Hα λ6563	[N II] λ6584	[S II] λ6716	[S II] λ6731
NGC 3265	91.4 ± 9.4	10.3 ± 4.7	63.8 ± 4.9	39.2 ± 4.4	427.3 ± 9.6	174.2 ± 9.1	92.2 ± 7.8	67.2 ± 6.1
Mrk 33	746 ± 12	135.9 ± 4.8	411.5 ± 5.6	747.5 ± 5.3	1954 ± 15	370.5 ± 10.0	232.8 ± 9.0	195.4 ± 8.0
NGC 3351	324 ± 51	94 ± 24	491 ± 32	219 ± 30	2496 ± 80	1124 ± 56	366 ± 57	293 ± 47
NGC 3521	730 ± 130	224 ± 72	881 ± 70	414 ± 58	5090 ± 170	2123 ± 98	1170 ± 160	572 ± 79
NGC 3621	1846 ± 92	410 ± 55	1377 ± 49	690 ± 50	7850 ± 120	2632 ± 78	1556 ± 87	1086 ± 54
NGC 3627	640 ± 69	82 ± 36	505 ± 36	348 ± 50	3070 ± 100	1432 ± 78	742 ± 95	544 ± 73
NGC 3773	463 ± 12	85.1 ± 5.1	251.2 ± 4.8	333.7 ± 5.9	1064 ± 11	179.8 ± 8.4	171.2 ± 9.1	120.6 ± 6.9
NGC 3938	···	···	250 ± 110	···	1620 ± 290	380 ± 190	···	···
NGC 4125	144 ± 71	134 ± 48	211 ± 74	129 ± 51	···	380 ± 110	···	···
NGC 4254	401 ± 58	134 ± 24	787 ± 36	180 ± 29	5789 ± 89	1694 ± 60	670 ± 67	482 ± 48
NGC 4321	393 ± 76	139 ± 36	560 ± 41	142 ± 34	3750 ± 96	1449 ± 63	508 ± 68	373 ± 50
NGC 4450	241 ± 39	···	49 ± 18	122 ± 19	327 ± 66	250 ± 41	142 ± 35	100 ± 28
NGC 4536	463 ± 37	61 ± 20	272 ± 18	108 ± 19	2433 ± 52	1065 ± 42	602 ± 43	455 ± 31
NGC 4552	···	···	115 ± 40	···	···	···	···	···
NGC 4559	2244 ± 68	266 ± 35	947 ± 34	999 ± 34	4817 ± 91	1162 ± 57	1000 ± 71	705 ± 44
NGC 4569	169 ± 33	···	57 ± 21	125 ± 22	764 ± 64	733 ± 52	233 ± 51	172 ± 36
NGC 4579	669 ± 50	···	167 ± 32	341 ± 30	904 ± 87	1199 ± 64	597 ± 88	339 ± 58
NGC 4594	···	···	···	···	···	···	···	···
NGC 4625	198 ± 29	34 ± 11	125 ± 11	36 ± 11	634 ± 27	272 ± 20	131 ± 22	98 ± 13
NGC 4631	5130 ± 130	478 ± 60	2168 ± 60	3271 ± 64	11380 ± 160	2480 ± 120	2710 ± 150	1863 ± 78
NGC 4725	···	···	56 ± 54	···	···	120 ± 120	···	···
NGC 4736	3500 ± 200	260 ± 120	1890 ± 150	1840 ± 160	9640 ± 350	5700 ± 310	2450 ± 250	1970 ± 230
NGC 4826	980 ± 140	···	748 ± 77	669 ± 83	4080 ± 190	2600 ± 170	1110 ± 160	820 ± 160
NGC 5033	204 ± 39	69 ± 23	292 ± 24	229 ± 29	2062 ± 83	1004 ± 61	452 ± 80	···
NGC 5055	···	···	1080 ± 370	···	4840 ± 950	2340 ± 590	···	···
NGC 5194	850 ± 260	260 ± 110	1260 ± 120	320 ± 120	8750 ± 360	4730 ± 210	920 ± 210	930 ± 200
NGC 5195	289 ± 80	···	···	195 ± 44	800 ± 120	1053 ± 92	216 ± 99	145 ± 51
Tol 89	590 ± 46	81 ± 19	337 ± 17	1165 ± 20	1438 ± 28	155 ± 31	132 ± 25	104 ± 18
NGC 5474	722 ± 34	93 ± 17	280 ± 18	399 ± 21	923 ± 36	133 ± 38	192 ± 34	140 ± 23
NGC 5713	656 ± 23	74 ± 12	434 ± 11	178 ± 12	2852 ± 29	1176 ± 24	617 ± 22	430 ± 18
NGC 5866	···	···	···	135 ± 46	···	···	···	···
NGC 6946	···	···	1980 ± 540	···	12300 ± 1100	5299 ± 1100	1560 ± 680	1729 ± 700
NGC 7331	383 ± 67	···	380 ± 46	428 ± 51	2160 ± 100	878 ± 73	800 ± 230	···
NGC 7793	800 ± 180	···	770 ± 110	450 ± 110	3520 ± 170	1010 ± 120	840 ± 140	580 ± 92

NOTE. — Optical emission-line fluxes in units of 10^{-15} erg s^{-1} cm^{-2}, corrected for foreground Galactic extinction ($R_V = 3.1$; O'Donnell 1994; Schlegel et al. 1998). Note that the uncertainties include only statistical measurement uncertainties, and do not include systematic errors due to, for example, imperfect continuum subtraction. For most applications we recommend that a minimum S/N > 2 signal-to-noise ratio cut be applied to the fluxes listed in this table.

TABLE 4
Optical Emission-Line Equivalent Widths

Galaxy	[O II] λ3727	Hγ λ4340	Hβ λ4861	[O III] λ5007	Hα λ6563	[N II] λ6584	[S II] λ6716	[S II] λ6731
				Nuclear				
NGC 0024	12.1 ± 4.3	···	2.08 ± 0.91	2.82 ± 0.84	10.6 ± 1.8	3.4 ± 1.2	2.6 ± 1.0	1.78 ± 0.69
NGC 0337	36.1 ± 2.5	2.79 ± 0.68	8.13 ± 0.63	4.48 ± 0.54	30.3 ± 1.1	7.34 ± 0.84	8.56 ± 0.68	6.67 ± 0.73
NGC 0584	3.0 ± 1.1	···	···	0.93 ± 0.44	···	···	···	···
NGC 0628	···	···	···	···	···	···	···	···
NGC 0855	23.1 ± 1.6	2.08 ± 0.51	7.42 ± 0.45	14.87 ± 0.52	36.3 ± 1.1	5.63 ± 0.59	7.88 ± 0.91	5.49 ± 0.58
NGC 0925	15.6 ± 1.7	1.89 ± 0.60	7.97 ± 0.65	4.48 ± 0.61	31.8 ± 1.4	6.8 ± 1.2	8.1 ± 1.5	4.48 ± 0.72
NGC 1097	8.7 ± 1.2	···	1.00 ± 0.29	2.71 ± 0.26	3.69 ± 0.40	5.79 ± 0.28	1.71 ± 0.32	1.15 ± 0.23
NGC 1266	11.4 ± 2.7	···	···	3.24 ± 0.49	8.3 ± 1.4	30.22 ± 0.94	8.09 ± 0.87	5.41 ± 0.53
NGC 1291	7.3 ± 1.3	···	0.41 ± 0.26	1.75 ± 0.24	1.70 ± 0.43	2.87 ± 0.32	1.32 ± 0.28	1.31 ± 0.34
NGC 1316	6.34 ± 0.71	···	···	0.93 ± 0.18	0.76 ± 0.38	2.85 ± 0.29	1.05 ± 0.25	1.07 ± 0.27
NGC 1377	···	···	···	···	···	2.11 ± 0.48	···	···
NGC 1404	···	0.87 ± 0.49	···	···	···	···	0.62 ± 0.33	···
NGC 1482	15.7 ± 2.8	5.73 ± 0.80	16.75 ± 0.67	2.89 ± 0.51	93.1 ± 1.3	38.12 ± 0.76	12.16 ± 0.57	10.10 ± 0.46
NGC 1512	···	···	···	0.68 ± 0.18	0.84 ± 0.37	1.35 ± 0.26	···	···
NGC 1566	13.02 ± 0.84	0.99 ± 0.57	4.69 ± 0.68	19.40 ± 0.35	16.6 ± 1.3	14.5 ± 1.1	3.24 ± 0.33	3.32 ± 0.31
NGC 1705	···	···	2.90 ± 0.26	5.25 ± 0.25	11.84 ± 0.77	0.90 ± 0.47	···	···
NGC 2798	15.24 ± 0.86	4.29 ± 0.27	15.67 ± 0.43	5.42 ± 0.34	82.25 ± 0.99	42.96 ± 0.66	10.31 ± 0.50	9.58 ± 0.54
NGC 2841	8.9 ± 1.3	0.48 ± 0.40	0.92 ± 0.31	2.01 ± 0.27	2.01 ± 0.55	3.05 ± 0.35	1.32 ± 0.43	1.34 ± 0.39
NGC 2915	8.4 ± 1.0	···	4.64 ± 0.42	14.58 ± 0.47	25.8 ± 1.0	1.30 ± 0.58	1.96 ± 0.92	1.16 ± 0.53
NGC 2976	83.0 ± 4.5	23.0 ± 1.8	60.9 ± 1.8	60.3 ± 1.7	352.1 ± 8.6	66.7 ± 2.7	38.4 ± 2.9	32.5 ± 2.0
NGC 3049	32.18 ± 0.88	13.94 ± 0.55	37.75 ± 0.57	12.27 ± 0.57	172.3 ± 2.5	66.7 ± 1.6	20.96 ± 0.94	19.18 ± 0.86
NGC 3031	16.1 ± 1.1	3.83 ± 0.78	2.6 ± 1.4	8.57 ± 0.35	7.1 ± 1.9	11.2 ± 1.4	2.31 ± 0.32	2.74 ± 0.44
NGC 3034	15.5 ± 1.4	6.03 ± 0.46	19.88 ± 0.42	5.81 ± 0.31	126.0 ± 2.6	67.9 ± 1.3	14.51 ± 0.34	15.40 ± 0.43
NGC 3190	6.1 ± 1.0	···	···	···	0.80 ± 0.44	3.05 ± 0.38	0.65 ± 0.18	0.81 ± 0.26
NGC 3184	6.2 ± 1.7	2.23 ± 0.57	8.31 ± 0.56	1.18 ± 0.47	46.0 ± 1.2	13.86 ± 0.79	4.91 ± 0.60	4.46 ± 0.62
NGC 3198	4.7 ± 2.4	1.12 ± 0.52	3.53 ± 0.40	1.17 ± 0.41	27.47 ± 0.81	11.42 ± 0.55	4.41 ± 0.64	3.08 ± 0.33
NGC 3265	24.2 ± 1.1	5.16 ± 0.42	15.45 ± 0.34	6.07 ± 0.35	78.88 ± 0.98	31.78 ± 0.63	11.52 ± 0.48	9.47 ± 0.44
Mrk 33	65.0 ± 1.2	13.40 ± 0.43	39.02 ± 0.58	73.78 ± 0.74	209.3 ± 2.9	38.9 ± 1.9	21.81 ± 0.87	17.53 ± 0.64
NGC 3351	4.24 ± 0.79	2.78 ± 0.30	5.86 ± 0.26	0.90 ± 0.26	11.81 ± 0.44	5.48 ± 0.42	1.63 ± 0.31	1.42 ± 0.30
NGC 3521	···	···	···	···	···	···	···	···
NGC 3621	11.6 ± 1.3	···	0.69 ± 0.32	7.54 ± 0.36	4.98 ± 0.46	5.42 ± 0.43	1.84 ± 0.39	1.51 ± 0.39
NGC 3627	5.81 ± 0.76	···	···	2.06 ± 0.21	3.35 ± 0.30	4.28 ± 0.31	1.92 ± 0.23	1.75 ± 0.24
NGC 3773	36.9 ± 1.1	8.08 ± 0.35	24.12 ± 0.38	36.35 ± 0.42	141.2 ± 1.8	20.84 ± 0.73	14.13 ± 0.67	10.49 ± 0.52
NGC 3938	···	···	···	···	0.93 ± 0.52	0.95 ± 0.44	···	···
NGC 4125	7.9 ± 1.1	···	···	1.14 ± 0.26	1.63 ± 0.37	2.26 ± 0.28	1.36 ± 0.35	···
NGC 4254	2.18 ± 0.88	···	1.71 ± 0.28	1.63 ± 0.27	11.84 ± 0.54	4.68 ± 0.40	0.78 ± 0.34	0.81 ± 0.39
NGC 4321	7.3 ± 1.3	···	1.24 ± 0.31	1.69 ± 0.34	9.17 ± 0.63	9.60 ± 0.52	2.38 ± 0.38	2.25 ± 0.43
NGC 4450	19.6 ± 1.0	···	0.97 ± 0.28	3.06 ± 0.20	3.54 ± 0.68	7.83 ± 0.43	2.69 ± 0.25	2.71 ± 0.31
NGC 4536	18.1 ± 1.1	1.99 ± 0.28	6.15 ± 0.23	2.82 ± 0.25	24.57 ± 0.47	14.60 ± 0.35	5.78 ± 0.32	4.43 ± 0.23
NGC 4552	···	0.91 ± 0.34	0.83 ± 0.19	0.76 ± 0.29	1.43 ± 0.91	0.82 ± 0.47	···	···
NGC 4559	6.4 ± 1.7	1.80 ± 0.51	2.10 ± 0.28	···	10.46 ± 0.55	3.85 ± 0.44	2.83 ± 0.70	2.02 ± 0.51
NGC 4569	5.96 ± 0.66	0.66 ± 0.16	2.29 ± 0.19	2.12 ± 0.18	11.01 ± 0.52	10.81 ± 0.44	2.91 ± 0.37	2.32 ± 0.29
NGC 4579	30.6 ± 1.3	0.73 ± 0.31	1.98 ± 0.25	8.41 ± 0.27	7.25 ± 0.77	15.38 ± 0.57	6.28 ± 0.38	5.75 ± 0.36
NGC 4594	11.96 ± 0.95	0.51 ± 0.30	0.77 ± 0.33	2.02 ± 0.27	2.33 ± 0.58	4.90 ± 0.65	1.40 ± 0.22	1.63 ± 0.31
NGC 4625	4.9 ± 2.1	···	1.30 ± 0.56	···	6.4 ± 1.0	3.02 ± 0.82	2.9 ± 1.0	2.67 ± 0.98
NGC 4725	6.6 ± 1.4	···	0.31 ± 0.24	2.85 ± 0.29	0.76 ± 0.35	1.08 ± 0.40	···	···
NGC 4736	5.19 ± 0.90	···	···	0.58 ± 0.12	0.76 ± 0.56	1.28 ± 0.44	0.58 ± 0.21	0.58 ± 0.17
NGC 4826	9.07 ± 0.78	···	1.02 ± 0.20	1.02 ± 0.20	3.76 ± 0.35	4.62 ± 0.26	1.84 ± 0.27	1.47 ± 0.21
NGC 5033	7.15 ± 0.91	0.43 ± 0.37	0.86 ± 0.39	3.64 ± 0.21	4.11 ± 0.70	7.82 ± 0.61	1.95 ± 0.39	1.68 ± 0.30
NGC 5055	4.5 ± 1.1	···	···	0.85 ± 0.17	0.82 ± 0.27	1.33 ± 0.30	0.95 ± 0.39	···
NGC 5194	10.91 ± 0.89	···	1.35 ± 0.23	9.64 ± 0.25	8.68 ± 0.63	23.55 ± 0.54	3.87 ± 0.33	3.99 ± 0.35
NGC 5195	4.2 ± 1.2	···	···	0.76 ± 0.22	0.59 ± 0.26	2.96 ± 0.18	2.10 ± 0.57	···
NGC 5713	13.5 ± 1.3	2.55 ± 0.35	10.27 ± 0.44	4.56 ± 0.44	62.0 ± 1.1	28.27 ± 0.85	10.12 ± 0.57	8.59 ± 0.58
NGC 5866	5.0 ± 1.5	···	0.31 ± 0.23	0.96 ± 0.28	1.00 ± 0.33	1.80 ± 0.29	···	···
NGC 6946	···	···	3.91 ± 0.46	1.48 ± 0.36	32.91 ± 0.73	19.34 ± 0.53	4.85 ± 0.41	5.17 ± 0.50
NGC 7331	4.8 ± 1.1	···	···	1.98 ± 0.30	1.13 ± 0.36	1.13 ± 0.32	···	···
NGC 7793	5.58 ± 0.77	···	2.05 ± 0.28	1.52 ± 0.28	7.80 ± 0.47	3.04 ± 0.40	1.65 ± 0.38	1.30 ± 0.32
				Circumnuclear				
NGC 0024	15.2 ± 2.4	1.24 ± 0.61	3.49 ± 0.54	3.00 ± 0.54	11.13 ± 0.72	3.64 ± 0.60	3.72 ± 0.62	2.52 ± 0.43
NGC 0337	27.0 ± 1.2	2.84 ± 0.38	8.91 ± 0.36	6.47 ± 0.35	45.23 ± 0.82	11.62 ± 0.53	10.62 ± 0.54	7.13 ± 0.35
NGC 0584	···	···	···	···	···	···	···	···
NGC 0628	···	···	1.21 ± 0.33	1.11 ± 0.26	3.22 ± 0.34	0.72 ± 0.23	···	···
NGC 0855	31.1 ± 1.3	2.74 ± 0.36	8.87 ± 0.35	16.71 ± 0.35	34.27 ± 0.64	5.64 ± 0.45	8.14 ± 0.47	6.09 ± 0.35
NGC 0925	19.7 ± 1.0	2.29 ± 0.40	7.38 ± 0.35	5.62 ± 0.39	35.69 ± 0.91	7.79 ± 0.58	8.46 ± 0.64	6.03 ± 0.47
NGC 1097	6.54 ± 0.67	1.92 ± 0.22	5.17 ± 0.16	1.76 ± 0.16	22.63 ± 0.42	10.54 ± 0.27	2.70 ± 0.22	2.37 ± 0.19
NGC 1266	24.5 ± 2.4	···	0.66 ± 0.41	4.27 ± 0.45	9.0 ± 1.7	23.3 ± 1.2	5.53 ± 0.65	4.82 ± 0.55
NGC 1291	4.6 ± 1.5	1.06 ± 0.47	0.73 ± 0.47	1.49 ± 0.30	1.30 ± 0.53	1.30 ± 0.37	···	···
NGC 1316	6.38 ± 0.79	···	···	0.82 ± 0.15	0.79 ± 0.26	1.94 ± 0.22	0.94 ± 0.26	0.82 ± 0.24
NGC 1377	5.7 ± 1.8	···	···	1.26 ± 0.33	1.09 ± 0.42	1.00 ± 0.38	0.51 ± 0.36	0.48 ± 0.40
NGC 1404	···	···	···	···	···	···	···	···
NGC 1482	24.7 ± 3.4	2.44 ± 0.45	8.57 ± 0.37	3.20 ± 0.36	46.00 ± 0.79	21.84 ± 0.53	8.38 ± 0.46	7.01 ± 0.38
NGC 1512	4.65 ± 0.92	0.92 ± 0.23	2.68 ± 0.18	0.94 ± 0.16	9.43 ± 0.29	3.72 ± 0.25	1.36 ± 0.22	1.14 ± 0.18
NGC 1566	9.78 ± 0.68	···	···	6.17 ± 0.20	7.59 ± 0.77	7.08 ± 0.42	1.70 ± 0.18	1.44 ± 0.19
NGC 1705	14.54 ± 0.46	3.36 ± 0.21	11.06 ± 0.25	46.07 ± 0.37	51.01 ± 0.67	2.58 ± 0.44	4.29 ± 0.47	2.92 ± 0.29

TABLE 4 — *Continued*

Galaxy	[O II] λ3727	Hγ λ4340	Hβ λ4861	[O III] λ5007	Hα λ6563	[N II] λ6584	[S II] λ6716	[S II] λ6731
NGC 2403	5.8 ± 1.1	···	1.31 ± 0.24	1.31 ± 0.29	5.37 ± 0.52	2.14 ± 0.35	1.66 ± 0.37	1.05 ± 0.24
DDO 053	81.2 ± 8.6	20.8 ± 2.5	38.5 ± 2.1	86.2 ± 2.8	133.6 ± 6.7	···	9.0 ± 3.1	9.6 ± 3.1
NGC 2798	17.59 ± 0.86	2.52 ± 0.25	9.24 ± 0.28	4.07 ± 0.26	51.03 ± 0.70	24.93 ± 0.46	8.33 ± 0.37	7.38 ± 0.32
NGC 2841	4.53 ± 0.70	1.11 ± 0.25	···	1.39 ± 0.20	···	1.10 ± 0.23	0.91 ± 0.38	···
NGC 2915	21.4 ± 1.3	2.39 ± 0.38	8.64 ± 0.39	24.54 ± 0.45	36.67 ± 0.81	2.86 ± 0.51	4.45 ± 0.52	2.82 ± 0.34
NGC 2976	20.0 ± 1.3	2.12 ± 0.36	6.06 ± 0.33	4.78 ± 0.32	21.51 ± 0.65	6.18 ± 0.45	4.76 ± 0.45	3.64 ± 0.34
NGC 3049	28.8 ± 1.4	7.42 ± 0.51	21.21 ± 0.58	7.34 ± 0.46	101.3 ± 1.4	37.0 ± 1.0	14.14 ± 0.73	12.30 ± 0.71
NGC 3031	6.45 ± 0.58	1.14 ± 0.67	···	2.67 ± 0.16	1.84 ± 0.39	2.62 ± 0.23	···	2.59 ± 0.27
NGC 3034	20.8 ± 1.4	4.97 ± 0.38	17.76 ± 0.37	5.70 ± 0.30	106.0 ± 1.9	59.1 ± 1.7	15.65 ± 0.30	14.67 ± 0.28
M 81 Dw B	35.5 ± 5.4	4.2 ± 1.7	11.8 ± 1.4	28.9 ± 1.5	55.4 ± 3.7	···	7.2 ± 3.3	4.9 ± 2.0
NGC 3190	6.32 ± 0.56	···	···	1.03 ± 0.20	0.84 ± 0.58	1.81 ± 0.39	···	···
NGC 3184	7.0 ± 2.0	1.72 ± 0.51	4.44 ± 0.40	1.09 ± 0.34	15.47 ± 0.60	6.24 ± 0.46	2.43 ± 0.44	2.26 ± 0.45
NGC 3198	2.3 ± 1.4	···	0.68 ± 0.30	1.18 ± 0.38	5.34 ± 0.48	3.21 ± 0.44	1.51 ± 0.41	1.14 ± 0.31
IC 2574	34.7 ± 5.7	8.0 ± 2.6	14.5 ± 1.8	52.5 ± 2.2	70.6 ± 5.2	···	8.7 ± 3.4	···
NGC 3265	16.9 ± 1.3	1.76 ± 0.40	6.61 ± 0.33	3.36 ± 0.31	32.20 ± 0.63	13.00 ± 0.47	5.80 ± 0.47	4.92 ± 0.37
Mrk 33	63.6 ± 1.3	9.51 ± 0.32	28.58 ± 0.40	51.79 ± 0.46	134.6 ± 1.4	25.30 ± 0.58	14.92 ± 0.56	12.34 ± 0.50
NGC 3351	4.45 ± 0.45	1.83 ± 0.15	5.97 ± 0.13	1.34 ± 0.13	24.49 ± 0.24	9.09 ± 0.19	2.77 ± 0.15	2.20 ± 0.13
NGC 3521	···	···	···	0.46 ± 0.15	0.98 ± 0.20	0.75 ± 0.17	0.31 ± 0.15	0.39 ± 0.23
NGC 3621	8.2 ± 1.3	···	2.27 ± 0.33	4.04 ± 0.36	11.31 ± 0.42	5.95 ± 0.34	2.61 ± 0.39	1.76 ± 0.27
NGC 3627	5.08 ± 0.70	···	···	1.15 ± 0.15	1.05 ± 0.23	2.02 ± 0.22	···	1.4 ± 1.3
NGC 3773	49.3 ± 1.2	7.83 ± 0.34	22.38 ± 0.37	29.96 ± 0.37	99.3 ± 1.3	15.93 ± 0.58	14.60 ± 0.71	10.24 ± 0.47
NGC 3938	···	···	1.54 ± 0.27	0.53 ± 0.24	5.98 ± 0.40	1.89 ± 0.37	···	···
NGC 4125	5.24 ± 0.75	···	0.36 ± 0.17	0.79 ± 0.16	1.00 ± 0.53	1.77 ± 0.27	0.74 ± 0.28	0.38 ± 0.16
NGC 4236	···	···	···	···	···	···	···	···
NGC 4254	1.86 ± 0.57	···	2.03 ± 0.17	0.58 ± 0.17	13.11 ± 0.37	4.53 ± 0.30	1.33 ± 0.28	0.94 ± 0.18
NGC 4321	2.98 ± 0.61	0.74 ± 0.20	4.17 ± 0.23	1.05 ± 0.20	26.18 ± 0.47	8.79 ± 0.38	2.00 ± 0.31	1.78 ± 0.26
NGC 4450	7.99 ± 0.72	···	0.51 ± 0.23	1.33 ± 0.19	1.77 ± 0.59	2.35 ± 0.41	1.33 ± 0.28	1.16 ± 0.22
NGC 4536	26.5 ± 1.5	3.25 ± 0.41	9.07 ± 0.33	3.78 ± 0.33	47.65 ± 0.71	21.41 ± 0.45	10.14 ± 0.38	7.94 ± 0.31
NGC 4552	···	···	···	0.96 ± 0.26	···	···	···	···
NGC 4559	11.3 ± 1.2	0.70 ± 0.40	3.05 ± 0.31	1.85 ± 0.37	14.80 ± 0.65	5.73 ± 0.48	3.42 ± 0.42	3.27 ± 0.40
NGC 4569	8.29 ± 0.70	···	1.21 ± 0.18	2.49 ± 0.20	6.82 ± 0.38	7.48 ± 0.28	2.67 ± 0.27	2.14 ± 0.22
NGC 4579	16.88 ± 0.74	···	···	2.95 ± 0.17	2.8 ± 2.0	7.31 ± 0.38	3.15 ± 0.31	2.07 ± 0.20
NGC 4594	4.8 ± 1.1	···	···	0.95 ± 0.30	1.6 ± 1.3	1.11 ± 0.93	0.93 ± 0.35	···
NGC 4625	8.9 ± 1.1	1.88 ± 0.43	4.23 ± 0.36	1.98 ± 0.38	18.44 ± 0.64	7.81 ± 0.52	4.01 ± 0.57	2.69 ± 0.36
NGC 4631	41.9 ± 3.0	2.69 ± 0.75	12.29 ± 0.90	14.64 ± 0.86	50.2 ± 1.5	11.2 ± 1.1	9.69 ± 0.96	6.06 ± 0.63
NGC 4725	6.4 ± 2.3	···	···	1.47 ± 0.32	···	···	0.75 ± 0.35	···
NGC 4736	4.21 ± 0.65	···	···	0.72 ± 0.17	···	1.09 ± 0.23	···	···
NGC 4826	8.27 ± 0.57	0.42 ± 0.21	1.66 ± 0.15	1.76 ± 0.15	7.60 ± 0.25	5.71 ± 0.19	2.13 ± 0.20	1.73 ± 0.18
NGC 5033	3.58 ± 0.78	···	1.20 ± 0.25	2.85 ± 0.22	6.54 ± 0.43	5.77 ± 0.39	1.26 ± 0.21	1.00 ± 0.22
NGC 5055	3.68 ± 0.71	···	0.66 ± 0.16	1.02 ± 0.16	2.67 ± 0.25	2.37 ± 0.19	1.26 ± 0.25	0.95 ± 0.19
NGC 5194	13.89 ± 0.67	0.41 ± 0.21	1.37 ± 0.15	3.85 ± 0.17	6.31 ± 0.34	14.01 ± 0.30	2.94 ± 0.33	2.04 ± 0.22
NGC 5195	3.68 ± 0.94	···	···	1.18 ± 0.19	0.52 ± 0.23	2.14 ± 0.17	0.96 ± 0.25	···
Tol 89	138.3 ± 6.1	32.1 ± 1.6	94.5 ± 1.8	349 ± 11	442 ± 13	34.6 ± 3.0	37.0 ± 2.7	25.4 ± 1.7
NGC 5474	12.7 ± 2.7	···	1.55 ± 0.58	3.33 ± 0.63	6.7 ± 1.2	2.5 ± 1.1	···	···
NGC 5713	13.54 ± 0.85	1.98 ± 0.22	7.34 ± 0.21	2.93 ± 0.22	42.75 ± 0.52	18.55 ± 0.41	7.93 ± 0.39	5.98 ± 0.27
NGC 5866	2.8 ± 1.0	···	···	0.97 ± 0.19	0.58 ± 0.20	1.22 ± 0.20	0.37 ± 0.19	0.42 ± 0.20
NGC 6946	···	···	3.83 ± 0.47	2.16 ± 0.42	27.41 ± 0.64	14.25 ± 0.45	4.28 ± 0.41	3.68 ± 0.39
NGC 7331	5.18 ± 0.54	···	···	1.36 ± 0.18	2.03 ± 0.35	1.16 ± 0.19	···	···
NGC 7793	9.9 ± 1.2	1.17 ± 0.45	4.32 ± 0.37	1.92 ± 0.36	18.54 ± 0.59	6.54 ± 0.45	3.53 ± 0.50	2.42 ± 0.33
				Radial Strip				
NGC 0024	18.0 ± 2.9	···	4.95 ± 0.70	4.78 ± 0.61	17.9 ± 1.6	5.1 ± 1.2	4.13 ± 0.96	3.90 ± 0.83
NGC 0337	36.0 ± 1.2	2.61 ± 0.22	9.59 ± 0.22	13.75 ± 0.25	48.37 ± 0.56	9.21 ± 0.37	10.54 ± 0.43	7.80 ± 0.30
NGC 0584	···	···	···	0.72 ± 0.25	···	···	···	···
NGC 0628	···	0.54 ± 0.27	1.62 ± 0.25	···	4.98 ± 0.43	2.06 ± 0.31	1.07 ± 0.29	0.69 ± 0.21
NGC 0855	31.5 ± 1.9	2.84 ± 0.42	5.64 ± 0.39	9.89 ± 0.35	22.17 ± 0.62	2.70 ± 0.53	5.80 ± 0.52	4.50 ± 0.46
NGC 0925	21.9 ± 1.6	2.72 ± 0.50	5.65 ± 0.42	4.36 ± 0.38	20.63 ± 0.91	4.43 ± 0.70	5.83 ± 0.63	4.94 ± 0.60
NGC 1097	6.27 ± 0.69	1.41 ± 0.24	3.39 ± 0.19	1.35 ± 0.16	15.37 ± 0.29	7.64 ± 0.21	2.15 ± 0.21	1.83 ± 0.16
NGC 1266	18.4 ± 2.4	···	···	2.39 ± 0.35	4.6 ± 1.2	11.2 ± 1.0	4.58 ± 0.95	···
NGC 1291	···	···	···	···	2.0 ± 1.3	···	···	···
NGC 1316	4.00 ± 0.92	···	···	0.63 ± 0.21	···	0.96 ± 0.59	0.67 ± 0.31	0.73 ± 0.34
NGC 1377	···	···	···	···	···	···	···	···
NGC 1404	···	···	0.74 ± 0.28	···	···	···	···	···
NGC 1482	26.5 ± 2.9	2.16 ± 0.46	5.62 ± 0.32	3.39 ± 0.34	26.03 ± 0.71	13.84 ± 0.42	6.44 ± 0.43	4.21 ± 0.24
NGC 1512	5.7 ± 1.4	0.66 ± 0.25	1.55 ± 0.23	0.87 ± 0.21	5.66 ± 0.38	2.87 ± 0.24	1.00 ± 0.25	0.94 ± 0.23
NGC 1566	9.14 ± 0.81	···	···	2.42 ± 0.24	13.19 ± 0.41	6.81 ± 0.28	2.77 ± 0.32	2.10 ± 0.23
NGC 1705	39.8 ± 1.0	6.98 ± 0.32	19.49 ± 0.36	69.61 ± 0.61	81.55 ± 0.93	4.78 ± 0.56	9.61 ± 0.51	6.54 ± 0.40
NGC 2403	18.0 ± 2.4	2.62 ± 0.92	6.49 ± 0.67	6.10 ± 0.79	29.2 ± 1.4	6.1 ± 1.1	6.8 ± 1.1	5.05 ± 0.74
DDO 053	66.0 ± 4.7	13.3 ± 1.7	40.7 ± 1.7	68.5 ± 2.2	168.6 ± 7.8	···	13.5 ± 3.7	9.8 ± 2.3
NGC 2798	14.0 ± 1.3	1.91 ± 0.35	5.75 ± 0.35	2.93 ± 0.30	32.23 ± 0.66	16.11 ± 0.46	5.72 ± 0.49	4.74 ± 0.35
NGC 2841	4.7 ± 1.1	0.50 ± 0.30	1.28 ± 0.25	1.00 ± 0.20	2.91 ± 0.55	2.14 ± 0.36	0.85 ± 0.27	0.70 ± 0.19
NGC 2915	27.7 ± 1.8	2.59 ± 0.47	7.97 ± 0.47	20.35 ± 0.41	32.04 ± 0.77	2.43 ± 0.55	5.06 ± 0.46	3.52 ± 0.34
NGC 2976	19.7 ± 1.2	1.62 ± 0.33	5.89 ± 0.26	3.87 ± 0.26	24.77 ± 0.46	6.70 ± 0.39	5.66 ± 0.34	3.79 ± 0.27
NGC 3049	20.6 ± 1.3	3.23 ± 0.47	10.22 ± 0.35	4.07 ± 0.38	44.76 ± 0.78	15.98 ± 0.53	7.46 ± 0.47	5.36 ± 0.42
NGC 3031	5.34 ± 0.87	···	0.80 ± 0.26	1.20 ± 0.17	1.73 ± 0.94	1.43 ± 0.66	···	···
M 81 Dw B	41.1 ± 5.1	4.5 ± 1.2	11.0 ± 1.1	24.67 ± 0.99	44.9 ± 3.8	···	4.8 ± 1.6	4.1 ± 1.4
NGC 3190	3.8 ± 1.5	···	···	0.79 ± 0.24	···	1.07 ± 0.28	···	0.70 ± 0.46
NGC 3184	4.3 ± 1.0	0.31 ± 0.28	2.32 ± 0.26	0.79 ± 0.27	10.47 ± 0.41	4.29 ± 0.36	1.82 ± 0.42	1.42 ± 0.29

TABLE 4 — *Continued*

Galaxy	[O II] λ3727	Hγ λ4340	Hβ λ4861	[O III] λ5007	Hα λ6563	[N II] λ6584	[S II] λ6716	[S II] λ6731
NGC 3198	12.9 ± 1.2	0.95 ± 0.33	2.73 ± 0.22	2.83 ± 0.26	13.16 ± 0.38	4.30 ± 0.38	3.09 ± 0.42	1.83 ± 0.24
NGC 3265	15.1 ± 1.6	1.05 ± 0.48	4.93 ± 0.38	2.97 ± 0.34	24.50 ± 0.57	10.12 ± 0.53	5.37 ± 0.46	3.93 ± 0.36
Mrk 33	62.1 ± 1.3	8.52 ± 0.30	24.07 ± 0.34	43.86 ± 0.36	112.2 ± 1.1	21.46 ± 0.69	13.18 ± 0.53	11.09 ± 0.46
NGC 3351	4.34 ± 0.69	0.71 ± 0.18	2.58 ± 0.17	1.14 ± 0.15	9.30 ± 0.30	4.25 ± 0.21	1.37 ± 0.21	1.10 ± 0.18
NGC 3521	5.14 ± 0.93	0.82 ± 0.26	2.39 ± 0.19	1.10 ± 0.15	9.89 ± 0.33	4.18 ± 0.20	2.25 ± 0.32	1.10 ± 0.15
NGC 3621	15.41 ± 0.81	2.12 ± 0.28	6.06 ± 0.22	2.96 ± 0.21	28.50 ± 0.44	9.69 ± 0.30	5.55 ± 0.31	3.86 ± 0.19
NGC 3627	5.38 ± 0.59	0.37 ± 0.16	1.69 ± 0.12	1.15 ± 0.17	7.62 ± 0.25	3.62 ± 0.20	1.87 ± 0.24	1.37 ± 0.18
NGC 3773	44.2 ± 1.3	6.01 ± 0.36	16.01 ± 0.31	20.80 ± 0.37	63.79 ± 0.81	10.78 ± 0.51	10.22 ± 0.54	7.23 ± 0.42
NGC 3938	···	···	2.9 ± 1.2	···	15.9 ± 2.9	3.8 ± 1.9	···	···
NGC 4125	2.3 ± 1.1	0.96 ± 0.35	0.92 ± 0.33	0.58 ± 0.23	···	1.19 ± 0.35	···	···
NGC 4254	5.00 ± 0.74	1.03 ± 0.19	5.14 ± 0.23	1.16 ± 0.19	30.39 ± 0.48	8.92 ± 0.32	3.56 ± 0.36	2.57 ± 0.26
NGC 4321	4.98 ± 0.97	1.00 ± 0.26	3.22 ± 0.23	0.81 ± 0.20	17.09 ± 0.44	6.73 ± 0.30	2.36 ± 0.32	1.73 ± 0.23
NGC 4450	7.1 ± 1.1	···	0.46 ± 0.16	1.12 ± 0.17	2.09 ± 0.42	1.63 ± 0.27	0.94 ± 0.23	0.66 ± 0.18
NGC 4536	13.6 ± 1.1	0.97 ± 0.32	3.30 ± 0.22	1.27 ± 0.22	20.61 ± 0.46	9.12 ± 0.37	5.07 ± 0.37	3.81 ± 0.26
NGC 4552	···	···	0.62 ± 0.22	···	···	···	···	···
NGC 4559	29.4 ± 1.0	2.28 ± 0.30	7.17 ± 0.26	7.55 ± 0.26	33.65 ± 0.66	8.24 ± 0.41	7.01 ± 0.49	4.94 ± 0.31
NGC 4569	3.45 ± 0.68	···	0.43 ± 0.16	0.94 ± 0.17	4.18 ± 0.35	4.07 ± 0.29	1.28 ± 0.28	0.94 ± 0.20
NGC 4579	9.57 ± 0.72	···	0.78 ± 0.15	1.60 ± 0.14	2.96 ± 0.28	3.99 ± 0.22	2.01 ± 0.30	1.14 ± 0.20
NGC 4594	···	···	···	···	···	···	···	···
NGC 4625	12.9 ± 1.9	1.43 ± 0.47	4.35 ± 0.39	1.28 ± 0.37	20.27 ± 0.89	8.80 ± 0.67	4.28 ± 0.71	3.19 ± 0.43
NGC 4631	27.40 ± 0.84	1.76 ± 0.22	7.45 ± 0.21	11.20 ± 0.22	34.89 ± 0.52	7.74 ± 0.37	8.13 ± 0.44	5.60 ± 0.23
NGC 4725	···	···	1.00 ± 0.96	···	···	1.5 ± 1.5	···	···
NGC 4736	7.03 ± 0.42	0.32 ± 0.14	1.62 ± 0.13	1.57 ± 0.14	6.40 ± 0.24	3.82 ± 0.21	1.64 ± 0.17	1.31 ± 0.16
NGC 4826	4.95 ± 0.69	···	1.37 ± 0.14	1.21 ± 0.15	5.35 ± 0.25	3.45 ± 0.22	1.47 ± 0.21	1.09 ± 0.21
NGC 5033	5.3 ± 1.0	0.89 ± 0.30	2.59 ± 0.21	2.00 ± 0.25	11.54 ± 0.46	5.65 ± 0.35	2.53 ± 0.45	···
NGC 5055	···	···	2.86 ± 0.98	···	9.5 ± 1.9	4.6 ± 1.2	···	···
NGC 5194	3.4 ± 1.1	0.70 ± 0.31	2.83 ± 0.27	0.72 ± 0.26	15.98 ± 0.65	8.74 ± 0.39	1.68 ± 0.39	1.71 ± 0.36
NGC 5195	6.2 ± 1.7	···	···	1.10 ± 0.25	2.69 ± 0.42	3.57 ± 0.31	0.71 ± 0.32	0.48 ± 0.17
Tol 89	58.5 ± 5.2	5.9 ± 1.4	23.8 ± 1.2	79.7 ± 1.6	94.9 ± 2.5	10.4 ± 2.1	8.7 ± 1.7	6.8 ± 1.2
NGC 5474	31.1 ± 1.7	2.53 ± 0.47	6.56 ± 0.43	9.26 ± 0.48	19.47 ± 0.77	2.85 ± 0.81	3.95 ± 0.70	2.88 ± 0.46
NGC 5713	16.58 ± 0.68	1.12 ± 0.18	5.77 ± 0.15	2.32 ± 0.16	32.01 ± 0.34	13.40 ± 0.31	6.94 ± 0.25	4.83 ± 0.20
NGC 5866	···	···	···	0.66 ± 0.22	···	···	···	···
NGC 6946	···	···	5.1 ± 1.4	···	23.9 ± 2.3	10.5 ± 2.1	3.0 ± 1.3	3.4 ± 1.4
NGC 7331	5.31 ± 0.94	···	1.67 ± 0.20	1.85 ± 0.22	6.31 ± 0.31	2.58 ± 0.21	2.35 ± 0.69	···
NGC 7793	10.0 ± 2.3	···	5.43 ± 0.75	3.05 ± 0.76	20.16 ± 1.00	5.72 ± 0.70	4.73 ± 0.81	3.27 ± 0.52

NOTE. — Rest-frame emission-line equivalent widths in Å. Note that the uncertainties include only statistical measurement uncertainties; they do not include systematic errors due to, for example, imperfect continuum subtraction. For most applications we recommend that a minimum S/N > 2 signal-to-noise ratio cut be applied to the EWs listed in this table.

TABLE 5
Optical Spectral Classifications

Galaxy (1)	Nuclear (2)	Circumnuclear (3)	Radial Strip (4)	Ho97 (5)	Adopted (6)
NGC 0024	SF	SF	SF	···	SF
NGC 0337	SF	SF	SF	···	SF
NGC 0584	?	?	?	···	AGN[a]
NGC 0628	?	SF	SF[b]	···	SF
NGC 0855	SF	SF	SF	···	SF
NGC 0925	SF	SF	SF	SF	SF
NGC 1097	AGN	SF	SF[e]	···	AGN
NGC 1266	AGN[b]	AGN[b]	AGN[b]	···	AGN
NGC 1291	AGN[b]	AGN[b]	?	···	AGN
NGC 1316	AGN[b]	AGN[b]	?	···	AGN
NGC 1377	?	SF[bc]	?	···	SF
NGC 1404	?	?	?	···	AGN[d]
NGC 1482	SF	SF	SF[e]	···	SF
NGC 1512	AGN[b]	SF	SF[e]	···	AGN
NGC 1566	AGN	AGN[b]	AGN[b]	···	AGN[f]
NGC 1705	?	SF	SF	···	SF
NGC 2403	···	SF[e]	SF	SF	SF
Ho II	···	···	···	···	SF[g]
M 81 Dw A	···	···	···	···	SF[g]
DDO 053	···	?	?	···	SF[g]
NGC 2798	SF/AGN	SF/AGN	SF/AGN	···	SF/AGN
NGC 2841	AGN	?	SF/AGN	AGN	AGN
NGC 2915	SF	SF	SF	···	SF
Ho I	···	···	···	···	SF[g]
NGC 2976	SF	SF	SF	SF/AGN	SF
NGC 3049	SF	SF	SF	···	SF
NGC 3031	AGN[b]	AGN[b]	?	AGN	AGN[f]
NGC 3034	SF[h]	SF[h]	···	SF/AGN	SF
Ho IX	···	···	···	···	SF[g]
M 81 Dw B	···	?	?	···	SF[g]
NGC 3190	?	?	?	AGN	AGN
NGC 3184	SF	SF	SF	SF	SF
NGC 3198	SF	SF[e]	SF	SF	SF
IC 2574	···	?	···	SF	SF
NGC 3265	SF	SF	SF	···	SF
Mrk 33	SF	SF	SF	···	SF
NGC 3351	SF	SF	SF	SF/AGN	SF
NGC 3521	?	AGN[b]	SF	AGN	AGN
NGC 3621	AGN	SF/AGN	SF	···	AGN
NGC 3627	AGN[b]	AGN[b]	SF/AGN	AGN	AGN
NGC 3773	SF	SF	SF	···	SF
NGC 3938	?	SF	?	AGN	AGN
NGC 4125	AGN[b]	?	?	AGN	AGN
NGC 4236	···	?	···	SF	SF
NGC 4254	SF/AGN	SF	SF	SF/AGN	SF/AGN
NGC 4321	AGN	SF	SF	AGN	AGN
NGC 4450	AGN	AGN	AGN	AGN	AGN
NGC 4536	SF/AGN	SF	SF	SF/AGN	SF/AGN
NGC 4552	?	?	?	AGN	AGN
NGC 4559	SF[b]	SF	SF	SF	SF
NGC 4569	AGN	AGN	AGN	AGN	AGN
NGC 4579	AGN	?	AGN	AGN	AGN[f]
NGC 4594	AGN	?	?	AGN	AGN[f]
NGC 4625	SF[b]	SF	SF	···	SF
NGC 4631	···	SF	SF	SF	SF
NGC 4725	AGN[b]	?	?	AGN	AGN
NGC 4736	?	?	SF/AGN	AGN	AGN
DDO 154	···	···	···	···	SF[g]
NGC 4826	AGN	SF/AGN	SF/AGN	AGN	AGN
DDO 165	···	···	···	···	SF[g]
NGC 5033	AGN	AGN	SF/AGN	AGN	AGN[f]
NGC 5055	AGN[b]	AGN	SF[b]	AGN	AGN
NGC 5194	AGN	AGN	SF/AGN	···	AGN
NGC 5195	AGN[b]	AGN[b]	AGN[b]	···	AGN
Tol 89	···	SF	SF	···	SF
NGC 5408	···	···	···	···	SF[g]
NGC 5474	···	SF/AGN	SF	SF	SF/AGN
NGC 5713	SF	SF	SF	···	SF
NGC 5866	AGN[b]	AGN[b]	?	AGN	AGN
IC 4710	···	···	···	···	SF[g]
NGC 6822	···	···	···	···	SF[g]

TABLE 5 — *Continued*

Galaxy (1)	Nuclear (2)	Circumnuclear (3)	Radial Strip (4)	Ho97 (5)	Adopted (6)
NGC 6946	SF[i]	SF[i]	SF[b]	SF/AGN	SF
NGC 7331	AGN[b]	AGN[b]	SF/AGN	AGN	AGN
NGC 7552	...	...	...	...	SF[j]
NGC 7793	SF	SF	SF	...	SF

NOTE. — Optical spectral classifications based on our nuclear, circumnuclear, and radial-strip spectra and the [N II]/Hα vs. [O III]/Hβ emission-line diagnostic diagram (see Fig. 4). For comparison we also tabulate the classifications based on the Ho et al. (1997, hereafter Ho97) nuclear spectra. Ellipses indicate no data are available, while a question mark indicates that one or more emission line failed our S/N > 2 requirement (see §3). We list the final, adopted classification for each galaxy, usually based on the nuclear or circumnuclear spectrum, in the last column. See §3 for additional details.

[a] The lower limit on the nuclear [N II]/Hα ratio for NGC 0584 suggests that it hosts a weak AGN.

[b] These spectra were classified as SF or AGN on the basis of the [N II]/Hα ratio alone because of an unconstrained [O III]/Hβ ratio, where we adopt $\log([\text{N II}]/\text{H}\alpha) = -0.25$ as the boundary between the two classes.

[c] NGC 1377 is a "nascent starburst" with a highly dust-obscured nucleus and AGN-like emission-line ratios (Roussel et al. 2006); therefore, although the formal classification based on our circumnuclear spectrum is an AGN, we have changed it to SF.

[d] Tajer et al. (2005) report an X-ray luminosity for NGC 1404 of $\log(L_X) = 41.46$ erg s^{-1}, suggesting the presence of a weak AGN in this elliptical galaxy.

[e] The radial strip spectra of NGC 1097, NGC 1482, and NGC 1512 formally yield a SF/AGN classification; however, the more physically realistic SF classification is consistent with the errors in the emission-line ratios, and with the uncertainty in the classification method. For the same reasons we have changed the circumnuclear classifications of NGC 2403 and NGC 3198 from SF/AGN to SF.

[f] One or more spectra of these objects exhibits broad Balmer emission lines.

[g] Ho II, M 81 Dw A, DDO 053, Ho I, Ho IX, M 81 DwB, DDO 154, DDO 165, NGC 5408, IC 4710, and NGC 6822 are clearly star-forming galaxies; they are diffuse, low-luminosity ($M_B \gtrsim -18$ mag) galaxies with no well-defined bulge or nucleus.

[h] Our nuclear and circumnuclear spectra of the starburst galaxy NGC 3034=M 82 exhibit enhanced [N II]/Hα ratios, likely from shock-ionized gas, resulting in AGN-like spectral classifications; therefore, we have changed these classifications to SF, although we note that recent evidence suggests that M 82 may host a low-luminosity AGN (Matsumoto et al. 2001).

[i] NGC 6946 is undergoing a powerful nuclear starburst, resulting in a shock-enhanced [N II]/Hα ratio in our nuclear and circumnuclear spectra; therefore, the formal SF/AGN classifications indicated by these two spectra have been changed to SF.

[j] We classify NGC 7552 as SF using the nuclear emission-line flux ratios published by Kewley et al. (2001b), although Durret & Bergeron (1988) argue that this object may host a weak AGN.

TABLE 6
Nebular Dust Reddening

Galaxy	Nuclear		Circumnuclear		Radial Strip	
	Hα/Hβ	$E(B-V)$	Hα/Hβ	$E(B-V)$	Hα/Hβ	$E(B-V)$
NGC 0024	6.48 ± 3.05	0.78 ± 0.45	4.09 ± 0.69	0.34 ± 0.16	4.00 ± 0.67	0.32 ± 0.16
NGC 0337	4.41 ± 0.38	0.41 ± 0.08	5.43 ± 0.24	0.61 ± 0.04	4.90 ± 0.12	0.51 ± 0.02
NGC 0855	5.24 ± 0.35	0.58 ± 0.06	4.44 ± 0.19	0.42 ± 0.04	4.64 ± 0.34	0.46 ± 0.07
NGC 0925	3.41 ± 0.31	0.17 ± 0.09	4.78 ± 0.25	0.49 ± 0.05	3.84 ± 0.33	0.28 ± 0.08
NGC 1097	...	...	6.52 ± 0.23	0.78 ± 0.03	6.51 ± 0.38	0.78 ± 0.06
NGC 1482	12.05 ± 0.49	1.36 ± 0.04	11.10 ± 0.51	1.29 ± 0.04	7.85 ± 0.49	0.96 ± 0.06
NGC 1512	...	...	5.01 ± 0.37	0.53 ± 0.07	5.11 ± 0.83	0.55 ± 0.15
NGC 1705	...	...	3.80 ± 0.10	0.27 ± 0.02	3.82 ± 0.08	0.28 ± 0.02
NGC 2403	...	...	5.17 ± 1.08	0.56 ± 0.20	4.81 ± 0.54	0.49 ± 0.11
DDO 053	...	...	3.79 ± 0.24	0.27 ± 0.06	3.76 ± 0.18	0.26 ± 0.05
NGC 2798	6.81 ± 0.20	0.82 ± 0.03	7.85 ± 0.26	0.96 ± 0.03	7.59 ± 0.48	0.93 ± 0.06
NGC 2841	...	...	...	...	3.29 ± 0.89	0.13 ± 0.26
NGC 2915	4.24 ± 0.42	0.37 ± 0.09	3.68 ± 0.18	0.24 ± 0.05	3.94 ± 0.25	0.30 ± 0.06
NGC 2976	5.65 ± 0.17	0.65 ± 0.03	4.18 ± 0.26	0.36 ± 0.06	4.89 ± 0.23	0.51 ± 0.04
NGC 3049	3.58 ± 0.06	0.21 ± 0.02	5.23 ± 0.15	0.57 ± 0.03	5.18 ± 0.19	0.56 ± 0.04
NGC 3034	13.13 ± 0.29	1.45 ± 0.02	11.47 ± 0.24	1.32 ± 0.02	...	...
M 81 Dw B	...	...	4.37 ± 0.57	0.40 ± 0.12	3.83 ± 0.48	0.28 ± 0.12
NGC 3184	7.42 ± 0.53	0.90 ± 0.07	5.04 ± 0.49	0.54 ± 0.09	5.83 ± 0.70	0.68 ± 0.11
NGC 3198	...	...	...	...	6.26 ± 0.54	0.74 ± 0.08
IC 2574	...	...	4.55 ± 0.64	0.44 ± 0.13	...	...
NGC 3265	6.52 ± 0.16	0.78 ± 0.02	6.46 ± 0.34	0.77 ± 0.05	6.70 ± 0.54	0.81 ± 0.08
Mrk 33	4.47 ± 0.07	0.42 ± 0.01	4.68 ± 0.07	0.47 ± 0.01	4.75 ± 0.07	0.48 ± 0.01
NGC 3351	2.94 ± 0.17	0.03 ± 0.05	5.60 ± 0.13	0.64 ± 0.02	5.08 ± 0.37	0.55 ± 0.07
NGC 3521	...	...	...	...	5.78 ± 0.50	0.67 ± 0.08
NGC 3621	...	...	6.77 ± 1.01	0.82 ± 0.14	5.70 ± 0.22	0.65 ± 0.04
NGC 3627	...	...	...	...	6.07 ± 0.48	0.71 ± 0.07
NGC 3773	4.73 ± 0.08	0.48 ± 0.02	4.29 ± 0.08	0.38 ± 0.02	4.23 ± 0.09	0.37 ± 0.02
NGC 4254	10.97 ± 1.86	1.28 ± 0.16	8.99 ± 0.80	1.09 ± 0.08	7.36 ± 0.35	0.90 ± 0.05
NGC 4321	...	...	7.59 ± 0.43	0.93 ± 0.05	6.70 ± 0.52	0.81 ± 0.07
NGC 4536	8.43 ± 0.34	1.03 ± 0.04	9.99 ± 0.38	1.19 ± 0.04	8.95 ± 0.63	1.08 ± 0.07
NGC 4559	...	...	6.22 ± 0.68	0.74 ± 0.10	5.08 ± 0.20	0.55 ± 0.04
NGC 4625	...	...	5.09 ± 0.47	0.55 ± 0.09	5.09 ± 0.51	0.55 ± 0.10
NGC 4631	...	...	5.93 ± 0.46	0.69 ± 0.07	5.25 ± 0.16	0.58 ± 0.03
NGC 4736	...	...	...	...	5.11 ± 0.45	0.55 ± 0.08
NGC 4826	...	...	7.40 ± 0.73	0.90 ± 0.09	5.46 ± 0.61	0.61 ± 0.11
NGC 5033	...	...	...	...	7.06 ± 0.64	0.86 ± 0.09
NGC 5194	...	...	...	...	6.93 ± 0.72	0.84 ± 0.10
Tol 89	...	...	4.31 ± 0.08	0.39 ± 0.02	4.27 ± 0.23	0.38 ± 0.05
NGC 5474	...	...	5.10 ± 2.11	0.55 ± 0.39	3.29 ± 0.25	0.13 ± 0.07
NGC 5713	7.28 ± 0.33	0.89 ± 0.04	6.85 ± 0.21	0.83 ± 0.03	6.58 ± 0.19	0.79 ± 0.03
NGC 7331	...	...	...	...	5.69 ± 0.74	0.65 ± 0.12
NGC 7793	4.26 ± 0.63	0.38 ± 0.14	5.02 ± 0.46	0.53 ± 0.09	4.55 ± 0.66	0.44 ± 0.14

Note. — Balmer decrement, Hα/Hβ, and corresponding color excess, $E(B-V)$, in magnitudes, asuming the O'Donnell (1994) Milky Way extinction curve and an intrinsic (unreddened) decrement of $2.86^{+0.18}_{-0.11}$. Note that the tabulated uncertainties only include the statistical measurement errors of the emission lines and the uncertainty in the adopted intrinsic Balmer decrement; they do not include possible systematic errors arising from, for example, a breakdown of our assumption of a foreground dust screen geometry (e.g., Witt & Gordon 2000, but see Kennicutt et al. 2009).

TABLE 7
Nuclear, Circumnuclear, & Radial Strip Oxygen Abundances

Galaxy (1)	R_{23} Branch (2)	R_{23} (3)	O_{32} (4)	P (5)	$\log(U)_{\rm KK04}$ (6)	$12+\log({\rm O/H})_{\rm KK04}$ (7)	$12+\log({\rm O/H})_{\rm PT05}$ (8)
			Nuclear				
NGC 0024	U	6.59 ± 16.16	0.33 ± 0.81	0.25 ± 0.53	-3.23 ± 0.57	8.66 ± 0.47	7.95 ± 0.73
NGC 0337	U	4.74 ± 2.18	0.18 ± 0.08	0.15 ± 0.06	-3.33 ± 0.22	8.85 ± 0.21	8.02 ± 0.32
NGC 0855	U	5.72 ± 1.88	0.77 ± 0.27	0.43 ± 0.12	-2.88 ± 0.20	8.77 ± 0.18	8.27 ± 0.21
NGC 0925	U	2.42 ± 1.13	0.42 ± 0.21	0.30 ± 0.13	-2.86 ± 0.27	9.06 ± 0.06	8.49 ± 0.20
NGC 1482	U	1.46 ± 0.39	0.17 ± 0.05	0.14 ± 0.04	-3.15 ± 0.13	9.14 ± 0.03	8.44 ± 0.10
NGC 2798	U	1.72 ± 0.27	0.32 ± 0.05	0.24 ± 0.04	-2.93 ± 0.08	9.11 ± 0.02	8.52 ± 0.05
NGC 2915	L	6.41 ± 3.02	1.56 ± 0.81	0.61 ± 0.24	-2.90 ± 0.19	8.21 ± 0.32	7.89 ± 0.39
NGC 2976	U	3.79 ± 0.59	0.48 ± 0.08	0.33 ± 0.04	-2.92 ± 0.10	8.95 ± 0.05	8.36 ± 0.08
NGC 3049	U	1.76 ± 0.16	0.31 ± 0.03	0.24 ± 0.02	-2.94 ± 0.05	9.11 ± 0.01	8.51 ± 0.04
NGC 3034	U	1.44 ± 0.19	0.32 ± 0.05	0.24 ± 0.03	-2.90 ± 0.07	9.13 ± 0.01	8.56 ± 0.05
NGC 3184	U	1.09 ± 0.49	0.19 ± 0.11	0.16 ± 0.09	-3.07 ± 0.26	9.17 ± 0.05	8.51 ± 0.14
NGC 3265	U	2.38 ± 0.31	0.26 ± 0.04	0.20 ± 0.03	-3.06 ± 0.07	9.07 ± 0.02	8.39 ± 0.06
Mrk 33	U	4.46 ± 0.33	1.03 ± 0.08	0.51 ± 0.03	-2.65 ± 0.05	8.90 ± 0.03	8.45 ± 0.04
NGC 3351	U	0.59 ± 0.19	0.55 ± 0.25	0.36 ± 0.15	-2.50 ± 0.27	9.19 ± 0.04	8.76 ± 0.08
NGC 3773	U	3.93 ± 0.33	0.91 ± 0.08	0.48 ± 0.03	-2.66 ± 0.06	8.95 ± 0.03	8.48 ± 0.04
NGC 4254	U	2.75 ± 2.41	0.69 ± 0.67	0.41 ± 0.31	-2.67 ± 0.51	9.03 ± 0.12	8.55 ± 0.29
NGC 4536	U	2.93 ± 0.64	0.25 ± 0.06	0.20 ± 0.04	-3.11 ± 0.11	9.03 ± 0.05	8.31 ± 0.11
NGC 5713	U	2.13 ± 0.52	0.34 ± 0.09	0.26 ± 0.06	-2.92 ± 0.13	9.08 ± 0.03	8.48 ± 0.10
NGC 7793	U	3.06 ± 2.29	0.45 ± 0.35	0.31 ± 0.21	-2.89 ± 0.38	9.01 ± 0.14	8.43 ± 0.34
			Circumnuclear				
NGC 0024	U	3.76 ± 3.24	0.42 ± 0.37	0.29 ± 0.22	-2.97 ± 0.46	8.95 ± 0.15	8.33 ± 0.45
NGC 0337	U	4.08 ± 0.94	0.28 ± 0.07	0.22 ± 0.05	-3.14 ± 0.11	8.92 ± 0.09	8.20 ± 0.15
NGC 0855	U	5.24 ± 1.09	0.85 ± 0.19	0.46 ± 0.08	-2.80 ± 0.13	8.83 ± 0.11	8.34 ± 0.13
NGC 0925	U	3.78 ± 1.03	0.34 ± 0.10	0.25 ± 0.06	-3.06 ± 0.15	8.95 ± 0.07	8.28 ± 0.16
NGC 1097	U	1.55 ± 0.30	0.37 ± 0.08	0.27 ± 0.05	-2.85 ± 0.11	9.12 ± 0.02	8.57 ± 0.07
NGC 1482	U	3.52 ± 0.98	0.15 ± 0.04	0.13 ± 0.04	-3.32 ± 0.13	8.97 ± 0.09	8.14 ± 0.16
NGC 1512	U	1.55 ± 0.63	0.40 ± 0.19	0.29 ± 0.11	-2.81 ± 0.24	9.11 ± 0.04	8.59 ± 0.13
NGC 1705	L	6.97 ± 0.85	3.07 ± 0.42	0.75 ± 0.08	-2.68 ± 0.05	8.19 ± 0.08	7.82 ± 0.12
NGC 2403	U	4.00 ± 4.20	0.46 ± 0.50	0.31 ± 0.29	-2.96 ± 0.47	8.93 ± 0.26	8.32 ± 0.43
DDO 053	L	4.94 ± 1.48	1.37 ± 0.47	0.58 ± 0.15	-2.97 ± 0.11	8.06 ± 0.17	7.69 ± 0.22
NGC 2798	U	2.68 ± 0.47	0.25 ± 0.05	0.20 ± 0.03	-3.09 ± 0.09	9.05 ± 0.03	8.35 ± 0.09
NGC 2915	L	6.17 ± 1.47	1.44 ± 0.38	0.59 ± 0.12	-2.93 ± 0.09	8.20 ± 0.15	7.87 ± 0.25
NGC 2976	U	3.13 ± 0.96	0.48 ± 0.16	0.32 ± 0.09	-2.87 ± 0.20	9.01 ± 0.07	8.44 ± 0.15
NGC 3049	U	2.16 ± 0.34	0.25 ± 0.04	0.20 ± 0.03	-3.05 ± 0.08	9.08 ± 0.02	8.42 ± 0.06
NGC 3034	U	1.87 ± 0.23	0.26 ± 0.04	0.21 ± 0.02	-3.02 ± 0.07	9.10 ± 0.01	8.46 ± 0.05
M 81 Dw B	L	6.08 ± 3.80	1.10 ± 0.75	0.52 ± 0.28	-3.00 ± 0.27	8.22 ± 0.37	7.88 ± 0.63
NGC 3184	U	1.39 ± 0.77	0.29 ± 0.19	0.23 ± 0.13	-2.93 ± 0.30	9.13 ± 0.05	8.55 ± 0.19
IC 2574	L	7.39 ± 4.92	1.45 ± 1.07	0.59 ± 0.33	-2.88 ± 0.32	8.31 ± 0.40	8.05 ± 0.72
NGC 3265	U	3.14 ± 0.90	0.25 ± 0.07	0.20 ± 0.05	-3.12 ± 0.15	9.01 ± 0.07	8.29 ± 0.16
Mrk 33	U	4.90 ± 0.34	0.86 ± 0.07	0.46 ± 0.03	-2.77 ± 0.05	8.86 ± 0.03	8.38 ± 0.04
NGC 3351	U	0.95 ± 0.13	0.41 ± 0.08	0.29 ± 0.05	-2.73 ± 0.09	9.15 ± 0.01	8.67 ± 0.04
NGC 3621	U	5.57 ± 4.18	0.65 ± 0.51	0.40 ± 0.25	-2.93 ± 0.41	8.79 ± 0.31	8.24 ± 0.42
NGC 3773	U	4.20 ± 0.38	0.68 ± 0.07	0.40 ± 0.03	-2.81 ± 0.06	8.92 ± 0.03	8.39 ± 0.05
NGC 4254	U	1.40 ± 0.73	0.32 ± 0.20	0.24 ± 0.13	-2.89 ± 0.32	9.13 ± 0.04	8.56 ± 0.18
NGC 4321	U	1.24 ± 0.42	0.32 ± 0.13	0.24 ± 0.09	-2.88 ± 0.20	9.14 ± 0.03	8.58 ± 0.11
NGC 4536	U	3.55 ± 0.76	0.17 ± 0.04	0.14 ± 0.03	-3.29 ± 0.10	8.97 ± 0.07	8.16 ± 0.12
NGC 4559	U	4.16 ± 2.45	0.22 ± 0.13	0.18 ± 0.10	-3.23 ± 0.30	8.91 ± 0.24	8.14 ± 0.36
NGC 4625	U	2.46 ± 1.20	0.32 ± 0.16	0.24 ± 0.11	-2.98 ± 0.29	9.06 ± 0.08	8.43 ± 0.21
NGC 4631	U	5.49 ± 2.20	0.37 ± 0.15	0.27 ± 0.09	-3.13 ± 0.24	8.78 ± 0.22	8.11 ± 0.30
NGC 4826	U	4.81 ± 2.45	0.36 ± 0.18	0.26 ± 0.12	-3.10 ± 0.28	8.85 ± 0.21	8.17 ± 0.37
Tol 89	U	6.83 ± 0.63	1.95 ± 0.21	0.66 ± 0.05	-2.58 ± 0.06	8.69 ± 0.06	8.35 ± 0.05
NGC 5474	A[b]	10.36 ± 21.91	0.36 ± 0.77	0.26 ± 0.48	-3.26 ± 6.06	8.44 ± 0.46	8.10 ± 1.39
NGC 5713	U	2.64 ± 0.45	0.23 ± 0.04	0.18 ± 0.03	-3.13 ± 0.08	9.05 ± 0.03	8.33 ± 0.09
NGC 7793	U	2.59 ± 1.26	0.28 ± 0.14	0.22 ± 0.10	-3.04 ± 0.27	9.05 ± 0.08	8.38 ± 0.23
			Radial Strip				
NGC 0024	U	4.09 ± 3.42	0.44 ± 0.38	0.30 ± 0.22	-2.98 ± 0.44	8.93 ± 0.18	8.30 ± 0.43
NGC 0337	U	5.44 ± 0.66	0.50 ± 0.06	0.33 ± 0.03	-3.03 ± 0.08	8.79 ± 0.07	8.19 ± 0.08
NGC 0855	U	6.29 ± 2.32	0.56 ± 0.21	0.36 ± 0.11	-3.04 ± 0.21	8.71 ± 0.23	8.13 ± 0.26
NGC 0925	U	3.59 ± 1.57	0.39 ± 0.18	0.28 ± 0.11	-2.99 ± 0.26	8.97 ± 0.13	8.33 ± 0.24
NGC 1097	U	2.03 ± 0.64	0.32 ± 0.11	0.24 ± 0.07	-2.95 ± 0.17	9.09 ± 0.04	8.48 ± 0.13
NGC 1482	U	4.55 ± 1.56	0.19 ± 0.07	0.16 ± 0.05	-3.30 ± 0.16	8.87 ± 0.16	8.06 ± 0.21
NGC 1512	U	3.02 ± 2.60	0.31 ± 0.28	0.23 ± 0.18	-3.04 ± 0.48	9.02 ± 0.15	8.35 ± 0.38
NGC 1705	L	6.91 ± 0.67	1.99 ± 0.21	0.67 ± 0.05	-2.81 ± 0.04	8.24 ± 0.06	7.92 ± 0.10
NGC 2403	U	3.74 ± 2.13	0.44 ± 0.26	0.31 ± 0.15	-2.95 ± 0.34	8.96 ± 0.16	8.35 ± 0.29
DDO 053	L	4.05 ± 0.91	1.11 ± 0.28	0.53 ± 0.10	-3.06 ± 0.07	7.98 ± 0.13	7.57 ± 0.15
NGC 2798	U	3.01 ± 1.03	0.26 ± 0.09	0.21 ± 0.06	-3.10 ± 0.19	9.02 ± 0.07	8.31 ± 0.17
NGC 2841	U	2.20 ± 2.73	0.86 ± 1.21	0.46 ± 0.52	-2.52 ± 0.61	9.06 ± 0.07	8.65 ± 0.27
NGC 2915	L	6.54 ± 2.01	1.02 ± 0.34	0.50 ± 0.13	-3.01 ± 0.10	8.27 ± 0.20	7.96 ± 0.33
NGC 2976	U	3.40 ± 0.83	0.32 ± 0.08	0.25 ± 0.05	-3.04 ± 0.13	8.99 ± 0.07	8.32 ± 0.13
NGC 3049	U	2.45 ± 0.49	0.26 ± 0.06	0.21 ± 0.04	-3.06 ± 0.11	9.06 ± 0.04	8.39 ± 0.09
M 81 Dw B	L	5.48 ± 3.17	1.11 ± 0.73	0.53 ± 0.27	-3.02 ± 0.22	8.15 ± 0.35	7.79 ± 0.50
NGC 3184	U	1.99 ± 1.32	0.27 ± 0.20	0.21 ± 0.14	-3.01 ± 0.35	9.09 ± 0.07	8.46 ± 0.27
NGC 3198	U	5.60 ± 2.56	0.30 ± 0.14	0.23 ± 0.09	-3.21 ± 0.22	8.77 ± 0.24	8.04 ± 0.38

TABLE 7 — *Continued*

Galaxy (1)	R_{23} Branch (2)	R_{23} (3)	O_{32} (4)	P (5)	$\log(U)_{\rm KK04}$ (6)	$12+\log({\rm O/H})_{\rm KK04}$ (7)	$12+\log({\rm O/H})_{\rm PT05}$ (8)
NGC 3265	U	3.77 ± 1.64	0.24 ± 0.11	0.20 ± 0.08	-3.17 ± 0.20	8.95 ± 0.12	8.21 ± 0.28
Mrk 33	U	5.11 ± 0.38	0.80 ± 0.07	0.45 ± 0.03	-2.81 ± 0.05	8.84 ± 0.04	8.34 ± 0.04
NGC 3351	U	1.65 ± 0.63	0.51 ± 0.22	0.34 ± 0.12	-2.72 ± 0.24	9.10 ± 0.04	8.62 ± 0.12
NGC 3521	U	2.11 ± 0.98	0.37 ± 0.19	0.27 ± 0.12	-2.89 ± 0.25	9.08 ± 0.06	8.50 ± 0.19
NGC 3621	U	3.08 ± 0.64	0.25 ± 0.05	0.20 ± 0.04	-3.12 ± 0.11	9.01 ± 0.06	8.30 ± 0.11
NGC 3627	U	3.30 ± 1.36	0.34 ± 0.15	0.25 ± 0.10	-3.02 ± 0.24	8.99 ± 0.10	8.34 ± 0.24
NGC 3773	U	4.29 ± 0.46	0.65 ± 0.08	0.39 ± 0.04	-2.84 ± 0.07	8.91 ± 0.04	8.37 ± 0.06
NGC 4254	U	1.44 ± 0.41	0.23 ± 0.08	0.19 ± 0.06	-3.03 ± 0.15	9.13 ± 0.03	8.50 ± 0.09
NGC 4321	U	1.79 ± 0.80	0.20 ± 0.10	0.17 ± 0.08	-3.10 ± 0.22	9.11 ± 0.05	8.43 ± 0.19
NGC 4536	U	5.11 ± 2.04	0.10 ± 0.04	0.09 ± 0.04	-3.52 ± 0.16	8.80 ± 0.23	7.87 ± 0.28
NGC 4559	U	5.25 ± 1.08	0.33 ± 0.07	0.25 ± 0.05	-3.16 ± 0.12	8.81 ± 0.13	8.11 ± 0.15
NGC 4625	U	3.00 ± 1.68	0.14 ± 0.08	0.12 ± 0.07	-3.32 ± 0.25	9.02 ± 0.13	8.20 ± 0.31
NGC 4631	U	5.91 ± 0.92	0.46 ± 0.08	0.32 ± 0.04	-3.08 ± 0.09	8.74 ± 0.10	8.12 ± 0.12
NGC 4736	U	4.30 ± 1.93	0.39 ± 0.18	0.28 ± 0.11	-3.04 ± 0.24	8.90 ± 0.20	8.25 ± 0.30
NGC 4826	U	3.42 ± 1.96	0.47 ± 0.29	0.32 ± 0.16	-2.89 ± 0.31	8.98 ± 0.13	8.40 ± 0.31
NGC 5033	U	2.49 ± 1.15	0.60 ± 0.31	0.38 ± 0.16	-2.71 ± 0.29	9.05 ± 0.06	8.56 ± 0.17
NGC 5194	U	1.77 ± 1.09	0.21 ± 0.15	0.17 ± 0.11	-3.09 ± 0.31	9.11 ± 0.07	8.43 ± 0.24
Tol 89	U	6.88 ± 1.77	1.76 ± 0.50	0.64 ± 0.14	-2.63 ± 0.18	8.68 ± 0.18	8.33 ± 0.17
NGC 5474	U	4.78 ± 1.76	0.64 ± 0.25	0.39 ± 0.12	-2.88 ± 0.23	8.86 ± 0.15	8.32 ± 0.22
NGC 5713	U	3.65 ± 0.57	0.16 ± 0.03	0.14 ± 0.02	-3.31 ± 0.07	8.96 ± 0.06	8.13 ± 0.10
NGC 7331	U	3.23 ± 2.09	0.75 ± 0.52	0.43 ± 0.24	-2.68 ± 0.38	9.00 ± 0.15	8.52 ± 0.27
NGC 7793	U	2.30 ± 1.73	0.47 ± 0.38	0.32 ± 0.22	-2.81 ± 0.43	9.07 ± 0.09	8.53 ± 0.28

NOTE. — (1) Galaxy name; (2-5) Adopted R_{23} branch (U=upper, L=lower, A=ambiguous), R_{23} parameter, and excitation parameters O_{32} and P (see §4.1 and §4.2); (6-8) Ionization parameter and oxygen abundances based on the KK04 and PT05 strong-line calibrations. Note that the uncertainties on the ionization parameter and oxygen abundances include statistical measurement errors only.

[a] The R_{23} branch of NGC 5474 based on its circumnuclear spectrum is ambiguous, according to the criteria defined in §4.2.

TABLE 8
H II-Region Oxygen Abundances

Galaxy (1)	R_{23} Branch (2)	Gradient (dex ρ_{25}^{-1}) (3)	12+log(O/H) at $\rho = 0$ (4)	12+log(O/H) at $\rho = 0.4\,\rho_{25}$ (5)	12+log(O/H) Average (6)	N(H II) (7)	Refs. (8)
			KK04				
NGC 0628	U	-0.57 ± 0.04	9.19 ± 0.02	9.02 ± 0.01	8.88 ± 0.15	34	1,2,3,4,5
NGC 0925	U	-0.42 ± 0.02	8.91 ± 0.01	8.79 ± 0.01	8.73 ± 0.15	55	2,5,6
NGC 1097	U	-0.29 ± 0.09	9.17 ± 0.01	9.09 ± 0.02	9.14 ± 0.05	15	7
NGC 1705	L	···	···	···	8.37 ± 0.06	9	8
NGC 2403	U	-0.26 ± 0.03	8.89 ± 0.01	8.81 ± 0.01	8.80 ± 0.13	46	1,4,5,9,10
Ho II	L	···	···	···	8.13 ± 0.11	21	11,12,13
DDO 053	L	···	···	···	7.98 ± 0.23	4	11,14
NGC 2841	U	-0.42 ± 0.28	9.34 ± 0.07	9.22 ± 0.02	9.19 ± 0.05	5	1,15
NGC 2915	L	···	···	···	8.36 ± 0.12	1	16
Ho I	L	···	···	···	8.04 ± 0.07	4	11,17
NGC 3049	U	···	···	···	9.11 ± 0.01	1	18
NGC 3031	U	-0.45 ± 0.07	9.11 ± 0.02	8.97 ± 0.01	8.94 ± 0.09	36	1,15,19,20
Ho IX	U[a]	···	···	···	8.98 ± 0.05	2	11
M 81 Dw B	L	···	···	···	8.20 ± 0.10	1	17
NGC 3184	U	-0.52 ± 0.05	9.30 ± 0.02	9.15 ± 0.01	9.07 ± 0.12	32	4,5,6
NGC 3198	U	-0.66 ± 0.11	9.10 ± 0.03	8.90 ± 0.02	8.78 ± 0.15	13	6
IC 2574	L	···	···	···	8.23 ± 0.12	21	11,13,17
Mrk 33	U	···	···	···	8.74 ± 0.14	1	21
NGC 3351	U	-0.15 ± 0.03	9.24 ± 0.01	9.19 ± 0.01	9.21 ± 0.05	25	1,4,15,22,23
NGC 3521	U	-0.69 ± 0.20	9.20 ± 0.03	9.00 ± 0.02	9.06 ± 0.09	12	1,6
NGC 3621	U	-0.91 ± 0.10	9.06 ± 0.01	8.79 ± 0.01	8.91 ± 0.14	30	6,24
NGC 4254	U	-0.42 ± 0.06	9.26 ± 0.02	9.14 ± 0.01	9.08 ± 0.11	18	4,25,26
NGC 4321	U	-0.35 ± 0.13	9.29 ± 0.04	9.18 ± 0.02	9.12 ± 0.07	9	4,26
NGC 4559	U	-0.36 ± 0.07	8.92 ± 0.02	8.81 ± 0.01	8.75 ± 0.13	18	6
NGC 4725	U	···	···	···	9.10 ± 0.08	8	6
NGC 4736	U	-0.11 ± 0.15	9.04 ± 0.01	9.01 ± 0.03	9.04 ± 0.04	15	1,4,15
DDO 154	L	···	···	···	8.02 ± 0.05	4	27,28
NGC 4826	U	···	···	···	9.24 ± 0.04	5	15
DDO 165	L	···	···	···	8.04 ± 0.07	1	11
NGC 5033	U	-0.34 ± 0.08	9.05 ± 0.03	8.95 ± 0.02	8.89 ± 0.13	7	6
NGC 5055	U	-0.54 ± 0.18	9.30 ± 0.04	9.14 ± 0.02	9.11 ± 0.10	5	4
NGC 5194	U	-0.50 ± 0.05	9.33 ± 0.01	9.18 ± 0.01	9.17 ± 0.11	34	1,4,29,30,31
NGC 5408	L	···	···	···	8.23 ± 0.06	1	32
NGC 6822	U	···	···	···	8.67 ± 0.10	19	33,34
NGC 6946	U	-0.28 ± 0.10	9.13 ± 0.04	9.05 ± 0.02	8.99 ± 0.11	8	3,4
NGC 7331	U	-0.56 ± 0.28	9.18 ± 0.05	9.02 ± 0.02	9.05 ± 0.05	10	1,15
NGC 7552	U	···	···	···	9.16 ± 0.01	1	35
NGC 7793	U	-0.36 ± 0.07	8.98 ± 0.02	8.87 ± 0.01	8.83 ± 0.12	12	4,36
			PT05				
NGC 0628	U	-0.27 ± 0.05	8.43 ± 0.02	8.35 ± 0.01	8.27 ± 0.12	33	1,2,3,4,5
NGC 0925	U	-0.21 ± 0.03	8.32 ± 0.01	8.25 ± 0.01	8.22 ± 0.14	52	2,5,6
NGC 1097	U	-0.37 ± 0.13	8.58 ± 0.01	8.47 ± 0.02	8.55 ± 0.09	15	7
NGC 1705	L	···	···	···	8.07 ± 0.08	5	8
NGC 2403	U	-0.32 ± 0.03	8.42 ± 0.01	8.33 ± 0.01	8.30 ± 0.14	44	1,4,5,9,10
Ho II	L	···	···	···	7.72 ± 0.14	20	11,12,13
DDO 053	L	···	···	···	7.57 ± 0.27	4	11,14
NGC 2841	U	-0.63 ± 0.46	8.72 ± 0.12	8.54 ± 0.03	8.52 ± 0.09	5	1,15
NGC 2915	L	···	···	···	7.98 ± 0.20	1	16
Ho I	L	···	···	···	7.61 ± 0.11	4	11,17
NGC 3049	U	···	···	···	8.54 ± 0.01	1	18
NGC 3031	U	-0.37 ± 0.09	8.54 ± 0.02	8.43 ± 0.01	8.37 ± 0.14	36	1,15,19,20
Ho IX	U[a]	···	···	···	8.14 ± 0.11	2	11
M 81 Dw B	L	···	···	···	7.85 ± 0.14	1	17
NGC 3184	U	-0.46 ± 0.06	8.65 ± 0.02	8.51 ± 0.01	8.42 ± 0.14	32	4,5,6
NGC 3198	U	-0.50 ± 0.14	8.49 ± 0.04	8.34 ± 0.02	8.26 ± 0.14	12	6
IC 2574	L	···	···	···	7.84 ± 0.15	18	11,13,17
Mrk 33	U	···	···	···	8.15 ± 0.20	1	21
NGC 3351	U	-0.28 ± 0.04	8.69 ± 0.01	8.60 ± 0.01	8.63 ± 0.10	25	1,4,15,22,23
NGC 3521	U	-0.16 ± 0.33	8.44 ± 0.05	8.39 ± 0.02	8.38 ± 0.11	11	1,6
NGC 3621	U	-0.19 ± 0.13	8.33 ± 0.02	8.27 ± 0.02	8.29 ± 0.14	29	6,24
NGC 4254	U	-0.37 ± 0.08	8.56 ± 0.02	8.45 ± 0.01	8.41 ± 0.14	18	4,25,26
NGC 4321	U	-0.38 ± 0.21	8.61 ± 0.07	8.50 ± 0.03	8.43 ± 0.08	9	4,26
NGC 4559	U	-0.10 ± 0.07	8.32 ± 0.02	8.29 ± 0.01	8.27 ± 0.10	16	6
NGC 4725	U	···	···	···	8.35 ± 0.13	8	6
NGC 4736	U	-0.33 ± 0.18	8.40 ± 0.01	8.31 ± 0.03	8.39 ± 0.08	15	1,4,15
DDO 154	L	···	···	···	7.54 ± 0.09	4	27,28
NGC 4826	U	···	···	···	8.59 ± 0.11	5	15
DDO 165	L	···	···	···	7.63 ± 0.08	1	11
NGC 5033	U	-0.58 ± 0.10	8.54 ± 0.03	8.37 ± 0.02	8.24 ± 0.24	7	6
NGC 5055	U	-0.63 ± 0.29	8.59 ± 0.07	8.40 ± 0.03	8.38 ± 0.18	5	4
NGC 5194	U	-0.31 ± 0.06	8.64 ± 0.01	8.55 ± 0.01	8.54 ± 0.09	34	1,4,29,30,31
NGC 5408	L	···	···	···	7.81 ± 0.09	1	32

TABLE 8 — *Continued*

Galaxy (1)	R_{23} Branch (2)	Gradient (dex ρ_{25}^{-1}) (3)	12+log(O/H) at $\rho = 0$ (4)	12+log(O/H) at $\rho = 0.4\,\rho_{25}$ (5)	12+log(O/H) Average (6)	N(H II) (7)	Refs. (8)
NGC 6822	U	···	···	···	8.12 ± 0.22	18	33,34
NGC 6946	U	-0.17 ± 0.15	8.45 ± 0.06	8.40 ± 0.03	8.37 ± 0.06	8	3,4
NGC 7331	U	-0.24 ± 0.35	8.41 ± 0.06	8.34 ± 0.02	8.36 ± 0.07	10	1,15
NGC 7552	U	···	···	···	8.35 ± 0.03	1	35
NGC 7793	U	-0.10 ± 0.08	8.34 ± 0.02	8.31 ± 0.02	8.26 ± 0.13	12	4,36

REFERENCES. — (1) Bresolin et al. (1999); (2) Castellanos et al. (2002); (3) Ferguson et al. (1998); (4) McCall et al. (1985); (5) van Zee et al. (1998); (6) Zaritsky et al. (1994); (7) Storchi-Bergmann et al. (1996); (8) Lee & Skillman (2004); (9) Garnett et al. (1997); (10) Garnett et al. (1999); (11) Croxall et al. (2009); (12) Lee et al. (2003b); (13) Masegosa et al. (1991); (14) Skillman et al. (1989); (15) Oey & Kennicutt (1993); (16) Lee et al. (2003a); (17) Miller & Hodge (1996); (18) Guseva et al. (2000); (19) Garnett & Shields (1987); (20) Stauffer & Bothun (1984); (21) Kong & Cheng (2002); (22) Bresolin & Kennicutt (2002); (23) Díaz et al. (2007); (24) Ryder (1995); (25) Henry et al. (1994); (26) Shields (1991); (27) Kennicutt & Skillman (2001); (28) van Zee et al. (1997); (29) Bresolin et al. (2004); (30) Diaz et al. (1991); (31) Garnett et al. (2004b); (32) Stasińska et al. (1986); (33) Lee et al. (2006b); (34) Peimbert et al. (2005); (35) Storchi-Bergmann et al. (1995); (36) Edmunds & Pagel (1984).

NOTE. — (1) Galaxy name; (2) Adopted R_{23} branch (U=upper, L=lower, A=ambiguous); (3) Slope of the radial abundance gradient; (4) Central oxygen abundance based on the derived abundance gradient; (5) Characteristic oxygen abundance, defined as the metallicity at $\rho = 0.4\rho_{25}$, based on the derived abundance gradient; (6) Unweighted average and standard deviation of all the H II-region abundances (see §4.3.2); (7) Number of H II regions with measured abundances; (8) References to the literature from which the H II-region line-ratios were taken (see Appendix B).

[a] Although Ho IX is among the faintest galaxies in our sample, the [N II]/Hα and [N II]/[O II] line-ratios clearly place it on the upper R_{23} branch (Croxall et al. 2009).

TABLE 9
Final Oxygen Abundances

Galaxy	$12+\log(O/H)_{KK04}$			$12+\log(O/H)_{PT05}$		
	Central	Characteristic	$L-Z$	Central	Characteristic	$L-Z$
NGC 0024	8.93 ± 0.11	8.93 ± 0.11	8.62	8.26 ± 0.29	8.26 ± 0.29	8.08
NGC 0337	8.84 ± 0.05	8.84 ± 0.05	9.10	8.18 ± 0.07	8.18 ± 0.07	8.45
NGC 0584	...	...	9.07	...	...	8.43
NGC 0628	9.25 ± 0.03	9.02 ± 0.01	9.02	8.45 ± 0.03	8.35 ± 0.01	8.39
NGC 0855	8.80 ± 0.09	8.80 ± 0.09	8.57	8.29 ± 0.10	8.29 ± 0.10	8.04
NGC 0925	8.96 ± 0.01	8.79 ± 0.01	8.95	8.34 ± 0.02	8.25 ± 0.01	8.34
NGC 1097	9.15 ± 0.01	9.09 ± 0.01	9.30	8.62 ± 0.03	8.47 ± 0.02	8.60
NGC 1266	...	...	8.89	...	...	8.29
NGC 1291	...	...	9.20	...	...	8.52
NGC 1316	...	...	9.52	...	...	8.77
NGC 1377	...	...	8.89	...	...	8.29
NGC 1404	...	...	9.21	...	...	8.54
NGC 1482	9.14 ± 0.03	8.95 ± 0.08	8.87	8.44 ± 0.10	8.11 ± 0.13	8.28
NGC 1512	9.11 ± 0.04	9.11 ± 0.04	8.97	8.56 ± 0.12	8.56 ± 0.12	8.35
NGC 1566	...	...	9.34	...	...	8.63
NGC 1705	8.28 ± 0.04	8.28 ± 0.04	8.33	7.96 ± 0.06	7.96 ± 0.06	7.86
NGC 2403	8.92 ± 0.02	8.81 ± 0.01	8.90	8.46 ± 0.02	8.33 ± 0.01	8.30
Ho II	8.13 ± 0.11	8.13 ± 0.11	8.51	7.72 ± 0.14	7.72 ± 0.14	8.00
M 81 Dw A	...	...	7.65	...	...	7.34
DDO 053	8.00 ± 0.09	8.00 ± 0.09	7.98	7.60 ± 0.11	7.60 ± 0.11	7.59
NGC 2798	9.11 ± 0.02	9.04 ± 0.03	8.91	8.52 ± 0.05	8.34 ± 0.08	8.30
NGC 2841	9.38 ± 0.13	9.21 ± 0.02	9.20	8.79 ± 0.22	8.54 ± 0.03	8.53
NGC 2915	8.28 ± 0.08	8.28 ± 0.08	8.37	7.94 ± 0.13	7.94 ± 0.13	7.89
Ho I	8.04 ± 0.07	8.04 ± 0.07	8.21	7.61 ± 0.11	7.61 ± 0.11	7.77
NGC 2976	8.98 ± 0.03	8.98 ± 0.03	8.59	8.36 ± 0.06	8.36 ± 0.06	8.06
NGC 3049	9.11 ± 0.01	9.10 ± 0.01	8.86	8.53 ± 0.01	8.53 ± 0.01	8.27
NGC 3031	9.15 ± 0.03	8.97 ± 0.01	9.12	8.57 ± 0.04	8.43 ± 0.01	8.47
NGC 3034	9.12 ± 0.01	9.12 ± 0.01	8.97	8.51 ± 0.03	8.51 ± 0.03	8.35
Ho IX	8.98 ± 0.05	8.98 ± 0.05	8.04	8.14 ± 0.11	8.14 ± 0.11	7.64
M 81 Dw B	8.19 ± 0.09	8.19 ± 0.09	8.08	7.84 ± 0.13	7.84 ± 0.13	7.67
NGC 3190	...	...	9.15	...	...	8.49
NGC 3184	9.27 ± 0.02	9.15 ± 0.01	9.06	8.68 ± 0.03	8.51 ± 0.01	8.42
NGC 3198	9.17 ± 0.06	8.90 ± 0.02	9.03	8.54 ± 0.08	8.34 ± 0.02	8.40
IC 2574	8.24 ± 0.11	8.24 ± 0.11	8.55	7.85 ± 0.14	7.85 ± 0.14	8.03
NGC 3265	9.07 ± 0.02	8.99 ± 0.06	8.81	8.39 ± 0.06	8.27 ± 0.14	8.23
Mrk 33	8.87 ± 0.02	8.87 ± 0.02	8.71	8.39 ± 0.02	8.39 ± 0.02	8.15
NGC 3351	9.19 ± 0.01	9.19 ± 0.01	8.98	8.71 ± 0.02	8.60 ± 0.01	8.36
NGC 3521	9.27 ± 0.06	9.01 ± 0.02	9.20	8.45 ± 0.11	8.39 ± 0.02	8.53
NGC 3621	9.15 ± 0.03	8.80 ± 0.01	9.00	8.35 ± 0.03	8.27 ± 0.02	8.37
NGC 3627	8.99 ± 0.10	8.99 ± 0.10	9.16	8.34 ± 0.24	8.34 ± 0.24	8.50
NGC 3773	8.95 ± 0.03	8.92 ± 0.03	8.53	8.43 ± 0.03	8.43 ± 0.03	8.02
NGC 3938	...	...	9.06	...	...	8.42
NGC 4125	...	...	9.30	...	...	8.61
NGC 4236	...	...	8.74	...	...	8.17
NGC 4254	9.23 ± 0.02	9.13 ± 0.01	9.23	8.60 ± 0.04	8.45 ± 0.01	8.55
NGC 4321	9.17 ± 0.01	9.17 ± 0.01	9.22	8.61 ± 0.08	8.50 ± 0.03	8.55
NGC 4450	...	...	9.13	...	...	8.47
NGC 4536	9.00 ± 0.04	9.00 ± 0.04	9.04	8.21 ± 0.08	8.21 ± 0.08	8.41
NGC 4552	...	...	9.14	...	...	8.48
NGC 4559	8.95 ± 0.03	8.81 ± 0.01	9.03	8.33 ± 0.04	8.29 ± 0.01	8.40
NGC 4569	...	...	9.26	...	...	8.58
NGC 4579	...	...	9.22	...	...	8.54
NGC 4594	...	...	9.22	...	...	8.54
NGC 4625	9.05 ± 0.07	9.05 ± 0.07	8.53	8.35 ± 0.17	8.35 ± 0.17	8.02
NGC 4631	8.75 ± 0.09	8.75 ± 0.09	9.04	8.12 ± 0.11	8.12 ± 0.11	8.40
NGC 4725	9.10 ± 0.08	9.10 ± 0.08	9.16	8.35 ± 0.13	8.35 ± 0.13	8.50
NGC 4736	9.06 ± 0.03	9.01 ± 0.03	9.07	8.44 ± 0.03	8.31 ± 0.03	8.42
DDO 154	8.02 ± 0.05	8.02 ± 0.05	8.12	7.54 ± 0.09	7.54 ± 0.09	7.70
NGC 4826	9.20 ± 0.04	9.20 ± 0.04	9.13	8.54 ± 0.10	8.54 ± 0.10	8.47
DDO 165	8.04 ± 0.07	8.04 ± 0.07	8.32	7.63 ± 0.08	7.63 ± 0.08	7.86
NGC 5033	9.09 ± 0.05	8.96 ± 0.02	9.11	8.60 ± 0.06	8.37 ± 0.02	8.46
NGC 5055	9.35 ± 0.08	9.14 ± 0.02	9.13	8.65 ± 0.13	8.40 ± 0.03	8.47
NGC 5194	9.38 ± 0.02	9.18 ± 0.01	9.19	8.67 ± 0.03	8.55 ± 0.01	8.52
NGC 5195	...	...	8.99	...	...	8.36
Tol 89	8.69 ± 0.06	8.69 ± 0.06	8.93	8.35 ± 0.05	8.35 ± 0.05	8.32
NGC 5408	8.23 ± 0.06	8.23 ± 0.06	8.49	7.81 ± 0.09	7.81 ± 0.09	7.99
NGC 5474	8.83 ± 0.14	8.83 ± 0.14	8.69	8.31 ± 0.22	8.31 ± 0.22	8.13
NGC 5713	9.08 ± 0.03	9.03 ± 0.03	9.18	8.48 ± 0.10	8.24 ± 0.06	8.51
NGC 5866	...	...	9.12	...	...	8.47
IC 4710	...	...	8.74	...	...	8.18
NGC 6822	8.67 ± 0.10	8.67 ± 0.10	8.22	8.12 ± 0.22	8.12 ± 0.22	7.78
NGC 6946	9.16 ± 0.06	9.05 ± 0.02	9.27	8.47 ± 0.09	8.40 ± 0.03	8.58
NGC 7331	9.24 ± 0.10	9.02 ± 0.02	9.27	8.44 ± 0.12	8.34 ± 0.02	8.58
NGC 7552	9.16 ± 0.01	9.16 ± 0.01	9.16	8.35 ± 0.03	8.35 ± 0.03	8.50
NGC 7793	9.02 ± 0.03	8.88 ± 0.01	8.81	8.35 ± 0.04	8.31 ± 0.02	8.23

TABLE 9 — *Continued*

Galaxy	$12+\log(O/H)_{KK04}$			$12+\log(O/H)_{PT05}$		
	Central	Characteristic	$L-Z$	Central	Characteristic	$L-Z$

NOTE. — Final central and characteristic nebular oxygen abundances for the SINGS galaxies based on the KK04 and PT05 abundance calibrations. The central abundance characterizes the inner, or nuclear metallicity of each galaxy, while the characteristic abundance is a globally-averaged metallicity. Note that the uncertainties on the oxygen abundances include statistical measurement errors only. We also provide the oxygen abundances inferred from the B-band luminosity-metallicity ($L-Z$) relation for every object; the uncertainty in the $L-Z$ abundance is at least 0.2 dex (see §4.4 and Fig. 11).

TABLE 10
Oxygen Abundances of the H II Regions in the SINGS Galaxies

No. (1)	Galaxy (2)	Region (3)	ρ/ρ_{25} (4)	R_{23} (5)	O_{32} (6)	P (7)	$12+\log(O/H)_{KK04}$ (8)	$12+\log(O/H)_{PT05}$ (9)	Ref. (10)
001	NGC 0628	H292	0.23	2.44 ± 0.17	0.24 ± 0.04	0.20 ± 0.03	9.06 ± 0.01	8.38 ± 0.04	1
002	NGC 0628	H451	0.26	1.75 ± 0.18	0.15 ± 0.06	0.13 ± 0.05	9.12 ± 0.02	8.38 ± 0.06	1
003	NGC 0628	H572	0.39	2.82 ± 0.18	0.15 ± 0.02	0.13 ± 0.02	9.04 ± 0.02	8.24 ± 0.04	1
004	NGC 0628	H598	0.41	3.13 ± 0.25	0.23 ± 0.05	0.19 ± 0.04	9.01 ± 0.02	8.27 ± 0.06	1
005	NGC 0628	H627	0.51	4.24 ± 0.18	0.80 ± 0.07	0.45 ± 0.03	8.92 ± 0.01	8.43 ± 0.03	1
006	NGC 0628	H154-155	0.72	5.29 ± 0.24	0.27 ± 0.02	0.21 ± 0.01	8.80 ± 0.03	8.04 ± 0.04	1
007	NGC 0628	H13	0.71	4.82 ± 0.18	0.48 ± 0.03	0.33 ± 0.02	8.86 ± 0.02	8.25 ± 0.03	1
008	NGC 0628	FGW628A	0.26	2.28 ± 0.08	0.10 ± 0.01	0.09 ± 0.01	9.08 ± 0.01	8.25 ± 0.02	2
009	NGC 0628	FGW628B	0.80	5.77 ± 0.25	0.59 ± 0.04	0.37 ± 0.02	8.76 ± 0.03	8.20 ± 0.04	2
010	NGC 0628	+081-140	0.55	3.68 ± 0.08	0.68 ± 0.03	0.40 ± 0.01	8.96 ± 0.01	8.45 ± 0.02	3
011	NGC 0628	+062-158	0.57	2.67 ± 0.16	0.15 ± 0.02	0.13 ± 0.01	9.05 ± 0.01	8.26 ± 0.03	3
012	NGC 0628	+047-172	0.59	3.65 ± 0.12	0.40 ± 0.02	0.28 ± 0.01	8.96 ± 0.01	8.33 ± 0.02	3
013	NGC 0628	+044-175	0.60	4.55 ± 0.11	0.83 ± 0.04	0.45 ± 0.01	8.89 ± 0.01	8.40 ± 0.02	3
014	NGC 0628	+180-008	0.62	2.97 ± 0.09	0.31 ± 0.01	0.24 ± 0.01	9.02 ± 0.01	8.36 ± 0.02	3
015	NGC 0628	+178-052	0.65	3.03 ± 0.07	0.60 ± 0.02	0.38 ± 0.01	9.01 ± 0.01	8.50 ± 0.02	3
016	NGC 0628	-086+186	0.69	5.03 ± 0.11	0.70 ± 0.03	0.41 ± 0.01	8.84 ± 0.01	8.32 ± 0.02	3
017	NGC 0628	-075+200	0.72	5.53 ± 0.21	0.36 ± 0.02	0.27 ± 0.01	8.78 ± 0.02	8.10 ± 0.04	3
018	NGC 0628	-073+203	0.72	4.71 ± 0.14	0.51 ± 0.02	0.34 ± 0.01	8.87 ± 0.01	8.27 ± 0.03	3
019	NGC 0628	-069+208	0.73	5.59 ± 0.12	0.94 ± 0.04	0.49 ± 0.01	8.79 ± 0.01	8.33 ± 0.02	3
020	NGC 0628	+254-043	0.90	5.96 ± 0.15	0.59 ± 0.03	0.37 ± 0.01	8.74 ± 0.02	8.18 ± 0.02	3
021	NGC 0628	+256-041	0.90	7.25 ± 0.27	0.52 ± 0.03	0.34 ± 0.02	8.59 ± 0.03	8.03 ± 0.03[a]	3
022	NGC 0628	-232+112	0.90	5.10 ± 0.25	0.20 ± 0.01	0.17 ± 0.01	8.81 ± 0.03	8.01 ± 0.04	3
023	NGC 0628	+262-041	0.92	6.37 ± 0.27	0.55 ± 0.04	0.35 ± 0.02	8.70 ± 0.03	8.12 ± 0.04	3
024	NGC 0628	+264-037	0.93	6.37 ± 0.17	0.86 ± 0.04	0.46 ± 0.02	8.71 ± 0.02	8.23 ± 0.03	3
025	NGC 0628	+265-041	0.93	7.40 ± 0.23	1.18 ± 0.08	0.54 ± 0.02	8.61 ± 0.03	8.21 ± 0.03	3
026	NGC 0628	-227+148	0.95	6.32 ± 0.17	0.87 ± 0.04	0.46 ± 0.02	8.71 ± 0.02	8.24 ± 0.03	3
027	NGC 0628	+049+052	0.23	3.04 ± 0.34	0.25 ± 0.04	0.20 ± 0.02	9.02 ± 0.03	8.30 ± 0.07	4
028	NGC 0628	-074-022	0.26	1.65 ± 0.18	0.22 ± 0.03	0.18 ± 0.02	9.12 ± 0.01	8.46 ± 0.05	4
029	NGC 0628	-060-107	0.39	2.97 ± 0.41	0.19 ± 0.04	0.16 ± 0.03	9.02 ± 0.03	8.26 ± 0.09	4
030	NGC 0628	+042-116	0.41	3.55 ± 0.41	0.26 ± 0.05	0.21 ± 0.03	8.97 ± 0.04	8.25 ± 0.08	4
031	NGC 0628	-042-154	0.51	5.02 ± 0.18	0.92 ± 0.06	0.48 ± 0.02	8.85 ± 0.02	8.38 ± 0.03	4
032	NGC 0628	-186+086	0.72	4.84 ± 0.46	0.45 ± 0.06	0.31 ± 0.03	8.85 ± 0.05	8.23 ± 0.08	4
033	NGC 0628	-089+192	0.71	6.30 ± 0.52	0.46 ± 0.06	0.31 ± 0.03	8.70 ± 0.06	8.07 ± 0.08	4
034	NGC 0628	H13	0.71	5.03 ± 0.11	0.70 ± 0.03	0.41 ± 0.01	8.84 ± 0.01	8.31 ± 0.02	5
035	NGC 0925	CDT1	0.03	4.01 ± 0.11	0.39 ± 0.02	0.28 ± 0.01	8.93 ± 0.01	8.29 ± 0.02	5
036	NGC 0925	CDT2	0.02	3.56 ± 0.10	0.50 ± 0.02	0.33 ± 0.01	8.97 ± 0.01	8.40 ± 0.02	5
037	NGC 0925	CDT3	0.04	4.23 ± 0.13	0.44 ± 0.02	0.31 ± 0.01	8.91 ± 0.01	8.29 ± 0.02	5
038	NGC 0925	CDT4	0.14	3.80 ± 0.12	0.35 ± 0.02	0.26 ± 0.01	8.95 ± 0.01	8.28 ± 0.02	5
039	NGC 0925	+002-002	0.01	2.73 ± 0.08	0.61 ± 0.03	0.38 ± 0.01	9.04 ± 0.01	8.53 ± 0.02	3
040	NGC 0925	-005+000	0.02	3.07 ± 0.09	0.29 ± 0.01	0.23 ± 0.01	9.01 ± 0.01	8.34 ± 0.02	3
041	NGC 0925	-008+000	0.03	3.79 ± 0.11	0.32 ± 0.01	0.24 ± 0.01	8.95 ± 0.01	8.26 ± 0.02	3
042	NGC 0925	+010-004	0.04	3.77 ± 0.12	0.28 ± 0.01	0.22 ± 0.01	8.95 ± 0.01	8.24 ± 0.02	3
043	NGC 0925	+015-005	0.05	2.58 ± 0.06	0.63 ± 0.03	0.38 ± 0.01	9.04 ± 0.01	8.55 ± 0.01	3
044	NGC 0925	+030-008	0.10	3.74 ± 0.14	0.17 ± 0.01	0.15 ± 0.01	8.95 ± 0.01	8.14 ± 0.03	3
045	NGC 0925	+036-010	0.12	4.29 ± 0.14	0.26 ± 0.01	0.21 ± 0.01	8.90 ± 0.01	8.16 ± 0.03	3
046	NGC 0925	+042-011	0.14	4.10 ± 0.12	0.45 ± 0.02	0.31 ± 0.01	8.93 ± 0.01	8.31 ± 0.02	3
047	NGC 0925	+087-031	0.30	5.73 ± 0.18	0.66 ± 0.04	0.40 ± 0.02	8.77 ± 0.02	8.23 ± 0.03	3
048	NGC 0925	-012-066	0.40	7.67 ± 0.16	2.02 ± 0.10	0.67 ± 0.02	8.60 ± 0.02	8.29 ± 0.02	3
049	NGC 0925	-047-058	0.41	6.11 ± 0.22	0.34 ± 0.02	0.25 ± 0.01	8.71 ± 0.03	8.01 ± 0.04	3
050	NGC 0925	+135-016	0.44	6.84 ± 0.21	0.66 ± 0.04	0.40 ± 0.01	8.65 ± 0.02	8.12 ± 0.03	3
051	NGC 0925	-109+062	0.44	5.34 ± 0.11	1.13 ± 0.05	0.53 ± 0.01	8.82 ± 0.01	8.39 ± 0.02	3
052	NGC 0925	+137+011	0.48	6.53 ± 0.22	1.15 ± 0.08	0.53 ± 0.02	8.70 ± 0.02	8.28 ± 0.03	3
053	NGC 0925	-137+056	0.49	5.88 ± 0.17	0.69 ± 0.04	0.41 ± 0.01	8.76 ± 0.02	8.23 ± 0.03	3
054	NGC 0925	-145-006	0.50	6.81 ± 0.12	1.50 ± 0.06	0.60 ± 0.01	8.68 ± 0.01	8.31 ± 0.01	3
055	NGC 0925	-080+087	0.51	6.81 ± 0.24	0.40 ± 0.02	0.29 ± 0.01	8.64 ± 0.03	7.98 ± 0.04	3
056	NGC 0925	-114+087	0.55	7.52 ± 0.26	0.55 ± 0.03	0.35 ± 0.01	8.57 ± 0.03	... [b]	3
057	NGC 0925	+161+015	0.57	6.00 ± 0.20	0.60 ± 0.03	0.38 ± 0.01	8.74 ± 0.02	8.18 ± 0.03	3
058	NGC 0925	+174+018	0.62	5.76 ± 0.29	0.23 ± 0.02	0.19 ± 0.01	8.74 ± 0.03	7.96 ± 0.05	3
059	NGC 0925	+182+019	0.65	7.03 ± 0.16	1.86 ± 0.10	0.65 ± 0.02	8.66 ± 0.02	8.33 ± 0.02	3
060	NGC 0925	-187-017	0.66	6.74 ± 0.14	1.03 ± 0.04	0.51 ± 0.01	8.67 ± 0.02	8.24 ± 0.02	3
061	NGC 0925	-192-018	0.68	7.42 ± 0.20	1.09 ± 0.06	0.52 ± 0.02	8.60 ± 0.02	8.19 ± 0.03	3
062	NGC 0925	-192-018	0.68	7.31 ± 0.15	1.06 ± 0.04	0.51 ± 0.01	8.61 ± 0.02	8.19 ± 0.02	3
063	NGC 0925	-198-013	0.69	7.86 ± 0.19	1.39 ± 0.07	0.58 ± 0.02	8.56 ± 0.02	8.20 ± 0.02	3
064	NGC 0925	+209-006	0.69	6.34 ± 0.27	0.37 ± 0.02	0.27 ± 0.01	8.69 ± 0.03	8.01 ± 0.04	3
065	NGC 0925	-200-020	0.71	6.58 ± 0.13	1.11 ± 0.05	0.53 ± 0.01	8.69 ± 0.02	8.27 ± 0.02	3
066	NGC 0925	+217-006	0.72	7.99 ± 0.19	1.59 ± 0.09	0.61 ± 0.02	8.55 ± 0.02	8.22 ± 0.02	3
067	NGC 0925	+156-114	0.73	6.59 ± 0.23	0.51 ± 0.03	0.34 ± 0.01	8.67 ± 0.03	8.07 ± 0.03	3
068	NGC 0925	-220+004	0.73	5.96 ± 0.19	0.50 ± 0.03	0.33 ± 0.01	8.74 ± 0.02	8.14 ± 0.03	3
069	NGC 0925	+221-006	0.73	8.99 ± 0.21	2.73 ± 0.17	0.73 ± 0.02	8.47 ± 0.02	8.23 ± 0.02	3
070	NGC 0925	+052+130	0.82	7.88 ± 0.20	1.32 ± 0.07	0.57 ± 0.02	8.56 ± 0.02	8.19 ± 0.03	3
071	NGC 0925	-250+019	0.82	6.10 ± 0.14	1.79 ± 0.10	0.64 ± 0.02	8.76 ± 0.01	8.40 ± 0.02	3
072	NGC 0925	+206-114	0.82	6.36 ± 0.19	0.88 ± 0.05	0.47 ± 0.02	8.71 ± 0.02	8.24 ± 0.03	3
073	NGC 0925	+019+143	0.85	8.88 ± 0.20	2.03 ± 0.11	0.67 ± 0.02	8.47 ± 0.02	8.20 ± 0.03[a]	3
074	NGC 0925	-174+140	0.87	7.35 ± 0.21	1.00 ± 0.06	0.50 ± 0.02	8.61 ± 0.02	8.18 ± 0.03	3

TABLE 10 — *Continued*

No. (1)	Galaxy (2)	Region (3)	ρ/ρ_{25} (4)	R_{23} (5)	O_{32} (6)	P (7)	$12+\log(\mathrm{O/H})_{\mathrm{KK04}}$ (8)	$12+\log(\mathrm{O/H})_{\mathrm{PT05}}$ (9)	Ref. (10)
075	NGC 0925	-262+011	0.86	7.40 ± 0.33	0.56 ± 0.04	0.36 ± 0.02	8.58 ± 0.04	8.05 ± 0.04[a]	3
076	NGC 0925	-272+016	0.89	6.92 ± 0.27	0.50 ± 0.03	0.34 ± 0.02	8.63 ± 0.03	8.04 ± 0.04	3
077	NGC 0925	-274+010	0.90	7.60 ± 0.20	1.03 ± 0.05	0.51 ± 0.02	8.58 ± 0.02	8.16 ± 0.03	3
078	NGC 0925	-285+023	0.93	6.88 ± 0.25	0.45 ± 0.03	0.31 ± 0.01	8.63 ± 0.03	8.01 ± 0.04	3
079	NGC 0925	-159+162	0.96	6.29 ± 0.30	0.27 ± 0.02	0.21 ± 0.01	8.69 ± 0.03	7.93 ± 0.05	3
080	NGC 0925	-308+035	1.00	6.48 ± 0.25	0.30 ± 0.02	0.23 ± 0.01	8.67 ± 0.03	7.94 ± 0.04	3
081	NGC 0925	-205-001	0.69	5.60 ± 0.48	1.04 ± 0.18	0.51 ± 0.09	8.79 ± 0.04	8.35 ± 0.04	6
082	NGC 0925	-179-022	0.65	6.92 ± 0.55	0.92 ± 0.15	0.48 ± 0.08	8.65 ± 0.06	8.20 ± 0.04	6
083	NGC 0925	-236+017	0.77	7.36 ± 0.81	1.24 ± 0.25	0.55 ± 0.12	8.61 ± 0.09	8.22 ± 0.05	6
084	NGC 0925	-259+007	0.86	7.09 ± 0.90	1.73 ± 0.39	0.63 ± 0.14	8.66 ± 0.09	8.31 ± 0.06	6
085	NGC 0925	+003-003	0.02	6.43 ± 1.19	0.60 ± 0.26	0.37 ± 0.16	8.69 ± 0.12	8.13 ± 0.12	6
086	NGC 0925	-004-068	0.40	6.93 ± 0.73	2.98 ± 0.50	0.75 ± 0.13	8.70 ± 0.06	8.39 ± 0.04	6
087	NGC 0925	-069+081	0.47	5.64 ± 0.60	0.44 ± 0.11	0.30 ± 0.08	8.77 ± 0.06	8.13 ± 0.08	6
088	NGC 0925	+060-077	0.44	4.56 ± 0.46	0.82 ± 0.18	0.45 ± 0.10	8.89 ± 0.04	8.40 ± 0.05	6
089	NGC 0925	+029+134	0.81	7.84 ± 1.59	3.02 ± 1.00	0.75 ± 0.25	8.60 ± 0.15	8.33 ± 0.10	6
090	NGC 1097	H130+9.0 RING	0.03	0.70 ± 0.08	0.27 ± 0.05	0.21 ± 0.04	9.20 ± 0.01	8.62 ± 0.04	7
091	NGC 1097	H130-9.0 RING	0.03	0.98 ± 0.11	0.25 ± 0.05	0.20 ± 0.04	9.17 ± 0.01	8.57 ± 0.05	7
092	NGC 1097	H130-121.5	0.43	2.53 ± 0.30	0.49 ± 0.13	0.33 ± 0.08	9.05 ± 0.02	8.51 ± 0.06	7
093	NGC 1097	H139+8.2 RING	0.03	0.63 ± 0.07	0.27 ± 0.05	0.21 ± 0.04	9.21 ± 0.01	8.64 ± 0.04	7
094	NGC 1097	H139+49.2	0.18	1.05 ± 0.18	0.44 ± 0.14	0.30 ± 0.09	9.14 ± 0.01	8.66 ± 0.07	7
095	NGC 1097	H139+55.2	0.20	1.28 ± 0.22	0.43 ± 0.14	0.30 ± 0.08	9.13 ± 0.01	8.63 ± 0.08	7
096	NGC 1097	H139+107.9	0.39	1.45 ± 0.25	0.43 ± 0.14	0.30 ± 0.08	9.12 ± 0.01	8.61 ± 0.08	7
097	NGC 1097	H139-9.0	0.03	0.80 ± 0.10	0.20 ± 0.04	0.16 ± 0.03	9.20 ± 0.01	8.56 ± 0.04	7
098	NGC 1097	H139-57.8	0.21	1.61 ± 0.19	0.43 ± 0.11	0.30 ± 0.08	9.11 ± 0.01	8.59 ± 0.06	7
099	NGC 1097	H139-70.8	0.26	1.00 ± 0.19	0.21 ± 0.07	0.17 ± 0.05	9.17 ± 0.01	8.54 ± 0.07	7
100	NGC 1097	H139-100.8	0.37	1.96 ± 0.25	0.15 ± 0.04	0.13 ± 0.03	9.10 ± 0.02	8.35 ± 0.06	7
101	NGC 1097	H139-112.8	0.41	1.76 ± 0.22	0.18 ± 0.05	0.15 ± 0.04	9.12 ± 0.02	8.41 ± 0.06	7
102	NGC 1097	H170+9.0 RING	0.04	0.82 ± 0.09	0.27 ± 0.05	0.22 ± 0.04	9.18 ± 0.01	8.61 ± 0.04	7
103	NGC 1097	H170-9.9 RING	0.04	0.76 ± 0.09	0.22 ± 0.04	0.18 ± 0.03	9.20 ± 0.01	8.58 ± 0.04	7
104	NGC 1097	H170-83.7	0.37	2.69 ± 0.32	0.33 ± 0.09	0.25 ± 0.06	9.04 ± 0.02	8.41 ± 0.07	7
105	NGC 1705	A1	...	7.75 ± 0.53	1.07 ± 0.14	0.52 ± 0.06	8.38 ± 0.05	8.16 ± 0.09	8
106	NGC 1705	A2	0.13	9.87 ± 1.36	1.93 ± 0.51	0.66 ± 0.15	8.42 ± 0.11[a]	8.24 ± 0.08[a]	8
107	NGC 1705	A3	0.22	8.21 ± 0.22	2.23 ± 0.13	0.69 ± 0.03	8.34 ± 0.02	8.08 ± 0.03	8
108	NGC 1705	A4	...	7.54 ± 1.34	2.10 ± 0.78	0.68 ± 0.19	8.29 ± 0.12	8.00 ± 0.20	8
109	NGC 1705	B1	0.19	8.21 ± 0.74	1.05 ± 0.19	0.51 ± 0.08	8.42 ± 0.06	8.18 ± 0.09[a]	8
110	NGC 1705	B2	...	9.65 ± 0.89	1.03 ± 0.19	0.51 ± 0.08	... [b]	... [b]	8
111	NGC 1705	B3	...	9.23 ± 0.23	2.37 ± 0.10	0.70 ± 0.03	8.42 ± 0.02	8.20 ± 0.02[a]	8
112	NGC 1705	B4	...	9.72 ± 0.77	2.11 ± 0.25	0.68 ± 0.09	8.42 ± 0.05[a]	... [b]	8
113	NGC 1705	B5	...	9.99 ± 0.81	1.86 ± 0.28	0.65 ± 0.09	... [b]	... [b]	8
114	NGC 1705	B6	0.22	10.06 ± 0.31	1.31 ± 0.08	0.57 ± 0.03	... [b]	... [b]	8
115	NGC 1705	B7	...	7.18 ± 0.52	1.72 ± 0.24	0.63 ± 0.08	8.28 ± 0.05	7.99 ± 0.07	8
116	NGC 1705	B8	...	7.85 ± 0.98	0.53 ± 0.13	0.35 ± 0.07	8.45 ± 0.09	8.06 ± 0.14[a]	8
117	NGC 1705	C1	...	8.27 ± 0.56	1.06 ± 0.14	0.52 ± 0.06	8.42 ± 0.05	8.18 ± 0.05[a]	8
118	NGC 1705	C2	0.22	8.81 ± 0.61	1.19 ± 0.16	0.54 ± 0.07	8.45 ± 0.05[a]	... [b]	8
119	NGC 1705	C3	...	9.94 ± 0.72	1.44 ± 0.20	0.59 ± 0.07	... [b]	... [b]	8
120	NGC 1705	C4	...	9.71 ± 1.12	1.76 ± 0.39	0.64 ± 0.12	8.43 ± 0.09[a]	... [b]	8
121	NGC 1705	C6	...	8.27 ± 0.20	1.74 ± 0.07	0.63 ± 0.03	8.37 ± 0.02	8.15 ± 0.03	8
122	NGC 2403	-096+035	0.17	5.57 ± 0.17	0.86 ± 0.05	0.46 ± 0.02	8.79 ± 0.02	8.31 ± 0.03	1
123	NGC 2403	-045+055	0.11	3.58 ± 0.12	0.70 ± 0.04	0.41 ± 0.02	8.97 ± 0.01	8.47 ± 0.02	1
124	NGC 2403	-186+045	0.35	4.77 ± 0.14	0.98 ± 0.06	0.49 ± 0.02	8.87 ± 0.01	8.41 ± 0.02	1
125	NGC 2403	+010+032	0.09	4.12 ± 0.13	0.81 ± 0.05	0.45 ± 0.02	8.93 ± 0.01	8.44 ± 0.02	1
126	NGC 2403	-133-146	0.56	7.18 ± 0.19	1.78 ± 0.10	0.64 ± 0.03	8.65 ± 0.02	8.31 ± 0.02	1
127	NGC 2403	+063-049	0.12	2.69 ± 0.24	0.15 ± 0.06	0.13 ± 0.05	9.05 ± 0.02	8.25 ± 0.06	1
128	NGC 2403	+165+136	0.60	6.68 ± 0.21	2.23 ± 0.15	0.69 ± 0.03	8.71 ± 0.02	8.38 ± 0.02	1
129	NGC 2403	+045+069	0.23	4.82 ± 0.49	0.32 ± 0.08	0.24 ± 0.06	8.85 ± 0.04	8.14 ± 0.08	1
130	NGC 2403	-494+137	0.91	6.41 ± 0.47	0.58 ± 0.11	0.37 ± 0.07	8.69 ± 0.05	8.13 ± 0.04	1
131	NGC 2403	VS38	0.09	4.58 ± 0.13	1.08 ± 0.06	0.52 ± 0.02	8.89 ± 0.01	8.45 ± 0.02	9
132	NGC 2403	VS44	0.26	6.12 ± 0.16	1.66 ± 0.09	0.62 ± 0.03	8.76 ± 0.02	8.38 ± 0.02	9
133	NGC 2403	VS9	0.56	7.54 ± 0.24	2.43 ± 0.23	0.71 ± 0.03	8.62 ± 0.03	8.32 ± 0.03	9
134	NGC 2403	+186-177	0.40	8.19 ± 0.17	1.31 ± 0.06	0.57 ± 0.02	8.52 ± 0.02	8.18 ± 0.02[a]	3
135	NGC 2403	+178-203	0.43	4.99 ± 0.09	1.41 ± 0.06	0.59 ± 0.01	8.86 ± 0.01	8.46 ± 0.01	3
136	NGC 2403	+176-211	0.44	4.81 ± 0.23	0.15 ± 0.01	0.13 ± 0.01	8.84 ± 0.02	7.98 ± 0.04	3
137	NGC 2403	+166-229	0.47	6.01 ± 0.17	0.52 ± 0.02	0.34 ± 0.01	8.73 ± 0.02	8.14 ± 0.03	3
138	NGC 2403	+356-195	0.64	7.93 ± 0.16	1.05 ± 0.04	0.51 ± 0.01	8.54 ± 0.02	... [b]	3
139	NGC 2403	+360-190	0.64	5.08 ± 0.16	0.34 ± 0.02	0.25 ± 0.01	8.82 ± 0.02	8.13 ± 0.03	3
140	NGC 2403	+377-163	0.67	6.13 ± 0.14	0.90 ± 0.04	0.47 ± 0.01	8.74 ± 0.01	8.26 ± 0.02	3
141	NGC 2403	+376-106	0.69	6.97 ± 0.13	1.48 ± 0.06	0.60 ± 0.01	8.66 ± 0.01	8.29 ± 0.02	3
142	NGC 2403	-377+104	0.70	5.66 ± 0.14	0.68 ± 0.03	0.41 ± 0.01	8.78 ± 0.02	8.24 ± 0.02	3
143	NGC 2403	-105-218	0.68	3.81 ± 0.14	0.57 ± 0.03	0.36 ± 0.02	8.95 ± 0.01	8.40 ± 0.02	3
144	NGC 2403	-105-224	0.69	4.49 ± 0.16	0.29 ± 0.01	0.23 ± 0.01	8.88 ± 0.02	8.16 ± 0.03	3
145	NGC 2403	-381+082	0.72	6.53 ± 0.17	0.77 ± 0.04	0.43 ± 0.01	8.69 ± 0.02	8.19 ± 0.03	3
146	NGC 2403	+383-056	0.75	6.44 ± 0.15	0.93 ± 0.04	0.48 ± 0.01	8.70 ± 0.02	8.24 ± 0.02	3
147	NGC 2403	-104-256	0.76	5.55 ± 0.18	0.35 ± 0.02	0.26 ± 0.01	8.78 ± 0.02	8.09 ± 0.03	3
148	NGC 2403	-425-002	0.90	5.93 ± 0.16	0.65 ± 0.03	0.39 ± 0.01	8.75 ± 0.02	8.20 ± 0.02	3

TABLE 10 — *Continued*

No. (1)	Galaxy (2)	Region (3)	ρ/ρ_{25} (4)	R_{23} (5)	O_{32} (6)	P (7)	$12+\log(\mathrm{O/H})_{\mathrm{KK04}}$ (8)	$12+\log(\mathrm{O/H})_{\mathrm{PT05}}$ (9)	Ref. (10)
149	NGC 2403	-423-010	0.91	5.71 ± 0.15	0.82 ± 0.04	0.45 ± 0.01	8.78 ± 0.02	8.28 ± 0.02	3
150	NGC 2403	-421-017	0.92	4.94 ± 0.18	0.14 ± 0.01	0.12 ± 0.01	8.83 ± 0.02	7.95 ± 0.03	3
151	NGC 2403	VS35	0.08	4.33 ± 0.43	0.76 ± 0.14	0.43 ± 0.06	8.91 ± 0.04	8.41 ± 0.08	10
152	NGC 2403	VS24	0.09	4.41 ± 0.30	0.82 ± 0.11	0.45 ± 0.05	8.90 ± 0.03	8.41 ± 0.04	10
153	NGC 2403	VS38	0.09	3.35 ± 0.29	0.75 ± 0.12	0.43 ± 0.06	8.99 ± 0.02	8.50 ± 0.05	10
154	NGC 2403	VS21	0.18	4.38 ± 0.63	0.25 ± 0.05	0.20 ± 0.03	8.89 ± 0.07	8.14 ± 0.11	10
155	NGC 2403	VS28	0.19	4.54 ± 0.31	1.48 ± 0.19	0.60 ± 0.07	8.90 ± 0.02	8.50 ± 0.02	10
156	NGC 2403	VS41	0.23	3.98 ± 0.29	1.00 ± 0.15	0.50 ± 0.06	8.94 ± 0.02	8.49 ± 0.04	10
157	NGC 2403	VS44	0.26	5.91 ± 1.15	1.11 ± 0.45	0.53 ± 0.12	8.76 ± 0.12	8.33 ± 0.18	10
158	NGC 2403	VS51	0.33	4.79 ± 0.83	1.10 ± 0.40	0.52 ± 0.10	8.87 ± 0.08	8.43 ± 0.13	10
159	NGC 2403	VS3	0.35	4.93 ± 0.62	1.18 ± 0.31	0.54 ± 0.09	8.86 ± 0.06	8.43 ± 0.09	10
160	NGC 2403	VS49	0.51	5.62 ± 0.43	1.56 ± 0.24	0.61 ± 0.08	8.80 ± 0.04	8.42 ± 0.04	10
161	NGC 2403	VS48	0.51	6.86 ± 0.50	1.72 ± 0.24	0.63 ± 0.08	8.68 ± 0.05	8.33 ± 0.04	10
162	NGC 2403	+010+032	0.09	4.15 ± 0.27	0.81 ± 0.10	0.45 ± 0.04	8.93 ± 0.02	8.44 ± 0.05	4
163	NGC 2403	+063-049	0.12	3.02 ± 0.45	0.17 ± 0.04	0.15 ± 0.03	9.02 ± 0.04	8.23 ± 0.09	4
164	NGC 2403	+045+069	0.23	7.47 ± 0.44	1.07 ± 0.13	0.52 ± 0.04	8.59 ± 0.05	8.18 ± 0.06	4
165	NGC 2403	-133-146	0.56	6.53 ± 0.21	2.67 ± 0.29	0.73 ± 0.03	8.73 ± 0.02	8.41 ± 0.03	4
166	NGC 2403	+165+136	0.60	8.31 ± 0.19	2.56 ± 0.19	0.72 ± 0.02	8.54 ± 0.02	8.27 ± 0.02	4
167	NGC 2403	-494+137	0.91	7.21 ± 0.84	0.75 ± 0.18	0.43 ± 0.10	8.61 ± 0.09	8.12 ± 0.09	4
168	Ho II	H2	0.69	6.01 ± 0.22	7.59 ± 0.57	0.88 ± 0.05	7.99 ± 0.02	7.51 ± 0.02	11
169	Ho II	H3	0.69	6.40 ± 0.22	7.25 ± 0.47	0.88 ± 0.04	8.03 ± 0.02	7.57 ± 0.03	11
170	Ho II	H4	0.69	5.55 ± 0.18	2.00 ± 0.13	0.67 ± 0.03	8.09 ± 0.02	7.72 ± 0.03	11
171	Ho II	H5	0.63	6.65 ± 0.21	2.30 ± 0.16	0.70 ± 0.04	8.19 ± 0.02	7.85 ± 0.03	11
172	Ho II	H7	0.20	6.51 ± 0.20	2.97 ± 0.19	0.75 ± 0.04	8.15 ± 0.02	7.77 ± 0.03	11
173	Ho II	H8	0.18	5.16 ± 0.20	0.76 ± 0.06	0.43 ± 0.03	8.16 ± 0.03	7.73 ± 0.03	11
174	Ho II	H9	0.13	6.79 ± 0.22	1.92 ± 0.13	0.66 ± 0.03	8.23 ± 0.02	7.91 ± 0.03	11
175	Ho II	H11	0.99	5.93 ± 0.18	2.37 ± 0.15	0.70 ± 0.03	8.12 ± 0.02	7.74 ± 0.03	11
176	Ho II	H13	0.60	5.32 ± 0.18	5.92 ± 0.39	0.86 ± 0.04	7.94 ± 0.02	7.47 ± 0.02	11
177	Ho II	H1	0.69	7.87 ± 0.61	0.78 ± 0.12	0.44 ± 0.06	8.42 ± 0.05	8.13 ± 0.06[a]	12
178	Ho II	H2	0.69	5.12 ± 0.33	0.99 ± 0.13	0.50 ± 0.06	8.12 ± 0.04	7.74 ± 0.05	12
179	Ho II	H3	0.69	3.96 ± 0.26	1.14 ± 0.15	0.53 ± 0.06	7.96 ± 0.03	7.55 ± 0.03	12
180	Ho II	H4	0.69	4.29 ± 0.31	0.74 ± 0.11	0.43 ± 0.05	8.05 ± 0.05	7.59 ± 0.05	12
181	Ho II	H5	0.68	5.40 ± 0.32	1.87 ± 0.21	0.65 ± 0.06	8.08 ± 0.03	7.71 ± 0.04	12
182	Ho II	H6	0.65	5.39 ± 0.29	1.10 ± 0.12	0.52 ± 0.05	8.14 ± 0.03	7.77 ± 0.05	12
183	Ho II	H7	0.65	5.17 ± 0.28	1.20 ± 0.13	0.55 ± 0.05	8.11 ± 0.03	7.73 ± 0.04	12
184	Ho II	H8	0.65	5.03 ± 0.27	1.32 ± 0.14	0.57 ± 0.05	8.08 ± 0.03	7.70 ± 0.04	12
185	Ho II	H9	0.63	5.40 ± 0.34	2.77 ± 0.32	0.73 ± 0.08	8.04 ± 0.03	7.63 ± 0.04	12
186	Ho II	AA	···	6.88 ± 0.11	1.87 ± 0.08	0.65 ± 0.01	8.24 ± 0.01	7.92 ± 0.02	13
187	Ho II	AA1	···	7.71 ± 0.17	2.69 ± 0.14	0.73 ± 0.02	8.28 ± 0.02	7.96 ± 0.03	13
188	Ho II	AS	···	6.85 ± 0.11	1.92 ± 0.08	0.66 ± 0.01	8.23 ± 0.01	7.92 ± 0.02	13
189	DDO 053	H3	0.87	5.42 ± 0.34	4.59 ± 0.53	0.82 ± 0.08	7.98 ± 0.04	7.53 ± 0.04	11
190	DDO 053	H4	0.65	3.24 ± 0.19	2.55 ± 0.30	0.72 ± 0.07	7.76 ± 0.03	7.36 ± 0.03	11
191	DDO 053	H5	0.02	6.22 ± 0.44	21.37 ± 2.49	0.96 ± 0.10	7.88 ± 0.04	7.43 ± 0.04	11
192	DDO 053	No.1	···	6.50 ± 0.23	0.75 ± 0.05	0.43 ± 0.03	8.30 ± 0.03	7.96 ± 0.04	14
193	NGC 2841	HK27	0.61	1.56 ± 0.17	0.16 ± 0.07	0.14 ± 0.06	9.13 ± 0.02	8.42 ± 0.07	1
194	NGC 2841	HK51	0.41	0.79 ± 0.15	0.23 ± 0.13	0.19 ± 0.10	9.19 ± 0.03	8.59 ± 0.09	1
195	NGC 2841	HK52	0.37	0.48 ± 0.09	0.12 ± 0.12	0.10 ± 0.10	9.28 ± 0.04	8.53 ± 0.09	1
196	NGC 2841	HK62	0.47	0.96 ± 0.08	0.10 ± 0.03	0.09 ± 0.03	9.19 ± 0.01	8.44 ± 0.04	1
197	NGC 2841	-042+086	0.41	0.81 ± 0.18	0.29 ± 0.18	0.22 ± 0.14	9.18 ± 0.03	8.62 ± 0.11	15
198	NGC 2915	H1	···	10.74 ± 1.29	0.63 ± 0.15	0.39 ± 0.08	···[b]	···[b]	16
199	NGC 2915	H1	···	6.82 ± 1.19	0.55 ± 0.17	0.35 ± 0.09	8.36 ± 0.12	7.98 ± 0.20	16
200	Ho I	H1	···	6.23 ± 0.23	7.40 ± 0.53	0.88 ± 0.05	8.01 ± 0.02	7.55 ± 0.02	11
201	Ho I	H3	···	5.26 ± 0.21	2.39 ± 0.24	0.71 ± 0.04	8.04 ± 0.03	7.64 ± 0.04	11
202	Ho I	H5	···	6.05 ± 0.20	2.95 ± 0.20	0.75 ± 0.04	8.10 ± 0.02	7.71 ± 0.03	11
203	Ho I	MH25	···	5.97 ± 1.38	6.46 ± 8.94	0.87 ± 0.24	8.00 ± 0.21	7.54 ± 0.36	17
204	NGC 3049	0952+095	···	1.69 ± 0.03	0.34 ± 0.01	0.25 ± 0.01	9.11 ± 0.01	8.54 ± 0.01	18
205	NGC 3031	GS1	0.39	3.50 ± 0.29	0.41 ± 0.06	0.29 ± 0.04	8.98 ± 0.02	8.35 ± 0.06	1
206	NGC 3031	GS2	0.34	3.83 ± 0.40	0.46 ± 0.08	0.32 ± 0.04	8.95 ± 0.03	8.35 ± 0.07	1
207	NGC 3031	GS4	0.63	5.91 ± 0.30	0.74 ± 0.07	0.43 ± 0.03	8.75 ± 0.04	8.24 ± 0.05	1
208	NGC 3031	GS7	0.66	4.46 ± 0.29	0.31 ± 0.04	0.24 ± 0.03	8.89 ± 0.03	8.18 ± 0.05	1
209	NGC 3031	GS9	0.46	3.11 ± 0.24	0.40 ± 0.06	0.29 ± 0.04	9.01 ± 0.02	8.40 ± 0.05	1
210	NGC 3031	GS11	0.39	3.50 ± 0.25	0.83 ± 0.11	0.45 ± 0.05	8.98 ± 0.02	8.51 ± 0.04	1
211	NGC 3031	GS12	0.35	4.05 ± 0.43	0.21 ± 0.06	0.18 ± 0.05	8.92 ± 0.04	8.14 ± 0.08	1
212	NGC 3031	GS13	0.35	1.87 ± 0.40	0.35 ± 0.18	0.26 ± 0.13	9.10 ± 0.03	8.52 ± 0.11	1
213	NGC 3031	Muench18	0.69	5.71 ± 0.35	2.66 ± 0.54	0.73 ± 0.05	8.81 ± 0.04	8.48 ± 0.04	1
214	NGC 3031	+107-291	0.39	3.12 ± 0.15	0.60 ± 0.06	0.38 ± 0.03	9.01 ± 0.01	8.48 ± 0.03	15
215	NGC 3031	HK472	0.29	2.37 ± 0.53	0.25 ± 0.11	0.20 ± 0.08	9.07 ± 0.03	8.39 ± 0.13	19
216	NGC 3031	HK230	0.35	1.94 ± 0.25	0.49 ± 0.16	0.33 ± 0.11	9.09 ± 0.02	8.58 ± 0.05	19
217	NGC 3031	HK152	0.40	2.94 ± 0.30	0.38 ± 0.08	0.28 ± 0.05	9.02 ± 0.02	8.41 ± 0.06	19
218	NGC 3031	HK343-50	0.34	3.55 ± 0.28	0.52 ± 0.08	0.34 ± 0.04	8.97 ± 0.02	8.40 ± 0.05	19
219	NGC 3031	HK453	0.35	3.72 ± 0.30	0.24 ± 0.06	0.19 ± 0.05	8.96 ± 0.03	8.21 ± 0.06	19
220	NGC 3031	HK305-12	0.36	3.59 ± 0.21	0.77 ± 0.09	0.43 ± 0.05	8.97 ± 0.02	8.48 ± 0.03	19
221	NGC 3031	HK268	0.39	2.91 ± 0.20	0.53 ± 0.07	0.35 ± 0.04	9.02 ± 0.01	8.48 ± 0.04	19
222	NGC 3031	HK500-9	0.39	3.10 ± 0.19	1.05 ± 0.13	0.51 ± 0.05	9.01 ± 0.01	8.59 ± 0.03	19
223	NGC 3031	HK652	0.46	2.84 ± 0.17	0.49 ± 0.06	0.33 ± 0.04	9.03 ± 0.01	8.47 ± 0.03	19

TABLE 10 — *Continued*

No. (1)	Galaxy (2)	Region (3)	ρ/ρ_{25} (4)	R_{23} (5)	O_{32} (6)	P (7)	$12+\log(\mathrm{O/H})_{\mathrm{KK04}}$ (8)	$12+\log(\mathrm{O/H})_{\mathrm{PT05}}$ (9)	Ref. (10)
224	NGC 3031	HK712	0.51	4.52 ± 0.26	1.83 ± 0.21	0.65 ± 0.06	8.91 ± 0.02	8.53 ± 0.02	19
225	NGC 3031	HK666-72	0.50	4.97 ± 0.31	0.89 ± 0.11	0.47 ± 0.04	8.85 ± 0.03	8.37 ± 0.05	19
226	NGC 3031	HK767	0.63	5.61 ± 0.23	0.84 ± 0.07	0.46 ± 0.04	8.79 ± 0.02	8.30 ± 0.02	19
227	NGC 3031	HK741-4	0.66	3.91 ± 0.18	0.38 ± 0.04	0.28 ± 0.03	8.94 ± 0.02	8.29 ± 0.03	19
228	NGC 3031	HK105	0.67	4.63 ± 0.56	0.15 ± 0.05	0.13 ± 0.04	8.86 ± 0.06	7.99 ± 0.09	19
229	NGC 3031	MUNCH18	0.69	5.76 ± 0.27	2.62 ± 0.38	0.72 ± 0.04	8.81 ± 0.03	8.47 ± 0.03	19
230	NGC 3031	HK537	0.76	4.59 ± 0.58	0.35 ± 0.10	0.26 ± 0.07	8.88 ± 0.06	8.20 ± 0.10	19
231	NGC 3031	HK74	0.61	4.71 ± 0.35	0.56 ± 0.08	0.36 ± 0.04	8.87 ± 0.04	8.29 ± 0.06	20
232	NGC 3031	HK169	0.39	3.60 ± 0.29	0.29 ± 0.04	0.23 ± 0.03	8.97 ± 0.03	8.27 ± 0.06	20
233	NGC 3031	HK305	0.36	3.50 ± 0.25	1.24 ± 0.18	0.55 ± 0.07	8.98 ± 0.02	8.57 ± 0.03	20
234	NGC 3031	HK361	0.30	4.19 ± 0.32	0.40 ± 0.06	0.28 ± 0.04	8.92 ± 0.03	8.27 ± 0.06	20
235	NGC 3031	HK385	0.32	3.05 ± 0.22	0.69 ± 0.10	0.41 ± 0.05	9.01 ± 0.01	8.52 ± 0.04	20
236	NGC 3031	HK453	0.35	4.01 ± 0.31	0.41 ± 0.06	0.29 ± 0.04	8.93 ± 0.03	8.30 ± 0.05	20
237	NGC 3031	HK740	0.60	3.90 ± 0.29	0.50 ± 0.07	0.33 ± 0.04	8.94 ± 0.03	8.36 ± 0.05	20
238	NGC 3031	HK744	0.65	4.38 ± 0.32	0.53 ± 0.08	0.35 ± 0.04	8.90 ± 0.03	8.32 ± 0.05	20
239	NGC 3031	HK755	0.64	4.76 ± 0.35	0.53 ± 0.07	0.34 ± 0.04	8.86 ± 0.04	8.28 ± 0.06	20
240	NGC 3031	SB84 A	0.49	5.62 ± 0.43	2.27 ± 0.32	0.69 ± 0.09	8.81 ± 0.04	8.47 ± 0.03	20
241	Ho IX	H3	···	3.08 ± 0.16	0.17 ± 0.01	0.14 ± 0.01	9.01 ± 0.01	8.22 ± 0.03	11
242	Ho IX	H12	···	3.88 ± 0.29	0.12 ± 0.02	0.11 ± 0.02	8.94 ± 0.03	8.06 ± 0.05	11
243	M 81 Dw B	MH1	0.61	6.69 ± 0.89	2.34 ± 0.64	0.70 ± 0.15	8.20 ± 0.10	7.85 ± 0.14	17
244	NGC 3184	-058-007	0.28	0.50 ± 0.02	0.27 ± 0.03	0.22 ± 0.02	9.24 ± 0.01	8.66 ± 0.02	3
245	NGC 3184	-064-006	0.30	0.82 ± 0.05	0.30 ± 0.04	0.23 ± 0.03	9.18 ± 0.01	8.63 ± 0.03	3
246	NGC 3184	-080-005	0.38	0.91 ± 0.03	0.32 ± 0.02	0.25 ± 0.01	9.17 ± 0.01	8.63 ± 0.01	3
247	NGC 3184	+085-004	0.40	1.20 ± 0.06	0.23 ± 0.03	0.18 ± 0.02	9.15 ± 0.01	8.53 ± 0.02	3
248	NGC 3184	+079+035	0.41	0.87 ± 0.04	0.17 ± 0.02	0.15 ± 0.01	9.19 ± 0.01	8.53 ± 0.02	3
249	NGC 3184	+059-079	0.44	1.40 ± 0.05	0.16 ± 0.01	0.14 ± 0.01	9.14 ± 0.01	8.44 ± 0.01	3
250	NGC 3184	+074+064	0.47	1.49 ± 0.07	0.35 ± 0.03	0.26 ± 0.02	9.12 ± 0.01	8.57 ± 0.02	3
251	NGC 3184	+092-093	0.59	1.81 ± 0.07	0.12 ± 0.01	0.11 ± 0.01	9.12 ± 0.01	8.34 ± 0.02	3
252	NGC 3184	+005+135	0.63	3.67 ± 0.11	0.40 ± 0.02	0.29 ± 0.01	8.96 ± 0.01	8.33 ± 0.02	3
253	NGC 3184	-002+136	0.63	1.80 ± 0.12	0.11 ± 0.02	0.10 ± 0.02	9.12 ± 0.01	8.32 ± 0.03	3
254	NGC 3184	-017+137	0.64	2.04 ± 0.07	0.21 ± 0.01	0.17 ± 0.01	9.09 ± 0.01	8.40 ± 0.02	3
255	NGC 3184	+111-102	0.68	5.03 ± 0.49	0.28 ± 0.04	0.22 ± 0.03	8.83 ± 0.05	8.08 ± 0.09	3
256	NGC 3184	-119-121	0.82	2.60 ± 0.12	0.13 ± 0.01	0.12 ± 0.01	9.06 ± 0.01	8.24 ± 0.03	3
257	NGC 3184	-113-127	0.82	5.59 ± 0.11	2.04 ± 0.11	0.67 ± 0.02	8.81 ± 0.01	8.46 ± 0.01	3
258	NGC 3184	-101-137	0.82	3.55 ± 0.13	0.51 ± 0.03	0.34 ± 0.02	8.97 ± 0.01	8.40 ± 0.03	3
259	NGC 3184	-110-130	0.82	3.58 ± 0.15	0.33 ± 0.02	0.25 ± 0.01	8.97 ± 0.01	8.30 ± 0.03	3
260	NGC 3184	-095-142	0.82	4.58 ± 0.12	0.86 ± 0.04	0.46 ± 0.01	8.89 ± 0.01	8.41 ± 0.02	3
261	NGC 3184	+106-020	0.50	1.76 ± 0.23	0.15 ± 0.06	0.13 ± 0.05	9.12 ± 0.02	8.38 ± 0.07	6
262	NGC 3184	+106-020	0.50	2.27 ± 0.23	0.09 ± 0.02	0.08 ± 0.02	9.09 ± 0.02	8.24 ± 0.05	6
263	NGC 3184	+000+068	0.32	0.97 ± 0.11	0.23 ± 0.08	0.19 ± 0.06	9.17 ± 0.02	8.56 ± 0.05	6
264	NGC 3184	-008+073	0.34	1.66 ± 0.23	0.27 ± 0.10	0.21 ± 0.08	9.12 ± 0.02	8.49 ± 0.07	6
265	NGC 3184	-020-097	0.47	2.13 ± 0.26	0.25 ± 0.11	0.20 ± 0.09	9.08 ± 0.02	8.42 ± 0.07	6
266	NGC 3184	-011+078	0.36	1.56 ± 0.21	0.23 ± 0.09	0.19 ± 0.07	9.13 ± 0.02	8.48 ± 0.07	6
267	NGC 3184	-012-089	0.42	1.66 ± 0.29	0.11 ± 0.05	0.10 ± 0.04	9.13 ± 0.02	8.35 ± 0.07	6
268	NGC 3184	-059-041	0.35	0.89 ± 0.09	0.19 ± 0.05	0.16 ± 0.04	9.19 ± 0.01	8.54 ± 0.04	6
269	NGC 3184	-075-087	0.56	1.75 ± 0.19	0.46 ± 0.10	0.31 ± 0.06	9.10 ± 0.01	8.59 ± 0.05	6
270	NGC 3184	-172-041	0.84	5.93 ± 0.53	0.92 ± 0.17	0.48 ± 0.09	8.76 ± 0.05	8.29 ± 0.04	6
271	NGC 3184	-067-039	0.37	0.97 ± 0.07	0.12 ± 0.03	0.11 ± 0.02	9.19 ± 0.01	8.47 ± 0.03	4
272	NGC 3184	-020-095	0.46	2.01 ± 0.22	0.32 ± 0.07	0.24 ± 0.04	9.09 ± 0.01	8.49 ± 0.05	4
273	NGC 3184	-077+093	0.54	4.05 ± 0.66	0.16 ± 0.04	0.14 ± 0.03	8.92 ± 0.06	8.09 ± 0.12	4
274	NGC 3184	+070+091	0.55	2.46 ± 0.32	0.30 ± 0.06	0.23 ± 0.04	9.06 ± 0.02	8.41 ± 0.08	4
275	NGC 3184	+073-147	0.74	3.31 ± 0.41	0.45 ± 0.08	0.31 ± 0.04	8.99 ± 0.03	8.40 ± 0.09	4
276	NGC 3198	-066-111	0.52	6.20 ± 0.90	0.80 ± 0.25	0.45 ± 0.14	8.73 ± 0.10	8.23 ± 0.08	6
277	NGC 3198	-089-110	0.56	5.45 ± 0.60	0.96 ± 0.21	0.49 ± 0.11	8.81 ± 0.05	8.34 ± 0.04	6
278	NGC 3198	-041-045	0.25	3.95 ± 0.42	0.57 ± 0.15	0.36 ± 0.10	8.94 ± 0.03	8.38 ± 0.05	6
279	NGC 3198	-040-009	0.34	5.54 ± 0.72	0.75 ± 0.21	0.43 ± 0.11	8.79 ± 0.07	8.28 ± 0.08	6
280	NGC 3198	-060-007	0.54	7.40 ± 1.80	1.39 ± 0.61	0.58 ± 0.27	8.61 ± 0.16	8.24 ± 0.10	6
281	NGC 3198	+030-030	0.48	5.42 ± 0.49	1.11 ± 0.19	0.53 ± 0.10	8.81 ± 0.04	8.38 ± 0.03	6
282	NGC 3198	+071+046	0.48	4.04 ± 0.27	0.49 ± 0.08	0.33 ± 0.06	8.93 ± 0.02	8.33 ± 0.04	6
283	NGC 3198	+038+044	0.24	2.13 ± 0.33	0.20 ± 0.09	0.16 ± 0.08	9.09 ± 0.02	8.37 ± 0.09	6
284	NGC 3198	+083+150	0.70	6.18 ± 0.50	0.63 ± 0.11	0.39 ± 0.07	8.72 ± 0.05	8.17 ± 0.06	6
285	NGC 3198	+093+152	0.71	5.23 ± 0.66	0.59 ± 0.19	0.37 ± 0.12	8.82 ± 0.06	8.26 ± 0.06	6
286	NGC 3198	+009+113	0.76	8.34 ± 1.03	1.35 ± 0.30	0.57 ± 0.14	8.51 ± 0.10	8.19 ± 0.08[a]	6
287	NGC 3198	+016+118	0.75	6.55 ± 0.66	0.26 ± 0.09	0.21 ± 0.07	8.66 ± 0.07	7.89 ± 0.09	6
288	NGC 3198	+026+126	0.75	8.97 ± 1.41	1.27 ± 0.37	0.56 ± 0.17	8.45 ± 0.11[a]	8.21 ± 0.11[a]	6
289	NGC 3198	+036+131	0.73	6.77 ± 0.79	0.84 ± 0.21	0.46 ± 0.12	8.66 ± 0.08	8.19 ± 0.06	6
290	IC 2574	H1	0.69	7.04 ± 0.45	5.12 ± 0.59	0.84 ± 0.08	8.14 ± 0.04	7.71 ± 0.05	11
291	IC 2574	H2	0.81	5.48 ± 0.32	1.91 ± 0.22	0.66 ± 0.06	8.09 ± 0.04	7.72 ± 0.05	11
292	IC 2574	H3	0.74	7.33 ± 0.48	5.87 ± 0.68	0.85 ± 0.08	8.15 ± 0.04	7.72 ± 0.05	11
293	IC 2574	H5	0.85	7.56 ± 0.47	4.21 ± 0.49	0.81 ± 0.08	8.21 ± 0.04	7.82 ± 0.06	11
294	IC 2574	H6	0.88	7.01 ± 0.43	3.66 ± 0.43	0.79 ± 0.08	8.18 ± 0.04	7.78 ± 0.05	11
295	IC 2574	H8	0.92	6.80 ± 0.43	4.40 ± 0.51	0.81 ± 0.08	8.14 ± 0.04	7.72 ± 0.05	11
296	IC 2574	H9	0.83	6.03 ± 0.37	3.28 ± 0.40	0.77 ± 0.07	8.09 ± 0.04	7.68 ± 0.05	11
297	IC 2574	H10	0.90	6.33 ± 0.39	3.58 ± 0.43	0.78 ± 0.08	8.11 ± 0.04	7.70 ± 0.05	11
298	IC 2574	H11	0.98	5.66 ± 0.33	1.65 ± 0.20	0.62 ± 0.06	8.13 ± 0.04	7.77 ± 0.05	11
299	IC 2574	H13	0.95	6.20 ± 0.39	3.98 ± 0.46	0.80 ± 0.08	8.09 ± 0.03	7.66 ± 0.04	11

TABLE 10 — *Continued*

No. (1)	Galaxy (2)	Region (3)	ρ/ρ_{25} (4)	R_{23} (5)	O_{32} (6)	P (7)	$12+\log(\mathrm{O/H})_{\mathrm{KK04}}$ (8)	$12+\log(\mathrm{O/H})_{\mathrm{PT05}}$ (9)	Ref. (10)
300	IC 2574	MH167	0.91	7.93 ± 0.98	5.01 ± 1.19	0.83 ± 0.16	8.23 ± 0.08	7.83 ± 0.12	17
301	IC 2574	MH198	0.85	7.59 ± 0.87	1.71 ± 0.40	0.63 ± 0.12	8.31 ± 0.08	8.05 ± 0.15	17
302	IC 2574	MH242	0.82	6.75 ± 0.77	1.64 ± 0.39	0.62 ± 0.11	8.24 ± 0.08	7.93 ± 0.12	17
303	IC 2574	IIA	···	7.10 ± 0.18	1.76 ± 0.10	0.64 ± 0.02	8.27 ± 0.02	7.97 ± 0.03	13
304	IC 2574	IIS	···	7.14 ± 0.16	2.03 ± 0.11	0.67 ± 0.02	8.25 ± 0.02	7.94 ± 0.03	13
305	IC 2574	IIAA	···	7.87 ± 0.26	2.04 ± 0.15	0.67 ± 0.03	8.32 ± 0.02	8.05 ± 0.05	13
306	IC 2574	IIAB	···	7.41 ± 0.12	2.30 ± 0.10	0.70 ± 0.02	8.27 ± 0.01	7.95 ± 0.03	13
307	IC 2574	IIIA	···	7.49 ± 0.27	1.14 ± 0.08	0.53 ± 0.03	8.35 ± 0.03	8.11 ± 0.05	13
308	IC 2574	IIIB	···	8.67 ± 0.41	1.23 ± 0.12	0.55 ± 0.04	8.44 ± 0.04	··· [b]	13
309	IC 2574	IIIC	···	7.66 ± 0.57	0.41 ± 0.06	0.29 ± 0.04	8.46 ± 0.05	··· [b]	13
310	IC 2574	IIIS	···	7.71 ± 0.25	0.94 ± 0.06	0.49 ± 0.02	8.39 ± 0.03	8.15 ± 0.04[a]	13
311	Mrk 33	H1	···	6.01 ± 1.34	0.55 ± 0.22	0.35 ± 0.12	8.74 ± 0.14	8.15 ± 0.20	21
312	NGC 3351	R1	0.03	0.59 ± 0.05	0.29 ± 0.03	0.23 ± 0.02	9.22 ± 0.01	8.65 ± 0.03	22
313	NGC 3351	R2	0.02	0.41 ± 0.02	0.78 ± 0.09	0.44 ± 0.03	9.23 ± 0.01	8.83 ± 0.02	22
314	NGC 3351	R3	0.03	0.44 ± 0.03	0.31 ± 0.04	0.24 ± 0.02	9.25 ± 0.01	8.69 ± 0.02	22
315	NGC 3351	R4	0.02	0.38 ± 0.03	0.39 ± 0.06	0.28 ± 0.04	9.27 ± 0.01	8.73 ± 0.03	22
316	NGC 3351	R5	0.03	1.04 ± 0.08	0.99 ± 0.15	0.50 ± 0.06	9.12 ± 0.01	8.79 ± 0.02	22
317	NGC 3351	H34	0.31	0.49 ± 0.02	0.25 ± 0.02	0.20 ± 0.01	9.25 ± 0.01	8.64 ± 0.01	23
318	NGC 3351	H19	0.33	0.42 ± 0.02	0.23 ± 0.02	0.18 ± 0.01	9.27 ± 0.01	8.63 ± 0.01	23
319	NGC 3351	PR2	0.02	0.65 ± 0.03	0.33 ± 0.02	0.25 ± 0.02	9.20 ± 0.01	8.67 ± 0.01	23
320	NGC 3351	PR3	0.03	0.46 ± 0.02	0.25 ± 0.02	0.20 ± 0.01	9.25 ± 0.01	8.64 ± 0.01	23
321	NGC 3351	PR7	0.03	0.41 ± 0.02	0.37 ± 0.03	0.27 ± 0.02	9.26 ± 0.01	8.72 ± 0.01	23
322	NGC 3351	PR1	0.03	0.56 ± 0.02	0.28 ± 0.02	0.22 ± 0.01	9.23 ± 0.01	8.65 ± 0.01	23
323	NGC 3351	HK45	0.31	0.42 ± 0.05	0.31 ± 0.10	0.24 ± 0.07	9.26 ± 0.03	8.69 ± 0.05	1
324	NGC 3351	HK80	0.67	1.27 ± 0.06	0.22 ± 0.02	0.18 ± 0.02	9.15 ± 0.01	8.51 ± 0.02	1
325	NGC 3351	HK101	0.58	0.67 ± 0.05	0.20 ± 0.04	0.16 ± 0.03	9.22 ± 0.01	8.58 ± 0.03	1
326	NGC 3351	HK109	0.74	1.69 ± 0.07	0.23 ± 0.02	0.19 ± 0.01	9.12 ± 0.01	8.47 ± 0.02	1
327	NGC 3351	+029-192	0.95	3.21 ± 0.14	0.41 ± 0.03	0.29 ± 0.02	9.00 ± 0.01	8.39 ± 0.03	1
328	NGC 3351	+023+067	0.32	0.42 ± 0.16	0.33 ± 0.32	0.25 ± 0.23	9.26 ± 0.05	8.70 ± 0.12	15
329	NGC 3351	+000+068	0.32	0.51 ± 0.17	0.22 ± 0.24	0.18 ± 0.19	9.25 ± 0.05	8.62 ± 0.11	15
330	NGC 3351	HK80	0.67	1.22 ± 0.13	0.28 ± 0.08	0.22 ± 0.07	9.14 ± 0.01	8.56 ± 0.06	15
331	NGC 3351	HK101	0.58	0.75 ± 0.13	0.19 ± 0.12	0.16 ± 0.10	9.20 ± 0.03	8.56 ± 0.09	15
332	NGC 3351	HK109	0.74	1.42 ± 0.13	0.27 ± 0.07	0.21 ± 0.06	9.13 ± 0.01	8.53 ± 0.04	15
333	NGC 3351	-001+006	0.03	0.49 ± 0.13	0.12 ± 0.18	0.11 ± 0.16	9.27 ± 0.04	8.53 ± 0.10	15
334	NGC 3351	-004-006	0.03	0.42 ± 0.05	0.26 ± 0.07	0.21 ± 0.05	9.27 ± 0.02	8.66 ± 0.05	4
335	NGC 3351	-088-026	0.58	0.59 ± 0.19	0.40 ± 0.23	0.28 ± 0.15	9.20 ± 0.03	8.71 ± 0.11	4
336	NGC 3351	-058-135	0.67	1.16 ± 0.13	0.24 ± 0.04	0.20 ± 0.02	9.15 ± 0.01	8.54 ± 0.04	4
337	NGC 3521	+013+097	0.39	2.99 ± 0.38	0.58 ± 0.18	0.37 ± 0.11	9.02 ± 0.03	8.49 ± 0.05	1
338	NGC 3521	-005+080	0.27	1.39 ± 0.17	0.17 ± 0.06	0.14 ± 0.05	9.14 ± 0.01	8.45 ± 0.06	1
339	NGC 3521	-048+047	0.29	2.57 ± 0.23	0.17 ± 0.04	0.14 ± 0.04	9.06 ± 0.02	8.29 ± 0.05	1
340	NGC 3521	+013+097	0.39	3.35 ± 0.46	0.77 ± 0.23	0.44 ± 0.14	8.99 ± 0.03	8.51 ± 0.05	6
341	NGC 3521	-005+080	0.27	1.46 ± 0.18	0.23 ± 0.08	0.18 ± 0.07	9.13 ± 0.02	8.49 ± 0.06	6
342	NGC 3521	-048+047	0.29	2.70 ± 0.24	0.23 ± 0.06	0.19 ± 0.04	9.04 ± 0.02	8.33 ± 0.06	6
343	NGC 3521	-048+043	0.29	2.88 ± 0.37	0.43 ± 0.13	0.30 ± 0.09	9.03 ± 0.03	8.44 ± 0.07	6
344	NGC 3521	-010-025	0.13	1.88 ± 0.25	0.06 ± 0.02	0.06 ± 0.02	9.12 ± 0.02	8.25 ± 0.05	6
345	NGC 3521	+040-035	0.24	1.47 ± 0.11	0.20 ± 0.04	0.16 ± 0.04	9.13 ± 0.01	8.46 ± 0.04	6
346	NGC 3521	+034-097	0.31	2.92 ± 0.35	0.14 ± 0.06	0.12 ± 0.05	9.03 ± 0.03	8.20 ± 0.08	6
347	NGC 3521	-033-118	0.56	8.22 ± 1.03	1.01 ± 0.25	0.50 ± 0.13	8.51 ± 0.10	8.17 ± 0.08[a]	6
348	NGC 3521	+062-170	0.55	4.96 ± 0.75	0.43 ± 0.16	0.30 ± 0.11	8.84 ± 0.07	8.20 ± 0.11	6
349	NGC 3521	-048+031	0.29	1.72 ± 0.32	0.12 ± 0.05	0.11 ± 0.04	9.12 ± 0.02	8.36 ± 0.08	6
350	NGC 3621	P1A2	0.32	6.98 ± 0.47	0.63 ± 0.08	0.39 ± 0.04	8.63 ± 0.06	8.09 ± 0.07	24
351	NGC 3621	P1A3	0.19	4.62 ± 0.38	0.24 ± 0.03	0.19 ± 0.02	8.87 ± 0.04	8.10 ± 0.07	24
352	NGC 3621	P1A4	0.21	4.14 ± 0.28	0.59 ± 0.07	0.37 ± 0.04	8.92 ± 0.03	8.37 ± 0.05	24
353	NGC 3621	P1A6	0.12	2.48 ± 0.23	0.25 ± 0.06	0.20 ± 0.05	9.06 ± 0.02	8.38 ± 0.05	24
354	NGC 3621	P1A7	0.19	3.74 ± 0.30	0.31 ± 0.04	0.24 ± 0.03	8.96 ± 0.03	8.26 ± 0.06	24
355	NGC 3621	P1A8	0.19	2.96 ± 0.30	0.42 ± 0.11	0.29 ± 0.08	9.02 ± 0.02	8.42 ± 0.05	24
356	NGC 3621	P1A9	0.35	6.13 ± 0.39	0.87 ± 0.11	0.47 ± 0.04	8.73 ± 0.04	8.26 ± 0.06	24
357	NGC 3621	P2A1	0.39	5.09 ± 0.39	0.34 ± 0.04	0.25 ± 0.03	8.82 ± 0.05	8.13 ± 0.06	24
358	NGC 3621	P2A2	0.23	4.63 ± 0.35	0.37 ± 0.05	0.27 ± 0.03	8.87 ± 0.04	8.20 ± 0.07	24
359	NGC 3621	P2A3	0.16	5.38 ± 0.51	0.26 ± 0.07	0.21 ± 0.05	8.79 ± 0.05	8.03 ± 0.07	24
360	NGC 3621	P2A6	0.09	1.28 ± 0.31	0.28 ± 0.11	0.22 ± 0.08	9.14 ± 0.02	8.55 ± 0.11	24
361	NGC 3621	P2A7	0.26	4.18 ± 0.28	0.60 ± 0.07	0.38 ± 0.04	8.92 ± 0.03	8.37 ± 0.05	24
362	NGC 3621	S1A3	0.19	3.28 ± 0.26	0.33 ± 0.04	0.25 ± 0.03	9.00 ± 0.02	8.33 ± 0.05	24
363	NGC 3621	S1A4	0.39	5.63 ± 0.33	1.51 ± 0.18	0.60 ± 0.06	8.80 ± 0.03	8.41 ± 0.03	24
364	NGC 3621	S2A1	0.39	5.30 ± 0.42	0.28 ± 0.03	0.22 ± 0.02	8.80 ± 0.04	8.06 ± 0.07	24
365	NGC 3621	S2A2	0.23	4.21 ± 0.34	0.28 ± 0.03	0.22 ± 0.02	8.91 ± 0.03	8.19 ± 0.07	24
366	NGC 3621	S2A3	0.10	2.19 ± 0.19	0.13 ± 0.02	0.11 ± 0.02	9.09 ± 0.01	8.30 ± 0.04	24
367	NGC 3621	S2A4	0.19	3.58 ± 0.34	0.17 ± 0.05	0.15 ± 0.04	8.97 ± 0.03	8.16 ± 0.06	24
368	NGC 3621	S3A1	0.66	6.97 ± 0.45	0.79 ± 0.10	0.44 ± 0.04	8.64 ± 0.05	8.15 ± 0.07	24
369	NGC 3621	S3A2	0.65	8.53 ± 0.57	0.69 ± 0.09	0.41 ± 0.04	8.47 ± 0.06[a]	··· [b]	24
370	NGC 3621	S4A2	0.39	7.98 ± 0.48	1.20 ± 0.15	0.55 ± 0.05	8.54 ± 0.05	8.17 ± 0.06[a]	24
371	NGC 3621	S5A1	0.22	2.64 ± 0.19	0.43 ± 0.05	0.30 ± 0.03	9.04 ± 0.01	8.47 ± 0.04	24
372	NGC 3621	S5A2	0.20	4.96 ± 0.33	0.65 ± 0.08	0.39 ± 0.04	8.85 ± 0.03	8.30 ± 0.06	24
373	NGC 3621	S5A3	0.21	3.88 ± 0.27	0.53 ± 0.07	0.35 ± 0.04	8.95 ± 0.02	8.37 ± 0.05	24
374	NGC 3621	+025+068	0.28	3.03 ± 0.20	0.46 ± 0.07	0.32 ± 0.05	9.02 ± 0.02	8.44 ± 0.04	6

TABLE 10 — *Continued*

No. (1)	Galaxy (2)	Region (3)	ρ/ρ_{25} (4)	R_{23} (5)	O_{32} (6)	P (7)	$12+\log(\mathrm{O/H})_{\mathrm{KK04}}$ (8)	$12+\log(\mathrm{O/H})_{\mathrm{PT05}}$ (9)	Ref. (10)
375	NGC 3621	-010+095	0.28	2.45 ± 0.27	0.48 ± 0.12	0.32 ± 0.08	9.06 ± 0.02	8.51 ± 0.06	6
376	NGC 3621	+061-015	0.27	4.91 ± 0.41	0.55 ± 0.11	0.36 ± 0.07	8.85 ± 0.04	8.27 ± 0.05	6
377	NGC 3621	+026-037	0.13	2.04 ± 0.21	0.14 ± 0.05	0.12 ± 0.05	9.10 ± 0.02	8.33 ± 0.06	6
378	NGC 3621	+067-058	0.30	3.69 ± 0.27	0.20 ± 0.04	0.17 ± 0.03	8.96 ± 0.03	8.18 ± 0.05	6
379	NGC 3621	+029-018	0.13	3.23 ± 0.28	0.23 ± 0.07	0.19 ± 0.06	9.00 ± 0.03	8.26 ± 0.06	6
380	NGC 3621	+091-068	0.40	4.97 ± 0.68	1.10 ± 0.29	0.52 ± 0.15	8.86 ± 0.06	8.42 ± 0.04	6
381	NGC 4254	H142	0.13	0.43 ± 0.09	0.33 ± 0.15	0.25 ± 0.11	9.26 ± 0.03	8.70 ± 0.08	25
382	NGC 4254	H78	0.24	0.93 ± 0.15	0.06 ± 0.06	0.06 ± 0.06	9.21 ± 0.02	8.39 ± 0.06	25
383	NGC 4254	H173	0.25	0.72 ± 0.07	0.15 ± 0.05	0.13 ± 0.04	9.22 ± 0.01	8.52 ± 0.04	25
384	NGC 4254	H134	0.42	1.65 ± 0.13	0.16 ± 0.02	0.14 ± 0.02	9.13 ± 0.01	8.41 ± 0.04	25
385	NGC 4254	H185	0.53	1.93 ± 0.32	0.33 ± 0.08	0.25 ± 0.05	9.09 ± 0.02	8.50 ± 0.08	25
386	NGC 4254	H184	0.62	3.05 ± 0.24	0.61 ± 0.08	0.38 ± 0.04	9.01 ± 0.02	8.50 ± 0.05	25
387	NGC 4254	H84	0.64	3.73 ± 0.44	0.21 ± 0.04	0.17 ± 0.03	8.95 ± 0.04	8.18 ± 0.08	25
388	NGC 4254	H22	0.80	4.33 ± 0.15	0.33 ± 0.02	0.25 ± 0.01	8.90 ± 0.01	8.21 ± 0.03	25
389	NGC 4254	H12	0.86	3.85 ± 0.51	0.17 ± 0.04	0.15 ± 0.03	8.94 ± 0.05	8.12 ± 0.09	25
390	NGC 4254	HK20	0.58	2.45 ± 0.31	0.25 ± 0.05	0.20 ± 0.03	9.06 ± 0.02	8.38 ± 0.07	26
391	NGC 4254	HK1	0.74	3.05 ± 0.33	0.48 ± 0.09	0.32 ± 0.05	9.01 ± 0.02	8.44 ± 0.07	26
392	NGC 4254	HK208	0.82	2.22 ± 0.28	0.24 ± 0.04	0.19 ± 0.03	9.08 ± 0.02	8.40 ± 0.06	26
393	NGC 4254	+013+006	0.10	0.47 ± 0.09	0.15 ± 0.05	0.13 ± 0.04	9.27 ± 0.02	8.56 ± 0.05	4
394	NGC 4254	-005+042	0.27	1.23 ± 0.14	0.09 ± 0.04	0.08 ± 0.03	9.17 ± 0.01	8.38 ± 0.05	4
395	NGC 4254	+055-042	0.49	1.98 ± 0.25	0.49 ± 0.10	0.33 ± 0.05	9.08 ± 0.01	8.57 ± 0.06	4
396	NGC 4254	-047-075	0.55	2.01 ± 0.19	0.26 ± 0.04	0.21 ± 0.03	9.09 ± 0.01	8.44 ± 0.05	4
397	NGC 4254	+093+039	0.67	3.08 ± 0.41	0.31 ± 0.09	0.24 ± 0.07	9.01 ± 0.03	8.35 ± 0.08	4
398	NGC 4254	+102+015	0.71	3.30 ± 0.34	0.35 ± 0.05	0.26 ± 0.03	8.99 ± 0.03	8.35 ± 0.07	4
399	NGC 4321	HK160	0.31	1.27 ± 0.22	0.20 ± 0.09	0.17 ± 0.07	9.15 ± 0.02	8.50 ± 0.09	26
400	NGC 4321	HK143	0.48	1.39 ± 0.19	0.35 ± 0.10	0.26 ± 0.07	9.13 ± 0.01	8.58 ± 0.06	26
401	NGC 4321	HK201	0.74	3.36 ± 0.45	0.29 ± 0.08	0.23 ± 0.06	8.99 ± 0.04	8.30 ± 0.09	26
402	NGC 4321	HK284	0.67	2.51 ± 0.31	0.34 ± 0.07	0.26 ± 0.04	9.05 ± 0.02	8.44 ± 0.07	26
403	NGC 4321	HK128	0.68	2.30 ± 0.30	0.23 ± 0.04	0.19 ± 0.03	9.07 ± 0.02	8.38 ± 0.07	26
404	NGC 4321	-051+091	0.53	0.83 ± 0.11	0.12 ± 0.03	0.11 ± 0.03	9.21 ± 0.01	8.48 ± 0.04	4
405	NGC 4321	+032-074	0.41	0.78 ± 0.10	0.09 ± 0.02	0.08 ± 0.02	9.22 ± 0.01	8.45 ± 0.03	4
406	NGC 4321	-114+010	0.59	1.63 ± 0.17	0.14 ± 0.02	0.13 ± 0.01	9.13 ± 0.01	8.39 ± 0.04	4
407	NGC 4321	+034+145	0.68	1.87 ± 0.23	0.17 ± 0.04	0.15 ± 0.03	9.11 ± 0.01	8.38 ± 0.06	4
408	NGC 4559	+011-008	0.06	3.76 ± 0.35	0.38 ± 0.09	0.28 ± 0.06	8.95 ± 0.03	8.31 ± 0.06	6
409	NGC 4559	-026+103	0.40	6.04 ± 0.47	0.98 ± 0.15	0.50 ± 0.08	8.75 ± 0.04	8.29 ± 0.04	6
410	NGC 4559	-043+117	0.42	6.02 ± 0.65	1.23 ± 0.25	0.55 ± 0.11	8.76 ± 0.06	8.34 ± 0.05	6
411	NGC 4559	-074-094	0.97	6.42 ± 0.63	1.64 ± 0.29	0.62 ± 0.11	8.72 ± 0.06	8.36 ± 0.04	6
412	NGC 4559	+135-092	0.76	5.59 ± 0.51	0.46 ± 0.11	0.32 ± 0.07	8.78 ± 0.05	8.15 ± 0.06	6
413	NGC 4559	+129-113	0.69	5.09 ± 0.65	0.54 ± 0.14	0.35 ± 0.08	8.83 ± 0.06	8.25 ± 0.10	6
414	NGC 4559	+128-112	0.69	6.60 ± 1.91	1.16 ± 0.64	0.54 ± 0.32	8.69 ± 0.17	8.28 ± 0.10	6
415	NGC 4559	+124-114	0.66	7.35 ± 0.91	1.02 ± 0.25	0.50 ± 0.12	8.61 ± 0.09	8.18 ± 0.07	6
416	NGC 4559	+102-153	0.58	6.34 ± 0.60	2.62 ± 0.40	0.72 ± 0.12	8.75 ± 0.06	8.43 ± 0.03	6
417	NGC 4559	+098-193	0.68	5.91 ± 0.57	0.46 ± 0.12	0.31 ± 0.08	8.74 ± 0.06	8.11 ± 0.06	6
418	NGC 4559	+095-191	0.67	7.81 ± 0.77	1.46 ± 0.26	0.59 ± 0.11	8.57 ± 0.07	8.22 ± 0.05	6
419	NGC 4559	-111+184	0.67	6.98 ± 0.65	0.58 ± 0.13	0.37 ± 0.08	8.63 ± 0.07	8.07 ± 0.06	6
420	NGC 4559	-116+187	0.69	7.27 ± 0.69	0.42 ± 0.11	0.30 ± 0.08	8.59 ± 0.07	7.98 ± 0.11[a]	6
421	NGC 4559	-081+170	0.60	8.39 ± 1.06	1.00 ± 0.25	0.50 ± 0.13	8.49 ± 0.12	8.18 ± 0.08[a]	6
422	NGC 4559	-085+173	0.61	10.63 ± 1.54	0.80 ± 0.25	0.44 ± 0.15	... [b]	... [b]	6
423	NGC 4559	-077+167	0.59	8.61 ± 1.18	0.60 ± 0.20	0.38 ± 0.13	8.47 ± 0.09[a]	... [b]	6
424	NGC 4559	+062-051	0.34	4.99 ± 0.42	0.92 ± 0.16	0.48 ± 0.08	8.85 ± 0.04	8.38 ± 0.04	6
425	NGC 4559	+041-074	0.26	5.22 ± 0.32	0.74 ± 0.10	0.43 ± 0.06	8.82 ± 0.03	8.31 ± 0.03	6
426	NGC 4559	-014-017	0.18	4.07 ± 0.33	0.38 ± 0.08	0.28 ± 0.06	8.93 ± 0.03	8.27 ± 0.05	6
427	NGC 4559	-016+004	0.11	3.69 ± 0.29	0.37 ± 0.07	0.27 ± 0.05	8.96 ± 0.03	8.31 ± 0.05	6
428	NGC 4725	+101+042	0.39	1.03 ± 0.10	0.14 ± 0.04	0.13 ± 0.04	9.18 ± 0.01	8.48 ± 0.05	6
429	NGC 4725	+050+125	0.43	0.94 ± 0.10	0.18 ± 0.06	0.15 ± 0.05	9.18 ± 0.01	8.52 ± 0.05	6
430	NGC 4725	-120-095	0.50	2.18 ± 0.26	0.20 ± 0.07	0.17 ± 0.06	9.08 ± 0.02	8.37 ± 0.07	6
431	NGC 4725	-066-127	0.45	1.17 ± 0.16	0.09 ± 0.02	0.09 ± 0.02	9.17 ± 0.01	8.40 ± 0.05	6
432	NGC 4725	-047-120	0.41	3.89 ± 0.78	0.22 ± 0.09	0.18 ± 0.07	8.94 ± 0.07	8.17 ± 0.15	6
433	NGC 4725	+040+124	0.42	2.11 ± 0.20	0.21 ± 0.06	0.17 ± 0.05	9.09 ± 0.01	8.39 ± 0.05	6
434	NGC 4725	+020+123	0.43	1.58 ± 0.25	0.09 ± 0.06	0.08 ± 0.06	9.14 ± 0.02	8.33 ± 0.08	6
435	NGC 4725	+122+010	0.49	2.87 ± 0.30	0.10 ± 0.02	0.09 ± 0.02	9.03 ± 0.02	8.16 ± 0.06	6
436	NGC 4736	HK8	0.12	3.23 ± 0.12	0.57 ± 0.03	0.36 ± 0.02	9.00 ± 0.01	8.46 ± 0.02	1
437	NGC 4736	HK45	0.10	2.19 ± 0.09	0.26 ± 0.02	0.21 ± 0.02	9.08 ± 0.01	8.42 ± 0.02	1
438	NGC 4736	HK52	0.12	2.07 ± 0.09	0.20 ± 0.01	0.16 ± 0.01	9.09 ± 0.01	8.38 ± 0.02	1
439	NGC 4736	HK53	0.13	2.93 ± 0.10	0.44 ± 0.03	0.31 ± 0.01	9.02 ± 0.01	8.44 ± 0.02	1
440	NGC 4736	+116-038	0.36	2.88 ± 0.13	0.20 ± 0.03	0.17 ± 0.03	9.03 ± 0.01	8.28 ± 0.03	15
441	NGC 4736	+123-055	0.40	3.16 ± 0.19	0.32 ± 0.04	0.24 ± 0.03	9.01 ± 0.02	8.34 ± 0.04	15
442	NGC 4736	+037+009	0.12	3.05 ± 0.15	0.60 ± 0.06	0.38 ± 0.03	9.01 ± 0.01	8.49 ± 0.03	15
443	NGC 4736	+037+003	0.11	2.70 ± 0.12	0.32 ± 0.04	0.24 ± 0.03	9.04 ± 0.01	8.40 ± 0.03	15
444	NGC 4736	+032-016	0.11	2.78 ± 0.27	0.27 ± 0.05	0.21 ± 0.04	9.04 ± 0.02	8.35 ± 0.06	15
445	NGC 4736	-029+014	0.10	2.14 ± 0.14	0.26 ± 0.05	0.21 ± 0.04	9.08 ± 0.01	8.43 ± 0.04	15
446	NGC 4736	-036-003	0.11	3.64 ± 0.16	0.20 ± 0.03	0.17 ± 0.02	8.96 ± 0.01	8.19 ± 0.03	15
447	NGC 4736	-038+009	0.12	2.01 ± 0.14	0.21 ± 0.05	0.17 ± 0.04	9.10 ± 0.01	8.40 ± 0.04	15
448	NGC 4736	-039+020	0.13	3.00 ± 0.13	0.34 ± 0.04	0.25 ± 0.03	9.02 ± 0.01	8.37 ± 0.03	15
449	NGC 4736	-039+017	0.13	2.55 ± 0.37	0.45 ± 0.10	0.31 ± 0.05	9.05 ± 0.02	8.49 ± 0.08	4

TABLE 10 — *Continued*

No. (1)	Galaxy (2)	Region (3)	ρ/ρ_{25} (4)	R_{23} (5)	O_{32} (6)	P (7)	$12+\log(\mathrm{O/H})_{\mathrm{KK04}}$ (8)	$12+\log(\mathrm{O/H})_{\mathrm{PT05}}$ (9)	Ref. (10)
450	NGC 4736	+040+010	0.13	2.63 ± 0.24	0.31 ± 0.05	0.24 ± 0.03	9.05 ± 0.02	8.40 ± 0.05	4
451	DDO 154	H2	0.28	4.57 ± 0.15	1.84 ± 0.13	0.65 ± 0.03	7.99 ± 0.02	7.60 ± 0.02	27
452	DDO 154	H3	0.41	3.72 ± 0.22	0.69 ± 0.08	0.41 ± 0.04	7.98 ± 0.04	7.49 ± 0.03	27
453	DDO 154	H1	0.90	4.65 ± 0.14	1.45 ± 0.09	0.59 ± 0.03	8.02 ± 0.02	7.64 ± 0.02	28
454	DDO 154	H2	0.41	4.17 ± 0.17	0.40 ± 0.03	0.29 ± 0.02	8.10 ± 0.03	7.45 ± 0.03	28
455	NGC 4826	-006+016	0.09	0.49 ± 0.14	0.10 ± 0.19	0.09 ± 0.17	9.28 ± 0.05	8.51 ± 0.11	15
456	NGC 4826	-012+019	0.10	0.46 ± 0.14	0.18 ± 0.22	0.15 ± 0.19	9.27 ± 0.05	8.59 ± 0.12	15
457	NGC 4826	-017+020	0.11	0.59 ± 0.14	0.32 ± 0.20	0.24 ± 0.15	9.21 ± 0.04	8.67 ± 0.10	15
458	NGC 4826	+008+012	0.09	0.77 ± 0.15	0.17 ± 0.13	0.15 ± 0.11	9.20 ± 0.03	8.54 ± 0.09	15
459	NGC 4826	+015+011	0.11	0.49 ± 0.14	0.24 ± 0.21	0.19 ± 0.17	9.25 ± 0.05	8.63 ± 0.11	15
460	DDO 165	H4	0.55	4.44 ± 0.51	0.97 ± 0.22	0.49 ± 0.09	8.04 ± 0.07	7.63 ± 0.08	11
461	NGC 5033	+144-155	1.00	4.77 ± 0.25	0.34 ± 0.05	0.25 ± 0.04	8.86 ± 0.02	8.17 ± 0.04	6
462	NGC 5033	+028-215	0.68	5.78 ± 0.34	0.43 ± 0.07	0.30 ± 0.05	8.75 ± 0.04	8.11 ± 0.04	6
463	NGC 5033	+022-217	0.69	8.11 ± 0.63	0.25 ± 0.06	0.20 ± 0.05	8.51 ± 0.04[a]	... [b]	6
464	NGC 5033	+052-097	0.41	4.92 ± 0.41	0.32 ± 0.08	0.24 ± 0.06	8.84 ± 0.04	8.13 ± 0.06	6
465	NGC 5033	-065+013	0.45	3.88 ± 0.28	0.49 ± 0.09	0.33 ± 0.06	8.95 ± 0.02	8.36 ± 0.04	6
466	NGC 5033	-065-001	0.46	4.54 ± 0.76	0.18 ± 0.07	0.15 ± 0.06	8.87 ± 0.08	8.04 ± 0.14	6
467	NGC 5033	-066-033	0.51	5.40 ± 0.64	0.46 ± 0.14	0.31 ± 0.10	8.80 ± 0.06	8.17 ± 0.08	6
468	NGC 5033	-014+028	0.11	0.79 ± 0.09	0.55 ± 0.15	0.35 ± 0.10	9.16 ± 0.02	8.74 ± 0.04	6
469	NGC 5055	-089-010	0.27	0.79 ± 0.14	0.15 ± 0.05	0.13 ± 0.05	9.20 ± 0.02	8.52 ± 0.07	4
470	NGC 5055	-112-034	0.40	1.09 ± 0.36	0.24 ± 0.12	0.20 ± 0.08	9.16 ± 0.02	8.55 ± 0.12	4
471	NGC 5055	+050-088	0.39	2.33 ± 0.34	0.08 ± 0.02	0.08 ± 0.02	9.08 ± 0.03	8.22 ± 0.06	4
472	NGC 5055	-165+034	0.45	1.41 ± 0.18	0.18 ± 0.03	0.15 ± 0.03	9.14 ± 0.01	8.45 ± 0.05	4
473	NGC 5055	-270+068	0.74	3.83 ± 0.46	0.22 ± 0.06	0.18 ± 0.05	8.95 ± 0.04	8.18 ± 0.10	4
474	NGC 5194	CCM10	0.47	1.42 ± 0.09	0.13 ± 0.01	0.11 ± 0.01	9.15 ± 0.01	8.40 ± 0.02	29
475	NGC 5194	CCM53	0.47	1.73 ± 0.09	0.34 ± 0.03	0.26 ± 0.02	9.11 ± 0.01	8.53 ± 0.03	29
476	NGC 5194	CCM54	0.49	1.70 ± 0.09	0.48 ± 0.04	0.33 ± 0.02	9.10 ± 0.01	8.60 ± 0.02	29
477	NGC 5194	CCM55	0.48	1.03 ± 0.05	0.33 ± 0.03	0.25 ± 0.02	9.15 ± 0.01	8.61 ± 0.02	29
478	NGC 5194	CCM57	0.47	1.35 ± 0.08	0.19 ± 0.02	0.16 ± 0.01	9.14 ± 0.01	8.47 ± 0.02	29
479	NGC 5194	CCM57A	0.43	3.29 ± 0.15	2.16 ± 0.19	0.68 ± 0.05	8.99 ± 0.01	8.66 ± 0.01	29
480	NGC 5194	CCM71A	0.71	2.09 ± 0.04	0.42 ± 0.02	0.30 ± 0.02	9.08 ± 0.01	8.53 ± 0.01	29
481	NGC 5194	CCM72	0.38	0.72 ± 0.06	0.14 ± 0.02	0.12 ± 0.01	9.22 ± 0.01	8.52 ± 0.02	29
482	NGC 5194	CCM84A	0.38	2.38 ± 0.14	0.91 ± 0.10	0.48 ± 0.04	9.05 ± 0.01	8.64 ± 0.03	29
483	NGC 5194	P203	0.18	0.39 ± 0.02	0.20 ± 0.02	0.17 ± 0.01	9.29 ± 0.01	8.62 ± 0.02	29
484	NGC 5194	CCM6A	0.10	0.21 ± 0.01	0.26 ± 0.02	0.21 ± 0.02	9.39 ± 0.01	8.68 ± 0.01	29
485	NGC 5194	CCM37A	0.11	0.22 ± 0.01	0.28 ± 0.03	0.22 ± 0.02	9.38 ± 0.01	8.70 ± 0.02	29
486	NGC 5194	CCM45	0.26	0.38 ± 0.02	0.12 ± 0.01	0.11 ± 0.01	9.31 ± 0.01	8.55 ± 0.02	29
487	NGC 5194	CCM56	0.21	0.37 ± 0.02	0.31 ± 0.04	0.23 ± 0.03	9.28 ± 0.01	8.69 ± 0.02	29
488	NGC 5194	CCM107	0.17	0.23 ± 0.01	0.13 ± 0.01	0.11 ± 0.01	9.39 ± 0.01	8.58 ± 0.01	29
489	NGC 5194	CCM72	0.38	0.78 ± 0.03	0.16 ± 0.01	0.14 ± 0.01	9.20 ± 0.01	8.53 ± 0.01	30
490	NGC 5194	CCM10	0.47	1.89 ± 0.12	0.16 ± 0.02	0.14 ± 0.02	9.11 ± 0.01	8.38 ± 0.03	30
491	NGC 5194	CCM37a	0.11	0.45 ± 0.11	0.18 ± 0.16	0.16 ± 0.13	9.27 ± 0.05	8.60 ± 0.11	1
492	NGC 5194	CCM10	0.47	1.24 ± 0.06	0.17 ± 0.02	0.15 ± 0.02	9.16 ± 0.01	8.47 ± 0.03	1
493	NGC 5194	CCM72	0.38	0.65 ± 0.03	0.14 ± 0.01	0.12 ± 0.01	9.23 ± 0.01	8.53 ± 0.02	1
494	NGC 5194	CCM55	0.48	1.10 ± 0.05	0.25 ± 0.03	0.20 ± 0.02	9.16 ± 0.01	8.56 ± 0.02	1
495	NGC 5194	CCM53	0.47	1.28 ± 0.06	0.23 ± 0.02	0.19 ± 0.02	9.14 ± 0.01	8.52 ± 0.02	1
496	NGC 5194	CCM84	0.25	1.18 ± 0.23	0.42 ± 0.20	0.30 ± 0.14	9.14 ± 0.02	8.64 ± 0.08	1
497	NGC 5194	CCM91	0.40	1.99 ± 0.18	0.27 ± 0.06	0.21 ± 0.05	9.09 ± 0.01	8.45 ± 0.05	1
498	NGC 5194	CCM71a	0.71	2.37 ± 0.11	0.42 ± 0.03	0.30 ± 0.02	9.06 ± 0.01	8.50 ± 0.02	1
499	NGC 5194	CCM68	0.42	0.98 ± 0.10	0.08 ± 0.05	0.07 ± 0.05	9.20 ± 0.02	8.41 ± 0.06	1
500	NGC 5194	X	...	1.47 ± 0.18	0.28 ± 0.12	0.22 ± 0.09	9.13 ± 0.02	8.53 ± 0.07	31
501	NGC 5194	CCM72	0.38	0.68 ± 0.07	0.11 ± 0.05	0.10 ± 0.04	9.23 ± 0.02	8.49 ± 0.05	31
502	NGC 5194	CCM24	...	1.25 ± 0.14	0.22 ± 0.13	0.18 ± 0.11	9.15 ± 0.02	8.52 ± 0.08	31
503	NGC 5194	CCM10	0.47	1.89 ± 0.12	0.16 ± 0.02	0.14 ± 0.02	9.11 ± 0.01	8.38 ± 0.03	31
504	NGC 5194	-007+061	0.18	0.45 ± 0.06	0.21 ± 0.05	0.17 ± 0.04	9.27 ± 0.02	8.62 ± 0.05	4
505	NGC 5194	-087-082	0.37	0.59 ± 0.07	0.15 ± 0.04	0.13 ± 0.03	9.24 ± 0.02	8.55 ± 0.04	4
506	NGC 5194	-137-182	0.71	2.86 ± 0.60	0.25 ± 0.07	0.20 ± 0.04	9.03 ± 0.04	8.33 ± 0.14	4
507	NGC 5194	-007-303	0.91	3.64 ± 0.42	0.63 ± 0.14	0.39 ± 0.07	8.97 ± 0.03	8.44 ± 0.09	4
508	NGC 5408	H1	...	8.71 ± 0.79	9.49 ± 1.34	0.90 ± 0.12	8.23 ± 0.06	7.81 ± 0.09	32
509	NGC 6822	H12	0.20	5.43 ± 0.07	0.22 ± 0.01	0.18 ± 0.01	8.78 ± 0.01	7.98 ± 0.01	33
510	NGC 6822	HUBBLEIII SE RING	0.98	7.37 ± 0.09	1.12 ± 0.03	0.53 ± 0.01	8.61 ± 0.01	8.20 ± 0.01	33
511	NGC 6822	HUBBLEIII NW ARC	0.98	6.15 ± 0.13	0.68 ± 0.03	0.41 ± 0.01	8.73 ± 0.01	8.20 ± 0.02	33
512	NGC 6822	HUBBLEIII NW RING	0.98	5.16 ± 0.08	0.59 ± 0.02	0.37 ± 0.01	8.83 ± 0.01	8.26 ± 0.01	33
513	NGC 6822	HUBBLEV BLUE	0.73	8.33 ± 0.07	4.91 ± 0.06	0.83 ± 0.01	8.57 ± 0.01	8.33 ± 0.01	33
514	NGC 6822	KBETA BLUE	0.88	8.91 ± 0.06	3.41 ± 0.05	0.77 ± 0.01	8.49 ± 0.01	8.26 ± 0.01	33
515	NGC 6822	KD22E	0.72	5.64 ± 0.07	0.19 ± 0.01	0.16 ± 0.01	8.75 ± 0.01	7.93 ± 0.01	33
516	NGC 6822	KD28E BLUE	0.08	7.97 ± 0.04	2.32 ± 0.02	0.70 ± 0.01	8.57 ± 0.01	8.28 ± 0.01	33
517	NGC 6822	HK16	0.58	5.75 ± 0.35	0.16 ± 0.03	0.14 ± 0.02	8.74 ± 0.04	7.87 ± 0.05	33
518	NGC 6822	HK42	0.62	9.70 ± 0.59	0.74 ± 0.08	0.42 ± 0.04	... [b]	... [b]	33
519	NGC 6822	HK70	0.11	10.75 ± 0.44	1.20 ± 0.11	0.55 ± 0.03	... [b]	... [b]	33
520	NGC 6822	H7	0.29	7.37 ± 0.31	0.55 ± 0.06	0.36 ± 0.04	8.58 ± 0.03	8.05 ± 0.03[a]	33
521	NGC 6822	H12	0.20	6.11 ± 0.24	0.14 ± 0.01	0.12 ± 0.01	8.69 ± 0.03	7.81 ± 0.04	33
522	NGC 6822	HUBBLEV LOW	0.73	8.62 ± 0.25	5.69 ± 0.34	0.85 ± 0.04	8.55 ± 0.02	8.33 ± 0.02	33
523	NGC 6822	KBETA LOW	0.88	6.65 ± 0.86	0.16 ± 0.04	0.14 ± 0.03	8.63 ± 0.11	7.76 ± 0.13	33
524	NGC 6822	KD9	0.59	4.88 ± 0.39	0.29 ± 0.05	0.23 ± 0.04	8.84 ± 0.04	8.12 ± 0.07	33

TABLE 10 — *Continued*

No. (1)	Galaxy (2)	Region (3)	ρ/ρ_{25} (4)	R_{23} (5)	O_{32} (6)	P (7)	$12+\log(\mathrm{O/H})_{\mathrm{KK04}}$ (8)	$12+\log(\mathrm{O/H})_{\mathrm{PT05}}$ (9)	Ref. (10)
525	NGC 6822	KD21	0.76	5.69 ± 0.26	0.33 ± 0.02	0.25 ± 0.01	8.76 ± 0.03	8.05 ± 0.04	33
526	NGC 6822	KD24	0.04	8.37 ± 0.90	0.03 ± 0.01	0.03 ± 0.01	... [b]	... [b]	33
527	NGC 6822	KD25	0.26	5.83 ± 0.18	0.08 ± 0.01	0.08 ± 0.01	8.72 ± 0.02	7.75 ± 0.03	33
528	NGC 6822	KD28E LOW	0.08	8.38 ± 0.14	1.74 ± 0.06	0.64 ± 0.02	8.52 ± 0.02	8.21 ± 0.01	33
529	NGC 6822	HUBBLEV	...	8.08 ± 0.06	7.64 ± 0.14	0.88 ± 0.01	8.63 ± 0.01	8.38 ± 0.01	34
530	NGC 6822	HUBBLEX	...	7.15 ± 0.07	3.88 ± 0.10	0.79 ± 0.01	8.68 ± 0.01	8.40 ± 0.01	34
531	NGC 6946	FGW6946A	0.61	4.69 ± 0.18	0.91 ± 0.07	0.48 ± 0.02	8.88 ± 0.02	8.41 ± 0.03	2
532	NGC 6946	FGW6946B	0.66	2.59 ± 0.15	0.23 ± 0.02	0.19 ± 0.01	9.05 ± 0.01	8.34 ± 0.03	2
533	NGC 6946	-008+066	0.22	1.73 ± 0.22	0.19 ± 0.04	0.16 ± 0.04	9.12 ± 0.01	8.42 ± 0.06	4
534	NGC 6946	+144-003	0.45	2.03 ± 0.33	0.20 ± 0.05	0.17 ± 0.04	9.09 ± 0.02	8.39 ± 0.08	4
535	NGC 6946	+182+103	0.61	5.44 ± 0.30	0.94 ± 0.10	0.48 ± 0.03	8.81 ± 0.03	8.34 ± 0.05	4
536	NGC 6946	-128+146	0.67	3.26 ± 0.30	0.38 ± 0.05	0.28 ± 0.03	9.00 ± 0.02	8.37 ± 0.06	4
537	NGC 6946	-245+055	0.81	3.04 ± 0.44	0.46 ± 0.10	0.32 ± 0.05	9.01 ± 0.03	8.44 ± 0.10	4
538	NGC 6946	-099-261	0.86	4.18 ± 0.24	0.42 ± 0.04	0.30 ± 0.02	8.92 ± 0.02	8.28 ± 0.04	4
539	NGC 7331	HK95	0.39	2.68 ± 0.23	0.19 ± 0.04	0.16 ± 0.04	9.05 ± 0.02	8.30 ± 0.05	1
540	NGC 7331	HK98	0.38	2.70 ± 0.17	0.16 ± 0.03	0.14 ± 0.02	9.05 ± 0.01	8.27 ± 0.04	1
541	NGC 7331	HK101	0.32	2.42 ± 0.24	0.21 ± 0.06	0.17 ± 0.05	9.07 ± 0.02	8.35 ± 0.06	1
542	NGC 7331	HK40	0.48	3.76 ± 0.18	0.50 ± 0.04	0.34 ± 0.03	8.96 ± 0.02	8.37 ± 0.03	1
543	NGC 7331	-032-016	0.36	2.77 ± 0.21	0.35 ± 0.05	0.26 ± 0.04	9.04 ± 0.02	8.41 ± 0.04	15
544	NGC 7331	-028+018	0.27	1.83 ± 0.16	0.24 ± 0.06	0.19 ± 0.05	9.11 ± 0.01	8.45 ± 0.05	15
545	NGC 7331	-028+013	0.28	2.52 ± 0.37	0.32 ± 0.09	0.24 ± 0.06	9.05 ± 0.03	8.42 ± 0.08	15
546	NGC 7331	-031+024	0.30	2.72 ± 0.17	0.30 ± 0.04	0.23 ± 0.03	9.04 ± 0.01	8.38 ± 0.03	15
547	NGC 7331	-034+037	0.32	2.96 ± 0.19	0.18 ± 0.04	0.15 ± 0.03	9.02 ± 0.02	8.25 ± 0.04	15
548	NGC 7331	-032+027	0.31	1.70 ± 0.19	0.15 ± 0.06	0.13 ± 0.05	9.12 ± 0.02	8.39 ± 0.07	15
549	NGC 7552	H1	...	1.34 ± 0.06	0.08 ± 0.02	0.07 ± 0.02	9.16 ± 0.01	8.35 ± 0.03	35
550	NGC 7793	W11	0.96	6.52 ± 0.43	1.06 ± 0.14	0.51 ± 0.05	8.70 ± 0.05	8.27 ± 0.05	36
551	NGC 7793	-010+033	0.18	5.31 ± 1.00	0.43 ± 0.12	0.30 ± 0.06	8.80 ± 0.11	8.17 ± 0.17	4
552	NGC 7793	-075-024	0.31	4.55 ± 0.50	0.76 ± 0.15	0.43 ± 0.05	8.89 ± 0.05	8.38 ± 0.08	4
553	NGC 7793	-104+035	0.40	5.13 ± 0.80	0.59 ± 0.16	0.37 ± 0.07	8.83 ± 0.09	8.27 ± 0.14	4
554	NGC 7793	-173+102	0.78	5.95 ± 1.27	0.45 ± 0.14	0.31 ± 0.07	8.74 ± 0.13	8.11 ± 0.22	4
555	NGC 7793	+092+098	0.66	5.55 ± 1.12	0.60 ± 0.27	0.37 ± 0.16	8.79 ± 0.11	8.22 ± 0.14	4
556	NGC 7793	NUCLEUS	0.00	2.53 ± 0.15	0.27 ± 0.03	0.21 ± 0.02	9.06 ± 0.01	8.38 ± 0.03	36
557	NGC 7793	W12	0.16	3.22 ± 0.19	0.54 ± 0.05	0.35 ± 0.02	9.00 ± 0.02	8.45 ± 0.04	36
558	NGC 7793	W2	0.26	5.14 ± 0.25	0.70 ± 0.07	0.41 ± 0.04	8.83 ± 0.03	8.30 ± 0.04	36
559	NGC 7793	W5 6	0.41	4.12 ± 0.17	0.24 ± 0.03	0.20 ± 0.02	8.92 ± 0.02	8.16 ± 0.03	36
560	NGC 7793	W13	0.66	6.73 ± 0.82	0.51 ± 0.09	0.34 ± 0.04	8.65 ± 0.10	8.06 ± 0.13	36
561	NGC 7793	DV132	0.81	6.12 ± 0.61	1.93 ± 0.35	0.66 ± 0.11	8.76 ± 0.05	8.41 ± 0.04	36

REFERENCES. — (1) Bresolin et al. (1999); (2) Ferguson et al. (1998); (3) van Zee et al. (1998); (4) McCall et al. (1985); (5) Castellanos et al. (2002); (6) Zaritsky et al. (1994); (7) Storchi-Bergmann et al. (1996); (8) Lee & Skillman (2004); (9) Garnett et al. (1999); (10) Garnett et al. (1997); (11) Croxall et al. (2009); (12) Lee et al. (2003b); (13) Masegosa et al. (1991); (14) Skillman et al. (1989); (15) Oey & Kennicutt (1993); (16) Lee et al. (2003a); (17) Miller & Hodge (1996); (18) Guseva et al. (2000); (19) Garnett & Shields (1987); (20) Stauffer & Bothun (1984); (21) Kong & Cheng (2002); (22) Díaz et al. (2007); (23) Bresolin & Kennicutt (2002); (24) Ryder (1995); (25) Henry et al. (1994); (26) Shields (1991); (27) Kennicutt & Skillman (2001); (28) van Zee et al. (1997); (29) Bresolin et al. (2004); (30) Garnett et al. (2004b); (31) Diaz et al. (1991); (32) Stasińska et al. (1986); (33) Lee et al. (2006b); (34) Peimbert et al. (2005); (35) Storchi-Bergmann et al. (1995); (36) Edmunds & Pagel (1984).

NOTE. — (1-2) Unique H II-region identification number and SINGS galaxy name; (3) H II-region name as listed in the originating reference, if available; (4) Deprojected galactocentric radius normalized by the ρ_{25} radius of the galaxy (see Table 1); (5-7) Abundance-sensitive R_{23} parameter and excitation parameters O_{32} and P (see §4.1) (8-9) Oxygen abundances derived using the KK04 and PT05 strong-line calibrations assuming the R_{23} branch listed in Table 7, unless otherwise noted; (10) References to the literature from which the H II-region line-ratios were taken (see Appendix B).

[a] The R_{23} branch of this H II region is ambiguous according to the criteria described in §4.2.

[b] The oxygen abundance of this H II region is not defined according to the criteria described in §4.2.